Large Eddy Simulations of plasma assisted combustion

Yacine Bechane

université PARIS-SACLAY

Large Eddy Simulations of plasma assisted combustion

Simulations aux grandes échelles de la combustion assistée par plasma

Thèse de doctorat de l'université Paris-Saclay

École doctorale n° 579, Sciences mécaniques et énergétiques, matériaux et géosciences (SMEMAG)
Spécialité de doctorat : Combustion
Graduate School : Sciences de l'ingénierie et des systèmes
Référent : CentraleSupélec

Thèse préparée dans l'unité de recherche : Laboratoire EM2C (Université Paris-Saclay, CNRS, CentraleSupélec) sous la direction de Benoît FIORINA, professeur.

Thèse soutenue à Paris-Saclay, le 30 Novembre 2022, par

Yacine BECHANE

Composition du jury

Membres du jury avec voix délibérative

Armelle CESSOU Directrice de recherche, CNRS, CORIA, Université de Rouen Normandie	Présidente
Fabrizio BISETTI Professeur, University of Texas	Rapporteur & Examinateur
Laurent SELLE Directeur de recherche, CNRS, IMFT, Université Toulouse III	Rapporteur & Examinateur
Christophe LAUX Professeur, CentraleSupélec, CNRS, EM2C, Université Paris-Saclay	Examinateur
Svetlana STARIKOVSKAIA Directrice de recherche, CNRS, LPP, Sorbonne Université	Examinatrice
Olivier VERMOREL Ingénieur de recherche, CERFACS, Toulouse INP	Examinateur

THESE DE DOCTORAT
NNT : 2022UPAST163

université PARIS-SACLAY

ÉCOLE DOCTORALE
Sciences mécaniques et énergétiques, matériaux et géosciences (SMEMAG)

Titre : Simulations aux grandes échelles de la combustion assistée par plasma
Mots clés : Combustion assistée par plasma, Décharges nanosecondes à impulsions répétitives, Flamme turbulente prémélangée, Simulations aux grandes échelles.

Résumé : Les normes environnementales de plus en plus sévères en matière d'émission de polluants imposent une rupture technologique aux industries du domaine de la combustion. Une solution efficace pour réduire la formation de polluants consiste à maintenir une température de flamme relativement basse en opérant à des régimes de combustion pauvres. Cependant, les flammes à basse température sont sujettes à des instabilités et des extinctions, ce qui pose des problèmes de sécurité. Une solution émergente pour permettre l'allumage et la stabilisation des flammes dans des régimes pauvres, adaptée à une large gamme d'applications de combustion, consiste à appliquer des décharges plasma à la base de la flamme. Parmi ces différents types de décharges, les décharges NRP (Nanosecond Repetitively Pulsed discharges) se sont révélées particulièrement efficaces. Ces décharges génèrent un plasma hors équilibre qui induit un échauffement local et une production importante d'espèces actives suffisante pour favoriser la combustion. Malgré une efficacité démontrée expérimentalement, les mécanismes de la combustion assistée par plasma ne sont pas compris, soulignant le besoin de simulations numériques. Un modèle phénoménologique de plasma a été récemment développé pour capturer l'influence des décharges NRP sur le processus de combustion à un faible coût de CPU. Le modèle est implémenté dans un code CFD à faible nombre de Mach, YALES2, pour réaliser des simulations 3D à grands echelles (LES) d'allumage et de combustion assistés par plasma dans des configurations industrielles. Les séquences d'allumage de la configuration expérimentale flow tunnel, une chambre de combustion de méthane-air en écoulement, et de la configuration Mini-PAC, un brûleur méthane-air prémélangé turbulent avec un accroche flamme, par une série d'impulsions de décharge NRP sont simulées pour donner un nouvel aperçu des mécanismes d'interaction entre la combustion et les décharges plasma. Des simulations LES de stabilisation de la flamme par des décharges NRP sont ensuite réalisés pour comprendre les mécanismes physiques et chimiques impliqués dans la combustion assistée par plasma.

université PARIS-SACLAY

ÉCOLE DOCTORALE
Sciences mécaniques et énergétiques, matériaux et géosciences (SMEMAG)

Title : Large Eddy Simulations of plasma assisted combustion
Keywords : Plasma-assisted combustion, Nanosecond Repetitively Pulsed discharges, Turbulent premixed flame, Large Eddy Simulations

Abstract : The more and more severe environmental norms on pollutant emission impose a technological breakthrough to combustion-related industries. An efficient solution to reduce pollutant formation is to maintain a relatively low flame temperature by operating at lean combustion regimes. However, low-temperature flames are subject to instabilities and extinction, causing safety issues. An emerging solution to enable flame ignition and stabilization in lean regimes, suitable to a wide range of combustion applications, is to apply plasma discharges at the flame basis. Among these various types of discharges, the Nanosecond Repetitively Pulsed discharges have shown to be particularly efficient. These discharges generate a non-equilibrium plasma that induces a local heating and an important production of active species sufficient to enhance the combustion. Despite this proven efficiency demonstrated experimentally, the mechanisms of plasma assisted-combustion are not understood, highlighting the need of numerical simulations. A phenomenological plasma model have been recently developed to capture the influence of NRP discharges on the combustion process at low CPU cost. The model is implemented in a low-Mach number CFD code YALES2 to perform 3-D Large Eddy Simulations (LES) of plasma-assisted ignition and combustion in practical configurations. The ignition sequences of the flow tunnel experimental setup, a flowing methane-air combustion chamber, and the Mini-PAC configuration, bluff-body turbulent premixed methane-air burner, by a series of NRP discharge pulses are simulated to give new insights into plasma discharge combustion interaction mechanisms. LES of the Mini-PAC burner flame stabilization by NRP discharges are then conducted to understand the physical and chemical mechanisms involved in plasma-assisted combustion.

Remerciements

Tout d'abord, je souhaite remercier les membres du jury d'avoir accepter d'évaluer mes travaux de thèse. Merci à Armelle Cessou d'avoir présider le jury. Merci à Laurent Selle et Fabrizio Bisetti pour avoir pris le temps de lire en détail mon manuscrit et pour les différents retours qu'ils m'ont faits. Merci aussi à Svetlana Starikovskaia, Olivier Vermorel et Christophe Laux pour leurs questions pertinentes et commentaires constructifs le jour de la soutenance.

Je tiens ensuite à remercier mon directeur de thèse Benoît Fiorina sans qui je n'aurai pas entrepris cette aventure et mené à bien ce travail. Merci de m'avoir encourager à me lancer dans la recherche et de m'avoir proposer de faire cette thèse. Merci de m'avoir encadrer, aider et soutenu tout au long de ces années. Merci de m'avoir fait confiance et de m'avoir permis de participer à différentes conférences et à faire de l'enseignement. Je suis honoré d'avoir pu travailler avec toi et espère pouvoir continuer le faire dans le futur.

Je remercie aussi Nasser Darabiha qui a grandement contribué à l'encadrement de ma thèse. Merci d'avoir apporter un oeil critique et une aide précieuse à ce travail, du premier jour jusqu'au dernier. Ton expertise, ta générosité et ta passion pour la recherche m'ont inspiré et continueront à m'inspirer tout au long de ma carrière.

Je remercie l'équipe plasma, Christophe Laux, Victorien Blanchard, Nicolas Minesi, Gabi Stancu avec qui j'ai eu la chance de collaborer dans le cadre du projet PASTEC et la réalisation de ce travail. Merci pour les données expérimentales, merci pour les discussions scientifiques, pour les séances de questions réponses mais aussi pour tout le bons moments qu'on a passé ensemble en conférences et voyages entre l'EM2C et le CORIA. Sans oublier les autres collaborateurs du projet PASTEC, l'équipe du CERFACS, l'équipe du CORIA et l'équipe de SAFRAN HELICOPTER ENGINES.

Merci à Brigitte, Nathalie et Noï pour leur gentillesse et le travail incroyable qu'elles font au quotidien pour assurer des conditions de travail optimales à l'EM2C. Merci aussi à Jean-Michel pour sa disponibilité en tout temps et son aider sur des problèmes de compilation et d'accès aux calculateurs. Merci au

directeur du laboratoire Sébastien Ducruix ainsi qu'à l'ensemble du personnel du laboratoire EM2C avec qui j'ai passé 3 ans et demi formidables. Merci aussi à tous les doctorants, Victorien, Guillaume, Livia, Nicolas, Karl, Junghwa, Kevin, Mateo, Giunio, Guilhem, Luc, Pierre, Victor, Erwan et bien d'autres pour tous les bons moments qu'on a passé ensemble durant les pauses café, les repas, les formations et les conférences.

Je remercie du fond du coeur les doctorants de l'équipe Benoît. Les anciens: Melody, Adrian, Cédric, Giampaolo, les nouveaux: Tan-Phong, Enrico, Samuel, Stéphane et plus particulièrement ceux de ma génération Hernando et Constantin avec qui j'étais en cours puis entrepris cette thèse. Ces les deux personnes avec qui j'ai passé le plus de temps ces dernières années bien sûr à bosser et à faire des meetings hebdomadaires mais aussi à discuter, à rigoler et à voyager. Merci les gars, merci pour votre amitié.

Merci à Vincent Moureau, Ghislain Lartigue et Pierre Benard de m'avoir permis d'utiliser le code YALES2 pour mes simulations et pour le temps qu'ils ont passé avec moi lors des Extreme CFD workshops à m'aider dans mes développements. Un grand merci aussi de m'avoir donné l'opportunité de rejoindre l'équipe YALES2 et de m'avoir permis de finir ma thèse dans de très bonnes conditions. Merci aussi aux doctorants et post-doctorant de l'équipe YALES2, François, Julien, Léa, Serge, Pierre, Adrien, Antoine, Félix, Iason, Ibtissem pour l'accueille chaleureux et les encouragements lors de la rédaction de ce manuscrit.

Pour finir, je tiens à remercier ma famille. Merci à ma tante, son mari et leurs enfants de m'avoir accueilli dans leur famille et de m'avoir souvent inviter à sortir et à voyager avec eux pour me changer les idées et profiter un peu de la vie. Merci à mes soeurs à qui me parlaient régulièrement, prenaient de mes nouvelles, me faisaient rire et m'encourager dans les moments difficiles. A mes parents, ceux à qui je dois tout, merci d'avoir toujours cru en moi et de m'avoir soutenu dans mes choix. C'est grâce à vous que je continue à avancer et que j'essaye chaque jour de faire de mon mieux.

Contents

List of Tables

List of Figures

Chapter 1

Introduction

Contents

1.1 General context

More than 80% of the world's primary energy is today produced by burning fossil fuels, including oil, natural gas and coal (International-Energy-Agency (2022)). A situation that is unsustainable due to the depletion of available fossil resources and the harmful impact of fossil fuel combustion processes exhaust gases, such as carbon dioxide (CO_2), carbon monoxide (CO), nitrogen oxides (NOx), soot, on the environment and human health. Since the COVID19 crisis, research in the field of combustion has been reoriented toward the development of alternative concepts for sustainable energy production and the replacement of fossil fuels with low-carbon or carbon-free fuels, such as hydrogen, ammonia or synthetic fuels, that can meet the increasing energy demand while minimizing environmental impacts.

Low and non-carbon fuels manufacturing processes start with the hydrogen (H_2). Produced renewably from green energy sources (solar or wind energy) via the electrolysis of water or steam reforming of fossil fuel (Midilli and Dincer (2008); Züttel et al. (2010)), H_2 can be utilized directly as fuel or transformed, to facilitate transport, storage and use in current combustion systems, into ammonia (NH_3) by combining it with nitrogen (N_2) (Rivarolo et al. (2019)) or into synthetic fuels (Brynolf et al. (2018)), also referred to as e-fuels, by mixing it with CO_2 captured from the atmosphere. The produced ammonia and e-fuels (e-methane, e-methanol, e-kerosene, ...) can in turn be used as fuels.

The strategy of using the hydrogen, hydrogen mixed with fossil-fuels, ammonia or synthetic hydrocarbons as fuels to achieve high combustion efficiency and low pollutants emission has been widely investigated and employed in internal combustion (Chintala and Subramanian (2017); Hänggi et al. (2019); Akal et al. (2020); Cardoso et al. (2021)) and gas turbine engines (Valera-Medina et al. (2017); Bothien et al. (2019); Elbaz et al. (2022)). Despite significantly reducing emissions when compared to fossil-based fuels these new fuels continue to generate emissions. Since there is no carbon in hydrogen fuel, the emission of greenhouse gases CO, CO_2 and soot is prevented. However, the high burn rate of hydrogen promotes NOx formation and intensifies flame instabilities and the risk of flashback due to the resulting high flame speeds and temperatures (Ilbas et al. (2005)). Similarly, the high nitrogen density in ammonia makes it a significant source of NOx. In addition, ammonia-air mixtures suffer from poor ignition quality and narrow flammability limits due to theirs low burning velocity (Kobayashi et al. (2018)). Concerning the e-fuels, the recycling circle allows the reduction of CO_2 emissions. It does not however prevent the formations of pollutants such CO and NOx.

To counter these negative aspects, research on low CO and NOx combustion has been undertaken. Studies have shown that the combustor primary-zone temperature is the key factor in the mechanisms of pollutants formation (Heywood (1988); Masiol and Harrison (2014)). Lefebvre and Ballal (2010) observed that CO production increases exponentially at temperatures lower than 1670 K, while overproduction of NOx is triggered at temperatures higher than 1900 K. The region for low CO and NOx emissions is limited between these two temperatures [1670 K, 1900 K]. The objective is therefore to find the optimal range(s) of operating conditions that guarantee temperatures in the combustion chamber between these two limits.

A solution to control the primary-zone temperature is to adapt the mixture equivalence ratio. The equivalence ratio is a key combustion variable, which compares the effective fuel-to-oxidizer ratio to the stoichiometric fuel-to-oxidizer ratio ($\phi = \frac{Y_{CH_4}/Y_{O_2}}{\left(Y_{CH_4}/Y_{O_2}\right)_{st}}$)). Analysis of flame temperature evolution for various hydrocarbon-air mixture as a function of the equivalence ratio presented in Fig. 1.1, show that low temperature flames that limit pollutant production are obtained by operating at lean premixed combustion regimes where the oxidizer, usually air, is in excess compared to the stoichiometric mixture composition ($\phi < 0.8$). For certain fuel-air mixtures, low-temperatures are also reached in rich combustion regime where the fuel is in excess $\phi > 1.6$). However, this solution is not viable as it leads to an over-consumption of fuel and the formation of pollutants such as carbon monoxide CO and soot (Frenklach and Wang (1994)).

Lean premixed and partially-premixed combustion are the strategies relayed

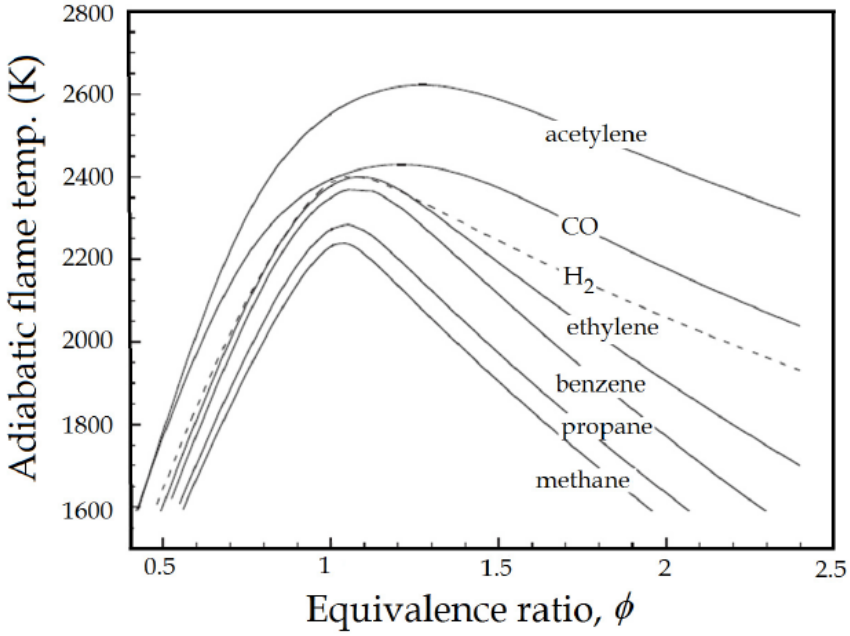

Figure 1.1: *The adiabatic flame temperature as a function of the equivalence ratio for various fuel-air mixtures at atmospheric pressure. Extracted from Law (2006).*

on in the the development of future combustion systems. Lean burn combustor concepts like lean direct injection (LDI) burners (Tacina et al. (2003); Marek et al. (2005)) or flameless combustion furnaces (MILD De Joannon et al. (2000); Galletti et al. (2009)) have been designed in the past few years and have shown promising capabilities to enhance combustion efficiency and lower pollutants emission. These technologies suffer however from a major drawback, difficulties of ignition, incomplete combustion and the increase of flame instabilities consequence of low flame temperatures that induce slower chemical reactions.

The challenge is to develop a novel flame ignition and stabilization methods to achieve efficient ultra-lean combustion. Usual approaches that consist in using conventional Spark-Ignition devices or optimizing flow dynamics in the combustion chamber to improve the flames ignition and stabilization failed to work in lean mixtures (Quader (1976); Barbosa et al. (2015)). Over the past decade, new techniques have been investigated, among which the plasma-assisted combustion which consists in applying electrical discharges at the flame basis to generate a non-equilibrium plasma that, by interacting with the flame, improves the combustion. Studies using plasma torch (Takita et al. (2000); Kobayashi et al. (2004)), microwave discharge (Esakov et al. (2004)), gliding arc discharges (Williams et al. (2004)), streamer high frequency (HF) discharge

(Klimov et al. (2004)), surface discharge (Shibkov et al. (2004)), or Nanosecond Repetitively Pulsed (NRP) discharges (Kruger et al. (2002)) have showed that non-equilibrium plasmas can significantly enhance the ignition process and flames stability over a wide range of combustion applications (Starikovskiy and Aleksandrov (2013); Ju and Sun (2015)). Among the various types of plasma discharges, the NRP discharges have proven to be particularly efficient. These high voltage pulsed discharges have been successful used to ignite lean combustion chamber (Pancheshnyi et al. (2006); Xu et al. (2015); Lefkowitz and Ombrello (2017)), extend lean flammability limit (Barbosa et al. (2015); Kim et al. (2020); Di Sabatino and Lacoste (2020)) and improve flames stability (Pilla et al. (2006); Kim et al. (2007); Blanchard et al. (2021)). In their recent works, Choe et al. (2021) and Choe and Sun (2022) have shown that NRP discharges can simultaneously reduce NOx emission and extend the lean blow-off-limits of ammonia flames. Figure. 1.2 shows NH_2* chemiluminescence photographs of ammonia-air flames (a) without and (b) with plasma at an equivalence ratio $\phi = 0.71$. The application of NRP discharges allows to stabilize the lifted ammonia flame near the burner and to improve the combustion.

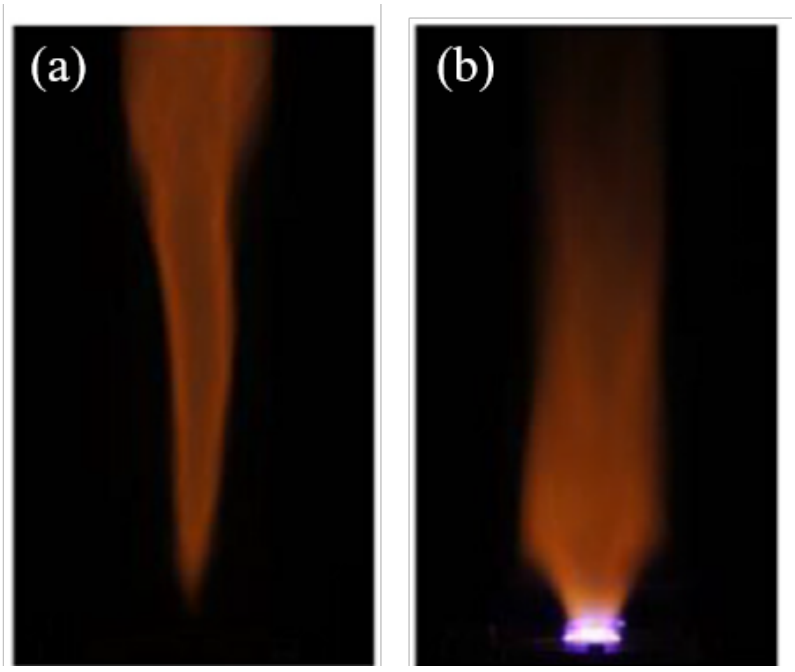

Figure 1.2: *Broadband chemiluminescence of ammonia flame (a) without and (b) with plasma at $\phi = 0.71$. Extracted from Choe and Sun (2022).*

Despite this proven efficiency, the fundamental mechanisms of plasma-assisted combustion are not well understood. Also, the numerical tools needed by engineers to assess the performance of NRP discharges in practical configurations

and optimize their design do not exist. To address these issues, the ANR project PASTEC (Plasma-ASsiTEd Combustion) project was put in place with the objective of developing and validating against experiments a modeling route suitable to perform simulations of realistic turbulent combustion systems accounting for plasma-flame interactions. The simulations will give insights into the mechanisms of combustion enhancement by NRP discharges.

1.2 PASTEC project

The **PASTEC** (**P**lasma **AS**sis**TE**d **C**ombustion) research project is a partnership project between four reseach laboratories: EM2C laboratory, a CNRS research unit associated with the Centrale-Supelec school, CORIA laboratory, a partnership between the CNRS, the University of Rouen Normandy and the INSA school in Rouen, LLP laboratory, a CNRS research unit associated with Ecole Polytechnique Palaiseau, CERFACS, a research organisation developing advanced methods for numerical simulation, and the industrial company SAFRAN HELICOPTER ENGINE, a member of the Propulsion branch of the Safran Group and a world leader in the design, production, sale and support of gas turbine engines for helicopters.

The objectives of the project are to develop and validate a modeling strategy able to perform numerical simulations of plasma-assisted combustion from academic to industrial environment and investigate the mechanisms of interaction plasma-flame that lead to combustion enhancement. To achieve this goal, the project is divided in five tasks:

Task 1 is the experimental study of the Mini-PAC configuration. The first objective of this task, led by CORIA, is to characterize the discharge properties in an environment representative of a combustor. This experimental characterization will be used to validate the detailed simulation of the plasma-flame interactions carried out in task 2. The second objective is to provide flame-scale data to validate the LES plasma-assisted combustion model developed in task 3.

Task 2 conducted by CERFACS, is devoted to detailed numerical simulations of plasma-assisted combustion. A first objective is to capture the impact of the plasma on the combustion chemistry, by developing an analytical chemical scheme taking into account chemical species created during the plasma phase. A second task, in collaboration with the LPP, is the development of a discharge code capable of simulating NRP discharges. The outputs of this code are the spatial and heat and chemical species distributions, which can be used in task 3. The discharge code combined

with the new combustion chemistry will be applied to the Mini-PAC configuration, in order to be compared with the measurements and results of task 3 on the same configuration.

Task 3 carried out by the EM2C numerical team, aims to develop and validate a LES plasma-assisted combustion model, using the discharge characterizations obtained in task 1 and task 2. The model will be then used to perform LES simulation of turbulent flames ignition and stabilization on practical configurations such us the Mini-PAC burner. The results of the simulations will be analyzed to understand the mechanisms of interaction between the plasma discharges and the flames.

Task 4 conducted by the EM2C experimental team, is dedicated to the experimental study of the lean blow off limit extension by plasma discharge on the the BIMER industrial configuration.

Task 5 conducted by the industrial partner SAFRAN HELICOPTER ENGINE, aims to simulate a helicopter combustion chamber with plasma discharges.

1.3 Thesis objectives and outline

This work is part of the third task of the PASTEC project. The objectives are to define and validate a numerical modeling strategy adapted for the simulation of plasma-assisted combustion in academic and industrial configurations. Then, to use the retained strategy to perform numerical simulations of flames ignition and stabilization by NRP discharges. Finally, to analyze the simulations results in order to understand the mechanisms of interaction between the plasma discharges and the flames.

The manuscript is organized into three parts briefly described below.

Part I is dedicated to the elaboration, implementation and validation of a modeling strategy for the simulation of plasma-assisted combustion. In Chapter. 2 presents the different types of plasma discharges and their characteristics with a focus on Nanosecond Repetitively Pulsed (NRP) discharge and their effects on combustion. The conventional plasma-assisted combustion numerical models are then reviewed and their limit discussed. Finally, novel phenomenological plasma model is introduced and described. This model is retained in this work to perform 3-D simulations of plasma-assisted combustion. In Chapter. 3, The YALES2 code used in the simulations is introduced. The fundamentals of turbulent combustion modeling are briefly presented. The LES approach and the

turbulent combustion model TFLES are then described. Next, the coupling between the set of LES governing equations and the phenomenological NRP discharges model is detailed and validated against experimental data.

Part II is dedicated to the numerical investigation of flame ignition by NRP discharges. Chapter. 4 discusses the limits of conventional ignition devices and the advantages of using NRP discharges for the ignition of lean combustion chambers. 3-D numerical study of flame ignition by a single NRP discharge pulse and the impact of the discharge hydrodynamic effects, performed using the phenomenological plasma model, is then presented. Chapter. 5 is devoted to the simulation of the flow tunnel configuration ignition by a series of NRP discharge pulses and the study of the flow and discharge parameters impact on the ignition efficiency. In Chapter. 6, the phenomenological NRP discharges model is used to simulate the ignition a bluff-body turbulent premix burner, the Mini-PAC configuration, representative of industrial combustors. Simulation results are analyzed to identify the interaction mechanisms between the thermal and chemical effects induced by the discharges and the combustion kinetics. In Chapter. 7, a low-order model of plasma-assisted ignition based on a perfectly stirred reactor (PSR) is derived. The model is used to perform parametric studies of flames ignition by NRP discharges to identify the optimal set of discharge parameters to used to initiate the combustion.

Part III is dedicated to the numerical study of flame stabilization by NRP discharges. A review of recent plasma-assisted combustion experiments performed with NRP discharges is presented in Chapter. 8. In Chapter. 9, Numerical simulations of turbulent flame stabilization by NRP discharge are preformed on the Mini-PAC configuration using the phenomenological plasma model. The results are compared to the experimental measurements obtained in task 1 of the PASTEC project. In Chapter. 10, A detailed chemical analysis of the Mini-PAC simulations is conducted in order to understand the mechanisms of flame stabilization by NRP discharges.

Part I

Plasma-assisted combustion modeling

Chapter 2

Phenomenological plasma-assisted combustion model

In this chapter, the numerical models developed for plasma assisted combustion simulations are described and examined in order to define the best strategy to adopt to investigate numerically the mechanisms of flames ignition and stabilization by plasma discharge in practical configurations. The physics of plasma discharges and their characteristics are first presented with a focus on Nanosecond Repetitively Pulsed (NRP) discharge and their effects on combustion. The conventional numerical strategies deployed to solve the set of equations governing the plasma and combustion phenomena are then described. Next, The limits of the conventional numerical strategies and the necessity of developing a simplified plasma are discussed. Finally, the principle and the mathematical framework of novel phenomenological plasma model developed by Castela et al. (2016) to capture the effects of NRP discharges on combustion at low CPU cost are presented. This model has been retained in the present work to perform the simulations of flames ignition and stabilization by NRP discharges.

Contents

2.1 Introduction

To reduce pollutant emissions such as nitrogen oxides, lean combustion chambers are under development in many energy-related sectors. However, a recurring problem to industrial applications is that lowering the flame temperature slows the chemical reactions, causing difficulties to ensure successful ignition and stabilization of the flames over the wide range of operating conditions covered by practical applications. An emerging solution to promote flames ignition and stabilization is to generate high-voltage electric discharges between two electrodes located inside the combustion chamber. It generates locally a plasma, which interacts with the combustion and enhance it. To fully control the ignition and stabilization of flames by plasma discharge a complete understanding of the governing physics is necessary. This chapter is dedicated to the elaboration of a modeling strategy for the simulations of plasma-assisted combustion in order to investigate the mechanisms of interactions plasma-flame.

The chapter is organized as follows. Section. 2.2 gives a brief introduction to plasma physics. Section. 2.3 describes the different types of plasma discharges and their characteristics. Among the various types of discharges, Nanosecond Repetitively Pulsed (NRP) discharges have shown to be a particularly energy efficient way to initiate and control combustion. This work investigate the impact of these discharges on combustion. Section. 2.4 focuses on the description of (NRP) discharges and their interaction with combustion. Section. 2.5 presents the conventional numerical method used to simulate plasma-assisted combustion and shows some of the simulations results obtained lately. The limitations of this method and the necessity of developing a simplified plasma models for the simulations of practical configurations are also discussed. Section. 2.6 presents the novel simplified phenomenological plasma model developed by Castela et al. (2016) to capture the effects of NRP discharges on combustion at low CPU cost.

2.2 The 4^{th} state of matter

Plasma is considered as the 4^{th} state of matter. It is a collection of neutral and charged particles which are electrically neutral on average and exhibit collective effects. This state is reached when an important quantity of energy is brought to a gas mixture causing the excitation, the dissociation and the ionization of the species that compose it (Ju and Sun (2015)). There are two types of plasmas: equilibrium or hot plasma in which the electron temperature, rotational and vibrational temperatures of particles are in equilibrium and the neutral gas temperature and electron number density are very high. Non-equilibrium or cold plasma in which the electronic, vibrational, and rotational temperatures are very different and the neutral gas temperature and electron number density are relatively low (Ju and Sun (2015); Starikovskiy and Aleksandrov (2013)).

Plasmas are extremely common in the Universe (stars, nebula, solar wind ...) accounting for more than 99% of ordinary matter, but are rarely a natural phenomenon on the surface of the earth as the conditions under which they appear are far from the temperature and pressure conditions of the Earth's atmosphere. However, the study of plasmas undertaken in the last decades made possible the production of plasma at industrial scale such as electric discharges, propulsion plasma, nuclear fusion, with applications in a wide variety of fields: astrophysics, aerodynamics, biological combustion. Figure. 2.1 shows a classification of plasmas ordered by their energy, temperature of their electrons, and the density of charged particles.

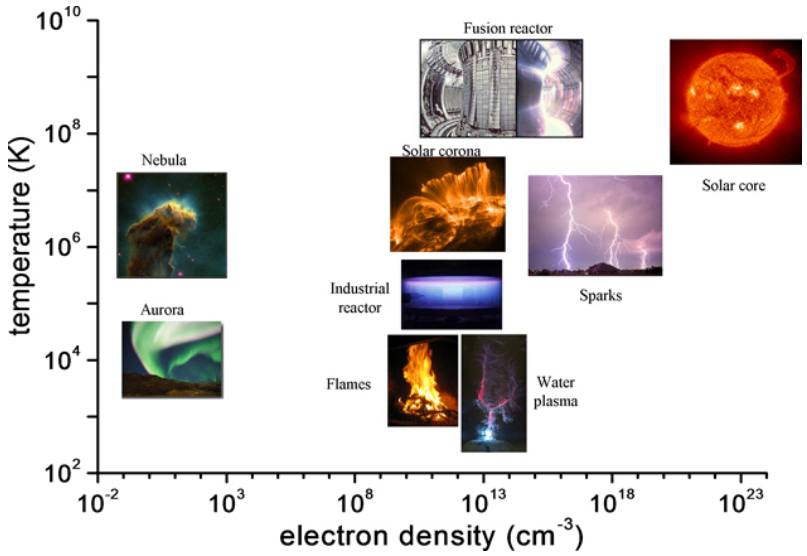

Figure 2.1: *Classification of natural and laboratory plasmas in a logarithmic diagram of charges density and temperature. Taken from https://www.lpp.polytechnique.fr/Our-research-in-a-few-words?lang=en.*

2.3 Plasma discharges classification

Industrial plasmas are usually generated by applying a potential difference between two electrodes to create an electric field. The generated electric field applies a coulomb force on the free electrons present in the inter-electrodes area which will strongly accelerate them. By colliding with the heavy particles, the accelerated electrons transfer some of their kinetic energy to the internal energy states of these particles (vibrational, electronic, rotational and translational energy states), which leads to their excitation, dissociation and ionization and therefore the creation of a plasma. This procedure is known as a ***plasma discharge***. An image of a plasma discharge, a spark NRP discharge, is shown

as an example in Fig. 2.2.

Figure 2.2: *Digital camera image of a spark plasma discharge. Extracted from (Pai et al. (2008)).*

The electron-particle impact processes strongly depend on the electrons energy (temperature) and density reached in the inter-electrode zone, which in turn depend on reduced field E/N imposed by the operating conditions and the experimental setup (applied voltage, gas composition, electrode geometry, ...) and defined as the electric field magnitude **E** divided by to the gas particle density **N**, usually in Townsend units, with 1 Td = 10^{-17} V.cm^2. A large range of electron temperature and number density can be obtained leading to the creation of different types of plasmas as shown in Fig. 2.3. Among this variety of plasma discharges, spark and arc discharges are known to produce equilibrium plasmas with high neutral gas temperature and electron number density, but a low electron temperature. They have been widely used to ignite reactive mixtures using spark-plug devices (Maly and Vogel (1979); Refael and Sher (1985); Sher et al. (1992)), however with the disadvantage of consuming a large amount of energy. On the other hand, non-equilibrium plasma generated by electric discharges such as corona, DC, glow, RF, DBD, NSD, gliding arc, and MW have high electron temperature but low gas temperature (Starikovskaia (2006)). Among the non-equilibrium plasma discharges, Nanosecond Repetitively Pulsed (NRP) discharge produce a very strong reduced electric field which leads to a significant increase of electrons density and temperature (Kruger et al. (2002)). The resulting high electrons density and temperature enable fast electron impact dissociation of chemical species in large volume and the production of important amount of chemical radicals that can be used as kinetic enhancers for the combustion (Rusterholtz et al. (2013)). For this reason, nanosecond repetitively pulsed (NRP) discharges have attracted increasing interest in plasma-assisted combustion.

The characteristics of NRP discharges and their effects on reactive flows are

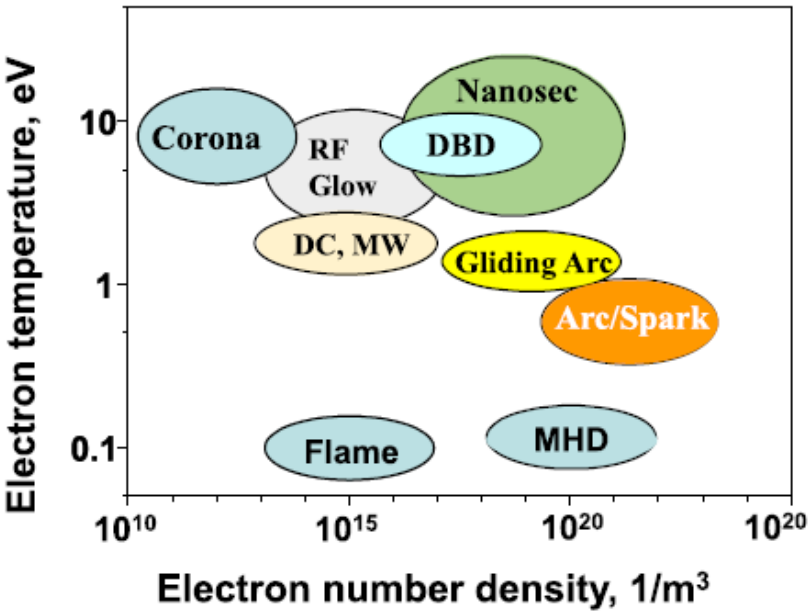

Figure 2.3: *Schematic of electron temperature and number density for different discharges, Corona, direct current (DC) discharge, microwave (MW) discharge; dielectric barrier discharge (DBD), radio-frequency discharge (RF), glow discharge, gliding arc, nanosecond repetitively pulsed discharge (NRP), arc, magneto-hydrodynamic discharge (MHD), and flame. Extracted from (Ju and Sun (2015)).*

described in the following section.

2.4 Nanosecond Repetitively Pulsed (NRP) discharges

Nanosecond Repetitively Pulsed (NRP) discharges are characterized by high voltage pulses (5 to 20 kV) that last few nanoseconds and are repeated at frequencies of the order of tens of kHz. A schematic representation of these discharge is shown in Fig. 2.4.

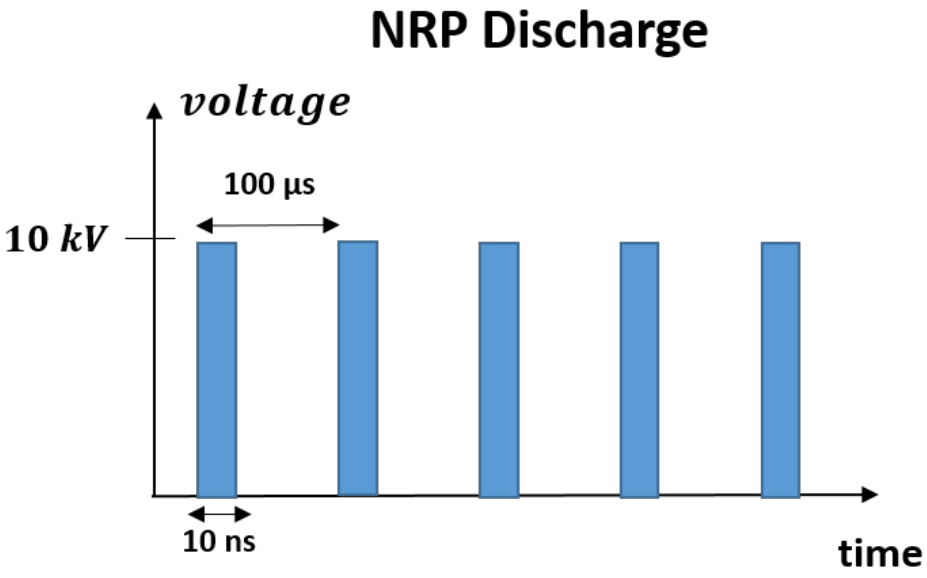

Figure 2.4: *Schematic representation of the pulse voltage in NRP discharges.*

The pulses generate a very strong reduced electric field (E/N) that leads to a significant increase of electrons density and temperature (Kruger et al. (2002)) in the inter-electrode region. Through elastic and inelastic collisions, the high-temperature electrons transfer part of their energy to the internal energy of the heavy molecules, which become excited rotationally, vibrationally, electronically (Stancu et al. (2010); Montello et al. (2013)). The excited molecules will further relax their energy into heat by energy exchange mechanisms (Starikovskiy and Aleksandrov (2013)) or into kinetics effect through collisional dissociations reactions which lead to the production of active radicals such as O, OH and H (Lo et al. (2012); Rusterholtz et al. (2013); Adamovich et al. (2015)).

Thermal and chemical effects of NRP discharges have been used to enhance the combustion process. The principle, illustrated in Fig. 2.5, consists of applying NRP discharges between two electrodes at flame basis to generates heat and ac-

tive species such as O, OH, H that will likely improve the combustion kinetics and promote flame ignition and stabilization. Over the past decade beneficial effects of plasma-assisted combustion have been observed in laboratory and industrial scale burners under the action of NRP discharges. These studies demonstrated that NRP discharges can successfully ignite lean combustion chamber (Pancheshnyi et al. (2006); Xu et al. (2015); Lefkowitz and Ombrello (2017); Merotto et al. (2022)), extend lean flammability limit (Barbosa et al. (2015); Bak et al. (2012); Kim et al. (2020); Di Sabatino and Lacoste (2020)) and improve flames stability (Pilla et al. (2006); Kim et al. (2007); Bak et al. (2013); Blanchard et al. (2021)) in both premixed and non-premixed regimes. These studies are presented in more detail in Chapter. 4 and Chapter. 8.

While experimental studies have demonstrated at several occasions the ability of the NRP discharge to improve combustion processes, they have not been able to explain in detail the complex fundamental mechanisms of plasma-flame interactions specially in realistic turbulent combustion systems. A good candidate to do so are the numerical simulations. Tremendous progress in modeling and in super-computing enables today the simulation of complex multi-physics phenomenons in industrial combustors (Poinsot and Veynante (2012)). The simulation of unsteady reactive flows, are an adequate tool to provide the missing insights in the understanding of emerging plasma-assisted combustion systems.

The objective of the present work is to elaborate and validate modeling strategy suitable to perform simulations of plasma-assisted combustion in practical configurations and investigate the plasma-flame interactions mechanisms.

A review of plasma-assisted combustion numerical modeling is performed in the following sections.

2.5 Conventional plasma-assisted combustion models

The numerical modeling of plasma-assisted combustion is very challenging due to the wide range of spatial and time scales involved in physics of flame chemistry, plasma and turbulence, as shown in Fig. 2.6. The discharge energy deposition and the plasma kinetic occur within a few nanoseconds on very small region of a few micrometers between the electrodes when the combustion and turbulence processes occur on microseconds to milliseconds scales with a typical size of tens to hundreds of micrometers over all the combustion chamber.

The strategy generally deployed to perform numerical simulations of plasma-assisted combustion consists in solving two distinct systems of governing equations. One for the neutral species composing the gas governed by the Navier-

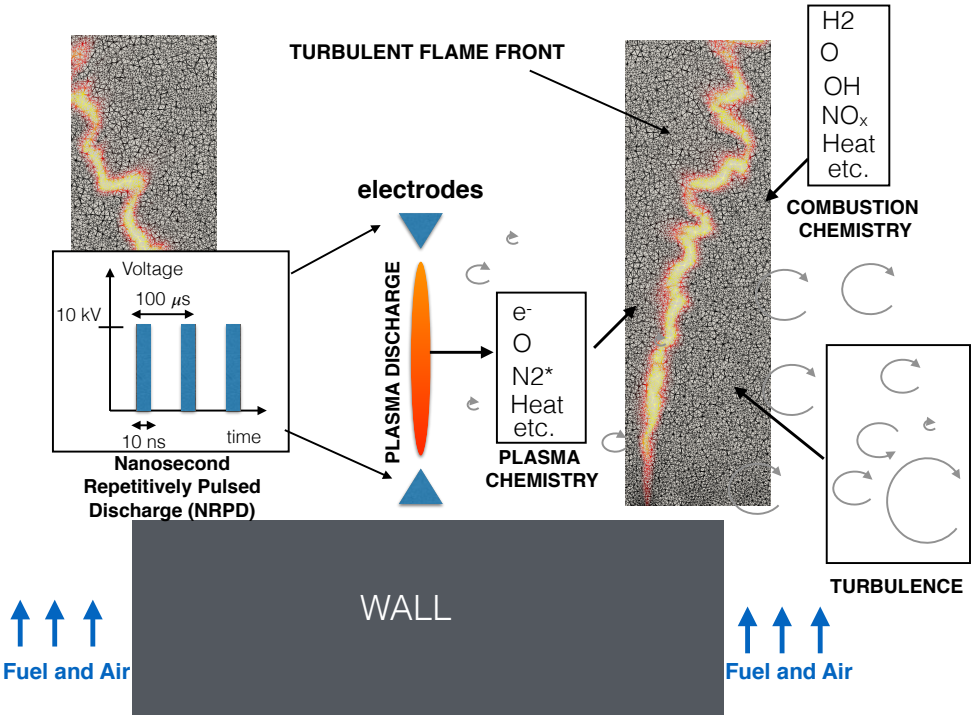

Figure 2.5: *Schematic view of major physical phenomena involved in plasma-assisted combustion. A nanosecond (repetitively pulsed) discharge generates a plasma in the vicinity of a flame. Heat and dissociated species (such as the radical O) interact with the flame front which is wrinkled by turbulence.*

Stokes equations, and second one for the charged species, electrons and ions, and the electric field generated by the plasma discharge and governed by the streamers equations. The two systems are coupled through species, energy and momentum source terms. The Navier-Stokes equations, the streamers equations as well as combustion and plasma kinetics mechanisms are described in the following subsections.

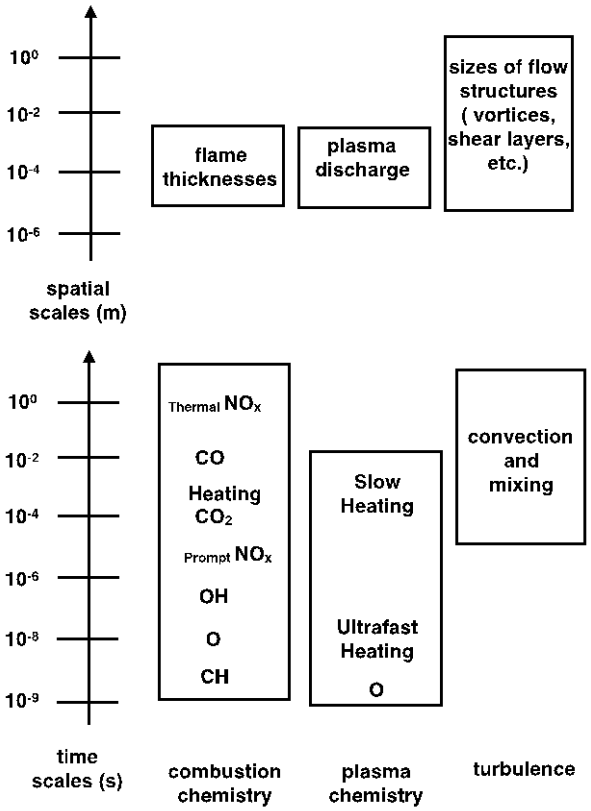

Figure 2.6: *Range of spatial and time scales involved in physics of flame chemistry, plasma and turbulence (courtesy of B. Fiorina).*

2.5.1 Navier-stokes equations

The Navier-Stokes equations are used in plasma-assisted combustion to describe the space-time evolution of neutral species composing the multicomponent reacting gas subject to flow transport, combustion and plasma reactions. The balance equations for mass, momentum, energy and species densities are the following:

$$\frac{\partial \rho}{\partial t} + \frac{\partial (\rho u_i)}{\partial x_i} = 0 \tag{2.1}$$

$$\frac{\partial(\rho u_j)}{\partial t} + \frac{\partial(\rho u_i u_j)}{\partial x_i} = -\frac{\partial p}{\partial x_j} + \frac{\partial \tau_{ij}}{\partial x_i} \tag{2.2}$$

$$\frac{\partial(\rho e)}{\partial t} + \frac{\partial(\rho u_i e)}{\partial x_i} = -\frac{\partial q_i}{\partial x_i} + \frac{\partial(\sigma_{ij} u_i)}{\partial x_i} \tag{2.3}$$

$$\frac{\partial(\rho Y_k)}{\partial t} + \frac{\partial(\rho u_i Y_k)}{\partial x_i} = -\frac{\partial(\rho V_{k,i} Y_k)}{\partial x_i} + W_k \dot{\omega_k} \tag{2.4}$$

where ρ is the density, u_i is the ith component of local flow velocity in direction x_i , p the pressure and τ_{ij} the viscous tensor defined by:

$$\tau_{ij} = -\frac{2}{3}\mu \frac{\partial u_l}{\partial x_l}\delta_{ij} + \mu\left(\frac{\partial u_i}{\partial x_j} + \frac{\partial u_j}{\partial x_i}\right) \tag{2.5}$$

with μ the dynamic viscosity and δ_{ij} the Kronecker symbol.

In equation (2.3), e refers to the total energy of gas per mass unit, defined as the sum of kinetic, thermal and chemical energies as follows:

$$e = \frac{1}{2} u_i u_i + \sum_{k=1}^{N_{sp}} (e_{sk} + \Delta h^o_{f,k}) Y_k \tag{2.6}$$

Where e_{sk} , $\Delta h^o_{f,k}$ and Y_k are, respectively, the sensible energy, the enthalpy of formation and the mass fraction of the kth species.
σ_{ij} is given by:

$$\sigma_{ij} = \tau_{ij} - \frac{\partial u_j}{\partial x_i} p \delta_{ij} \tag{2.7}$$

The energy flux q_i is the combination of the Fourier flux and the enthalpy flux induced by the species diffusion:

$$q_i = -\lambda \frac{\partial T}{\partial x_i} + \rho \sum_{k=1}^{N_{sp}} h_k Y_k V_{k,i} \tag{2.8}$$

where λ is the heat conduction coefficient of the mixture and $h_k = h_{s,k} + \Delta h^o_{f,k}$ is the sum of the sensible enthalpy and the enthalpy of formation of the kth species.

$\rho Y_k V_{k,i}$ is the molecular diffusion term calculated with the Hirschfelder and Curtiss approximation.

In equation (3.5), $\dot{\omega_k}$ is the molar production rate of the kth species due to the combustion reactions described in Subsection. 2.5.3.

Unlike neutral species, the charged species produced in the plasma are strongly affected by the electric field created by the discharge.

2.5.2 Plasma discharge mechanism and streamers equations

During a pulse, the free electrons present in the inter-electrode region are subjected to a strong acceleration induced by the electric field of the discharge. The collision of the accelerated electrons with the surrounding molecules leads to the ionization of the heavy species resulting on the release of additional electrons. The new electrons repeat the same process of acceleration, collision and ionization, increasing exponentially the total number of electrons and ions. This phenomenon is known as an electron avalanche (Townsend (1910)). The increase of the charge density induces an increase of the electric field in the inter-electrode zone. The acceleration of electrons and ions becomes stronger and the collisions more frequent. Thus, multiple reactions of excitation, dissociation and ionization take place, creating a plasma. During this process, the negatively charged species, electrons and negative ions, propagate from the cathode to the anode forming a negative streamer while the positively charged species, positive ions, propagate in the opposite direction from the anode to the cathode forming a positive streamer (Loeb and Meek (1940a); Loeb and Meek (1940b)) as shown in Fig. 2.7.

Several numerical models have been developed to describe the dynamics of formation of streamers. These models are divided into two categories: particle models, which follow the individual motion of charged particles (Chanrion and Neubert (2008); Teunissen and Ebert (2017)) and fluid models, in which the species are modeled as fluids and evolve following a transport equations (Kulikovsky (1997); Pancheshnyi (2005); Celestin (2008); Tholin (2012)). More recently, Hybrid models, which rely on particle and fluid models, have been proposed (Li et al. (2010)). they consist of modeling some species using a particle approach, while the fluid model is used for the others.

The most used method in the literature belongs to the fluid models. Based on the drift-diffusion approximation (Kushner (2003); Celestin (2008); Tholin

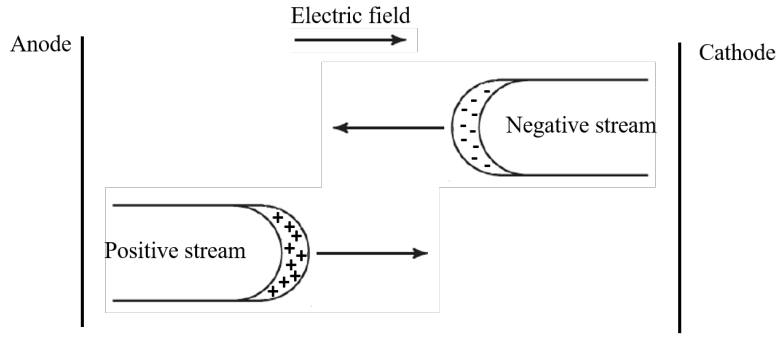

Figure 2.7: *Illustration of a positive streamer propagating from the anode toward the cathode and a negative propagating from the cathode toward the anode under the effect of the discharge electric field.*

(2012)), it consists in solving only the density of the charged species and the electric field induced by the discharge using the following equations :
with

$$\frac{\partial n_e}{\partial t} + \vec{\nabla} \cdot \left(\mathrm{n_e} \overrightarrow{\mathrm{v}}_\mathrm{e} - \mathrm{D_e} \vec{\nabla} \mathrm{n_e} \right) = \dot{\omega}_\mathrm{e} + \dot{\omega}_\mathrm{ph} \tag{2.9}$$

$$\frac{\partial \mathrm{n_n}}{\partial t} + \vec{\nabla} \cdot \left(\mathrm{n_n} \overrightarrow{\mathrm{v}}_\mathrm{n} - \mathrm{D_n} \vec{\nabla} \mathrm{n_n} \right) = \dot{\omega}_\mathrm{n} \tag{2.10}$$

$$\frac{\partial \mathrm{n_p}}{\partial t} + \vec{\nabla} \cdot \left(\mathrm{n_p} \overrightarrow{\mathrm{v}}_\mathrm{p} - \mathrm{D_p} \vec{\nabla} \mathrm{n_p} \right) = \dot{\omega}_\mathrm{p} + \dot{\omega}_\mathrm{ph} \tag{2.11}$$

$$\nabla^2 \, \mathrm{V} = -\frac{\mathrm{q_e}}{\epsilon_0} \left(\mathrm{n_p} - \mathrm{n_n} - \mathrm{n_e} \right) \tag{2.12}$$

$$\vec{v_i} = \mu_i \vec{E} \tag{2.13}$$

where subscripts "e", "p" and "n" refer to electrons, positive and negative ions, respectively. n_i is the number density of species i, D_i and μ_i are the diffusion coefficient and the mobility of species i, respectively. q_e is the absolute value of electron charge, and ϵ_0 is the permittivity of free space. E is the absolute value of the electric field and V is the electric potential. $\dot{\omega}_{ph}$ is the photoionization source term and the $\dot{\omega}_i$ terms stand for the source terms of specie i due to chemical reactions. The transport coefficients and chemical source terms are functions of the local reduced electric field E/N, where E is the electric field

magnitude and N the gas density. The following Poisson equation is solved to derive the electric field:

$$\vec{E} = -\vec{\nabla}\ \mathrm{V} \tag{2.14}$$

This model has been widely studied in the literature and has proven its efficiency for the simulation of streamer discharges at atmospheric pressure (Kulikovsky (1997); Tholin et al. (2014); Bagheri et al. (2018)).

In addition to ionization reactions, collisions between the accelerated electrons and surrounding molecules induce energy exchanges as well as excitation and dissociation reactions related to plasma kinetics. This results in the increase of the gas temperature and the production of active chemical species that enhance the combustion kinetics.The chemical evolution of the system is driven by the plasma-related reactions and the combustion-related reactions and the interaction between them. These two kinetics are described in the following subsection.

2.5.3 Plasma-assisted combustion kinetic mechanisms

Combustion kinetic mechanisms

A combustion kinetic mechanism describes the set of chemical reactions that take place during the process of fuel oxidation, usually hydrocarbons, by an oxidizer, usually air, to form combustion products. This transformation is accompanied by a heat release used in combustion systems as thermal source of energy. Combustion mechanisms are mainly composed of simple species dissociation or formation reactions. Considering a system composed by N_{sp} species that react with each other, the reactions can be written as follow:

$$\sum_{k=1}^{N_{sp}} \nu_{ki}^{'} \chi_k \rightarrow \sum_{k=1}^{N_{sp}} \nu_{ki}^{''} \chi_k \qquad \text{for i = 1,...,I} \tag{2.15}$$

Where $\nu_{ki}^{'}$ and $\nu_{ki}^{''}$ are the stoichiometric coefficients of the k^{th} species appearing in the i^{th} reaction as reactant and as product, respectively. χ_k is the chemical symbol of the k^{th} species.

The conservation of mass implies:

$$\sum_{k=1}^{N_{sp}} \nu_{ki}^{'} M_k = \sum_{k=1}^{N_{sp}} \nu_{ki}^{''} M_k \qquad \text{for i = 1,...,I} \tag{2.16}$$

The overall production rate of the k^{th} species $\dot{\omega_k}$ is the sum of all the reaction rates of the elementary reactions I :

$$\dot{\omega_k} = \sum_{i=1}^{I} (\nu_{ki}^{'} - \nu_{ki}^{''}) Q_i \tag{2.17}$$

$$Q_i = K_{fi} \prod_{j=1}^{N_{sp}} [X_j]^{\nu_{ji}^{'}} - K_{ri} \prod_{j=1}^{N_{sp}} [X_j]^{\nu_{ji}^{''}} \tag{2.18}$$

Where Q_i is the rate of progress of the i^{th} reaction, $[X_j]$ is the molar concentration of the j^{th} species, K_{fi} and K_{ri} are the rate of the forward and backward reaction.

In combustion, the forward and backward rates of these reactions depend only on the gas temperature and follow the Arrhenius formula given by:

$$K_i = A_i T_g^{b_i} \exp(-\frac{E_i}{RT_g}) \tag{2.19}$$

with A_{fi} the pre-exponential factor, b_i a constant, E_i the activation energy, T_g the temperature of the gas and R the universal gas constant.

Plasma kinetic mechanisms

Several detailed plasma kinetic mechanisms have been proposed in the literature (Popov (2001); Popov (2011); Kozak and Bogaerts (2014); Wang et al. (2018)) to model non-equilibrium plasma reactions in various gas mixtures. These mechanisms are more complex then the combustion mechanisms as they include different types of reactions:

- Electron-impact ionization, dissociation and excitation reactions: The rate constants associated with these reactions depend on the Electron Energy Distribution Function (EEDF). They are calculated directly as a function of the reduced electric field E/N by solving the Boltzmann equation to obtain the EEDF. A two-term approximation solver for the Boltzmann equation, BOLSIG+ (Hagelaar and Pitchford (2005)). For examples (Bak et al. (2012)):

$O_2 + e^- \rightarrow O_2^+ + 2e^-$ electron-impact ionization .
$O_2 + e^- \rightarrow 2O + e^-$ electron-impact dissociation.
$N_2 + e^- \rightarrow N_2(A) + e^-$ electron-impact excitation.

- Electrons-ions recombination reactions : The rate constants involving ions-electrons reactions are often calculated as a function of the electron temperature T_e and gas temperature T_g following Arrhenius formula given by :

$$K_i = A_i T_g^{b_i} \exp(-\frac{E_i}{RT_g}) T_e^{b'_i} \exp(-\frac{E'_i}{RT_e}) \tag{2.20}$$

An example of this type of reactions (Bak et al. (2012)):

$e^- + O_2^+ + O_2 \rightarrow 2O_2^+$ electron-ion recombination.

where A_i is the pre-exponential constant, b_i and b'_i are the gas temperature and electron temperature exponents, E_i is the activation relative to the gas temperature, and E'_i is the activation energy relative to the electron energy.

- Quenching of excited states by ground state molecules reactions: The available rate constants are either constant values or dependent on the overall gas temperature T_g. As an example (Bak et al. (2012)):

$N_2(A) + O_2 \rightarrow N_2 + 2O$ quenching dissociation.

In plasma assisted combustion simulations, the detailed plasma kinetic mechanisms are coupled with combustion mechanisms to compute the overall species production rate (Bak et al. (2012); Cheng et al. (2022)).

2.5.4 Detailed simulations of plasma-assisted combustion

The numerical strategy of solving the governing equations for the electric field and charged species, as well as the continuity equations for the neutral and excited species, the energy, mass and momentum balance equations for the gas mixture, with a coupled complex plasma and combustion kinetics, has been successfully used for the numerical simulations of NRP discharges applied in air and in hydrocarbon-air mixtures.

For instance, 2D simulations of the dynamics of formation of a nanosecond repetitively pulsed (NRP) discharge between two point electrodes in air at atmospheric pressure at 1000 K have been performed by Tholin and Bourdon (2013) to investigate the effects of the discharge on air mixture. Figure. 2.8

shows the 2-D field of gas temperature, air density, pressure and magnitude of the flow velocity at the end of the NRP pulse, obtained in these simulations. The results indicate that the energy deposited during the pulse induces an isochoric ultra-fast heating of the air with a significant increase of the gas temperature and pressure while the density remains constant. An acceleration of the gas is also visible near the electrode. These simulations highlighted one of the thermal effects of NRP discharges: the ultra-fast gas heating.

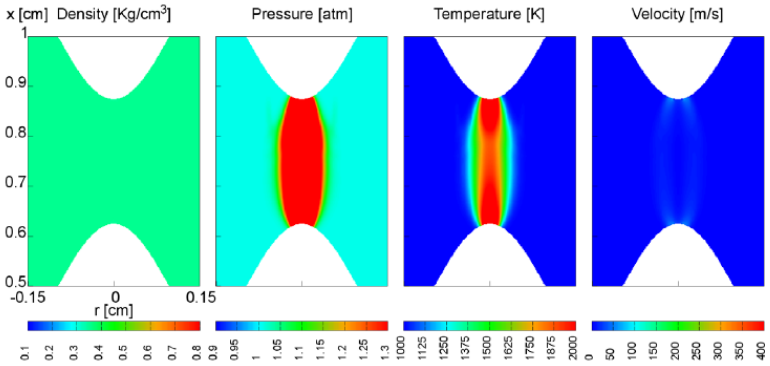

Figure 2.8: *Cross-sectional views of the density, pressure, air temperature and magnitude of the flow velocity at the end of NRP discharge pulse in air at T_g = 1000K. Extracted from Tholin and Bourdon (2013)*

In an other work, numerical simulations of a laminar premixed methane-air mixture ignition by Nanosecond Repetitively Pulsed (NRP) discharges in a pin-pin configuration was performed by Barleon et al. (2022). A 500 μJ single pulse of NRP discharge is applied in methane-air mixture at an equivalence ratio of 0.8 and an initial temperature of 600 K. To assess the importance of the discharge chemical effects, two simulations were computed. In the first one, only the thermal effects of the discharge were considered, referred to as heat deposit (HD) case in which all the energy is assumed to be converted to heat. In the second one, both the thermal and chemical effects with the production of radicals were taken into account, referred to as single pulse (SP) case. Temperature fields at different instants after the pulse for the HD, SP cases is shown in Fig. 2.9. No ignition was observed in the (HD) case. the 3000 K temperature reached after the pulse decreases quickly and return almost to its initial value of 600 K after 500 μs. When in the (SP) case an ignition kernel is formed in the discharge zone with a temperature around 2000 K. These simulations highlighted the significant impact of NRP discharge chemical effects on combustion process.

Several other numerical studies of flames ignition and stabilization by NRP discharges have been carried out using the fully solved plasma and combustion methodology (Bak et al. (2012); Takana and Nishiyama (2014); Tholin et al.

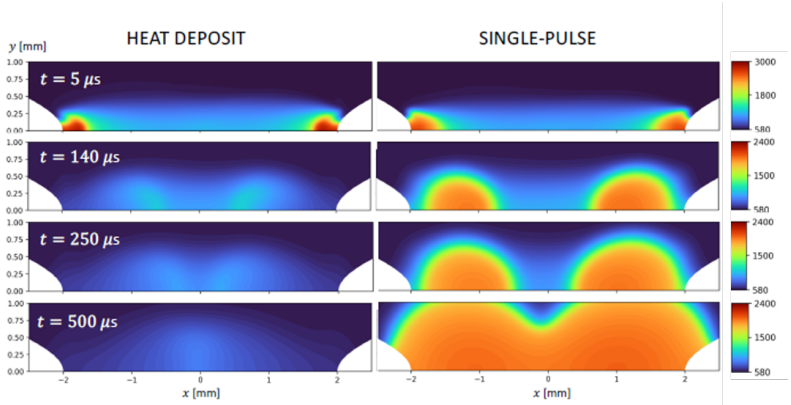

Figure 2.9: *Temperature fields in Kelvin at different instants after the pulse for the heat deposit (HD) and single pulse (SP) cases. A single NRP discharge pulse with an energy deposition of 500 μJ applied in a lean methane-air mixture ($\phi = 0.8$).No ignition is observed in the HD case while a successful ignition is observed in the SP case. Extracted from Barleon et al. (2022)*

(2014); Casey et al. (2017); Barleon (2022)). These simulations give insights into the impact of plasma on combustion. However, they are limited to 1-D and 2-D simulations in laminar flow conditions because of their high computational cost. Computational domains are restricted to the plasma discharge vicinity and consequently too small to capture all scales involved in a turbulent combustion chamber. Detailed simulations of plasma-assisted combustion are today still too expensive to be directly included in 3-D turbulent flame simulations.

An alternative is to simplify the description of the complex plasma processes using a phenomenological model which focuses on the main effects of nanosecond repetitively pulsed (NRP) discharges on combustion. This approuch has been developed by Castela et al. (2016) to perform simulations of plasma-assisted combustion in academic and industrial complex configuration at low CPU cost.

2.6 Phenomenological plasma model

To enable 3-D simulations of plasma-assisted combustion, a semi-empirical simplified NRP discharges model has been proposed by Castela et al. (2016), to significantly reduce the computational costs. Instead of solving a continuity equation for each additional excited and charged species, the electric field and the detailed plasma chemistry, the model captures non-equilibrium plasma effects by adding only source terms in energy and species balance equations and a new scalar balance equation.

The plasma source terms were derived by analyzing in detail the mechanisms

of plasma formation induced by NRP discharges.

2.6.1 Analysis of NRP discharges plasma physics

Based on the simulation and experimental results reported in the literature (Popov (2001); Starikovskiy and Aleksandrov (2013); Stancu et al. (2010); Rusterholtz et al. (2013)), the phenomenological NRP discharge model was constructed by analyzing the distribution of the electrons kinetic energy, accelerated by the discharge electric field, over the different internal energy modes of molecules and the channels through which these excited states impact the thermochemical state of the gas when they relax.

Figure. 2.10a and b show the distribution of the discharge energy into the different degrees of freedom of molecules as a function of the reduced field E/N , computed with detailed plasma kinetics for (a) air and (b) methane-air mixtures (Starikovskiy and Aleksandrov (2013)). It is shown that, for values of E/N in the range 100-400Td (1 Td = 10^{-17} V.cm^2), the collision of electrons accelerated by the electric field mainly produce electronically and vibrationally excited molecular nitrogen N_2. More then 90% of the discharge energy is transferred and stored in vibrational and electronic states of N_2. This is the case in air (Fig. 2.10a), but also to a large extent in hydrocarbon–air mixtures, since the mass fraction of hydrocarbons represents only a small fraction of the mixture composition (for instance, stoichiometric methane–air mixtures only contain 5.5% of methane in mass, Fig. 2.10a).Thus the impact of NRP discharges on combustion is mainly associated with the impact of the vibrationally and electronically excited N_2 molecules.

At the and of the pulse, the vibrational and electronic excited states of N_2 relax by quenching with the surrounding molecules. The mechanism of excitation and electronic relaxation of N_2 has been describe in Popov (2001); Popov (2011); Rusterholtz et al. (2013) and can represented by a two-step reaction process:

$$N_2(X) + e^- \rightarrow N_2(A, B, C, a^{'}, ...) + e^- \tag{2.21}$$

$$N_2(A, B, C, a^{'}, ...) + O_2 \rightarrow 2O + N_2(X) + heat \tag{2.22}$$

In reaction (2.21), the electrons e- collide with the N2 molecules of the ground state N_2(X) exciting the electronic states N_2(A,B,C,a' , ...). This reaction occurs in the characteristic time scale of the pulse ($\tau_{pulse} \approx 10\ ns$) when the electric field E is active. After the pulse, The excited electronic states N_2(A,B,C,a' , ...) are rapidly quenched, mainly by a dissociative quenching reaction with O_2, reaction (2.22), which takes place on time scales of about $\tau_{electr} \approx 50\ ns$

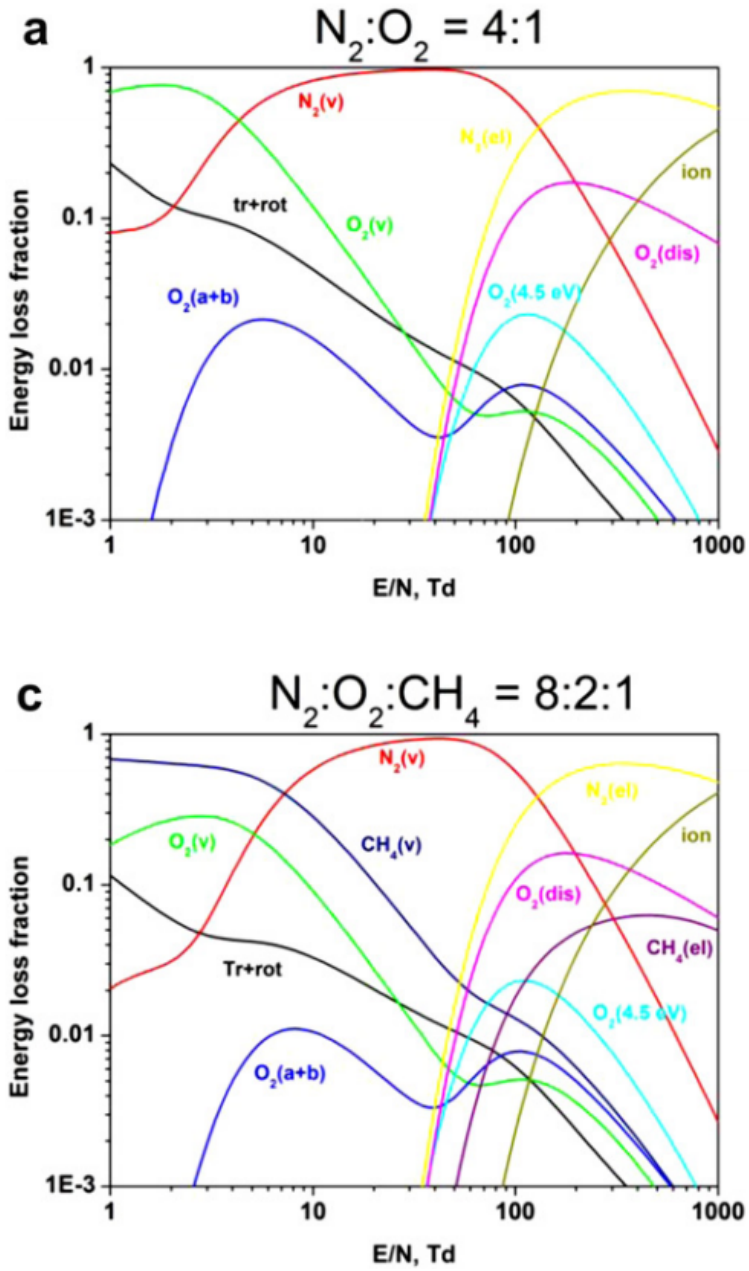

Figure 2.10: *Fractional power dissipated by electrons into various channels as a function of E/N. (a) Air; (b) methane-air stoichiometric mixture. Extracted from Starikovskiy and Aleksandrov (2013)*

and leads to an ultra-fast dissociation of O_2 into atomic O accompanied with an ultra-fast gas heating.

The vibrational excitation and relaxation mechanism of N_2 is also given by a two-step reaction process (Millikan and White (1963); Park (1993); Popov (2011)):

$$N_2(X) + e^- \rightarrow N_2(v) + e^- \tag{2.23}$$

$$N_2(v) \rightarrow N_2(X) + heat \tag{2.24}$$

N_2 vibrational excitation into N_2(v) occurs in the pulse characteristic time scale ($\tau_{pulse} \approx 10\ ns$), whereas relaxation of the vibrational states of N_2, through reaction (2.24), occurs on a much longer time $\tau_{vib} \approx 1$ to 1000 μs, and leads to a slow heating of the gas.

2.6.2 Plasma-assisted combustion model equations

According to the previous analysis, the two main channels through which the NRP discharges impact the gas are:

1. the excitation and the subsequent relaxation of electronic states of nitrogen molecules, leading to an ultra-fast increase of gas temperature and ultra-fast dissociation of O_2 into atomic O, reaction (2.22).

2. the excitation and relaxation of vibrational states of nitrogen molecules, causing a much slower gas heating, reaction (2.24).

The phenomenological NRP discharges model proposed by Castela et al. (2016) considers that the discharge deposited energy is split into three contributions:

- A chemical energy that leads to ultra-fast dissociation of species O2 into atomic O.

- A thermal energy that leads to ultra-fast gas heating.

- A vibrational energy that will relax into gas heating but with a higher time scale compared to the previous two phenomenon at a rate $\dot{R}^p_{VT}$.

A schematic representation of the model developed is shown in Fig. 2.11. The discharge energy deposition rate per unit volume, $\dot{E}^p$, deposited at each pulse, can therefore be written as the sum of three contributions:

$$\dot{E}^p = \dot{E}^p_{chem} + \dot{E}^p_{heat} + \dot{E}^p_{vib} \tag{2.25}$$

The chemical $\dot{E}^p_{chem}$ and thermal $\dot{E}^p_{heat}$ terms refer to the amount of energy transferred into the ultra-fast dissociation of O_2 molecules and gas heating, respectively. The rate of energy $\dot{E}^p_{vib}$ contributes to the vibrational excitation of N_2.

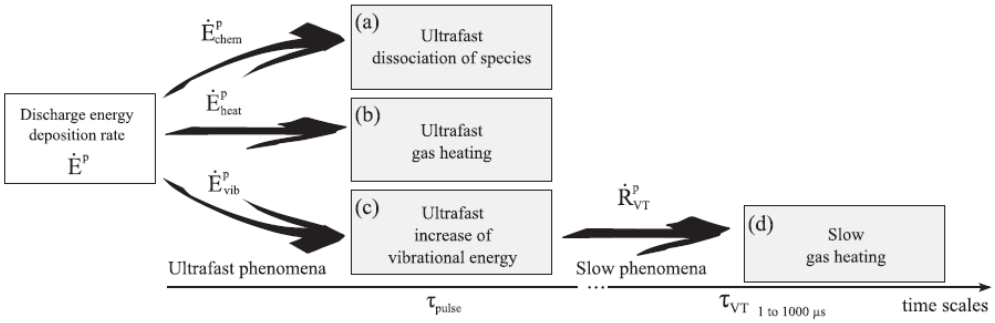

Figure 2.11: *Schematic representation of the NRP discharge model assumptions. The discharge energy is assumed to be deposited into (a) chemical, (b) sensible and (c) vibrational energies within the pulse characteristic time τ_{pulse}. The vibrational energy relaxes after the pulse, leading to an increase of the (d) sensible energy within a characteristic time τ_{VT}. Extracted from Castela et al. (2016)*

The equations governing the reacting flow and accounting for the impact of NRP discharges reads:

$$\frac{\partial \rho}{\partial t} + \frac{\partial (\rho u_i)}{\partial x_i} = 0 \tag{2.26}$$

$$\frac{\partial (\rho u_j)}{\partial t} + \frac{\partial (\rho u_i u_j)}{\partial x_i} = -\frac{\partial p}{\partial x_j} + \frac{\partial \tau_{ij}}{\partial x_i} \tag{2.27}$$

$$\frac{\partial (\rho e)}{\partial t} + \frac{\partial (\rho u_i e)}{\partial x_i} = -\frac{\partial q_i}{\partial x_i} + \frac{\partial (\sigma_{ij} u_i)}{\partial x_i} + \dot{E}^p_{chem} + \dot{E}^p_{heat} + \dot{R}^p_{VT} \tag{2.28}$$

$$\frac{\partial (\rho e_{vib})}{\partial t} + \frac{\partial (\rho u_i e_{vib})}{\partial x_i} = \frac{\partial}{\partial x_i}(\rho D \frac{\partial e_{vib}}{\partial x_i}) + \dot{E}^p_{vib} - \dot{R}^p_{VT} \tag{2.29}$$

$$\frac{\partial(\rho Y_k)}{\partial t} + \frac{\partial(\rho u_i Y_k)}{\partial x_i} = -\frac{\partial(\rho V_{k,i} Y_k)}{\partial x_i} + W_k \dot{\omega}_k^c + W_k \dot{\omega}_k^p \tag{2.30}$$

where $\dot{\omega}_k^p$ is the species molar production rate induced by ultra-fast species dissociation by the plasma discharge.

The energy equation (2.28) incorporates additional source terms from the plasma discharge. Equation (2.29) is the additional conservation equation for the vibrational energy e_{vib}, carried by N_2 molecules, where D is taken as equivalent to the diffusion coefficient of N_2 . The term $\dot{R}_{VT}^p$ in both equations (2.28) and (2.29) refers to the relaxation rate of the vibrational energy into gas heating and it is modelled considering the Landau-Teller harmonic oscillator approach Landau and Teller (1936):

$$\dot{R}_{VT}^p = \rho \, \frac{e_{vib} - e_{vib}^{eq}(T)}{\tau_{VT}} \tag{2.31}$$

where the equilibrium value of the vibrational energy, $e_{vib}^{eq}(T)$, at a given gas temperature T, is given by:

$$e_{vib}^{eq}(T) = \frac{r \ \Theta_1}{\exp \Theta_1/T - 1} \tag{2.32}$$

$\Theta_1 = 3396K$ and $r = R/W_{N_2}$, with R the gas constant and W_{N_2} the molar mass of nitrogen. τ_{VT} is computed as a function of τ_{VT}^k , the vibrational-translational relaxation time of N_2 molecules by the k^{th} collisional species partner (O_2 , O and N_2), given by the experimental correlation of Millikan et White (1963) Millikan and White (1963) :

$$\tau_{VT} = \left(\frac{1}{\tau_{VT}^{O}} + \frac{1}{\tau_{VT}^{O_2}} + \frac{1}{\tau_{VT}^{N_2}} \right) \tag{2.33}$$

$$\tau_{VT}^k = c/p_k \exp\left[a_k(T^{-1/3} - b_k) - 18.42\right] \tag{2.34}$$

$c = 1 \ atm$, p_k is the partial pressure of the k^{th} species and a_k and b_k are experimental constants depending on the k^{th} species.

2.6.3 Model closure

The fraction of discharge energy going into the chemical $\dot{E}^p_{chem}$, thermal $\dot{E}^p_{heat}$ and vibrational $\dot{E}^p_{vib}$ contributions depends on the local species concentration $X_{k=1,..,N_{sp}}$, temperature T , and pressure p of the gas mixture prior to the pulse. $\dot{E}^p_{chem}$ and $\dot{E}^p_{heat}$ can be written as follows:

$$\dot{E}^p_{\text{heat}} = g_{\text{heat}} \left(X_{k=1,..,N_{sp}}, T, p\right) \cdot \dot{E}^p \tag{2.35}$$

$$\dot{E}^p_{\text{chem}} = g_{\text{chem}} \left(X_{k=1,..,N_{sp}}, T, p\right) \cdot \dot{E}^p \tag{2.36}$$

where g_{heat} and g_{chem} are the fractions of the discharge energy deposited at the ultra-fast scale and transferred into sensible and chemical energy, respectively. The chemical energy source term can be expressed in terms of the rate of production of the k^{th} species, $\dot{\omega}^p_k$, associated with the plasma chemical processes occurring during the pulse:

$$\dot{E}^p_{chem} = \sum_{k=1}^{Nsp} e_k W_k \dot{\omega}^p_k \tag{2.37}$$

where $\dot{\omega}^p_k$ is the plasma production rate of the k^{th} species. e_k and W_k are the internal energy and the molar mass of the k^{th} species, respectively.

Combining equation (2.36) and equation (2.37) gives :

$$g_{chem} \left(X_{k=1,..,N_{sp}}, T, p\right) \cdot \dot{E}^p = \sum_{k=1}^{Nsp} e_k W_k \dot{\omega}^p_k \tag{2.38}$$

where g_{chem} can be expressed as:

$$g_{chem} = \sum_{k=1}^{Nsp} g^k_{chem} \tag{2.39}$$

where g^k_{chem} the fraction of the discharge power consumed by the production of the k^{th} species.

The rate of production of the k^{th} species during the pulse can then be written as:

$$\dot{\omega}^p_k = g^k_{chem} \left(X_{k=1,..,N_{sp}}, T, p\right) \cdot \frac{\dot{E}^p}{e_k W_k} \tag{2.40}$$

The rate of increase of vibrational energy $\dot{E}^p_{vib}$ is the remaining fraction of the discharge power that is not transferred into $\dot{E}^p_{chem}$ and $\dot{E}^p_{heat}$. From equations (2.25), (2.35) and (2.36) , $\dot{E}^p_{vib}$ is therefore expressed as:

$$\dot{E}^p_{vib} = [1 - (g_{heat} + g_{chem})] \cdot \dot{E}^p \tag{2.41}$$

2.6.4 Model parameters

The NRP discharge phenomenological model proposed by Castela et al. (2016) involves two parameters g_{heat} and g_{chem}, the fractions of the discharge energy transferred into sensible and chemical energy. The values of these two parameters are estimated from the detailed theoretical, numerical and experimental studies.

As previously discussed, the nanosecond scale relaxation of the excited electronic states of N_2 formed during the pulse, by dissociative quenching reaction with O_2 (reaction (2.22)) results in an ultra-fast heating of the gas and ultra-fast dissociation of O_2 into atomic O. 0-D numerical simulations of NRP discharges in air performed by various authors (Popov (2001); Flitti and Pancheshnyi (2009); Aleksandrov et al. (2010)), have shown that 10 to 30% of the discharge energy is transferred into ultra-fast gas heating. Similar results were later found by Rusterholtz et al. (2013). The fraction of pulse energy that goes into ultra-fast heating was estimated from the experimental measurements to be around 20%.

The second important parameter is the fraction of energy going into O_2 dissociation. The dissociation energy of O_2 is about 5.2 eV, the average energy necessary to excite electronically a ground state N_2 molecule into N_2(A,B,C,a' , ...) states, main contributors to the ultra-fast mechanism, is about 8.2 eV. Thus, for reaction .(2.22), the ratio of energy going into dissociation (5.2 eV) over the energy going into heating (8.2 - 5.2 = 3.0 eV) is approximately 1.74. Knowing that the fraction of pulse energy that goes into ultra-fast heating is equal approximately to 20%, the fraction of energy going into O2 dissociation is then equal to 34.8% (0.2 * 1.74 = 0.348). In the experiments of Rusterholtz et al. (2013) and simulations of Popov (2013a), this ratio was found to be about 1.75 (35% into dissociation and 20% into heating), which is consistent with the foregoing analysis.

The phenomenological model parameters are based on these experimental and numerical values with 35% of energy going into ultra-fast dissociation, and 20% into ultra-fast heating. Finally, the rest of the discharge energy, i.e. about 45%, is spent on the vibrational excitation of N_2 by electron impact. The energy stored in vibrational states of N_2 will then impact the thermal-equilibrium

system through a slow heat release.

The reaction rate of O_2 dissociation involved in the plasma reaction depends also on the available quantity of O_2, therefore g_{chem} is assumed to be proportional to the ratio $Y_{O_2}/Y^f_{O_2}$ where $Y^f_{O_2}$ represents the mass fraction of O_2 in the fresh mixture:

$$g_{chem} = \eta \, \frac{Y_{O_2}}{Y^f_{O_2}} \tag{2.42}$$

where η is the fraction of the discharge power leading to O_2 dissociation, with $\eta = 0.35$ as discuss above.

From equation (2.40) the molar production rates of the species can then be expressed :

$$\dot{\omega}^p_O = \eta \, \frac{Y_{O_2}}{Y^f_{O_2}} \, \frac{\dot{E}^p}{e_O \, W_O} \tag{2.43}$$

$$\dot{\omega}^p_{O2} = -\frac{W_O}{W_{O2}} \, \dot{\omega}^p_O \tag{2.44}$$

$$\dot{\omega}^p_k = 0 \quad \text{, if k} \neq O_2, O \tag{2.45}$$

where W is the molar mass, e_O is the energy of specie O.

$\dot{E}^p_{chem}$ finally writes:

$$\dot{E}^p_{chem} = \eta \, \frac{Y_{O_2}}{Y^f_{O_2}} \, (1 - \frac{e_{O_2}}{e_O}) \, \dot{E}^p \tag{2.46}$$

The sum of the power going into ultra-fast dissociation ($\dot{E}^p_{chem}$) and ultra-fast heating ($\dot{E}^p_{heat}$) is equal to the power going into the electronic excitation of N_2. Thus it is proportional to $\dot{E}^p$

$$\dot{E}^p_{chem} + \dot{E}^p_{heat} = \alpha \dot{E}^p \tag{2.47}$$

with $\alpha \approx 0.55$ ($0.\ 35 + 0.20 = 0.55$) as discussed previously.

Combining equation (2.46) and equation (2.47) gives:

$$\dot{E}^p_{heat} = [\alpha - \eta \, \frac{Y_{O_2}}{Y^f_{O_2}} \, (1 - \frac{e_{O_2}}{e_O})] \, \dot{E}^p \tag{2.48}$$

The fraction $\dot{E}^p_{heat}$ increases when Y_{O_2} decreases, and reaches $\alpha \dot{E}^p$ when O_2 vanishes. The relaxation of electronically excited N_2 will then occur mainly by collisions with ground state N_2 which results mainly in an ultra-fast heating as shown in Rusterholtz et al. (2013).

As mentioned previously, the vibrational energy is the remaining energy and read:

$$\dot{E}_{vib} = (1 - \alpha) \, \dot{E}^p \tag{2.49}$$

The phenomenological plasma model proposed by Castela et al. (2016) is retained in this work to perform simulations of flames ignition and stabilization by NRP discharges. The implementation of the model in the YALES2 CFD code, the coupling with the LES formalism and combustion kinetic mechanisms as well as the validation of the model are presented in the next chapter.

Chapter 3

Numerical Methods for plasma-assisted combustion

This chapter is devoted to the description of the numerical tools and methods used in this work to perform plasma-assisted combustion simulations. The YALES2 Computational Fluid Dynamics (CFD) library for low-Mach number reactive flows simulations is first introduced along with the numerical methods employed for turbulent reactive flows with a focus on the Large-Eddy Simulation (LES) formalism and the flame thickening model retained for the simulations. The coupling between the set of LES governing equations and the phenomenological NRP discharges model is detailed. Finally, a series of test cases performed to validate the implementation and the behavior of the NRP discharges model is presented.

Contents

3.1 Introduction

Numerical simulations are used in this work to understand and explain the complex fundamental mechanisms of plasma-assisted combustion. The objective of this chapter is to review the numerical tools retained to carry out the simulations. Section. 3.2 is dedicated to the presentation of the YALES2 Computational Fluid Dynamics (CFD) code developed by Moureau et al. (2011) to perform low-Mach number reactive flows simulations, as well as the numerical methods used for the simulations. The coupling and implementation of the phenomenological NRP discharges model (Castela et al. (2016)) in the YALES2 code are described in Sections. 3.3. Finally, The validation of the coupling and the implementation of the model through a series of test cases is presented in Sections. 3.4.

3.2 YALES2 library

3.2.1 The YALES2 CFD code

YALES2 is a Computational Fluid Dynamics (CFD) library developed to solve the Navier-Stokes equations in two-phase reactive low-Mach number flows (Moureau et al. (2011)). Based on the finite volume method for the integration of the transport equations, it can handle one, two and three dimensions simulations on structured and unstructured meshes composed of triangles, tetrahedrons, prisms, pyramids, quadrilaterals or hexahedrons. The code uses the MPI (Message Passing Interface) library to perform massively parallel computations on supercomputers.

In order to overcome the multi-scale time constraint, the YALES2 solver uses the operator splitting method which consists in separately solving each operator (convection, diffusion and reaction) with its own characteristic time step. The interest of such a method lies in the choice of the time step of an iteration, taken as the largest characteristic time between each phenomenon. As a general rule, it is the convective time step. The diffusion and reaction phenomena perform several substeps within this fluid iteration in order to respect their stability condition.

Taking advantage of the operator splitting method, the chemical source terms are computed independently of other physical phenomena using a "stiff" integration library capable of solving systems of ordinary differential equations (ODE) with implicit multi-step methods, dedicated to the temporal integration of stiff problems. The one used in YALES2 is CVODE. It allows solving the chemical system with a variable order and time step and a controlled error.

The low-Mach formalism used in the code is describe in Majda and Sethian

(1985). The simplification of the Navier-Stokes equations using this method allows larger time steps compared to the compressible formulation constrained by the propagation speed of the acoustic waves. Several numerical schemes are implemented in YALES2. For the time integration, the code disposes of the third and fourth order Runge-Kutta schemes or the more recent TFV4A scheme proposed by Kraushaar (2011), which combines the Runge-Kutta and Lax-Wendroff methods. For the spatial integration a second or fourth order centered schemes are available (Vantieghem (2011)).

The YALES2 library is composed of several solvers (Incompressible solver (ICS), Scalar solver (SCS), Lagrangian solver (LGS), Triple phase solver (TPS), ...) dedicated to the resolution of different physical phenomena. In this work, the simulations are performed using the variable density solver (VDS) which solves the reactive Navier-Stokes equations at low Mach number. A brief description of this solver is presented in the following section.

3.2.2 Variable Density Solver (VDS)

The Variable Density Solver (VDS) solves the Navier-Stokes equations for low Mach number reactive flows assuming that the pressure, density and temperature variations due to acoustic waves are negligible. The temperature variations modify the density through an equation of state. For all simulations performed in this work the equation of state follows the ideal gas law:

$$P = \rho r T \tag{3.1}$$

where P, ρ, T and r are the pressure, density, temperature and gas constant, respectively.
The Navier-Stokes equations under the low-Mach number approach are written as follows:

$$\frac{\partial \rho}{\partial t} + \frac{\partial (\rho u_i)}{\partial x_i} = 0 \tag{3.2}$$

$$\frac{\partial (\rho u_j)}{\partial t} + \frac{\partial (\rho u_i u_j)}{\partial x_i} = -\frac{\partial P_2}{\partial x_j} + \frac{\partial \tau_{ij}}{\partial x_i} \tag{3.3}$$

$$\frac{\partial}{\partial t}\rho h_s + \frac{\partial}{\partial x_i}\rho u_i h_s = \frac{dP_0}{dt} + \frac{\partial \mathcal{Q}_i}{\partial x_i} + \dot{\omega}_T \tag{3.4}$$

$$\frac{\partial (\rho Y_k)}{\partial t} + \frac{\partial (\rho u_i Y_k)}{\partial x_i} = -\frac{\partial (\rho V_{k,i} Y_k)}{\partial x_i} + W_k \dot{\omega}_k \tag{3.5}$$

where ρ is the density, u_i is the i-th component of local flow velocity in direction x_i and τ_{ij} the viscous tensor defined in Eq. (2.7). Y_k, $\rho Y_k V_{k,i}$, $\dot{\omega}_k$ are the mass fraction, the molecular diffusion term and the molar production rate of the species k, respectively.

Under the low-Mach number approach, the pressure can then be decomposed into two terms: the thermodynamic pressure P_0 assumed constant in space and the dynamic pressure P_2 variable in space and time. In an open system, the thermodynamic pressure of the system P_0 is also considered constant in time. The equation of state is written:

$$P_0 = \rho_0 r_0 T_0 \tag{3.6}$$

where ρ_0, T_0 and r_0 the initial density, temperature and gas constant, respectively, defined at t = 0 s of the simulation.

The total energy balance equation Eq. (2.3) is rewritten as the sensible enthalpy balance equation Eq. (3.4), more suitable for isobar simulations. $\dot{\omega}_T$ is the heat release generated by chemical reactions.

$$\dot{\omega}_T = -\sum_{k=1}^{N_{sp}} \Delta h^0_{f,k} \dot{w}_k \tag{3.7}$$

$\mathcal{Q}_i$ is the heat flux defined as follow:

$$\mathcal{Q}_i = -\lambda \frac{\partial T}{\partial x_i} + \rho \sum_{k=1}^{N_{sp}} h_{s,k} Y_k V_{k,i} \tag{3.8}$$

where λ is the heat conduction coefficient of the mixture and $h_{s,k}$ is the sensible enthalpy of the species k .

3.2.3 Numerical methods in turbulent flows

Most flows encountered in industrial processes (gas turbines, internal combustion engines, furnaces ...) or even in nature are described as unsteady and highly turbulent. The turbulence of these flows is characterized by the formation of multitude turbulent structures (eddies) associated with different time, length and energy scales. The energy of the large scales structures flows to the smaller scales through an energy cascade introduced by Kolmogorov (1941) and known as the Kolmogorov cascade.

The description of turbulent processes using Computational Fluid Dynamics (CFD) may be achieved using three levels of computations:

Direct Numerical Simulation (DNS): consists in solving the full instantaneous Navier-Stokes equations without any turbulence model. All turbulence scales and their effects are explicitly determined, making this approach extremely expensive. With current computing resources, this strategy is out of reach for industrial configurations and is limited to simple academic flows (typically, combustion in a small cubic box).

Reynold-Averaged Navier-Stokes (RANS) computations: historically developed to reduce the computational cost of the numerical simulations, this approach aims to solve the mean values of the transported quantities. The balance equations are obtained by averaging the instantaneous Navier-Stokes equations. The averaged equations require closure rules, turbulence models, to deal with the flow dynamics in combination with a turbulent combustion interactions.

Large- Eddy Simulations (LES): the Navier-Stokes equations are solved for the large energetic eddies while the small scale energetic structures are modeled using subgrid closure rules. The main advantage of LES compared to RANS is a better reproduction of the turbulent mixing processes (Pope (2000)), and therefore a better characterization of turbulent-flame interactions and prediction of chemical species (Poinsot and Veynante (2012)). The filter size Δ linked to the LES grid element defines a cut-off wave number $k_c = \Delta/\pi$, which determines the limit in the spectral space between large and small turbulent energy structures.

Figure. 3.1 shows the scope of the three techniques used in CFD simulations in the physical and spectral spaces, which depicts how each one handles the turbulent energy structures found in the turbulent flow. The CPU cost increases when considering these approaches in the following direction: RANS $\rightarrow$ LES $\rightarrow$ DNS.

Being a good compromise between the cost and the precision of the computations, LES has been lately extensively used in CFD codes, such as the YALES2 library, for the simulations of turbulent combustion in practical applications. In this thesis, plasma assisted combustion simulations are computed using the LES technique.

3.2.4 Large-Eddy Simulation (LES) formalism

Large-Eddy Simulation (LES) is based on the transport of spatially-filtered density, momentum, energy and chemical species balance equations. Any filtered

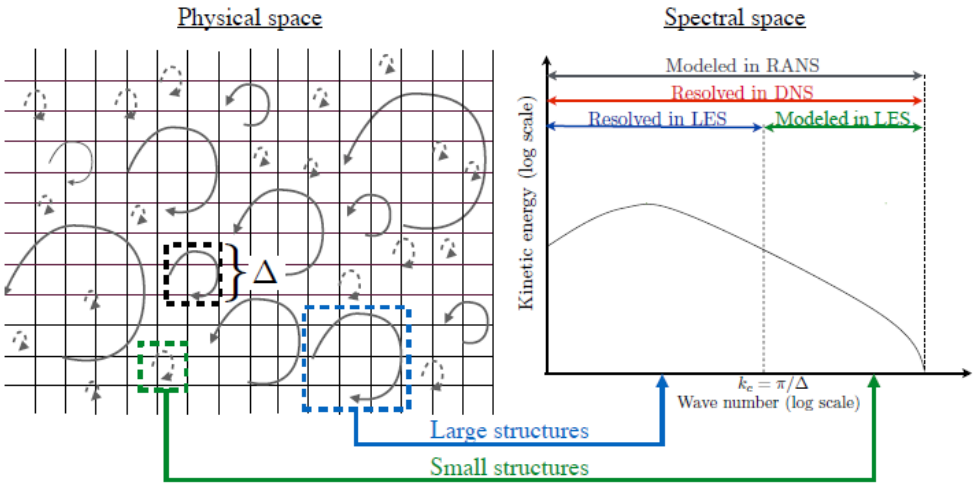

Figure 3.1: *CFD approaches in turbulent flows considering homogeneous and isotropic turbulence. The filter size Δ of the numerical grid determines whether the turbulent energy structures are resolved or not (left). Resolution and modeling considerations for DNS, RANS and LES approaches regarding the turbulent energy structures in the energy cascade (right). $k_c = \Delta/\pi$ denotes the cut-off wave number used in LES filtering. Extracted From Mercier (2015)*

variable $\bar{\varphi}$ is then defined as follows:

$$\bar{\varphi}(\mathrm{x},t) = \int \varphi\left(\mathrm{x}',t\right) G_\Delta\left(\mathrm{x}-\mathrm{x}'\right) d\mathrm{x}' \tag{3.9}$$

where G_Δ is a LES filter of width Δ. The Favre-filtering operation $(\,\widetilde{.}\,)$ on φ is defined as:

$$\widetilde{\varphi}(\mathrm{x},t) = \frac{\overline{\rho\varphi}}{\bar{\rho}} \tag{3.10}$$

In this regard, any quantity φ is now defined as the sum of its filtered resolved part and its sub-filter or sub-grid value $\varphi = \widetilde{\varphi} + \varphi''$. The decoupling of resolved and sub-filter components is implicitly made by the LES grid, where turbulent structures larger than twice the size of the filter Δ_x are typically resolved.

In LES formalism, the Low-Mach number flows governing equation are written as follow:

$$\frac{\partial\bar{\rho}}{\partial t} + \frac{\partial}{\partial x_i}(\bar{\rho}\widetilde{u_i}) = 0 \tag{3.11}$$

$$\frac{\partial(\bar{\rho}\widetilde{u_j})}{\partial t} + \frac{\partial}{\partial x_i}(\bar{\rho}\widetilde{u_i}\widetilde{u_j}) = -\frac{\partial}{\partial x_i}(\bar{\rho}(\widetilde{u_i u_j} - \widetilde{u_i}\widetilde{u_j})) - \frac{\partial\bar{P}_2}{\partial x_j} + \frac{\partial\overline{\tau_{ij}}}{\partial x_i} \tag{3.12}$$

$$\frac{\partial \bar{\rho}\widetilde{h_s}}{\partial t} + \frac{\partial(\bar{\rho}\widetilde{u_i}\widetilde{h_s})}{\partial x_i} = -\frac{\partial}{\partial x_i}(\bar{\rho}(\widetilde{u_i h_s} - \widetilde{u_i}\widetilde{h_s})) + \frac{d\bar{P}_0}{dt} + \frac{\partial \bar{\mathcal{Q}}_i}{\partial x_i} + \bar{\dot{\omega}}_T \tag{3.13}$$

$$\frac{\partial \bar{\rho}\widetilde{Y_k}}{\partial t} + \frac{\partial}{\partial x_i}(\bar{\rho}\widetilde{u_i}\widetilde{Y_k}) = -\frac{\partial}{\partial x_i}(\bar{\rho}(\widetilde{u_i Y_k} - \widetilde{u_i}\widetilde{Y_k})) - \frac{\partial}{\partial x_i}(\rho \bar{V_{k,i}} Y_k) + \bar{\dot{\omega}}_k^M \tag{3.14}$$

$$P_0 = \bar{\rho}\widetilde{rT} \tag{3.15}$$

Unclosed terms of the filtered equations are expressed as follows (Poinsot and Veynante (2012)):

Reynolds stress tensor: represents the impact of the unresolved flow motions on the resolved momentum. Using the Boussinesq assumption that supposes that the effects of the smallest unresolved scales are similar to the addition of a new term of viscosity, $\bar{\tau}_{ij}^{sgs}$ is modeled as follows:

$$\bar{\tau}_{ij}^{sgs} = \bar{\rho}(\widetilde{u_i u_j} - \widetilde{u_i}\widetilde{u_j}) = \bar{\rho}\nu_t \left[\left(\frac{\partial \widetilde{u_i}}{\partial x_j} + \frac{\partial \widetilde{u_j}}{\partial x_i} \right) - \frac{2}{3}\frac{\partial \widetilde{u_k}}{\partial x_k}\delta_{ij} \right] \tag{3.16}$$

where ν_t is the sub-grid turbulent kinematic viscosity. Several closures exist for ν_t in the literature (Smagorinsky (Germano et al. (1991)), WALE (Nicoud and Ducros (1999)), Sigma (Nicoud et al. (2011))).

Energy and species fluxes: $\bar{\mathcal{Q}}_i^{sgs}$ and $\bar{J}_{i,k}^{sgs}$ have gradient-type closures, respectively as:

$$\bar{\mathcal{Q}}_i^{sgs} = \bar{\rho}(\widetilde{u_i h_s} - \widetilde{u_i}\widetilde{h_s}) = -\frac{\mu_t \bar{cp}(\bar{T}, \bar{Y_k})}{Pr_t}\frac{\partial \widetilde{T}}{\partial x_i} + \sum_{k=1}^{N_{sp}} \bar{J}_{i,k}^{sgs}\widetilde{h}_{s,k} \tag{3.17}$$

$$\bar{J}_{i,k}^{sgs} = \bar{\rho}(\widetilde{u_i Y_k} - \widetilde{u_i}\widetilde{Y_k}) = \bar{\rho}\left(\frac{\nu_t}{Sc_{t,k}}\frac{W_k}{W}\frac{\partial \widetilde{X_k}}{\partial x_i} - \widetilde{Y}_k \widetilde{V}_i^{c,sgs} \right) \tag{3.18}$$

where the turbulent Schmidt number $Sc_{t,k}$ of species k and the turbulent Prandtl number Pr_t are usually set to a constant value or evaluated dynamically (Moin et al. (1991)).

Filtered laminar diffusion fluxes of momentum, energy and species: have a gradient kind closure, as follows:

$$\bar{\tau}_{ij} \simeq \overline{\rho\nu}\left[\left(\frac{\partial\widetilde{u_i}}{\partial x_j}+\frac{\partial\widetilde{u_j}}{\partial x_i}\right)-\frac{2}{3}\frac{\partial\widetilde{u_k}}{\partial x_k}\delta_{ij}\right] \tag{3.19}$$

$$\bar{\mathcal{Q}}_i = -\overline{\lambda\frac{\partial T}{\partial x_i}+\rho\sum_{k=1}^{N_{sp}}h_{s,k}Y_kV_{k,i}} \simeq -\bar{\lambda}\frac{\partial\widetilde{T}}{\partial x_i}+\sum_{k=1}^{N_{sp}}\bar{J}_{i,k}\widetilde{h}_{s,k} \tag{3.20}$$

$$\bar{J}_{i,k} = \overline{\rho V_{i,k}Y_k} \simeq \bar{\rho}\left(-\bar{D}_k\frac{W_k}{W}\frac{\partial\widetilde{X_k}}{\partial x_i}+\widetilde{Y}_k\widetilde{V}_i^c\right) \tag{3.21}$$

Filtered chemical source term: the term $\bar{\dot{\omega}}_k^M$ is challenging to close in turbulent combustion systems, especially because of the high interaction with the turbulent structures and its peculiar behavior at the flame front, which is highly dependent on the turbulent combustion regime (Poinsot and Veynante (2012)). Numerous models exist in the literature to retrieve the subgrid-scale effects in the turbulent reactive flow. A summary of the main techniques are presented in Section. 3.2.5.

3.2.5 Turbulent combustion modeling in LES

The turbulent flame structure is severely affected by the size of the numerical grid in LES, especially in large industrial configurations where fine resolution of the flame front cannot be afforded due to CPU limitations. To properly resolve the flame front, the turbulence-chemistry interactions must be modeled at the subgrid scale. The expression of the filtered source term $\bar{\dot{\omega}}_k^M$, key in LES combustion simulations, has been extensively studied in the literature. Some of these methods are reviewed in (Poinsot and Veynante (2012)) and (Fiorina et al. (2015)), classified into three main categories:

- **The turbulent mixing method**, the reaction rate is controlled by the turbulent mixing, described in terms of scalar dissipation (Bray (1996)). Some examples of this method are the Eddy Dissipation Model (Magnussen and Hjertager (1977)) and the Linear-Eddy Model (Menon and Calhoon-Jr (1996)). This approach is only possible when the characteristic time of turbulence τ_t is very high compared to the characteristic time of chemistry τ_c this why it's mainly used in RANS calculations rather than LES.

- **The statistical methods** describe the turbulent reactive flow properties in LES through a Probability Density Function (PDF) (Pope (1985)) or a Filtered Density Function (FDF) (Haworth (2010)). These approaches

have been extensively used in LES of turbulent flames. However, it can be computational demanding and may require complex modeling hypothesis when Lagrangian and Eulerian strategies are involved.

- **The geometrical methods** characterize and track the turbulent flame front as a moving geometric surface that divides the fresh and burnt gases zones in physical space. A first approach, called the G-equation model (Kerstein et al. (1988)), considers the flame front thickness negligible and traces the flame surface with the help of a field variable $\widetilde{G}$. In other approaches, in order to have enough mesh points in the flame front and thus not neglect its thickness, the flame is artificially thickened in zones where the mesh cell size is larger than the flame thickness while maintaining the essential flame properties. The main examples of these strategies are the Thickened Flame model for LES (TFLES, Colin et al. (2000)) and the Filtered- Tabulated Chemistry for LES (F-TACLES, Fiorina et al. (2010)). In FTACLES the flame front is explicitly filtered in the physical space, while in TFLES the flame front is artificially thickened.

The model used in this work is the TFLES model, described in the following section.

3.2.6 Artificial thickened flame model for LES (TFLES)

The TFLES model provides a good description of the chemical source terms. It is characterized by its easy implementation and robustness in combustion modeling. The thickening operation is done preserving the flame consumption speed, while the diffusion and species source terms are modified. According to Kuo and Acharya (2012), the consumption speed s_L^0 and the laminar thickness δ_L^0 of a flame, can be written as a function of the reaction rate $\dot{\omega}$ and the thermal diffusion coefficient D_{th} as follows:

$$s_L^0 \propto \sqrt{D_{th}\dot{\omega}} \quad \delta_L^0 \propto \frac{D_{th}}{s_L^0} = \sqrt{\frac{D_{th}}{B}} \tag{3.22}$$

To ensured a thickening by factor F of the flame while preserving the flame speed, the following transformation are performed :

$$D_{th}^F = D_{th} \cdot F \quad \dot{\omega}^F = \frac{\dot{\omega}}{F} \tag{3.23}$$

where the diffusion coefficient and the species source terms are multiplied and divided by F, respectively.

When the flame is thickened, the interaction between turbulence and flow is modified, because the Damkohler number is also divided by a factor F:

$$D_a = \frac{\tau_t}{\tau_c} = \frac{l_t}{u'}\frac{s_L}{\delta_L^0} \tag{3.24}$$

When D_a decreases, the flame becomes less sensitive to turbulent motion, in particular, resolved wrinkling is diminished, hence the effective flame surface decreases and so does the fuel consumption speed Fig. 3.2. To compensate for these effects, and efficiency function Ξ acting as a subgrid-scale wrinkling factor is added to the model to correct the turbulent flame speed (Poinsot and Veynante (2012)).

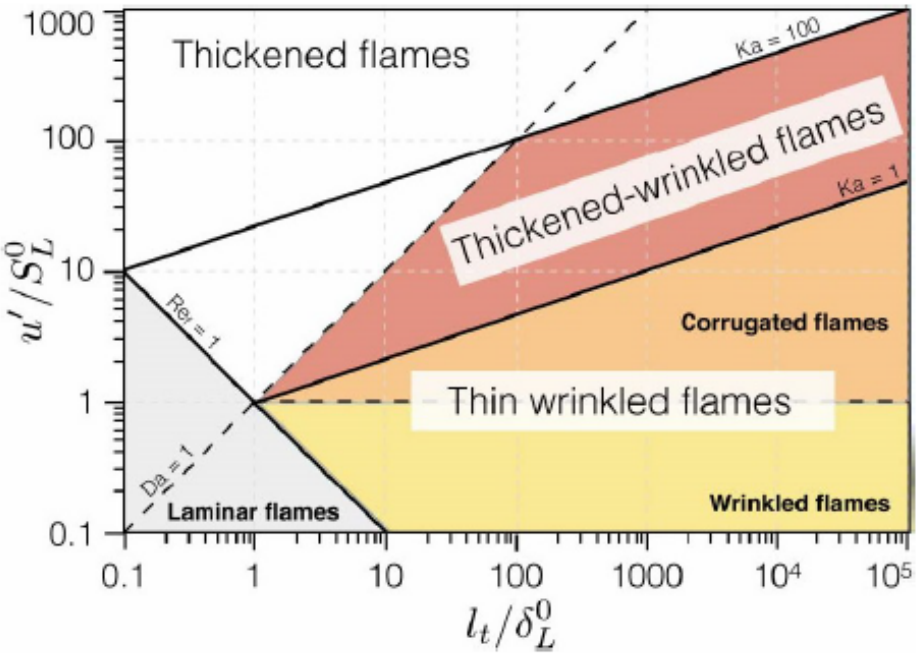

Figure 3.2: *Classical turbulent combustion diagram; changing the Damkohler number affects flame-turbulence interactions. Extracted from Poinsot and Veynante (2012).*

$$D_{th} \longrightarrow FD_{th} \longrightarrow \Xi F D_{th} \tag{3.25}$$

$$\dot{\omega} \longrightarrow \frac{\dot{\omega}}{F} \longrightarrow \Xi\frac{\dot{\omega}}{F} \tag{3.26}$$

The flame speed and flame thickness become:

$$s_T^0 = \Xi s_L^0 \tag{3.27}$$

$$\delta_T = F\delta_L^0 \tag{3.28}$$

where s_T^0 and δ_T are the turbulent flame speed and thickness, respectively.

In this work, a dynamic TFLES model is used. A flame sensor S tracks the position of the flame front as the region of space where species production rates are above defined percentage of the maximum value reached in the reaction zone of a pre-computed laminar premixed flame.

Based on a laminar flame thickness δ_L^0 pre-computed by the user with a 1D laminar flame simulation and a minimum desired number of points in the flame front N_{pt}, a variable thickening factor F depending on the local mesh size Δ is imposed only where the flame sensor S is 1:

$$F = 1 + S \cdot \left[max\left(N_{pt}\frac{\Delta}{\delta_L^0}, 1 \right) - 1 \right] \tag{3.29}$$

The efficiency function of Charlette (Charlette et al. (2002)) with a clipping factor to handle the case $\frac{\Delta}{\delta_L^0} < 1$ reads:

$$\Xi = 1 + S \cdot \left[\left(1 + \min\left[\max\left(\frac{\Delta}{\delta_L^0}, 1 \right) - 1, \quad f\left(\frac{\Delta}{\delta_L^0}, \frac{u'}{s_L^0}, \mathrm{Re} \right) \frac{u'}{s_L^0} \right] \right)^{\beta} - 1 \right] \tag{3.30}$$

3.3 Phenomenological plasma model in the LES formalism

The phenomenological NRP discharges model has been implemented in the YALES2 code (Moureau et al. (2011)) and coupled with the LES reactive flow governing equations combined with the Thickened Flame model for TFLES (Colin et al. (2000)). In addition to the mass and momentum transport equations, Eq. (3.11) and Eq. (3.12) respectively, the following balance equations are solved for sensible enthalpy h_s, vibrational energy e_{vib} and species mass fractions Y_k:

$$\begin{aligned} \frac{\partial \overline{\rho}\widetilde{h_s}}{\partial t} + \frac{\partial (\overline{\rho}\widetilde{u_i}\widetilde{h_s})}{\partial x_i} &= \frac{\partial}{\partial x_i}\left(C_p \left[F\Xi\frac{\mu}{P_r} + (1-S)\frac{\mu_t}{P_r^t} \right] \frac{\partial \widetilde{T}}{\partial x_i} \right) \\ &+ \frac{\partial}{\partial x_i}\left(\sum_{k=1}^{N} \left[F\Xi\frac{\mu}{S_{c,k}} + (1-S)\frac{\mu_t}{S_{c,k}^t} \right] \frac{\partial \widetilde{Y_k}}{\partial x_i}\widetilde{h}_{s,k} \right) \\ &+ \frac{\partial \bar{P}_0}{\partial t} + \bar{\dot{\omega}}_T + \overline{\dot{E}}_{chem}^p + \overline{\dot{E}}_{heat}^p + \overline{\dot{R}}_{VT}^p \end{aligned} \tag{3.31}$$

$$\frac{\partial \overline{\rho}\widetilde{e}_{vib}}{\partial t} + \frac{\partial(\overline{\rho}\widetilde{u}_i\widetilde{e}_{vib})}{\partial x_i} = \frac{\partial}{\partial x_i}\left(\left[\frac{\overline{\mu}}{S_{c,evib}} + \frac{\mu_t}{S^t_{c,evib}}\right]\frac{\partial \widetilde{e}_{vib}}{\partial x_i}\right) + \overline{\dot{E}}^p_{vib} - \overline{\dot{R}}^p_{VT} \tag{3.32}$$

$$\frac{\partial \overline{\rho}\widetilde{Y_k}}{\partial t} + \frac{\partial(\overline{\rho}\widetilde{u}_i\widetilde{Y_k})}{\partial x_i} = \frac{\partial}{\partial x_i}\left(\left[F\Xi\frac{\overline{\mu}}{S_{c,k}} + (1-S)\frac{\mu_t}{S^t_{c,k}}\right]\frac{\partial \widetilde{Y_k}}{\partial x_i}\right) + \frac{\Xi}{F}W_k\overline{\dot{\omega}}^c_k + W_k\overline{\dot{\omega}}^p_k \tag{3.33}$$

$\overline{\dot{\omega}}^c_k$, the chemical reaction rate due to combustion, is modeled by a detailed mechanism. The plasma chemical reaction rate $\overline{\dot{\omega}}^p_k$ is closed to account for the O_2 dissociation induced by the electrical discharge. For sensible enthalpy formulation the terms reads:

$$\overline{\dot{\omega}}^p_O = \eta\,\frac{\widetilde{Y}_{O_2}}{Y^f_{O_2}}\,\frac{\dot{E}^p}{e_O\,W_O} \tag{3.34}$$

$$\overline{\dot{\omega}}^p_{O2} = -\frac{W_O}{W_{O2}}\,\overline{\dot{\omega}}^p_O \tag{3.35}$$

$$\overline{\dot{\omega}}^p_k = 0 \quad \text{if k} \neq O_2,\, O \tag{3.36}$$

For all the simulations performed in this work, the mesh is refined in the plasma discharge zone to ensure that the small turbulence scales and laminar flame thickness are well resolved and no sub-grid scale model or TFLES coupling is necessary. The filtered rate of energy, $\overline{\dot{E}}^p_{chem}$,$\overline{\dot{E}}^p_{heat}$ and $\overline{\dot{E}}^p_{vib}$ are closed from Eq. (2.46), Eq. (2.48) and Eq. (2.49) by assuming that $\overline{\dot{E}^p_y} = \dot{E}^p_y(\widetilde{Y}_{O_2}, \overline{\dot{E}}^p)$.

3.4 Model validation

To validate the implementation of the phenomenological plasma model in the YALES2 code, a series of numerical test cases is performed and compared to experimental measurements and DNS simulations of NRP discharges applied in air or in hydrocarbon-air mixtures.

3.4.1 NRP discharges in the air

The first test case is performed to validate the model behavior during a single NRP discharge pulse applied in the air. For this, 0-D simulations are compared

to the experimental measurement of Rusterholtz et al. (2013) and the numerical results of Castela et al. (2016).

In the experiment, Rusterholtz et al. (2013) applied a series of NRP discharge pulses between two pins separated by an inter-electrode gap distance of 4 mm in a flow of atmospheric pressure air preheated to 1000 K. The gas was injected from the grounded cathode side with a velocity of 2.6 m/s. The pulses of 10 ns duration and a voltage of 5.7 V were applied at a frequency of 10 kHz. An image of the experimental setup is shown in Fig. 3.3

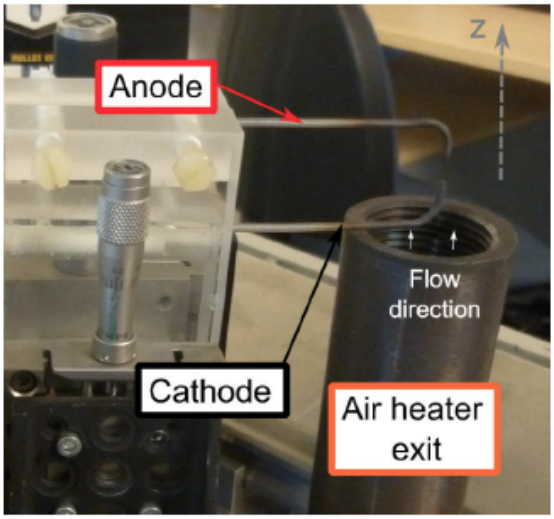

Figure 3.3: *Photo of air heater exit and electrode assembly. Extracted from Rusterholtz (2012)*

Figure. 3.4 shows the temporal evolution of a) voltage, b) current, c) gas temperature and d) atomic oxygen density, measured in the steady-state pulse regime. The energy deposited per pulse was obtained by first multiplying the measured voltage and current signals and then by integrating in time over the pulse duration. The obtained value was about 670 μJ. The plasma diameter was obtained based on the number density profiles of electronic excited nitrogen N2(B) and N2(C) species and is approximately equal to 450 μm (Rusterholtz et al. (2013)). After multiple pulses when the steady-state is reached, the temperature of the gas just before a pulse is 1500 K with a temperature rise of about 900 K when the pulse is applied. About 15% of the O2 has been dissociated into atomic O at the beginning of the pulse by the previous discharges. At the end of the pulse around 50% of oxygen is dissociated.

The test case consists of applying a single NRP discharge pulse in the air mixture once pulsing regime has reached a steady state and compare the evolution

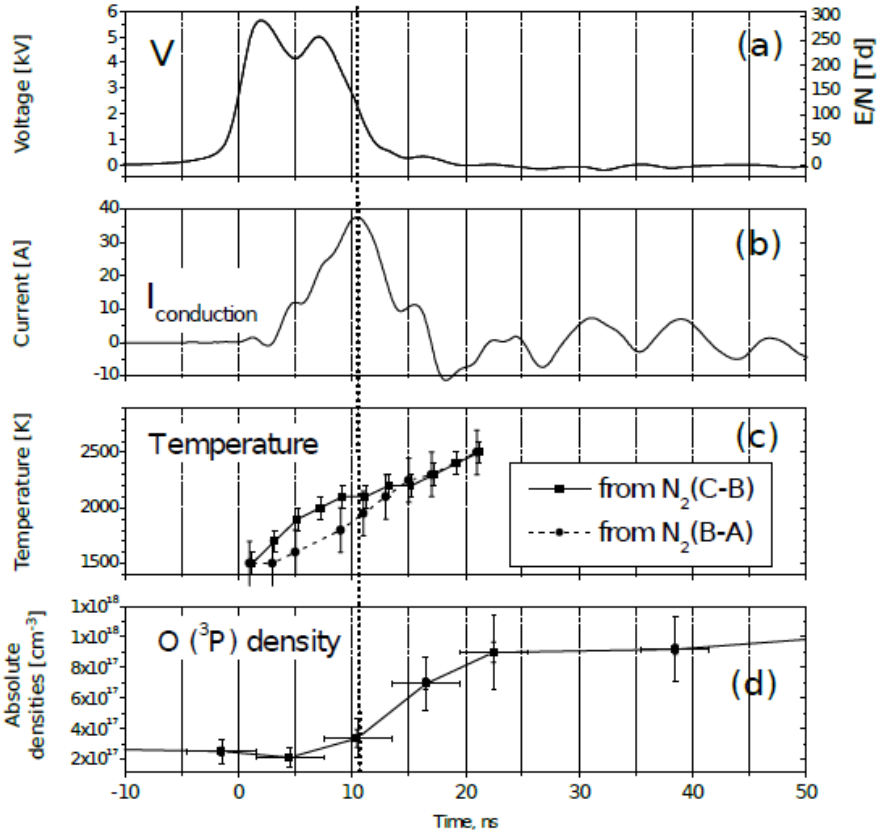

Figure 3.4: *Temporal evolution of (a) pulse voltage and corresponding reduced electric field E/N, (b) conduction current, (c) temperature and (d) O density measured in the steady-state pulse regime of NRP dischrage applied in atmospheric pressure air preheated at 1000 K. Extracted from Rusterholtz et al. (2013)*

of the gas temperature and atomic O concentration obtained in the simulation with the experimental measurements (Rusterholtz et al. (2013)). The initial and operating conditions for the test are extracted from the experimental study. The initial gas temperature: $T_i = 1500$ K, the pressure: P = 1 atm. At the beginning of the pulse about 15% of the O2 has been dissociated by the previous pulses, therefore, the initial mole fractions of the mixture are: $X_O = 0.063$, $X_{O_2} = 0.1785$ and $X_{N_2} = 0.7585$. For the NRP discharge, the energy per pulse: $E_{pulse} = 670$ μJ, the discharge radius and length are equal to $r_d = 225$ μm and $L_d = 4$ mm, respectively and the pulse duration: $\tau_{pulse} = 50$ ns. Experimental measurements show that the temperature increase due to the energy deposition by the pulse lasts 25 ns while the O production lasts 50 ns. Because of the small difference between the two durations and for simplification reasons in the simulation the pulse energy is deposited in 50 ns.

A constant value of the model parameter $\alpha = 0.55$ (fraction of that goes into ultra-fast heating and ultra-fast dissociation of O_2 into atomic O) is retained whereas two values of the parameter η (fraction of energy that goes into ultra-fast dissociation of O_2 into O) $\eta = 0$ and $\eta = 0.35$ are considered in order to analyze and understand the impact of the discharge energy distribution into $\dot{E}^p_{chem}$ and $\dot{E}^p_{heat}$ on the pulse effects.

Figure. 3.5 and Fig. 3.6 show the evolution of the gas temperature and O radicals concentration during the pulse, respectively. The symbols (black squares) correspond to the experimental measurement (Rusterholtz et al. (2013)), the red lines correspond to the numerical results of Castela et al. (2016) obtained using the phenomenological NRP discharges model and the blue lines are the results obtained in the present work with the same NRP discharges model implemented in the YALES2 code (Moureau et al. (2011)). For the case, where η is set to 0.35 (meaning that 35% of the pulse energy is routed to the dissociation of O_2), the gas temperature initialy at 1500 K increases by about 1100 K and reaches 2500 K at the end of the pulse. The O radical concentration rises from 3 up to $9 \cdot 10^{17}$ particles.cm^{-3}. The simulations performed with the YALES2 and REGATH code using the NRP discharges model are in good agreement with the experimental values. The only difference come from the characteristic rise time of the gas temperature that was considered here equal to $\tau_{pulse} = 50$ ns versus the experimental value of 25 ns. Nevertheless, The choice of $\tau_{pulse} = 50$ ns seems to be a good compromise as both values of the gas temperature and of the O radicals concentration agree well with experimental data. When η is set to 0, meaning that all the 55% of the discharge energy is transferred directly into $\dot{E}^p_{heat}$ (and $\dot{E}^p_{chem} = 0$), the gas temperature increases by about 1900 K and reaches 3300 K at the end of the pulse, overestimating the experimental results.
When η is set to 0, meaning that all the 55% of the discharge energy is transferred directly into $\dot{E}^p_{heat}$ (and $\dot{E}^p_{chem} = 0$), the gas temperature increases by about 1900 K, overestimating the experimental results.

3.4.2 2-D simulations of NRP discharges in air

The second test case consists in 2-D simulations of a series of 10 NRP discharges pulses applied in a quiescent air mixture. The air is initially at p = 1 atm and T = 300 K. The NRP discharges represent the ones characterized in the experimental work of Rusterholtz et al. (2013), also used in the previous test case. The plasma discharge channel has a quasi-cylindrical shape, with diameter $r_d = 225$ μm and height $L_d = 4$ mm as shown in Fig. 3.7. The pulse repetition frequency and the energy per pulse are equal to PRF = 10 kHz and $E_{pulse} = 670$ μJ, respectively. For 2-D computation, a plane domain of 5.12 × 5.12 mm perpendicular to the electrode tips is considered, shown in Fig. 3.7. In this plane, the discharge takes the form of a circle cross-section of

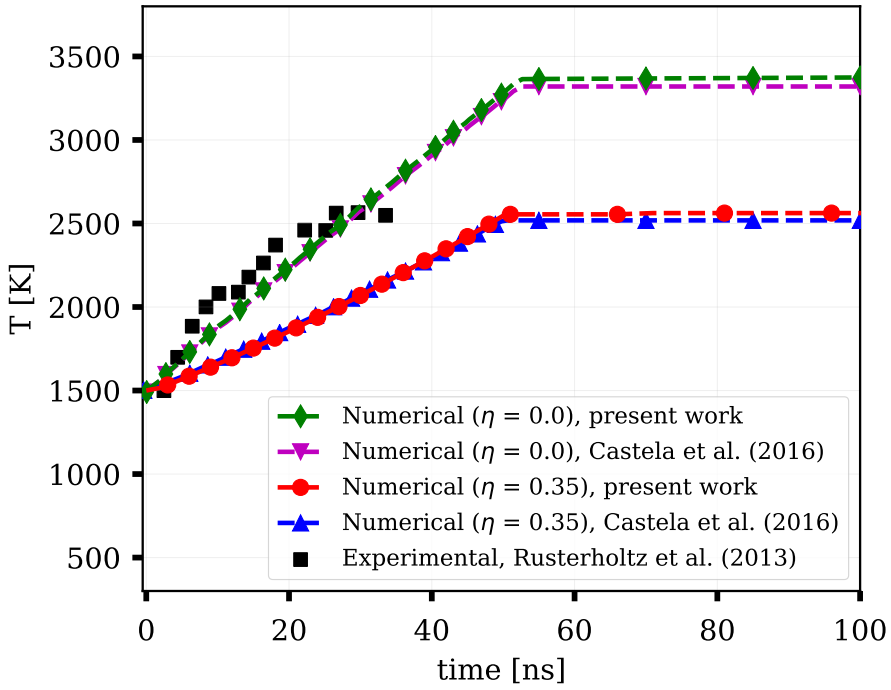

Figure 3.5: *Temporal evolution of the maximum value of gas temperature during the pulse. The following discharge parameter values were used: pulse energy* E_{pulse} *= 670* μJ *and model parameters:* α *= 0.55 and two values of* η *= 0.0 (without* O_2 *dissociation) and 0.35 (with* O_2 *dissociation into atomic O). Model results obtained in the present work using the low-MACH number YALES2 code are compared with numerical results of Castela et al. (2016) obtained using the compressible code YWC and with the experimental measurement obtained in Rusterholtz et al. (2013).*

the cylindrical-shape. A uniform grid with a mesh size $\Delta x = 10$ μm is used in the simulations.

Two simulations are performed. First, considering only the thermal effects of the discharge, all the discharge energy goes into ultra-fast heating ans slow heating with the model parameters $\alpha = 0.55$ and $\eta = 0.0$. Then considering both the thermal and chemical effects of the discharge with the ultra-fast dissociation of O_2 into atomic O, $\alpha = 0.55$ and $\eta = 0.35$. The results of the simulations performed with the low-Mach number YALES2 code are compare to the one obtained by Castela et al. (2016) using the compressible YWC code (Coussement (2012); Caudal (2013)).

Castela et al. (2016) observed, in the simulations performed using the compressible code YWC, that the ultra-fast deposition of energy generates at each pulse a pressure wave that detaches 0.25 μs after the pulse from the center of

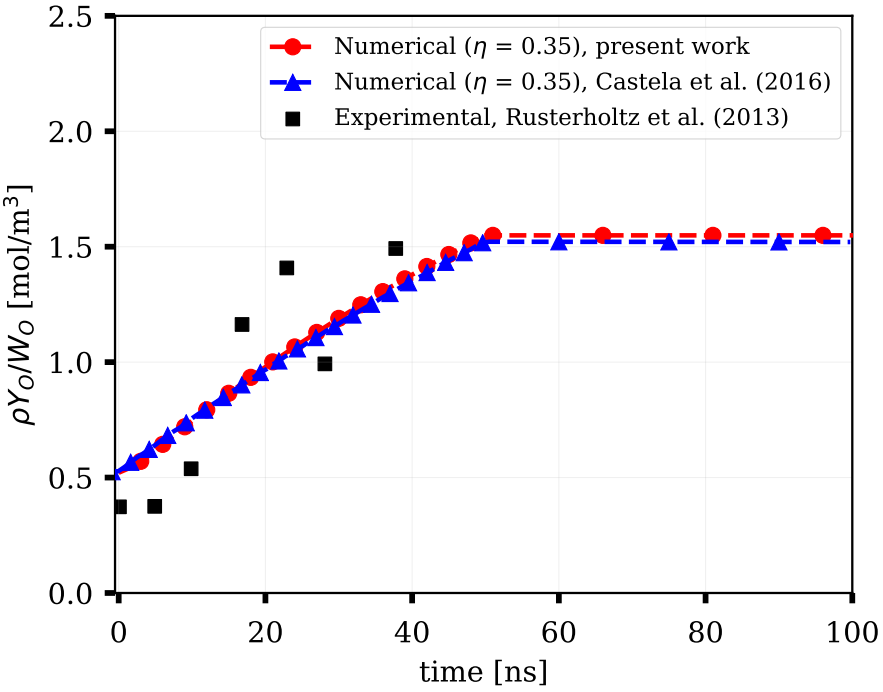

Figure 3.6: *Temporal evolution of the maximum value of O radical concentration during the pulse. The following discharge parameter values were used: pulse energy E_{pulse} = 670 μJ and model parameters: α = 0.55 and η = 0.35 (with O_2 dissociation into atomic O). Model results obtained in the present work using the low-MACH number YALES2 code are compared with numerical results of Castela et al. (2016) obtained using the compressible code YWC and with the experimental measurement obtained in Rusterholtz et al. (2013).*

the discharge channel and propagates outwards. Due to this pressure wave, part of the deposited energy leaves the discharge zone as acoustic energy causing a fast temperature decay. This energy has been estimated by Castela et al. (2016) to be around 10% of the total discharge deposited energy is the case where $\eta = 0.35$ (both thermal and chemical effects are taken into account) and around 20% when $\eta = 0.0$ (only the thermal effects are taken into account). The low-Mach formalism used in YALES2 cannot captured such behavior. The pressure waves resulting from a variation of the thermodynamic pressure during the pulse, the low Mach number assumption, which assume that this pressure does not vary and is always constant prevent the generation of these waves. The energy that should be lost in acoustic form is instead converted into thermal energy, which leads to an overestimation of the temperature. To correct this error, the amount of acoustic discharge energy leaving the discharge zone, evaluated by Castela et al. (2016), is deducted directly from the amount of energy deposited at each pulse in the low-Mach number YALES2 code.

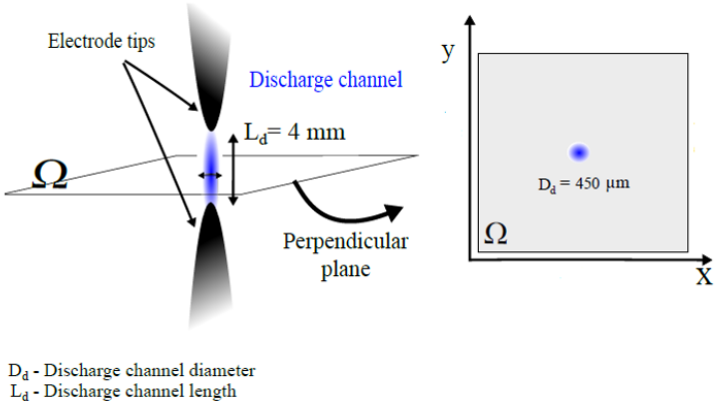

Figure 3.7: *Schematics of a pin to pin configuration of NRP discharges device. The 2-D computational domain is a plane perpendicular to the inter-electrode axis. Extracted from Castela et al. (2016).*

Figure. 3.8 shows the temporal evolution of the gas temperature at the center of the discharge zone for the sequence of pulses in the case where only the thermal effects of the discharges are considered, so all the discharge energy goes to ultra-fast and slow gas heating ($\eta = 0.0$). During each pulse, the results obtained by Castela et al. (2016) plotted in blue with triangle symbols, show an ultra-fast increase of the gas temperature by about 1000 to 3000 K. Just after the pulse, the loss of energy due to gas expansion and the detachment of a pressure wave from the hot discharge kernel induces a fast drop of the temperature of approximately 200 to 700 K. Then, the temperature decreases progressively between the pulses due to diffusion effects. At the end of each period, the value of the gas temperature is higher than that of the previous period. The minimum temperature reaches a quasi-stationary value of about 2000 K after height pulses when diffusive fluxes are balanced with the heat released by the discharge. In the present work, since 20% of the pulse energy has been a priori removed from the part that goes to the ultra-fast heating to reproduce the acoustic loss that are not captured by the low-Mach number formalism, the results plotted in red line with circle symbols show that the ultra-fast increase of temperature during the pulse is underestimated by about 200 to 700 K. However, the rapid temperature drop just after the pulse in the compressible case brings both simulations to the same temperature level very quickly in about 1 μs, and throughout the temperature decrease between two pulses, the results are in good agreement.

Figure. 3.9 shows the temporal evolution of the gas temperature at the center of the discharge zone for the sequence of pulses in the case where both the thermal and chemical effects (O_2 dissociation into atomic O, $\eta = 0.35$) of the discharges

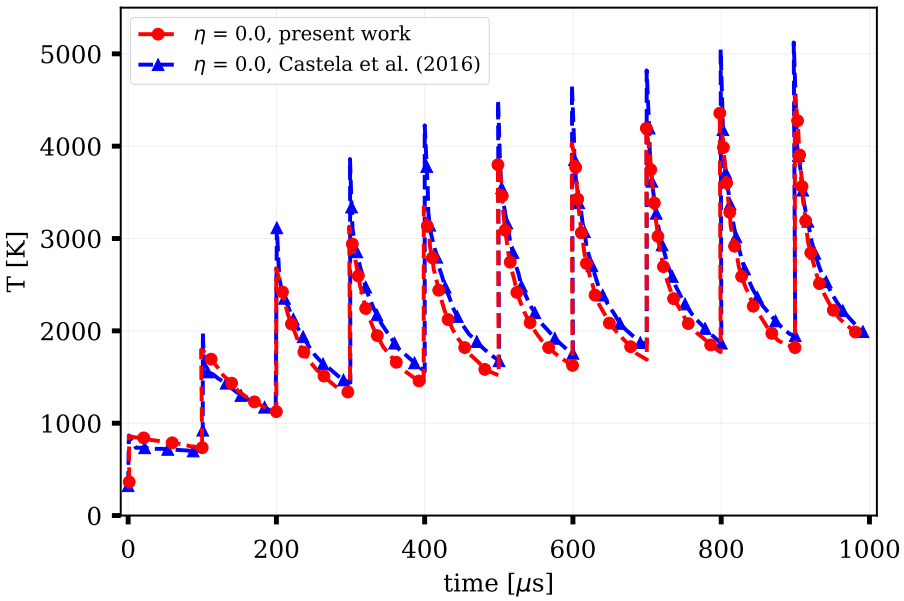

Figure 3.8: *Temporal evolution of the gas temperature at the center of the discharge channel in a sequence of* 10 *pulses in air. The following parameter values were used: f = 10 kHz, E_{pulse} = 670 μJ, α = 0.55 and η = 0.0. Numerical results of present work obtained with the low-Mach number YALES2 code (in red) are compare to the results obtained by Castela et al. (2016) using the compressible YWC code (in blue).*

are considered. The ultra-fast increase of the temperature, about 800 to 2000 K, is less important then the previous case ($\eta = 0.0$) since part of the energy is used for the dissociation of O_2. Similarly to the previous case, a fast drop of energy occurs just after the pulse in the compressible simulation followed by a slow temperature decrease. In the low-Mach number simulation, present work, 8% of the pulse energy has been a priori removed from the part that goes to the ultra-fast heating to reproduce the acoustic loss. A discrepancy between the two simulations is observed during the pulse where the low-Mach simulation underestimates the total ultra-fast thermal energy deposited. Once the pressure wave has detached and acoustic losses occurred, the results are again in good agreement. The minimum temperature reaches a quasi-stationary value of about 1500 K after height pulses which is in good agreement with experimental measurement of Rusterholtz et al. (2013).

Figure. 3.10 shows the temporal evolution of O radical concentration at the center of the discharge zone for the sequence of pulses in the case where both the thermal and chemical effects (O_2 dissociation into atomic O, $\eta = 0.35$) are considered. During each pulse, O concentration rapidly increases and then decreases due to gas expansion, diffusion and to the recombination of O radicals into O2 molecules. In the compressible case, the pulse energy deposition oc-

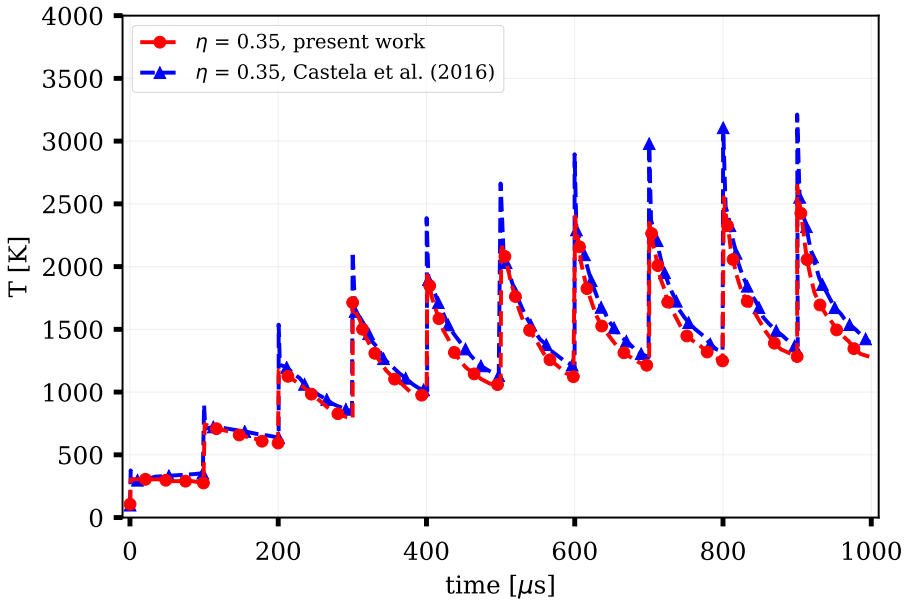

Figure 3.9: *Temporal evolution of the gas temperature at the center of the discharge channel in a sequence of* 10 *pulses in air. The following parameter values were used: f = 10 kHz, E_{pulse} = 670 μJ, α = 0.55 and η = 0.35 (O_2 dissociation into atomic O). Numerical results of present work obtained with the low-Mach number YALES2 code (in red) are compare to the results obtained by Castela et al. (2016) using the compressible YWC code (in blue).*

curs in quasi-isochore regime. The pressure and the temperature vary strongly while the density remains almost constant. Just after the pulse, the pressure waves detach and the pressure returns to its initial value lowering the density of the mixture and thus the O radicals concentration in the discharge zone. In the low-Mach case, the deposition is isobaric, the density and the temperature vary while the pressure remains constant. The oxygen peak is therefore not captured. The concentration of O at the end of the pulse is equal to that of the compressible case after the pressure and density drop. Between two pulses, the results of the two simulations are in good agreement. The minimum value of the O radical concentration in the stationary regime is also in good agreement with the ones observed in the experimental work of Rusterholtz et al. (2013).

In all the following simulations, 20% of of the pulse energy is a priori removed from the part that goes to the ultra-fast heating when η = 0.0 and 8% when η = 0.35 to reproduce the acoustic loss that are not captured by the low-Mach number.

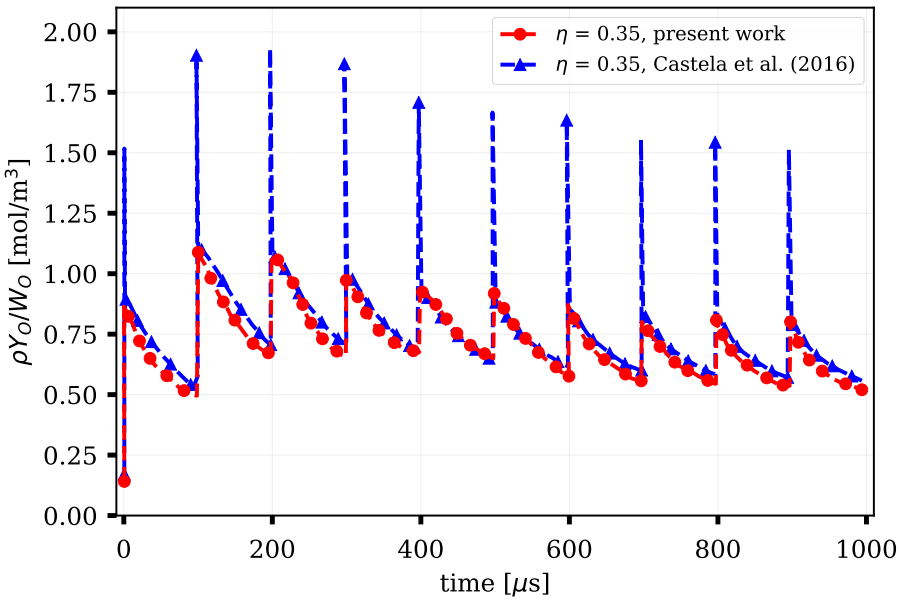

Figure 3.10: *Temporal evolution of O radical concentration at the center of the discharge channel in a sequence of* 10 *pulses in air. The following parameter values were used: f = 10 kHz, E_{pulse} = 670 μJ, α = 0.55 and η = 0.35 (O_2 dissociation into atomic O). Numerical results of present work obtained with the low-Mach number YALES2 code (in red) are compare to the results obtained by Castela et al. (2016) using the compressible YWC code (in blue).*

3.4.3 2-D simulations of NRP discharge assisted ignition in quiescent methane-air mixture

In this test case, ignition sequences of a quiescent methane-air mixture by a series of NRP discharge pulses are simulated. The 2-D computational domain perpendicular to the electrode tips used in the previous test case is considered (see Fig. 3.7). A methane-air mixture with an equivalence ratio $\phi = 0.8$ is uniformly distributed over the computational domain at the beginning of the computations. The initial conditions of mixture pressure and temperature are p = 1 atm and T = 300 K, respectively. The pulse are applied at a repetition frequency PRF = 10 kHz with a deposited energy per pulse E_{pulse} = 670 μJ. COFFEE kinetic scheme involving 14 species and 38 reactions is used for the combustion mechanism (COFFEE (1984)).

To evaluate the impact of the ultra-fast O_2 dissociation, the ultra-fast gas heating and the slow gas heating on the ignition phenomena, two simulations are performed. The First one, considering only the thermal effects of the discharge, all the discharge energy goes into ultra-fast heating ans slow heating with the model parameters $\alpha = 0.55$ and $\eta = 0.0$. The second one, considering both the

thermal and chemical effects of the discharge with the ultra-fast dissociation of O_2 into atomic O, $\alpha = 0.55$ and $\eta = 0.35$. The results of the simulations performed with the low-Mach number YALES2 code are compare to the one obtained by Castela et al. (2016) using the compressible YWC code (Coussement (2012); Caudal (2013)).

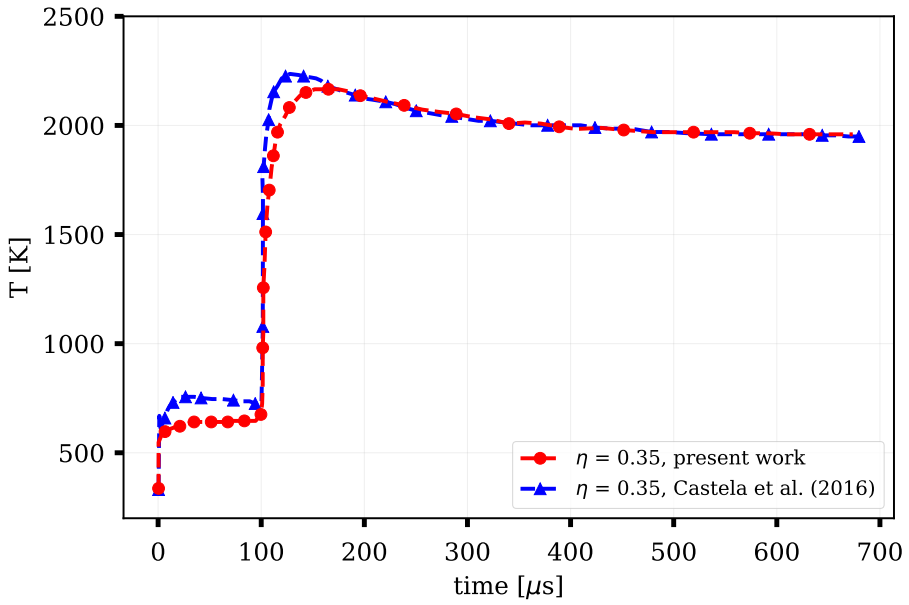

Figure 3.11: *Temporal evolution of the maximum value of gas temperature for a methane-air mixture, $\phi = 0.8$. For $\eta = 0.35$ the mixture ignites after two NRP discharge pulses. Numerical results of present work obtained with the low-Mach number YALES2 code (in red) are compare to the results obtained by Castela et al. (2016) using the compressible YWC code (in blue).*

Figure. 3.11 shows the temporal evolution of the maximum gas temperature for η= 0.35 simulations. The blue line with triangle symbols corresponds to the results obtained by Castela et al. (2016) using the compressible YWC code. The red line with circle symbols corresponds to the results obtained in the present work using the low-Mach number YALES2 code. When O_2 dissociation is considered the mixture ignites after two discharge pulses. The gas temperature increases during the first discharge and, when the second discharge is applied, the temperature further increases following an asymptotic decrease towards the adiabatic flame temperature. When O_2 dissociation by the NRP discharges is neglected ($\eta = 0.0$), the maximum gas temperature evolution plotted in Fig. 3.12 shows that four discharge pulses are needed to ignite the mixture. In order the initiate the combustion a higher temperature had to be reached. The results of the present work are consistent with those obtained by Castela et al. (2016). The ignition of the mixture is well predicted in both

cases. This is explained by the fact that the relaxation time of the temperature after the pulse due to the pressure wave detachment from the ignition kernel is much shorter than the chemical time scales. Therefore, the method that consists of removing a priori the energy that will be lost in acoustic effect in the low-MACH YALES2 code has no influence on the combustion process.

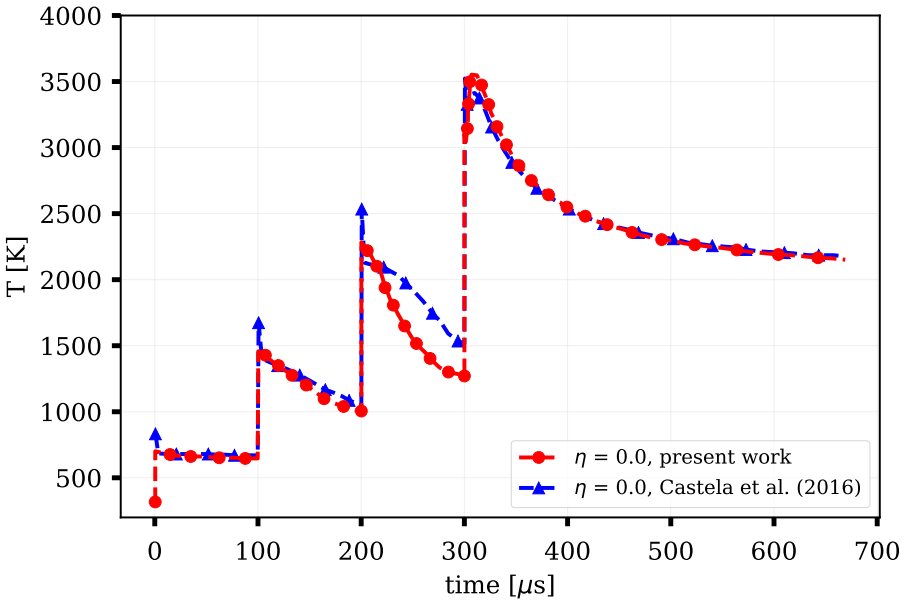

Figure 3.12: *Temporal evolution of the maximum value of gas temperature for a methane-air mixture, $\phi = 0.8$. For $\eta = 0.0$ the mixture ignites after four NRP discharge pulses. Numerical results of present work obtained with the low-Mach number YALES2 code (in red) are compare to the results obtained by Castela et al. (2016) using the compressible YWC code (in blue).*

These simulation results show that O radicals play a major role in the ignition enhancement of low gas temperature mixtures and lead to a decrease of the ignition delay and of the external source of energy needed to ignite. The impact of O radicals on flame ignition process is studied more in detail in Chapter. 6.

The different test cases presented here allowed the validation of the phenomenological plasma model proposed by Castela et al. (2016) and its implementation in the CDF low-Mach number code YALES2. In part II and III of this manuscript, this model will be used to simulate the processes of flames ignition and stabilization by NRP discharge.

Part II

Numerical simulations of flames ignition by NRP discharges

Chapter 4

Toward new ignition systems

In this chapter, the limits of conventional ignition devices and the advantages of using NRP discharges the ignition of lean combustion chambers are discussed and illustrated through an experimental study that compares the efficiency of the two technologies in the ignition of a lean internal combustion engine. 3-D simulation of plasma assisted ignition performed by Castela to investigate the dynamic of flame ignition by a single NRP discharge pulse using the phenomenological plasma model is then presented. The results of this simulation are analyzed to understand the mechanisms of plasma-flame-flow interaction, in particular the hydrodynamic effects induced by the discharges which can reduce the capacity of the NRP discharges to ignite reactive mixtures.

Contents

4.1 Introduction

The development of efficient and robust ignition systems has always been an important subject of study in the field of combustion. Among the different ignition devices developed over time: torch igniters (Lefebvre and Ballal (2010)), plasma jet igniters (Clements et al. (1981)), flammable chemical products (Lefebvre and Ballal (2010)), laser igniters (Nakaya et al. (2017)), the spark plugs have stood out as the most reliable and easiest to use despite their low energy efficiency. For the last decades, this technology has equipped most combustion systems whether it's internal combustion engines or aeronautical gas turbines. Today, however, this solution seems to have reached its limits. With the development of new combustion technologies that tend to operate around the lean flammability limit in order to reduce pollutant emissions, it is becoming more and more difficult to initiate the combustion process and spark plugs have proven to be rather inefficient and too energy costly. New solutions have been investigated lately as an alternative to the spark plugs. Among them nanosecond repetitively pulse (NRP) discharges have shown very promising results. Flames ignition by NRP discharges id the subject of the studies conducted in the following four chapters.

This chapter is dedicated to the state of the art concerning flames ignition by NRP discharges. Section. 4.2 discusses the limits from which suffer the spark plug discharges and how NRP discharges can tackle these limits. An experimental comparison between the two technologies is presented. Section. 4.3 describes the dynamic of flame ignition by a single NRP discharge pulse through the results of one of the first numerical simulations of ignition by NRP discharge performed by Castela et al. (2017) with the phenomenological plasma model presented in Chapter. 2. Finally, the conclusions of the this chapter are given in Section. 4.5

4.2 Flames ignition systems

4.2.1 Spark ignition

The studies of spark plug ignition (Maly and Vogel (1979); Refael and Sher (1985); Lim et al. (1987); Sher et al. (1992); Kono et al. (1989)) showed that the process is decomposed in four steps: the pre-breakdown, breakdown phase ($t \propto 10^{-9}$ s), the arc phase ($t \propto 10^{-6}$ s), and the glow phase ($t \propto 10^{-3}$ s), as shown in Fig. 4.1.

In the pre-breakdown phase, because of the very high voltage applied between electrodes (up to 10 kV as shown in Fig. 4.1) free electrons move rapidly from the cathode towards the anode. On their way, some of them collide with gas molecules creating a plasma kernel composed of positive ions, electrons, neg-

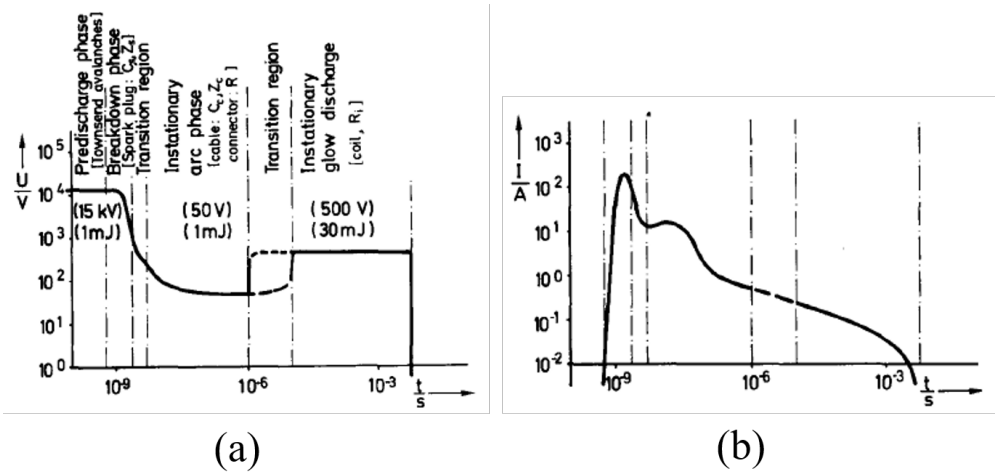

Figure 4.1: *Diagram of (a) voltage and (b) current during ignition, indicating the four steps of ignition. Extracted from Maly and Vogel (1979).*

ative ions and excited species. The newly formed charged species are also accelerated by the electric field from the cathode towards the anode for the electrons and negative ions, negative streamer, and from the anode toward the cathode for the positive ions, positive streamer. At this point, the plasma is at a non-equilibrium state. The electrons are at very high temperature $T_e \approx 10$ 000 K while other species remain at low temperature (1000 K).

The breakdown phase occurs when a continuous streamer joins the cathode and the anode so that the gap is bridged (after few nanosecond). The gap impedance drops, the voltage diminishes and the current is dramatically boosted for 20-60 ns up to 200 A. The collisions become stronger. The plasma is heavily heated up to 60 000 K (hot equilibrium plasma), the molecules are fully dissociated and ionized. The gas dilatation due to the temperature increase induces a strong blast wave which expands the kernel in all directions.

After the breakdown, the electric power level is reduced by 2-3 orders of magnitude. This is the arc phase. During this period, the ionized gas cools down progressively towards the adiabatic flame temperature. Ionized species thus recombine into uncharged species. At this time, the hot kernel growth is a the competition between heat release by combustion and thermal diffusion.

The spark ends with the glow phase. It's the longest phase ($t \propto 10^{-3}$ s) that provides most of the external energy to the gas. When it takes place, the hot kernel has already propagate away from the spark plug zone. The energy deposited during this phase acts as a heat source term for the burnt gases.

Analysis of spark plug energy efficiency shows that a large amount of the electric energy released is lost or useless for combustion initiation even when transmitted to the gas. The spark energy is split between the phases as follow: the pre-breakdown and breakdown phases represents roughly 3% of the total energy, the arc phase energy 3% and the glow phase energy, the most energetic one, about 94%. About 40% of the energy is lost in the electrical circuit during the breakdown, arc and glow phases due to the Joule effect induced by the established electric current (Verhoeven (1997)). The remaining energy, about 60% is given to the gas but not all of it is actually useful for combustion initiation. The energy deposited during the glow phase does not contribute much to the ignition process as it arrives way after the kernel has propagated away from the discharge zone and has only as effect the heating of the hot burnt gases present in the inter-electrodes region. The transition of the plasma from a non-equilibrium state (partially ionized low temperature gas) to an equilibrium state (fully ionized high temperature gas) during the phase breakdown is also an important source of energy loss. The significant increase of gases temperature, from 1000 K to 60 000 K, during the transition leads to the formation of a strong shock wave that removes part of the deposited energy when it propagates away from the kernel. Gases radiation, also induced by the high gases temperature, removes also a part. The energy that contributes to the ionization of the species, an endothermic process is also lost energy as the ionized species don't help improvement of the combustion process. The only phase that is effective without great loss of energy is the pre-breakdown phase that allows the formation of non-equilibrium plasma composed of highly-reactive low-temperature species that greatly improves the combustion process. Ultimately, the overall energy efficiencies of spark ignition is around 10% to 30% (Maly and Vogel (1979); Teets and Sell (1988)).

Despite the energy losses, The spark plugs have been for a long time the most efficient way to ignite combustion chambers. However, with the advent of the new combustion technologies that operate at lean regimes in order to reduce pollutants emissions, it becomes more and more difficult to initiate the combustion process and spark plugs have proven to be rather inefficient and too energy costly.

4.2.2 NRP discharges ignition

The solution proposed to improve the performances of electric discharges consists of generating only a non-equilibrium plasma which allows the dissociation of chemical species into reactive radicals while limiting the heating and ionization of the gas sources of energy losses. This can be done by reducing the intensity and shortening the duration of the discharges and therefore canceling the breakdown, arc and glow phases to prevent the transition toward an equi-

librium plasma. This principle is used in the Nanosecond Repetitively Pulsed (NRP) discharges.

A comparison between spark plugs and NRP discharges ignition was performed by (Xu et al. (2015)). An audi coil spark plug and a series of 82 NRP pulses at PRF = 30 kHz, set to have approximately the same power and the same total deposited energy, were used to ignite a propane-air mixture with an equivalence ratio $\phi = 0.7$ in a constant volume cylindrical chamber. The experimental configuration shown in Fig. 4.2 has been operated at different pressure levels (3 bar, 5 bar, 10 bar).

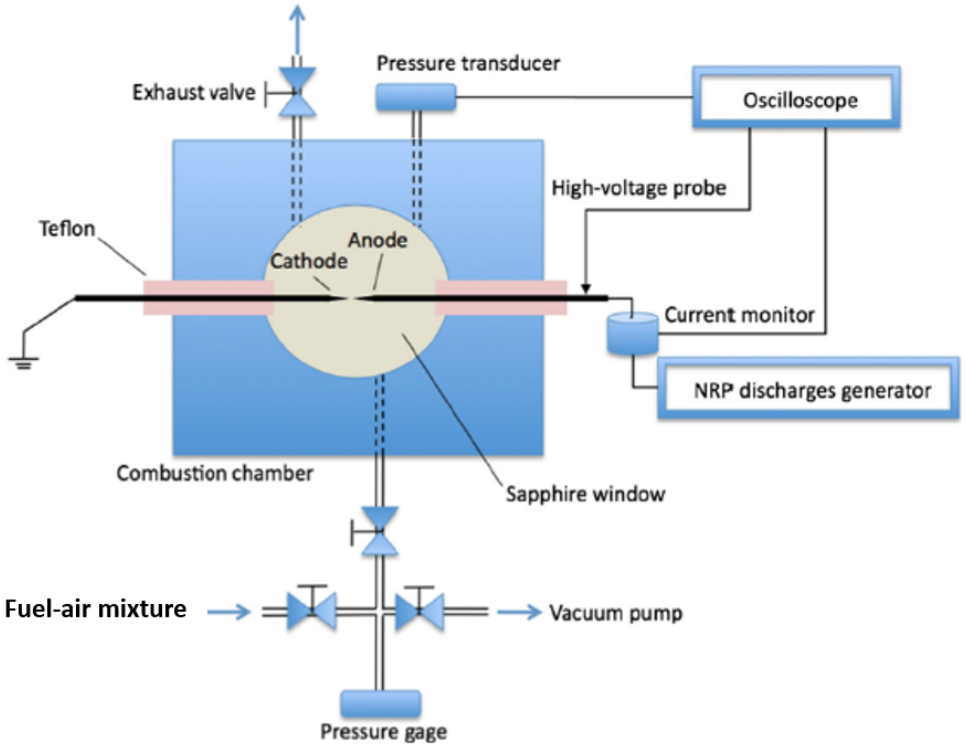

Figure 4.2: *Schematic representation of the combustion chamber and the electric circuit used by Xu et al. (2015).*

High-speed schlieren images of the mixture ignition by a conventional spark plug and NRP discharges at different pressure levels 3, 5 and 10 bar are shown in Fig. 4.3. For all the cases, a flame is formed in the discharge channel and propagates outward. The results show that the flames ignited by NRP discharges are more wrinkled and propagate at a greater speed, especially at high pressures. At 15 ms for instance, the flame radius in the 5 and 10 bar cases is about 2 mm greater than with the spark plug.

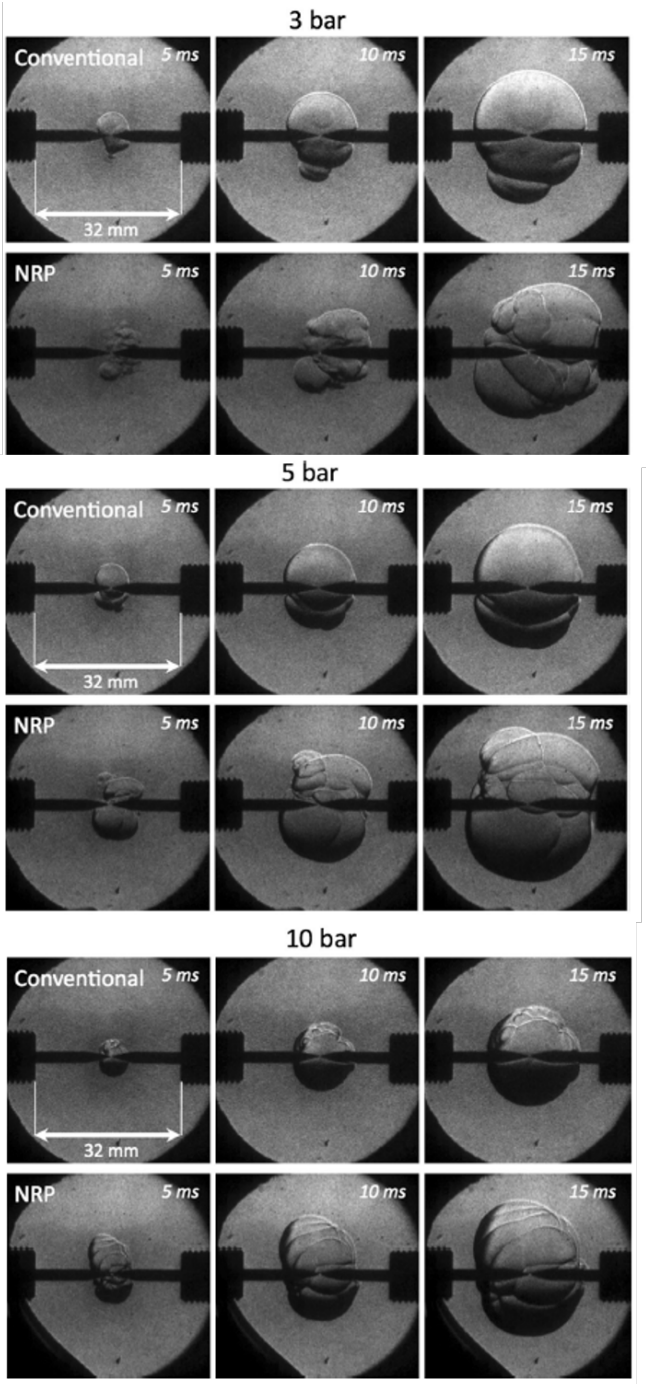

Figure 4.3: *Schlieren images of C_3H_8/air ($\phi = 0.7$) flames at 3, 5 and 10 bar ignited by 82 NRP discharges at 30 kHz (55 mJ − 22 W − 2.7 ms) and by a conventional spark plug Audi coil (57 mJ − 16 W − 3.5 ms). Extracted from Xu et al. (2015).*

This study and others (Starikovskiy and Aleksandrov (2013); Ju and Sun (2015); Merotto et al. (2022)) have shown that NRP discharges are a more energy efficient way to initiate combustion processes compared to conventional ignition systems. However, in order to integrate this new technology in future combustion systems and fully control the ignition by NRP discharge, a complete understanding of the governing physics and the impact of the different discharge parameters is necessary.

Numerical studies, lately performed, have given new insights into the fundamental mechanisms of plasma-assisted ignition. 0-D detailed simulations performed by Popov (2007); Aleksandrov et al. (2009); Adamovich et al. (2015); Mao and Chen (2018) to investigate the influence of the atomic particles (O, H, N) and excited species ($O_2(a^1\Delta_g)$, $H_2(v)$, $N_2(A,B,C,a^{'})$, ...), produced by nanosecond discharges, identified new kinetic pathways in the combustion process. 1-D and 2-D simulations of lean laminar flame ignition by NRP discharges (Breden et al. (2013); Tholin et al. (2014); Casey et al. (2017); Sharma et al. (2019)) showed a discharge chemical effects on the combustion with an important production of radicals such as O, OH, H, CH3 that causes a kinetic enhancement and a thermal effect that leads to a thermal enhancement. These numerical methods adopted on these studies consist on solving the governing equations for the electric field, electrons, ions and the electron energy (streamers equations), as well as the continuity equations for neutral and excited species, the energy, mass and momentum balance equations for the gas mixture (Navier-Stokes equations). Despite their accuracy, these strategies require high computational resources which are too expensive for 3-D flame simulations.

Using the phenomenological plasma model they developed in Castela et al. (2016), Castela et al. (2017) performed one of the first 3D simulations of plasma-assisted ignition by NRP discharges in which the dynamics of flame ignition is well captured in respect to experimental measurements. In particular, the simulation highlighted the existence of hydrodynamic effects induced by the NRP discharges, which are not captured in the 1-D and 2-D simulations, that play an important role in the efficiency of the ignition process. The results of these simulations are presented and discussed in the following section.

4.3 Dynamic of flame ignition by a single NRP discharge pulse

Flame ignition by a single pulse NRP discharge has been recently investigated both experimentally and numerically by Castela et al. (2017) in order to understand the dynamics of NRP discharges kernel formation and development. The experimental setup designed by Xu et al. (2015) is used to monitor the temporal evolution of the gas density distribution after a NRP discharge pulse.

the configuration consists of a constant volume chamber (V = 100 cm^3) with two sapphire optical windows of 5 cm diameter each installed into the chamber walls to provide access for optical diagnostics. Two co-linear graphite electrodes connected a pulse generator are placed in the center of the chamber and used to apply the NRP discharge, Fig. 4.2.

The chamber is filled with a lean methane-air mixture (ϕ=0.7) at pressure of p = 1 atm and temperature of T = 300 K. A NRP discharge pulse of 1.4 mJ and 20 ns duration is then applied to ignite the quiescent mixture. Using a schlieren technique, images of the gases density distribution are taken.

3-D simulation of the experiment were performed with the DNS compressible code YWC (Coussement (2012)) using the phenomenological NRP discharge model and a detailed methane-air combustion mechanism of 29 species and 141 elementary reactions (Lindstedt (1998)). The computational domain is shown in Fig. 4.4(a). The discharge channel, has quasi-cylindrical shape displayed in Fig. 4.4(b).

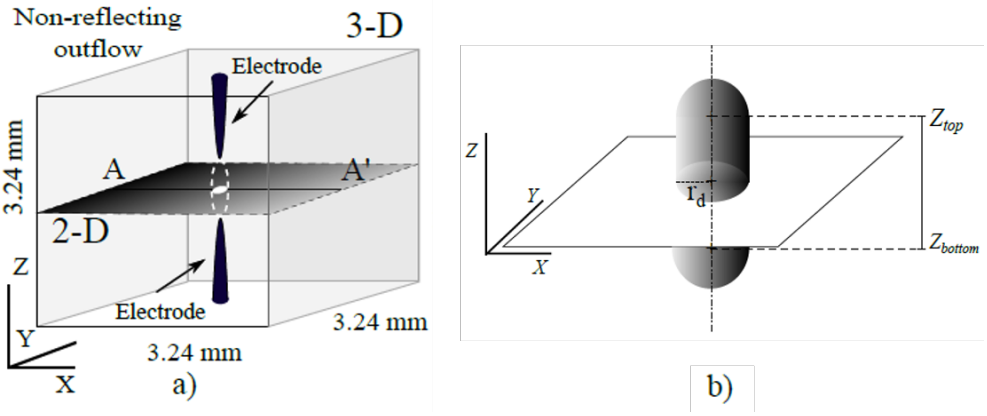

Figure 4.4: *a) Schematic representation of the 2-D and 3-D computational domain used for the one pulse NRP discharge simulations. b) Schematic representation of the shape and the location where the energy of the discharge is deposited in the 3-D computational domain. From Castela et al. (2017).*

Side-by-side experimental (left) and 3-D computational (right) schlieren images captured at 5 instants following the discharge pulse are shown in Fig. 4.5 (a). Figure. 4.5 (b) shows for the same instants, the flow streamlines superposed with the gas temperature fields. By the end of the pulse, t = 0.3 μs, the energy deposition has generated a hot reacting kernel of a cylindrical shape in the discharge zone in which the temperature reaches a maximum value of 2100 K. At t = 2 μs, the images show that the hot gases have expanded increasing the radius of the kernel and decreasing its temperature. After that, t = 9 μs, 80 μs and

200 μs, two recirculation zones are formed in the near-field of the electrodes accelerating the flow towards the center of the discharge channel. Fresh gas are entrained into the discharge channel and gas temperature decreases from 2000 to 600 K. The initially cylindrical hot kernel (at t = 2 μs) evolves into a toroidal shape. The OH mass fraction spatial and temporal evolution shown in Fig. 4.6 follows the same pattern. It reaches a maximum value of 5.10^{-3} at the end of the pulse, decreases a little bit when the gases expand, then collapses under the effect of the reciculation zones, evolving from a cylindrical shape a toroidal. The fresh gases brought to the center of the kernel by the flow recirculation gradually decrease the temperature and radicals first at the center then the edges of the kernel inducing it's extinction. As observed experimentally the chamber does not ignite.

This study shows the complexity of the flame ignition process by NRP discharges. On the one hand, a NRP discharge pulse, thanks to its thermal and chemical effects, is able to create a hot reactive ignition kernel and initiate combustion, but on the other hand, generates hydrodynamic effects that prevent the propagation of this ignition kernel which leads, in most of the case where only one pulse is applied, to an ignition failure.

The origins of these hydrodynamic effects and the means to prevent them are investigated in the next section.

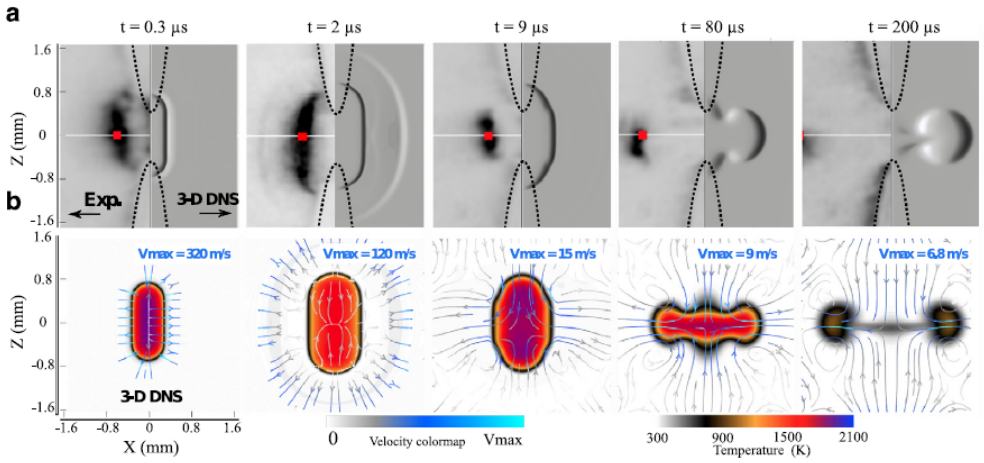

Figure 4.5: *Hot kernel topology captured at 5 instants after the plasma discharge in methane-air mixture: (a) Experimental (left side) and computational (right side) schlieren images. (b) Superposition of the computed gas temperature field and flow streamlines coloured by velocity magnitude. The same color map of velocity magnitude is used in for all images shown here, but the maximum value V max varies and is indicated above each image. From Castela et al. (2017).*

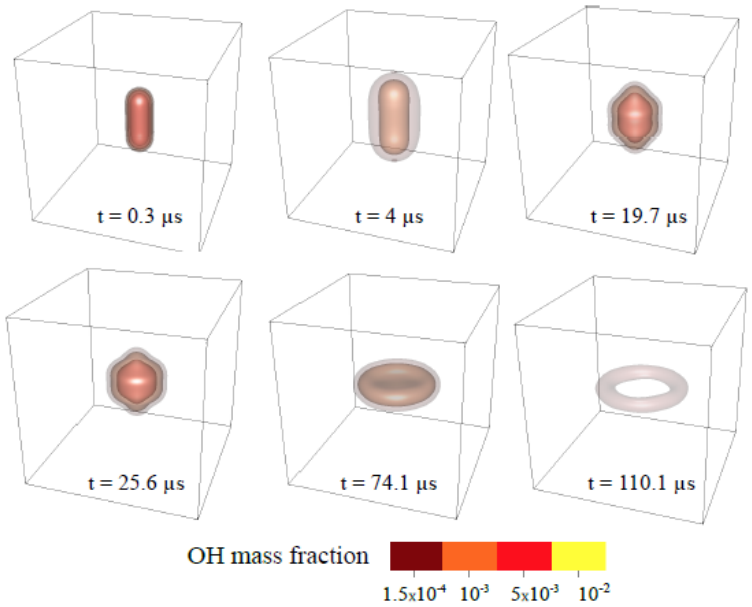

Figure 4.6: *3-D plot of the OH mass fraction at 6 instants following the discharge pulse. The initial cylinder-shaped hot kernel evolves into a toroidal shape. From Castela et al. (2017).*

4.4 NRP discharges hydrodynamic effects

The hydrodynamic effects inducing the toroidal collapse of the plasma kernel have been previously observed in other ignition systems. (Kono et al. (1989)) presented a study describing the process of formation of hot kernels by short duration conventional spark discharges (about 300-nanosecond duration). The study showed that for small inter-electrode gap distance a gas flow is formed in the discharge zone after the plasma pulse turning the initially cylinder-shaped hot kernel into a toroidal kernel, Fig. 4.7. Resembling effects have been later observed in laser induced spark ignition and studied by Bradley et al. (2004). However none of these studies provided an explanation of the gas flow generation in the post-discharge.

Dumitrache et al. (2019) conducted a detailed experimental and numerical study to identify the mechanisms responsible of these hydrodynamic effects. The experiment was performed on the same configuration studied by Castela et al. (2017), Fig. 4.4(a). Movable electrodes were added to the set-up to adjust the inter-electrode gap distance and using the same optical diagnostics high speed schlieren images of the kernel were captured. The numerical simulations were performed with a simplify NRP discharge where only the ultra-fast heating was modeled.

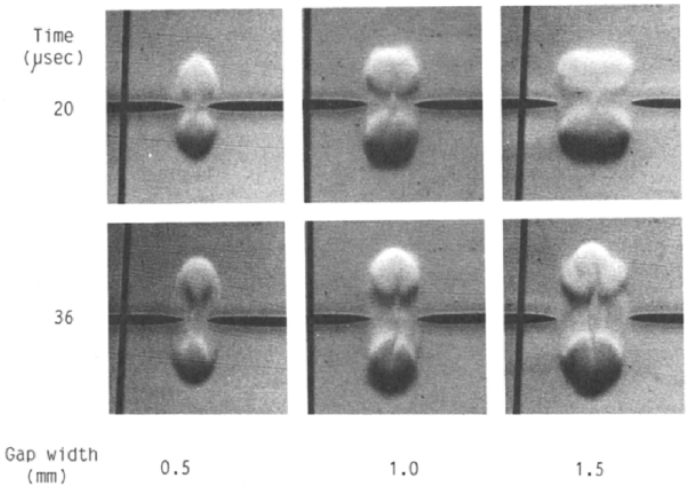

Figure 4.7: *Schlieren photographs of short spark kernel in air. Spark energy: 4.6 mJ. Reproduced from Kono et al. (1989).*

The results showed that gas flow leading to the toiridal collapse of the hot kernel is due to a generation of vorticity at the top and bottom edges of the kernel (Dumitrache et al. (2019)), schematize in Fig. 4.8.

To identify the source of flow rotation a numerical analysis of the vorticity equation, obtained by taking the curl of the momentum equation was performed. The terms composing the vorticity equation are the following, Eq. (4.1) :

$$\frac{D\vec{\omega}}{Dt} = (\vec{\omega}\cdot\vec{\nabla})\vec{u} - \vec{\omega}(\vec{\nabla}\cdot\vec{u}) + \frac{1}{\rho^2}[\vec{\nabla}\rho\times\vec{\nabla}p] + \nu\vec{\nabla}^2\vec{\omega} \tag{4.1}$$

where $\vec{\omega}$, $\vec{u}$, ρ and p are the vorticity, the velocity, the density and the pressure of the flow respectively.

The left-hand side $\frac{D\vec{\omega}}{Dt}$ is the material derivative of the vorticity.

The first term on the right-hand side $(\vec{\omega}\cdot\vec{\nabla})\vec{u}$ describes the enhancement of vorticity by stretching and is the mechanism through which turbulent eddies transfer energy to smaller scales.

The second term on the right-hand side $\vec{\omega}(\vec{\nabla}\cdot\vec{u})$ corresponds to the volumetric expansion of the gas flow.

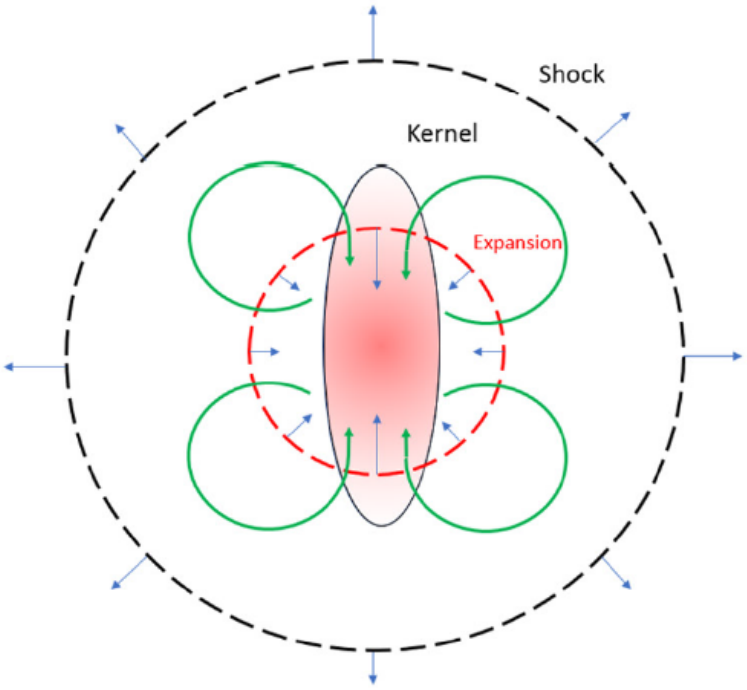

Figure 4.8: *Schematic diagrams showing the vorticity generated at the top and bottom edges of the kernel after a pulse of NRP discharges. From Dumitrache et al. (2019).*

the third term on the right-hand side $\frac{1}{\rho^2}[\vec{\nabla}\rho \times \vec{\nabla}p]$ describes vorticity generated by a baroclinic instability in the flow. It is created by a misalignment between the density and pressure gradients that induces baroclinic torque.

The fourth term on the right-hand side $\nu\vec{\nabla}^2\vec{\omega}$ describes the effects of viscous diffusion on vorticity generation.

The contribution of each term to the rate of vorticity generation when NRP discharge pulse is applied in the air is shown in Fig. 4.9 . The rate of vorticity generation is maximal immediately after the pulse then decreases gradually. The main contributor to vorticity generation is the baroclinic torque term which accounts for more than 85% of the total rate. This term is due to misalignment between the density and pressure gradients which are created by the ultra-fast heating induced by the plasma discharge.

The source of the vorticity being related to amplitude of density and pressure gradients created by the gases heating, reducing the pulse energy density, by increasing the inter-electrode gap distance or by decreasing the discharge energy, allows to reduce or even prevent the baroclinic instabilities, as shown by

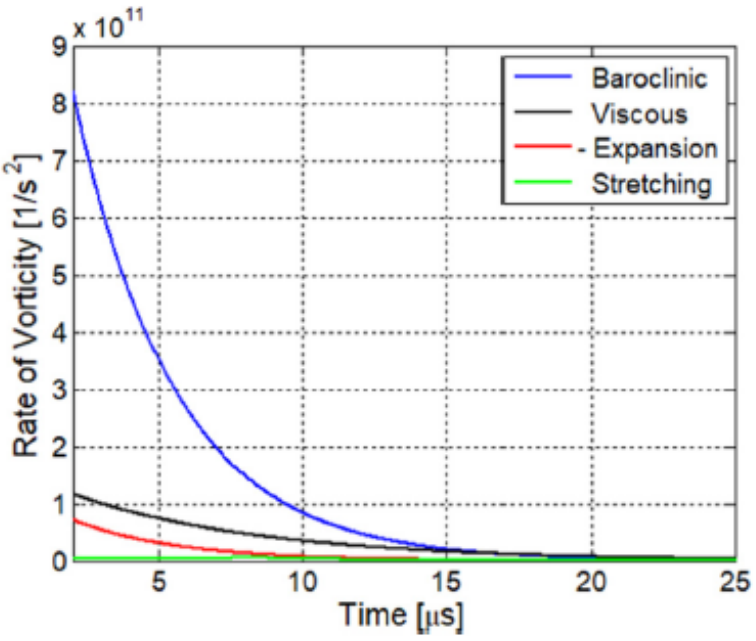

Figure 4.9: *Contribution of each term in the vorticity equation to the rate of vorticity generation as a function of time for an interelectrode gap corresponding to: $d = 1$ mm. From Dumitrache et al. (2019).*

Dumitrache et al. (2019). However, this does not ensure the ignition of the flame with a single NRP pulse, even if the undesirable hydrodynamic instabilities are canceled, because the deposited energy is too low.

4.5 Conclusion

Nanosecond Repetitively Pulsed (NRP) discharges have shown to be a particularly energy efficient way to promote flame ignition in lean regimes especially when conventional ignition systems such as spark plugs are rather ineffective or too energy costly. However, contrary to conventional spark plugs where a single energy deposit ensures generally the ignition of the combustion chambers, a single pulse of NRP discharges is often not sufficient, either because of hydrodynamic instabilities or because the deposited energy is too low. A solution consists therefore in applying a series of NRP discharge pulses to supply the ignition kernel with energy until the ignition of the reactive mixture. The dynamics of flame ignition by a series of NRP pulses is studied in the following chapter.

Chapter 5

Dynamic of flame ignition by a series of NRP discharge pulses

The aim of this chapter is to study the dynamics of flame ignition by a series of NRP discharge pulses. The target configuration is the flow tunnel combustor, a flowing methane-air combustion chamber designed by Lefkowitz and Ombrello (2017) to investigate plasma-assisted ignition mechanisms. Depending on the flow and discharge parameters, three pulses interaction regimes have been observed experimentally, a fully coupled regime, a partially coupled regime, and a decoupled regime. Each regime is characterized by distinct ignition probabilities and kernel structures. An analysis of the experimental results is performed to identify the parameters that control the pulse interaction regimes and therefore the ignition efficiency. 3-D Large Eddy Simulations (LES) of the flow tunnel ignition by NRP discharges are then performed using the phenomenological plasma model of Castela et al. (2016). The objective is to further investigate the influence of the flow and discharge properties, to understand the plasma-flow-combustion interaction mechanisms and to define the best set of parameters to be used to ensure successful flames ignitions.

Contents

5.1 Introduction

Experimental and numerical studies of flame ignition have shown that a single NRP discharge pulse is often not sufficient to ensure the ignition of hydrocarbon-air mixtures. The entrainment of fresh gases towards the center of the discharge channel, due to the hydrodynamic instabilities generated by the ultra-fast energy deposition, progressively reduces the temperature and radicals concentration of the hot kernel leading ultimately to it extinction. The solution that was naturally considered, to make the NRP discharges more effective, consists in applying a series of consecutive pulses. The objective is to successively supply, pulse after pulse, the hot kernel with heat and radicals until the flame ignites. The objective of this chapter is to investigate numerically the dynamic of flames ignition by a series of NRP discharges pulses.

The chapter is structured as follows. Section. 5.2 introduces the flow tunnel configuration, a flowing methane-air combustion chamber designed to study the ignition of flames by NRP discharges. Section. 5.2 is devoted to the investigation of the pulses interaction regimes observed by Lefkowitz and Ombrello (2017) in his experimental study of the flow-tunnel configuration, and to the identification of the parameters that influence the efficiency of flames ignition by NRP discharge. A dimensionless approach is then proposed to predict the pulses interaction regimes and the ignition probability according to the flow and discharge parameters. Section. 5.4 presents the 3-D LES of the flow tunnel ignition by NRP discharges performed using the phenomenological plasma model of Castela (2016). Two parametric studies are conducted. The first one investigate the impact of the flow velocity on the ignition process while the second one investigate the impact of pulse repetition frequency. The conclusions of the studies are summarized in Section. 5.5.

5.2 Flow tunnel configuration

To study the dynamics of flame ignition by a series of NRP discharge pulses, Lefkowitz and Ombrello (2017) designed an experimental combustion chamber, the flow tunnel configuration, that allows an easy and precise control of the flow operating conditions (velocity, equivalence ratio) and plasma discharges parameters (pulse energy, pulse repetition frequency, ...). The configuration, shown in Fig. 5.1, consists of a square cross-section tube of 3.81 cm side and 25.2 cm length with windows of fused silica on three lateral faces that give access to optical measurements. A methane-air mixture at atmospheric pressure and 295K is introduced from the inlet. The inflow Reynolds numbers ranges between 6 000 and 24 000. The flow is regularized by using a three meshed screens to reduce large scale eddies and have a uniform flow-rate across the tunnel section. Right before the end of the tunnel, a small cross-flow of inert gases is injected to prevent flame holding. Two tungsten electrodes of 1.6 mm

diameter and 20° tip angle are placed 5.18 cm downstream the gases inlet perpendicular to the direction of the flow. The electrodes are connected to a pulse generator capable of supplying up to 500 pulses at 300 kHz and at voltages up to 15 kV. The inter-electrode distance can be adjusted with micrometers with an optimal distance found by Lefkowitz and Ombrello (2017) to be equal to 2 mm. For smaller inter-electrode distances significant heat losses are induced at the electrodes, quenching the hot gases kernel and leading to poor ignition performances. As for larger distances, the amplitude of the electric field generated between the two electrodes is not sufficient to deposit the minimum amount of energy needed for the flame ignition.

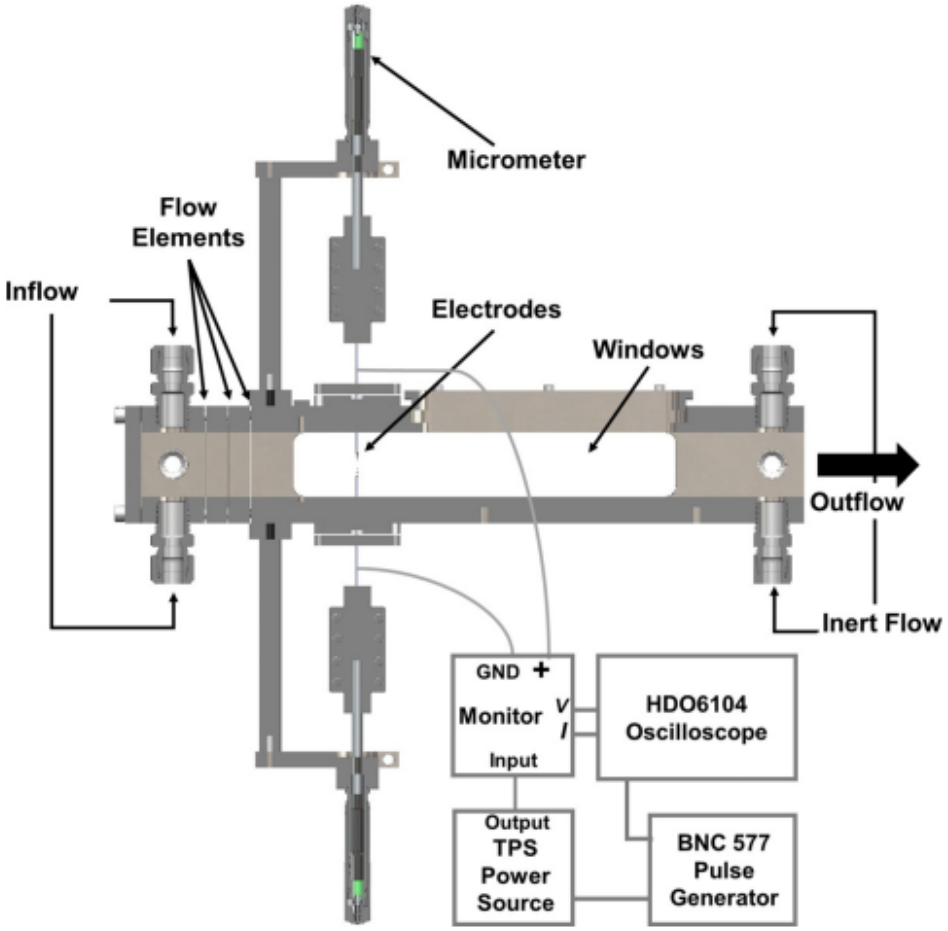

Figure 5.1: *Diagram of flow tunnel. Extracted from Lefkowitz and Ombrello (2017).*

5.3 NRP discharge pulses interaction regimes

A parametric exploration was performed by Lefkowitz and Ombrello (2017) to study the impact of flow and discharge parameters on the ignition process of the flow tunnel configuration by NRP discharges. The effects of flow velocity in the range of 2.5-10 m.s^{-1} and pulse repetition frequency (PRF) in the range of 1-300 kHz were investigated. The results showed the existence of three pulses interaction regimes characterized by distinct ignition probabilities and kernel structures :

Fully coupled regime: the pulses are deposited on top of each other in the discharge zone which results in the formation of a single, coherent ignition kernel with very high ignition probability as shown in case a, b, c and d of Fig. 5.2.

Partially coupled regime: the volume of heated gases created by the different pulses are connected but not completely merged. The resulting ignition kernel has an elongated shape as observed in the e, f and g case of Fig. 5.2. Depending on the operating conditions and the plasma parameters the interaction between the pulses can lead in some cases to a successful ignition in and others to an ignition failure. The ignition probability in this regime is low compared to the fully coupled regime.

Decoupled regime: the pulses are spaced out and independent from each other. The ignition kernels formed at each energy deposition don't interact as observed in case h and i of Fig. 5.2. The overall ignition probability is a linear function of the probability that a single pulse induces a successful ignition. As in most cases, it is impossible to ignite the flame with a single NRP discharge pulse, the ignition probability of this regime is often equal to zero.

The main parameters that influence the regime of interaction between the pulses are the flow velocity (V_{flow}) and the pulse repetition frequency (PRF). These two parameters control two characteristic times :

- The residence time of the gases in the discharge zone, τ_{res}. It is assumed that the gases cross the plasma discharge at a uniform velocity V_{flow} as indicated in Fig. 5.3. The residence time is then approximated as follow:

$$\tau_{res} \approx \frac{D_{discharge}}{V_{flow}} \tag{5.1}$$

  where $D_{discharge}$ is the discharge diameter.

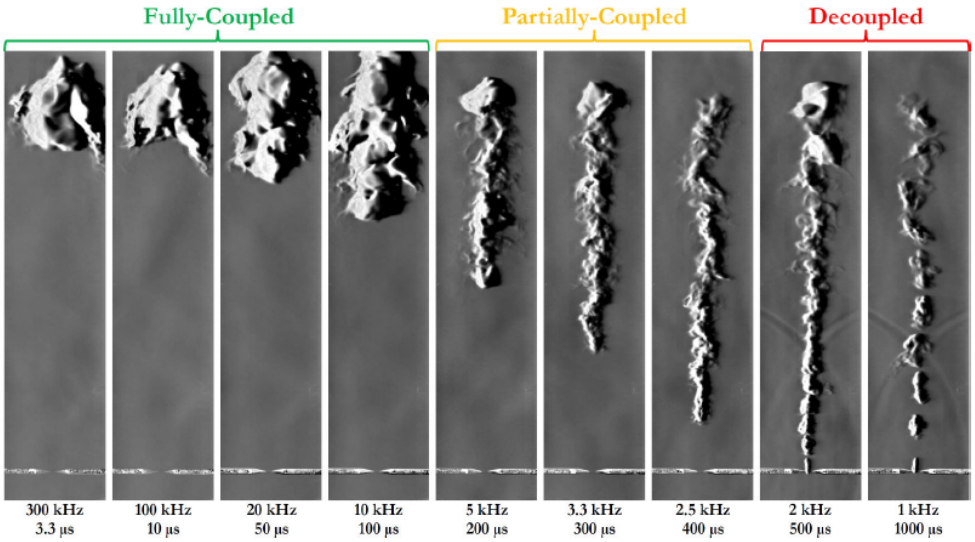

Figure 5.2: *Schlieren images of flow tunnel ignition by NRP discharges for various pulse repetition frequency, taken at ϕ= 0.6, U = 10 m/s, D = 2 mm, and N = 20. Three pulses interaction regimes are observed. A fully coupled regime for high frequencies ($f \geq$ 10 KHz). A partially coupled regime for intermediate frequencies (10 KHz $< f <$ 2 KHz). A decoupled regime for low frequencies ($f \leq$ 2 KHz). Reproduced from Lefkowitz and Ombrello (2017).*

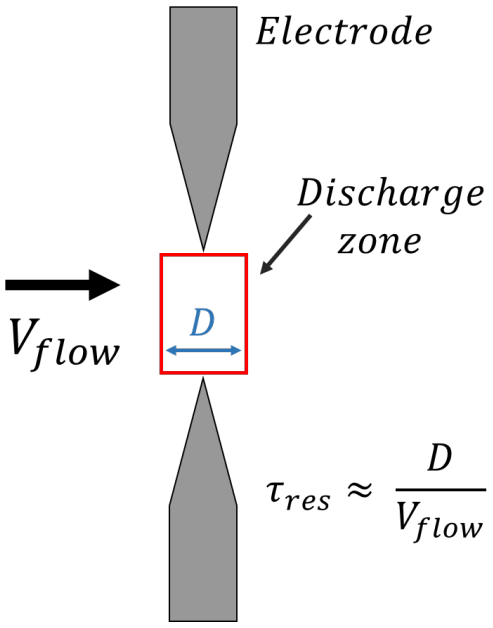

Figure 5.3: *Schematic representation of the inter-electrode region. The residence time of the gases in the discharge zone of diameter D for a flow at a uniform velocity V_{flow} is equal to $\tau_{res} \approx D_{discharge}/V_{flow}$.*

- The inter-pulse time $\tau_{interpulse}$ represents the time between two consecutive pulses and is given by the inverse of the pulse repetition frequency (PRF) or (f_{pulse}):

$$\tau_{inter-pulse} = \frac{1}{f_{pulse}} \tag{5.2}$$

These two characteristic times are compared by introducing the dimensionless number α defined as the ratio between the residence time of the gases in the discharge zone and the inter-pulse time:

$$\alpha = \frac{\tau_{res}}{\tau_{inter-pulse}} = \frac{D_{discharge} \times f_{pulse}}{V_{flow}} \tag{5.3}$$

If $\alpha > 1$, the residence time of the gases in the discharge zone is greater than the time between two pulses ($\tau_{res} > \tau_{inter-pulse}$). The flow velocity that convects the hot gases created by a plasma pulse away from the discharge zone is smaller than the pulse repetition frequency. The pulses are deposited on top of each other and accumulate their effects to create a large hot kernel that leads to flame ignition. This case corresponds to the fully coupled regime observed experimentally with a high ignition probability.

if $\alpha \approx 1$, the residence time of the gases in the discharge zone and the time between two pulses are almost equivalent ($\tau_{res} \approx \tau_{inter-pulse}$). The hot reactive gases of the pulses have almost completely left the discharge zone before the next pulse. A partial accumulation of the pulses effects is obtained which can lead in some cases to the creation of a sufficiently large hot kernel to induce the flame ignition. This case corresponds to the partially coupled regime with a low ignition probability.

if $\alpha < 1$, the residence time of the gases in the discharge zone is smaller than the time between two pulses ($\tau_{res} < \tau_{inter-pulse}$). The hot reactive gases generated by a pulse are convected away from the discharge zone before the next one. The pulses effects don't accumulate and the small separated kernel formed by each pulse are not sufficient to allow the flame ignition. This case corresponds to the decoupled regime with a very low ignition probability.

The computation of the dimensionless number α can be used to identify the pulses interaction regime that results from the imposed flow operating conditions and the plasma parameters and thus predict whether the ignition probability is going to be high or low.

This simple analysis is applied to the cases investigated in (Lefkowitz and Ombrello (2017)) where the impact of the residence time and the inter-pulse time

on the ignition probability were studied by varying the gases injection velocity and the pulse repetition frequency (PRF). Three bulk velocities U_b were considered ($U_b = 2.5$ m.s^{-1}, $U_b = 5$ m.s^{-1}, $U_b = 10$ m.s^{-1}) for which a series of 10 NRP discharges pulse were applied at different pulse repetition frequencies (f = 1.0 KHz, f = 2.0 KHz, f = 5.0 KHz, f = 10.0 KHz, f = 300.0 KHz). The schlieren images and the value of the dimensionless number α of each case are shown in Fig.5.4

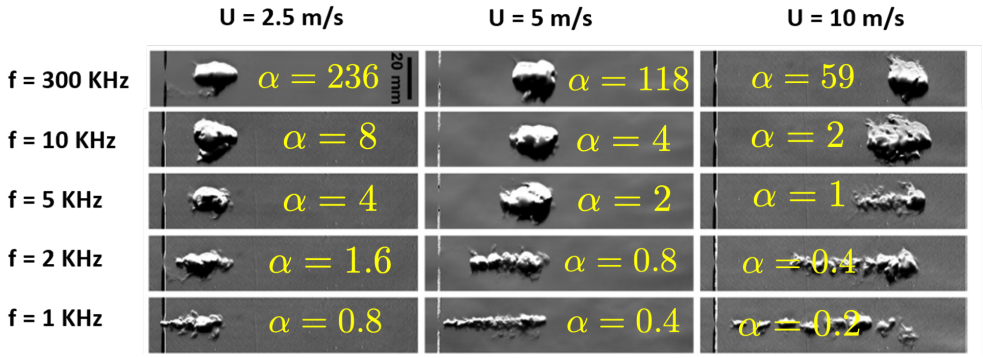

Figure 5.4: *Schlieren images of flow tunnel ignition by NRP discharges for various flow inlet velocity ($U_b = 2.5$ $m.s^{-1}$, $U_b = 5.0$ $m.s^{-1}$, $U_b = 10$ $m.s^{-1}$) and pulse repetition frequency(PRF = 1 kHz, PRF = 2 kHz, PRF = 5 kHz, PRF = 10 kHz, PRF = 300 kHz), taken at ϕ= 0.6, D = 2 mm, and N = 10 (Lefkowitz and Ombrello (2017)). The number α indicated for each case corresponds to the interaction regime dimensionless number $\tau_{res}/\tau_{inter-pulse}$. Three pulses interaction regimes are observed. A fully coupled regime ($\alpha > 1$). A partially coupled regime ($\alpha \approx 1$). A decoupled regime ($\alpha < 1$).*

For the cases where $\alpha > 1$, the schlieren images show the formation of a single, large coherent hot reactive kernel indicative of the flame ignition and propagation, corresponding well to the fully coupled regime.

For $\alpha < 1$ ($\alpha = 0.4$, $\alpha = 0.2$), the schlieren images show the formation of either a very elongated kernel or spaced small kernels with no visible flame propagation indicating a non ignition of the mixture as reported by the experimental study. This cases corresponds well to the decoupled regime where the ignition probability is zero.

Finally for $\alpha \approx 1$ ($\alpha = 1.0$, $\alpha = 0.8$) the schlieren images show an elongated kernel which leads in some cases ($U_b = 5$ m, KHz, f = 2.0, $\alpha = 0.8$ for example) to flame ignition and in other cases ($U_b = 10$ m, KHz, f = 5.0, $\alpha = 1.0$) to a no ignition. This cases correspond to the partially coupled regimes where the ignition probability is low but not zero.

This dimensionless approach can be used as a preliminary step to estimate the NRP discharge properties that ensure an efficient ignition of combustion chambers. Depending on the target configuration, the first choices concerning the positioning of the discharges in the flow, preferably in low velocity zone to have a residence time of the gases in the discharge zone high enough, and the pulse repetition frequency to have an alpha higher than 1 can already be made.

This approach is however limited for the following reasons. First, while it is easy to compute the inter-pulse time, the estimation of the residence time is not straightforward. It is necessary to take into account the mean flow, the turbulence and also the hydrodynamic instabilities generated by the NRP discharges which are case dependent and difficult to estimate precisely. Secondly, this approach does not give the number of pulses and the energy needed for the ignition which are primordial information needed to build the electric system (pulse generator power, cables, electrodes) of the discharges.

To address these physical phenomena, we propose to conduct 3-D unsteady simulations of the complex interactions between the turbulence, the plasma and the combustion.

5.4 LES of flow tunnel ignition by NRP discharges

Large eddy simulations of the flow tunnel flame ignition by NRP discharges are performed using the phenomenological NRP discharge described in Chapter. 2. The objective is to evaluate the ability of the model and the numerical methods to reproduce the effects of the discharges and investigate the impact of the flow operating conditions and the discharge properties on the pulses interaction regimes and the ignition process.

5.4.1 Numerical set-up

The simulated domain is displayed in Fig. 5.5. The inlet is located after the meshed screens used to regularized the flow which are not modeled in the simulations. The dimensions given by the authors in the experimental article are reproduced, with a chamber side square-section of 3.81 cm and a 25.2 cm length. Two electrodes of 1.6 mm diameter and 20° tip angle are placed 5.18 cm downstream the gases inlet perpendicular to the direction of the flow and separated by a 2 mm gap. The walls (tunnel lateral walls, electrodes) are considered adiabatic since no cooling system is used in the experiment and the impact of heat transfer was not quantified. This choice remains correct as the flame kernels remain at the center of the flow tunnel and do not interact with the walls of the chamber.

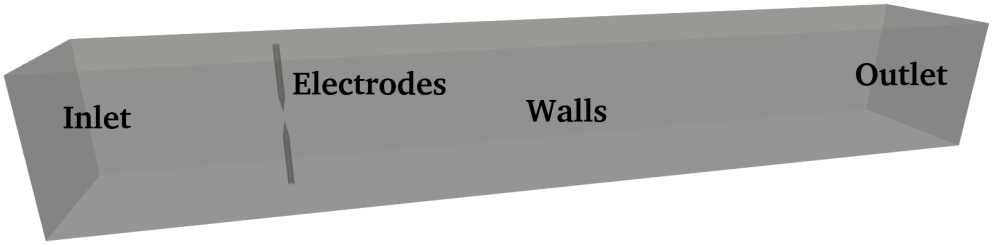

Figure 5.5: *Flow tunnel 3-D geometry.*

To identify the optimal spatial resolution of the plasma, a series of five electrical low energy pulses has been computed on three different grids characterized by cells size of 25 μm, 50 μm, and 100 μm in the discharge zone, respectively. Figure. 5.6 shows that the evolution of the maximum temperature and O concentration at the discharge center are the same for the three meshes.

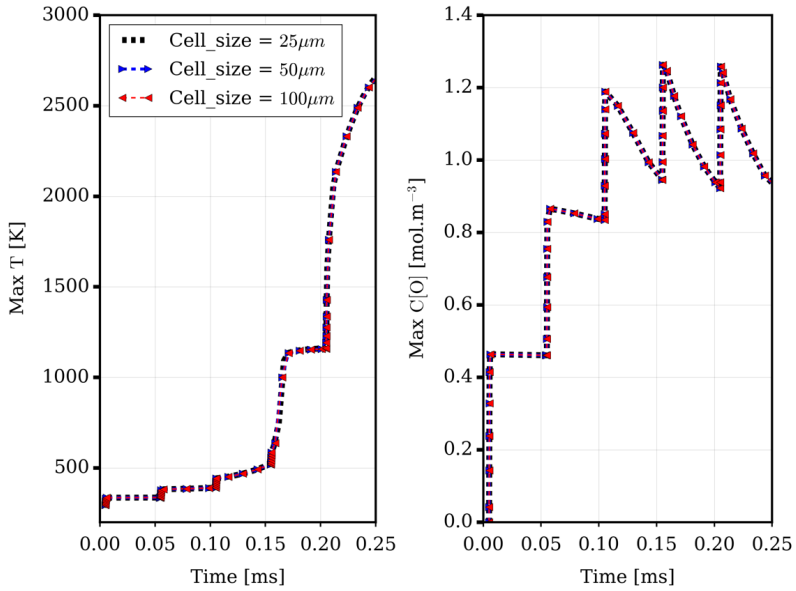

Figure 5.6: *Sensitivity study of the grid resolution in the discharge zone. Temporal evolution of maximal values of temperature and atomic oxygen O concentration reached in the discharge are plotted during* 5 *pulses. Three different mesh size are tested, corresponding to cell size of 25 µm (black), 50µm (blue) and 100 µm (red, retained for the LES) in the discharge zone.*

The retained mesh for this study is the 100 μm mesh , shown in Fig. 5.7. It consists of 40 millions tetrahedral elements, refined in the inter-electrodes re-

gion, with a cells size of 0.1 mm. In the flame zone, shown in red, the cells size ranges between 0.1 mm to 0.2 mm.

The simulations are performed with the YALES2 unstructured finite-volume low-Mach number solver (Moureau et al. (2011)). The time integration uses a fourth-order temporal scheme with a centered fourth order scheme for spatial discretization. The sub-grid Reynolds stresses tensor is closed using the Dynamic Smagorinsky model (Germano et al. (1991)). The analytical LU19 kinetic scheme involving 19 species and 184 reactions is used for the methane-air mixture chemistry. Species equations are coupled with turbulence using the thickened flame model for LES (TFLES Colin et al. (2000)) with a dynamic flame sensor and the Charlette sub-grid scale flame wrinkling model (Charlette et al. (2002)). The average and maximum thickening obtained in the simulations are around 1.5 and 2, respectively.

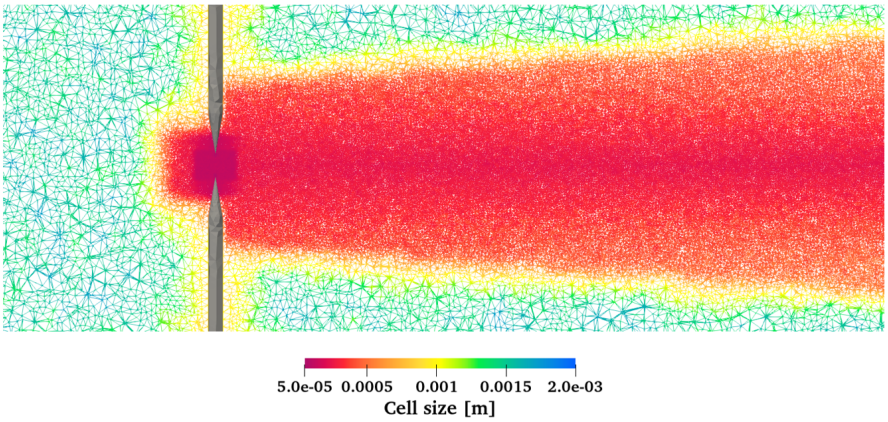

Figure 5.7: *2-D view of flow tunnel mesh colored by the cell size dimension.*

The plasma discharge has a quasi-cylindrical shape filtered with the spatial function $F(r) = erfc[(r/a)^b]$ where r the radius is equal to 0.5 mm, $a = 3.10^{-8}$ and $b = 2.5$ are geometric filter parameters, fitted to insure that the discharge radius is well reproduce and that there is a sufficient number of mesh points (3 points) at the interface between the plasma and the gas to avoid the generation of strong gradients during the pulse that can cause numerical issues. The discharge length is equal to 2 mm corresponding to the inter-electrode distance. The average electric energy deposited at each pulse has been measured by the authors. They concluded that the deposited energy per pulse is almost constant, 2.9 0.23mJ per pulse, except for the first pulse which has 0.4mJ less deposited energy.

5.4.2 Effect of the flow velocity

The first study focuses on the effects of the flow velocity on the process of ignition by NRP discharges. The three bulk velocities U_b investigated experimentally are retained :

1. $U_b = 2.5$ m.s^{-1}.
2. $U_b = 5.0$ m.s^{-1}.
3. $U_b = 10.0$ m.s^{-1}.

For each simulation, the flow tunnel is fed with a methane-air mixture at an equivalence ratio of ($\phi = 0.6$).

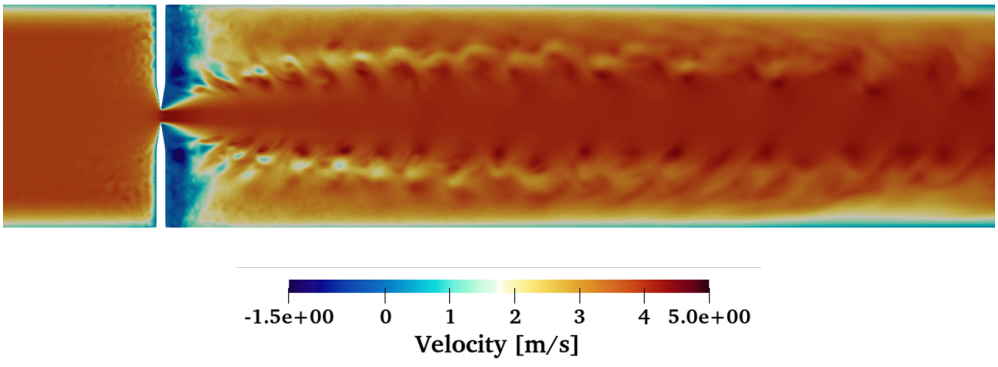

Figure 5.8: *Instantaneous axial velocity field in the centerline plane of the flow tunnel configuration obtained for a bulk velocity $U_b = 2.5$ $m.s^{-1}$. Recirculation zones are formed behind the electrodes.*

Figures. 5.8, 5.9, 5.10 show the instantaneous 2-D axial velocity field in the centerline plane of the flow tunnel configuration (plane of the electrodes). For the three cases, the presence of the electrodes induces an important acceleration of the flow in the inter-electrode zone with a 60% increase of the velocity for the $U_b = 2.5$ m.s^{-1} case, from 2.5 m.s^{-1} to 4 m.s^{-1}, a 50% increase for the $U_b = 5$ m.s^{-1} case, from 5 m.s^{-1} to 7.5 m.s^{-1} and also 50% for the $U_b = 10$ m.s^{-1} case, from 10 m.s^{-1} to 15 m.s^{-1}.the increase is accompanied by a creation of turbulence downstream the electrodes.
Once the chamber is filled with the methane-air mixture and the steady state reached, a series of 10 pulses is applied to ignite the chamber. A constant pulse repetition repetition frequency (PRF) of 5 KHz is used for the three cases.

Temperature and OH radical concentration 2-D fields images at different instants of the ignition events are shown in Fig.5.11, along with the bulk velocity of each case.

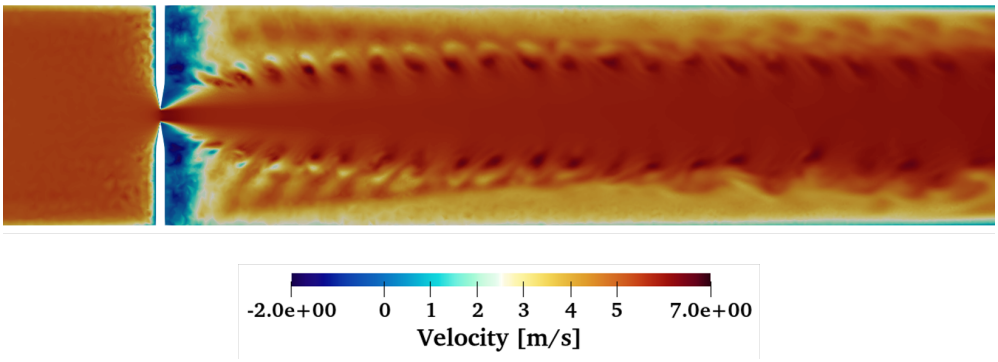

Figure 5.9: *Instantaneous axial velocity field in the centerline plane of the flow tunnel configuration obtained for a bulk velocity* $U_b = 5.0\ m.s^{-1}$. *Recirculation zones are formed behind the electrodes.*

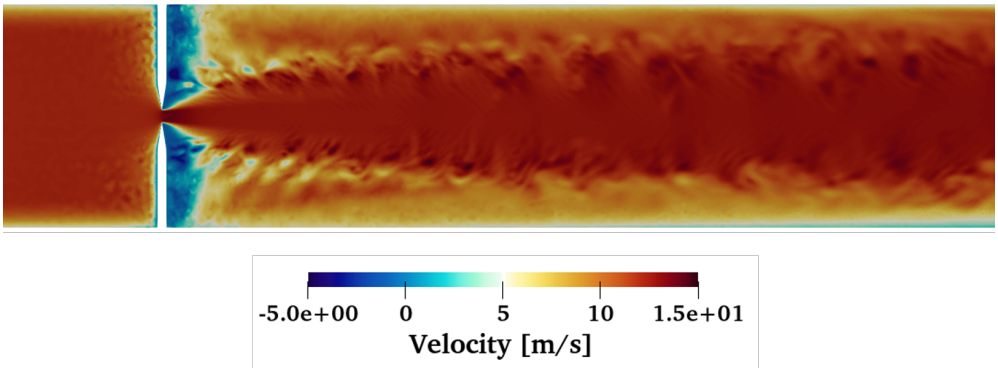

Figure 5.10: *Instantaneous axial velocity field in the centerline plane of the flow tunnel configuration obtained for a bulk velocity* $U_b = 10.0\ m.s^{-1}$. *Recirculation zones are formed behind the electrodes.*

The first column, taken at 4.5 μs after the first discharge pulse, shows that the NRP pulse induces a significant increase of gases temperature, from 295 K to 1400 K, accompanied by a production of OH radical that reaches a concentration of $6 \cdot 10^{-2}$ mol.m^{-3}. For the three cases, these effects lead to the formation of quasi cylindrical hot reactive kernel in the discharge zone for the three cases.

At 50 μs, second column, the reactive hot kernel has evolved from its initial quasi-cylindrical shape to a toroidal shape under the effect of the baroclinic instabilities induced by the discharge as discussed in Section. 4.4. In the centerline plane of the flow tunnel configuration, the toroidal shape of the kernel is seen as two small round regions of high temperature and OH radicals. The kernel is stretched by the two recirculation zones formed by the instabilities, half is convected in the same direction as the flow, to the right of the discharge zone (right-part), and the other half in the opposite direction of the flow, to the left of the discharge zone (left-part). If the flow velocity is too low, the

hot gases convected in the opposite direction may travel upstream. It is the case for U_b =2.5 m.s^{-1} and U_b = 5.0 m.s^{-1}, where the left-part of the kernel is located at the left of the electrodes, outside the discharge zone.

At 205 μs, the second pulse has been applied for all three cases. For U_b = 2.5 m.s^{-1} and U_b = 5.0 m.s^{-1} the left-part of the first pulse kernel is still in the discharge zone when the second pulse is applied. The effects of the second pulse add up to the first one and results in an additional increase of temperature and OH concentration that reach 3500 K and $1.6 \cdot 10^{-1}$ mol.m$_{-3}$ respectively. The right-part of the kernel has been transported by the flow away from the discharge zone and does not interact with the second pulse. Due to thermal diffusion and chemical recombination the temperature and the OH concentration of this region have significantly decreased.
For the U_b = 10 m.s^{-1} case, the hot reactive kernel transported by the flow is outside the discharge zone when the second pulse is applied and does not interact with it. Due to thermal diffusion and chemical recombination, it has lost a significant amount of its heat and chemical reactivity. The second pulse is deposited in fresh gases conditions similar to the ones encountered by the first pulse inducing the same effects, an increase of temperature and OH concentration.

At 840 μs, 5 pulses have been applied. For U_b = 2.5 m.s^{-1} and U_b = 5.0 m.s^{-1} cases the pulses continue to overlap, the trend of increasing the temperature and OH concentration is repeated. A large kernel has formed and began to propagate downstream and upstream the discharge zone. In these two cases, the pulses are in a fully coupled interaction regime. For the U_b = 10.0 m.s^{-1} case, the hot reactive kernels created at each pulse partially merge with each other. However, This weak interaction does not allow to increase or maintain the heat and the reactivity of the kernels which end-up being quenched by the flow as seen here for the first four kernels. The simulation indicates that in this case the pulses are in a partially coupled regime.

At 1.74 ms, all 10 pulses have been applied. In line with what was observed previously, the pulses continued to be deposited on top of each other for the U_b = 2.5 m.s^{-1} and U_b = 5.0 m.s^{-1} cases. The region of high temperature and OH concentration has expanded for both cases indicating a successful ignition. For U_b = 10.0 m.s^{-1}, spaced hot gases region are visible. A chemical activity seems to persist in the last formed kernel with a small amount of OH still presents near the electrodes. All the other kernels have however been quenched.

At 2.5 ms, 700 μs after the end of the 10 pulses burst, the ignited kernels of the U_b = 2.5 m.s^{-1} and U_b = 5.0 m.s^{-1} cases have developed downstream into self-propagating flames. Inside the kernel, temperature and OH concentration reach equilibrium (T = 1670 K and [OH] = $2.9 \cdot 10^{-2}$ mol.m^{-3}). For U_b = 10.0

$m.s^{-1}$ case, all the kernels are quenched. OH radical is no more present and hot gases have been cooled down.

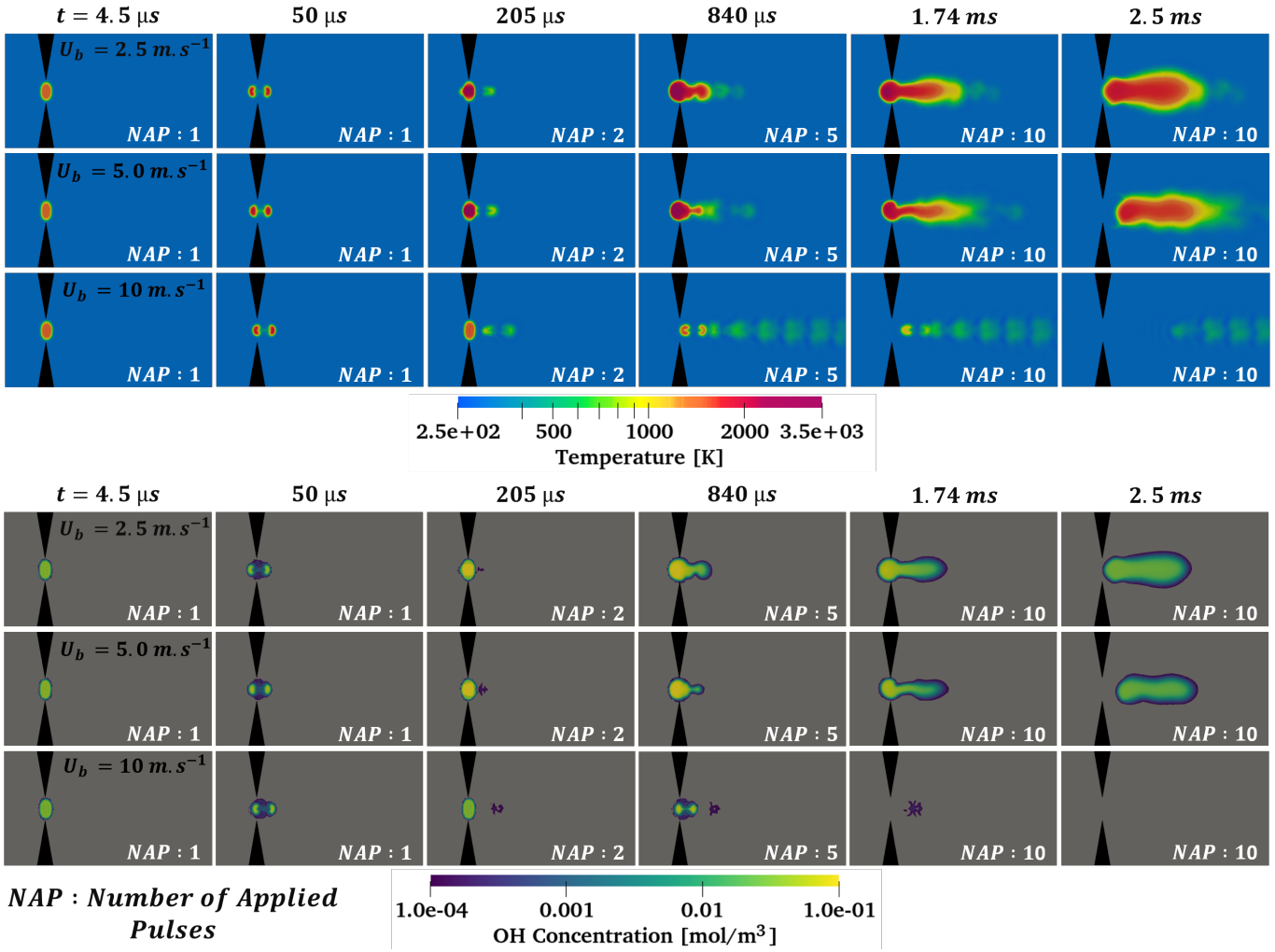

Figure 5.11: *Temperature (top) and OH concentration (bottom) instantaneous 2-D fields in the centerline plane of the flow tunnel configuration taken at different instants for various bulk velocities. The methane-air mixture equivalence ratio ($\phi = 0.6$) and the pulse repetition frequency ($PRF = 5$ kHz) are constant for the three cases. The images show that the ignition occurs for $U_b = 2.5$ $m.s^{-1}$ and $U_b = 5.0$ $m.s^{-1}$ cases, but does not for the $U_b = 10.0$ $m.s^{-1}$ case.*

The successful ignition of the $U_b = 2.5$ m.s^{-1} and $U_b = 5.0$ m.s^{-1} and the non-ignition of the $U_b = 10.0$ m.s^{-1} predicted by the the numerical simulations are in agreement with the experimental observations of Lefkowitz and Ombrello (2017) as summarized in Tab. 5.1.

Flow bulk velocity	Experiment	Simulation
$U_b = 2.5$ m.s^{-1}	Ignition	Ignition
$U_b = 5.0$ m.s^{-1}	Ignition	Ignition
$U_b = 10.0$ m.s^{-1}	Non-ignition	Non-ignition

Table 5.1: *Comparison between the numerical simulations (present work) and the experiment observations (Lefkowitz and Ombrello (2017)) of the flow tunnel ignition success or failure by NRP discharges for three bulk velocity ($U_b = 2.5$ $m.s^{-1}$, $U_b = 5.0$ $m.s^{-1}$, $U_b = 10.0$ $m.s^{-1}$) and constant pulse repetition frequency (PRF = 5 kHz).*

The simulations are also in agreement with results of the dimensionless approach which predicted a coupled regime of pulses and thus a high probability of ignition for the $U_b = 2.5$ m.s^{-1} and $U_b = 5.0$ m.s^{-1} cases with a $\alpha = 4$ and $\alpha = 2$, respectively, and a partially coupled regime, low ignition probability, for the $U_b = 10$ m.s^{-1} case with $\alpha = 1.0$, the scaled approach indicates a $\alpha = 1.0$.

The efficiency of flame ignition by a series of NRP discharge pulses is highly dependent on the pulse interaction regime. The simulations show that to operate in a fully coupled regime and ensure a high ignition probability, NRP discharges must be applied in low velocity regions that allow a residence time of the hot reactive gases greater than the inter-pulse time and thus ensure the accumulation of the pulse effects. Unfortunately, such low velocity regions do not always exist in combustion chambers. The alternative will be to decrease the inter-pulse time by increasing the pulse repetition frequency instead of increasing the gas residence time. This solution is studied in the next section.

5.4.3 Effect of the pulse repetition frequency

The impact of pulse repetition frequency (PRF) on flame ignition by NRP discharges process has been investigated experimentally by Lefkowitz et al. (2020) on the flow tunnel configurations. A sequence of 10 NRP pulses was applied in the methane-air mixture injected in the combustion chamber at a constant inlet velocity of $U_b = 10$ m.s^{-1}, for different PRF = 2, 5, 10, and 50 kHz.

Numerical simulations of these cases are performed using the NRP phenomenological discharge model. The mesh, numerical methods, kinetic mechanism and operating conditions are those presented in Section. 5.4.1. Four pulse repetition frequencies (PRF) are considered :

1. PRF = 2 kHz.

2. PRF = 5 kHz.
3. PRF = 10 kHz.
4. PRF = 50 kHz.

The objective is to investigate the impact of the pulse repetition frequency on the efficiency of flames ignition by NRP discharges.

Figure. 5.12 shows the temperature and OH radical concentration 2-D fields in the centerline plane of the flow tunnel configuration at different instants of the ignition events along with the pulse repetition frequency used in each case and the corresponding inter-pulse time (IPT = 1/PRF).

The first column of images, taken at 4.5 μs after the first pulse, shows the formation of an quasi cylindrical hot reactive kernel in the discharge zone in which the temperature has increased from 295 K to 1400 K and the OH concentration form 0 to $6 \cdot 10^{-2}$ mol.m^{-3}.

At 24.5 μs, second column, a difference is observed between the 50 kHz and the other cases. By this time, the 50 kHz PRF case has had a second pulse deposited. The pulse adds-up to the first pulse kernel increasing the temperature and the OH concentration to 4800 K and $1.8 \cdot 10^{-1}$ mol.m^{-3}, respectively. For PRF = 2, 5 and 10 kHz, only one pulse has been deposited. Under the effects of hydrodynamic instabilities, presented in Section. 4.4, the reactive hot kernel generated by the first pulse is transitioning from its initial quasi-cylindrical shape to a toroidal shape. Inside the kernel, the temperature and OH concentration have reached 2100 K and $0.8 \cdot 10^{-1}$ mol.m^{-3}, respectively.

At 44.5 μs, 3 pulses have been deposited in the 50 kHz case. The temperature and OH concentration continue to increase as the pulses overlap. However, only one pulse has been deposited for the other cases (PRF = 2, 5, and 10 kHz). The hot kernel has now a toroidal shape. In the 2-D centerline plane, the toroidal shape of the kernel is seen as two separated high temperature and OH round regions.

At 165 μs, only one pulse has been deposited for the two lowest PRF cases (PRF = 2 kHz and 5 kHz). The hot reactive kernel created by the first pulse has been convected by the flow away from the discharge zone. Inside, the temperature and OH concentration have significantly decreased indicating that the kernel is being quenched. For PRF = 10 kHz, the second pulse has now been applied. Its interaction with the first kernel allows to maintain a high temperature and OH concentration in the discharge zone. Finally, for PRF = 50 kHz, 9 overlapping pulses were applied. A voluminous high temperature, high OH concentration expanding kernel is now visible.

At 365 μ s, 1 pulse have been deposited in the 2 kHz case, 2 pulses in the 5 kHz case, 4 pulses in the 10 kHz case, and 10 pulses in the 50 kHz case. The kernel of the 50 kHz case has developed into self-propagating flame. In the 10 kHz case, the hot reactive kernel, supplied by the overlapping pulses, is expending downstream. In 5 kHz case, the two generated kernels have partially merged but appear to be quenching with only a small amount of OH remaining near the electrodes. The single kernel of the PRF = 2 kHz almost completely quenched.

At 765 μ, the ignited flame of the 50 kHz case has moved downstream. its temperature and OH concentration have returned to the equilibrium (T = 1670 K and [OH] = $2.9 \cdot 10^{-2}$). The 8 pulses applied in the PRF = 10 kHz case have created an elongated kernel that experiences some local quenching at the top. In the 5 kHz The same trend is repeated. The consecutive pulses merge partially with each other but end up quenching. For PRF = 2 kHz, the two formed kernels are independent from each other and both being quenched.

Finally, after 2 ms, the freely propagating flame of the 50 kHz case continues to develop. The kernel of the 10 kHz case led ultimately to the ignition of the flowing mixture, while in both the 2 kHz and 5 kHz cases the ignition is not achieved.

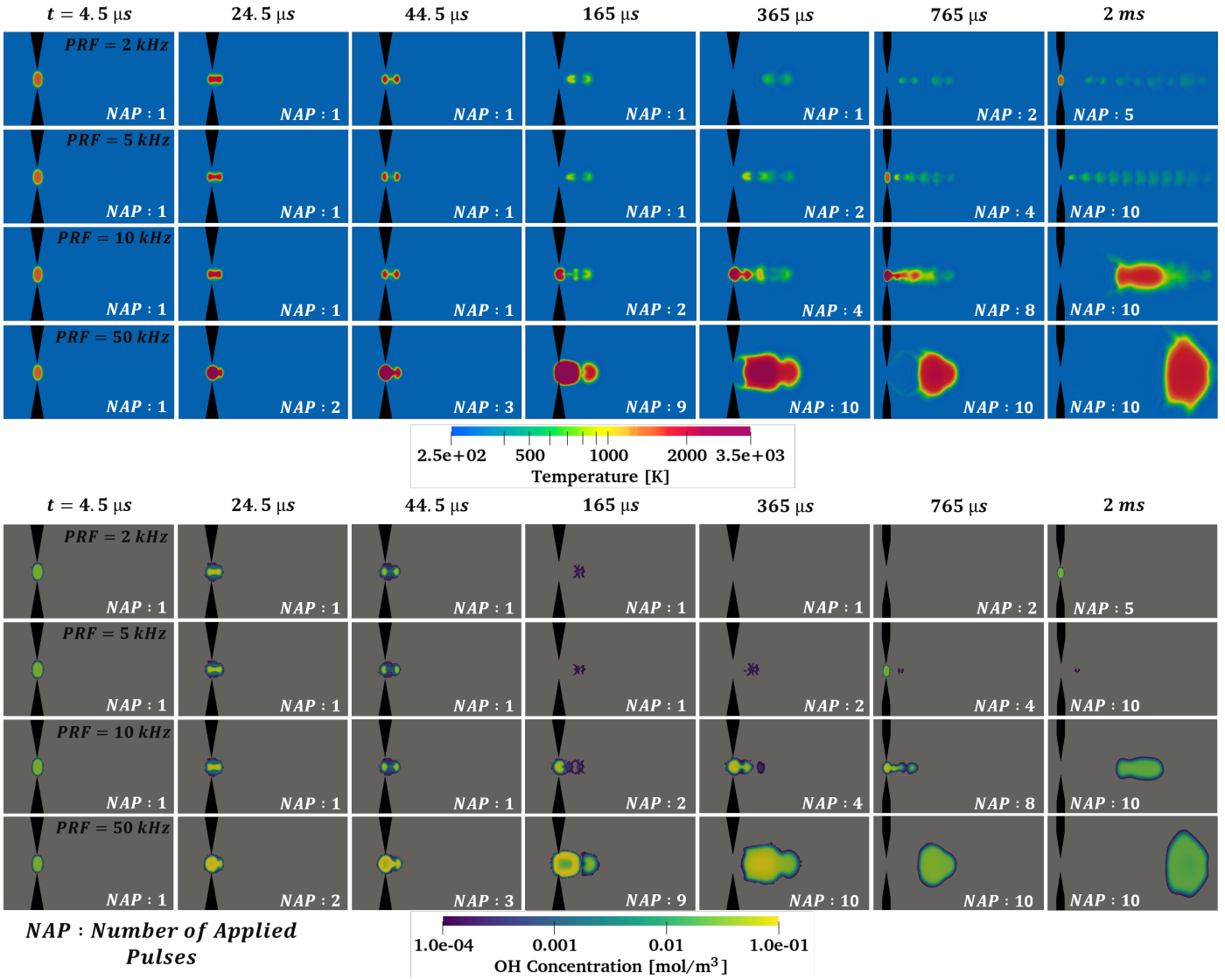

Figure 5.12: *Temperature (top) and OH concentration (bottom) instantaneous 2-D fields in the centerline plane of the flow tunnel configuration taken at different instants of the ignition events for various pulse repetition frequencies (PRF). The methane-air mixture equivalence ratio ($\phi = 0.6$) and the inlet velocity ($U_b = 10.0\ m.s^{-1}$) are constant for all the cases. The images show that the ignition occurs for PRF = 10 kHz and PRF = 50 kHz, and does not for PRF = 2 kHz and PRF = 5 kHz.*

In the experimental study, Lefkowitz et al. (2020) counted, over 20 repeated pulse-bursts performed at each frequency, the number of pixels with a detectable OH signal in the OH-PLIF frames he measured at the centerline plane of the flow tunnel configuration. The same data is extracted from the numerical simulations by summing the surfaces of all the mesh cells with detectable OH concentration in the plane corresponding to the field of view of the OH-PLIF displayed in Fig.5.13. The number of pixel corresponding to detectable OH-signal is the computed by dividing the total surface by the camera pixel surface given in Lefkowitz et al. (2020).

Figure 5.13: *Schematic representation of the OH analysis regions. The green rectangle indicates the field of view of the OH-PLIF. The white rectangle indicates the Region Of Interest (ROI) in the discharge zone.*

Figure. 5.14 shows the temporal evolution of the number of pixels with detectable OH for the investigated pulse repetition frequencies (PRF = 2 kHz, 5 kHz, 10 kHz, 50 kHz). The symbols correspond to the measured values and the continuous lines to the numerical results.
For the case PRF = 2 kHz, the experimental (black circles) and numerical (black line) results show that at each pulse the number of pixels increases rapidly reaching a value of 2500 pixels at the end of the energy deposition indicating the formation of an OH region. Shortly after the pulse, the number of pixels starts to decrease and eventually returns to its initial value of 0 before the following pulse is applied. The temporal evolution of the pixels number indicate that the pulses are fully decoupled in this case. In the absence of pulses effects accumulation, the ignition attempt fails.
For PRF = 5 kHz, the trend of pixels number increase during the pulse, OH production, followed by the pixels number decrease between pulses, OH recombination, is again observed. However, as the inter-pulse time (IPT = 1/PRF = 200 μs) in this case is smaller than the recombination time of OH a small OH region remains between the pulses. The OH region formed by the following pulse adds up with the remaining OH region of OH without however increasing the maximum size of the overall OH region which . This weak interaction indicates that the pulses are in a partially coupled regime.
For the PRF = 10 kHz case, the inter-pulse time is even smaller (IPT = 1/PRF

= 100 μs). Thus the amount of OH (number of pixels with a detectable OH-signal) that remains between two pulses is more important.The number of pixels increases gradually to reach a value at the end of pulse-burst of 16000 pixels in the experiment (blue diamonds) and 14000 in the numerical simulation (blue line), leading to a successful flame ignition. After which it continues to grow as flame propagates without the assistance of the plasma. This behavior characterizes the fully coupled regime where the pulses effects add-up and always leads to a successful ignition event.
For the 50 kHz case, the OH region (number of pixels) builds-up quicker then the 10 KHz case. The OH quantities produced at each pulse add up, and since the inter-pulse period is much smaller than the recombination time of the OH no decay of the latter is observed. The number of pixels increases continuously and reaches experimentally (green square) and numerically (green line) a value 11000 pixels at the end of pulse-burst. After that, it continues to increase as the flame freely propagates, at a faster rate in the numerical simulations compared to the experiment.

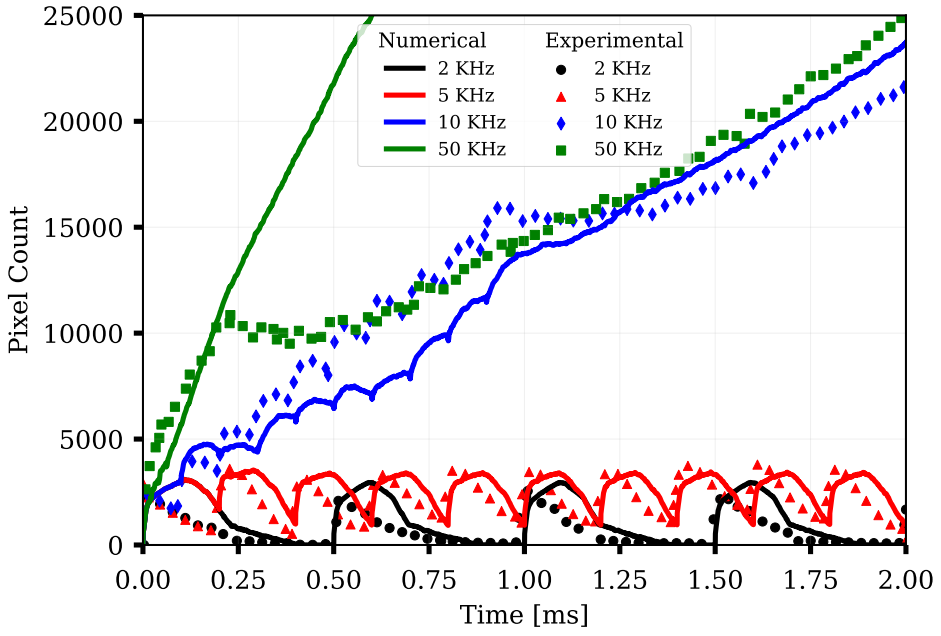

Figure 5.14: *Temporal evolution of the number of pixels with detectable OH for various pulse repetition frequency (PRF) conditions. Simulations results (colored lines) are compared with the experimental measurements (colored symbols) from (Lefkowitz et al. (2020)).*

To analyze the dynamics of OH formation in the discharge zone, the number of pixels with detectable OH is now computed in the area surrounding the electrode gap. The region of interest (ROI), displayed in Fig. 5.13, extends 2.30

mm in the streamwise direction and 3.07 mm in the spanwise direction, centered on the inter-electrode gap.

Figure. 5.15 shows the temporal evolution of the number of pixels in ROI for the investigated pulse repetition frequency (PRF = 2, 5, 10, 50 kHz), where the symbols, lines represent the experimental, numerical values, respectively. In the 50 kHz case, the size of the OH region builds up rapidly. The number of pixels reaches a maximum at the end of the pulse train (t = 0.18 ms) of 3200 pixels in the experiment and 3800 in the simulation, the largest values of all conditions. It then decreases progressively until it nullifies at t = 0.4 ms. Considering that the flow velocity in the discharge zone is equal to 15 m.s^{-1} and that the ROI has 2.3 mm streamwise length, It takes approximately 0.15 ms for the bulk flow to completely leave the ROI. However, since a part of the kernel is convected upstream by the hydrodynamic effects, the residence time of the gases is increased. The 2 kHz case shows that the decrease of pixels number, that reaches a value of 2200 pixels after a pulse, takes approximately 0.2 ms which matches the time it took the OH region to decay in the 50 kHz case. As the inter-pulse time is equal to 0.5 ms in the 2 kHz case, no OH remains in the ROI when the following pulse is applied and in the absence of pulses effects accumulation, corresponding to a decoupled pulses interaction regime, the OH region vanishes preventing the flame ignition. For 5 kHz PRF, with an inter-pulse time of 0.2 ms, only a few pixels with detectable OH remain between pulses resulting in a partial accumulation of the pulses effects, partially coupled interaction regime, which is however not sufficient to ignite the mixture. Finally, for both 10 kHz and 50 kHz cases, the inter-pulse times are 0.1 ms and 0.02 ms, respectively. A residual amount of OH is still present when the following pulse is applied, creating an overlapping region of OH that lead eventually to flame ignition. The interaction in this case and for the 50 kHz case corresponds to the fully coupled regime.

This analysis confirms that the competition between the gas residence time in the discharge zone and the time between two pulses is what drives the pulse interaction regime and thus the ignition efficiency of NRP discharge. In the case where the flow velocity is high and therefore the gas residence time is low, the results show that increasing the pulse repetition frequency (PRF) to decrease the inter-pulse time is indeed an efficient solution to have a coupled pulse interaction regime and ensure a high ignition probability.

5.5 Conclusion

The dynamics of flames ignition by a series of NRP discharge pulses has been investigated in this chapter. 3-D Large Eddy Simulations (LES) of a flowing methane-air mixture ignition by NRP discharges have been performed. The

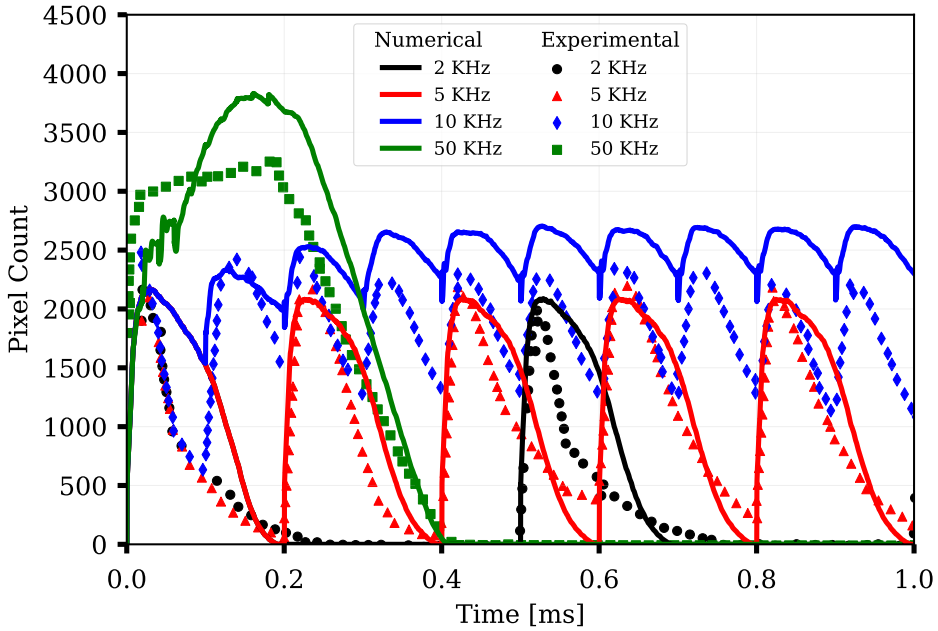

Figure 5.15: *Temporal evolution of the number of pixels in region of interest with detectable OH for various pulse repetition frequency (PRF) conditions. Simulations results (colored lines) are compared with the experimental measurements (colored symbols) from (Lefkowitz et al. (2020))*

experimental investigation conducted by Lefkowitz and Ombrello (2017) on this configuration, the flow tunnel configuration, has shown that depending on the flow and discharge parameters, three pulses interaction regimes can be obtained. A fully coupled regime in which the pulses are deposited on top of each other, creating a large ignition kernel that has a high probability of developing into a self-propagating flame. A partially coupled regime in which the hot reactive kernel created by each pulse partially merge, resulting on elongated shape kernel that has a low probability of developing into a self-sustaining flame. A decoupled regime in which the generated kernel are spaced out and independent from each other. The overall ignition probability in this case is a linear function of the probability that a single pulse will induce a successful ignition, which is extremely low and often equal to zero.

The analysis of the experimental results carried out in this chapter has shown that the pulses interaction regimes depend on two parameters. The residence time of the gases in the discharge zone and the inter-pulse time, the period between two consecutive pulses, given by the inverse of the pulse repetition frequency (PRF). When the residence time of the gases in the discharge zone is greater than the time between two pulses, the pulses are deposited on top of each other leading to the formation of a large ignition kernel which corre-

sponds to the fully coupled regime. When the residence time of the gases in the discharge zone and the time between two pulses are almost equal, the pulses partially interact creating an elongated thin ignition kernel. It corresponds to the partially coupled regime. Finally, when the residence time of the gases in the discharge zone is shorter than the time between two pulses, no interaction between the pulses takes place. A trail of small hot kernels separated from each other is created which corresponds to the decoupled regime. Therefore, in order to operate in a fully coupled pulses interaction regime and ensure a high ignition probability, the inter-pulse time must be smaller than the residence time of the gases in the discharge zone.

While it is easy to compute and adapt the inter-pulse time by varying the pulse repetition frequency (PRF), the control and the estimation of the residence time are not straight forward. In addition to the influence of the flow velocity, the simulation performed by Castela et al. (2017) has shown that the residence time in the discharge zone is strongly impacted by the hydrodynamic effects induced by the discharges. To capture the plasma-flow-flame complex interactions and accurately predict the ignition by NRP discharges, 3D unsteady simulations of plasma-assisted ignition are required.

3-D Large Eddy Simulations of the flow tunnel ignition by NRP discharges have been performed using the phenomenological plasma model developed by Castela et al. (2016). The effect of flow velocity in the range of U = 2.5 - 10 $m.s^{-1}$ and pulse repetition frequency in the range of PRF = 2 - 50 kHz have been investigated. In agreement with the experimental observations, three pulses interaction regimes have been obtained, fully coupled, partially coupled and decoupled regime depending on the imposed flow velocity or pulse repetition frequency. The simulations have confirmed that these regimes are the result of a competition between the residence time of the gases in the discharge zone and the inter-pulse time. More precisely, the results have shown that the ignition success or failure is the results of a competition between the heat and radicals accumulation in the discharge zone induced by pulses interaction and heat and radicals loss due to transport, discharges hydrodynamic effect, thermal dissipation and chemical recombination.

In conclusion, a necessary condition to ensure an efficient ignition is to apply the NRP discharges in low-velocity region at high pulse repetition frequency. This methodology will be used in the next chapter for the simulation of turbulent flame ignition by NRP discharges in a burner representative of the practical combustion chambers.

Chapter 6

Numerical simulations of turbulent flame ignition by NRP discharges

In the present chapter, the phenomenological NRP discharges model is used to simulate the ignition sequence of the Mini-PAC configuration, a bluff-body turbulent premix burner representative of industrial combustors. Two numerical computations are performed. In the first simulation, only the thermal effects of the discharge (ultra-fast heating and slow heating due to vibrational energy relaxation) are taken into account. In the second one, both the thermal and chemical effects (O2 dissociation into O) are considered. The results of the simulations are then analyzed and compared to identify the impact of each effect on the mechanism of turbulent flames ignition.

Contents

6.1 Introduction

The numerical methodology that consists of coupling the phenomenological NRP discharge model developed by Castela et al. (2016) with the LES combustion equations to perform numerical simulations of plasma assisted combustion, is used here to simulate the ignition sequence of a configuration representative of industrial combustion chamber, the Mini-PAC burner. The objective is to characterize the impact of the thermal and chemical effects of NRP discharges on turbulent flames ignition process under operating conditions close to those encountered in aeronautic engines.

Section. 6.2 of this chapter presents the Mini-PAC experimental configuration. Section. 6.3 describes the numerical methods and the plasma model used for the Mini-PAC ignition LES along with the operating and initial conditions of two performed simulations, the simulation where only the thermal effects of NRP discharges are considered (LES-T) and the simulations where both the thermal and chemical effects are taken into account (LES-TC). The results of the two simulations are presented and analyzed in Section. 6.4. Conclusions are presented in Section. 6.5 .

6.2 The Mini-PAC burner

The Mini-PAC configuration shown in Fig. 6.1(left) is a bluff-body axisymmetric burner specially designed to study the impact of plasma discharges on turbulent flames ignition and stabilization. It consists of an annular ceramic injection tube of 20 cm long, 16 mm internal diameter and a concentric stainless-steel bluff-body of the same length and 10 mm diameter that acts as a flame-holder. The NRP discharges are applied Nanosecond discharge downstream the bluff-body between a horizontal tungsten anode of 1 mm diameter centered 5 mm above the bluff-body that acts as a grounded cathode Fig. 6.1(right). The two electrodes are connected to a Marx type pulse discharge generator that produces high frequency nanosecond pulses.

For the ignition simulations, the burner is fed with a methane-air mixture ($\phi = 0.95$), injected at a constant mass flow rate $\dot{m} = 15\ m^3\ h^{-1}$ which corresponds to a bulk velocity $U_b = 37.5\ \mathrm{m.s}^{-1}$. 10 kV discharges, corresponding to a reduced electric field (E/N) of 100 Td to 300 Td ($1\mathrm{Td} = 10^{-21}\mathrm{V.m}^2$) are applied using the tungsten electrode positioned above the bluff body. The images of the discharge during the pulses show that the discharge has a quasi-cylindrical shape of 5 mm length corresponding to the inter-electrode distance, and a diameter equal to 1.75 mm. Electrical measurements of the voltage and the current showed that each discharge pulse transfers 3.5 mJ to the flow. The deposit lasts 50 ns and is repeated at a frequency of 20 kHz.

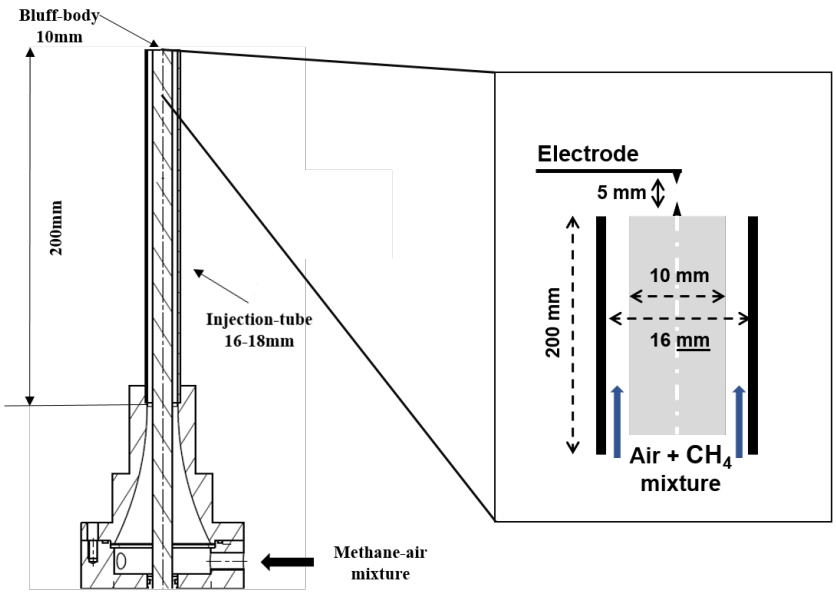

Figure 6.1: *(left) MiniPAC configuration scheme, (right) Bluff-body nozzle and electrodes.*

6.3 Simulations numerical set-up

LES of the MiniPAC burner ignition sequence are performed using the YALES2 unstructured finite-volume low-Mach number solver (Moureau et al. (2011)). The time integration is performed using a fourth-order temporal scheme with a centred fourth order scheme for spatial discretization. The sub-grid Reynolds stresses tensor is closed using the Dynamic Smagorinsky model (Germano et al. (1991)). The COFFEE kinetic scheme involving 14 species and 38 reactions is used for the methane-air mixture chemistry (COFFEE (1984)), species equations are coupled with turbulence using the Thickened Flame model for LES (TFLES) (Colin et al. (2000)) and the Charlette sub-grid scale flame wrinkling model (Charlette et al. (2002)).

The discharges properties have been set to be consistent with experimental measurements for the temperature and the atomic oxygen spatial distribution and the deposited energy. The discharge has a cylindrical shape filtered with the spatial function $F(r) = erfc[(r/a)^b]$ where r is the radial distance from the discharge axis. a and b are geometric parameters, fitted to model the measured discharge radius and to ensure a sufficient numerical resolution of the discharge interface.

The computational domain includes half of the injection tube and covers 35 D_b and 30 D_b in downstream and radial directions, respectively.The mesh consists

of 40 millions of tetrahedral elements. In the plasma discharge zone the cells size equals 0.1 mm while in the flame zone it ranges from 0.1 mm to 0.5 mm. A 2-D view of the mesh in (x,z) plane is illustrated in Fig. 6.2 in the near-electrode region.

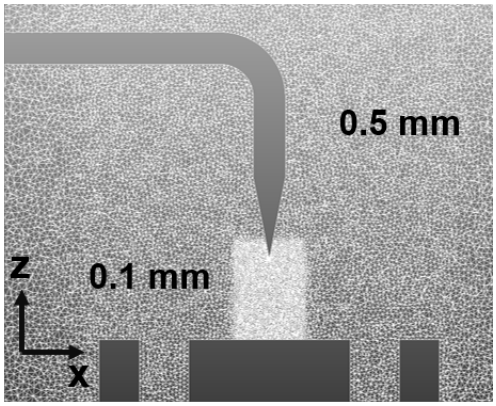

Figure 6.2: *Mini-PAC configuration mesh in the near-electrode region*

Two different simulations, indicated as cases LES-T and LES-TC in Tab. 6.1, are performed to understand the role of species dissociation in the turbulent flame ignition mechanism. In both simulations, 55% of the energy is deposited at the ultra-fast scale ($\alpha = 0.55$) whereas 45% is transferred into the vibrational energy, which relax slowly into gas heating. In LES-T case, only thermal effects are considered in the plasma discharge model ($\eta = 0$). In LES-TC case, in accordance with experimental and numerical observations (Rusterholtz et al. (2013); Popov (2013b)) 35 % of O_2 is dissociated into O atoms during the pulse. For both cases, the same amount of energy of 3.5 mJ per pulse is transferred to the flow.

Case	α	η	Discharge properties
LES-T	0.55	0.0	heating
LES-TC	0.55	0.35	heating and O_2 dissociation

Table 6.1: *Numerical case properties. The same amount of energy per pulse E_p=3.5 mJ is deposited for each case. Discharge frequency f = 20KHz. Pulse duration τ_{pulse} = 50 ns.*

Figure. 6.3 (a) shows the 2-D mean axial velocity on the centerline plane of the Mini-PAC configuration for the non-reacting flow, before the flame ignition attempt. The black line indicates the isocontour of zero axial velocity. The simulation shows that the flow has high axial velocity magnitude $\|\overrightarrow{u_z}\| \approx 50 m.s^{-1}$

in the injection tube which decreases as the flow propagates in the combustion chamber to reach a magnitude of 35 m.s^{-1} to 25 m.s^{-1} except above the bluff-body where a recirculation zone is formed as indicated by the zero axial velocity isocontour in which the velocity is much lower $\|\overrightarrow{u_z}\| < 5\ m.s^{-1}$.

A 2-D instantaneous CH_4 (fuel) mass fraction on the centerline plane of the Mini-PAC configuration for the non-reacting flow is represented in Fig. 6.3 (b). It shows that the CH_4 mass fraction in the injected methane-air mixture is equal to $Y_{CH_4} = 5.2\ 10^{-2}$ which corresponds to the expected value for an equivalence ratio of $\phi = 0.95$. The mass fraction value remains the same $Y_{CH_4} + 5.2\ 10^{-2}$ in the vicinity of the injection tube outlet and in the recirculation zone above the bluff-body then decreases gradually as the flow turbulence mixes it with the ambient air.

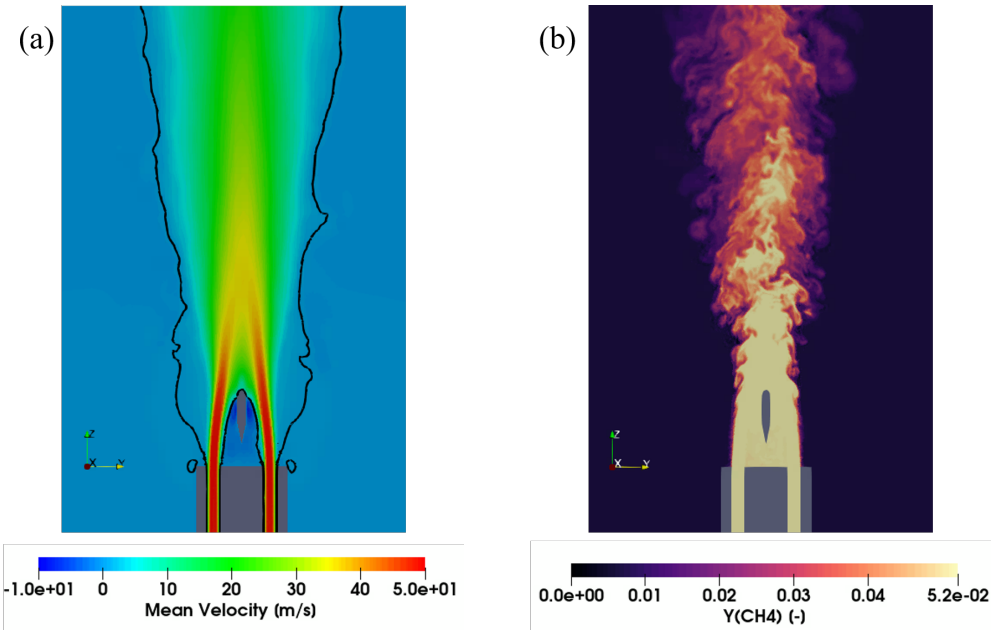

Figure 6.3: *Non-reacting mean LES of the axial velocity on the centerline plane of the Mini-PAC configuration (a), the black line indicates the isocontour of zero axial velocity. (b) Instantaneous fuel (CH_4) mass fraction field of the non-reacting flow.*

In view of these observations, the electrodes are located in the low velocity zone behind the bluff-body to insure an efficient interaction between the consecutive NRP discharges pulses as shown in the study of the flow tunnel ignition (Chapter. 5, Section. 5.4.2).

6.4 LES of Mini-PAC ignition by NRP discharges

For both cases, the NRP discharges are applied at time $t = 0$ s with a pulse frequency of 20 kHz. Figure. 6.4 shows a series of 2-D instantaneous snapshots in the plane (y,z) of the temperature field for case LES-T, where only thermal effects of the plasma are considered. The temperature in the discharge zone increases after each pulse until it reaches a steady state after approximately 15 pulses. The heat brought by the discharge diffuses in the recirculation zone located downstream the bluff-body but the mixture does not ignite. Although the pulse generator is always turned on, no flame kernel is formed.

Figure. 6.5 shows instantaneous fields of temperature for LES-TC solution, where both thermal and chemical properties of the plasma are considered. A reactive kernel is now clearly identified after only 5 pulses at $t = 200\ \mu s$, leading to local ignition. Even if the pulse generator is turned off after the 10^{th} discharges, the kernel still growths and transits to a turbulent V shaped flame, which reach a steady-state regime at $t = 7.5$ ms.

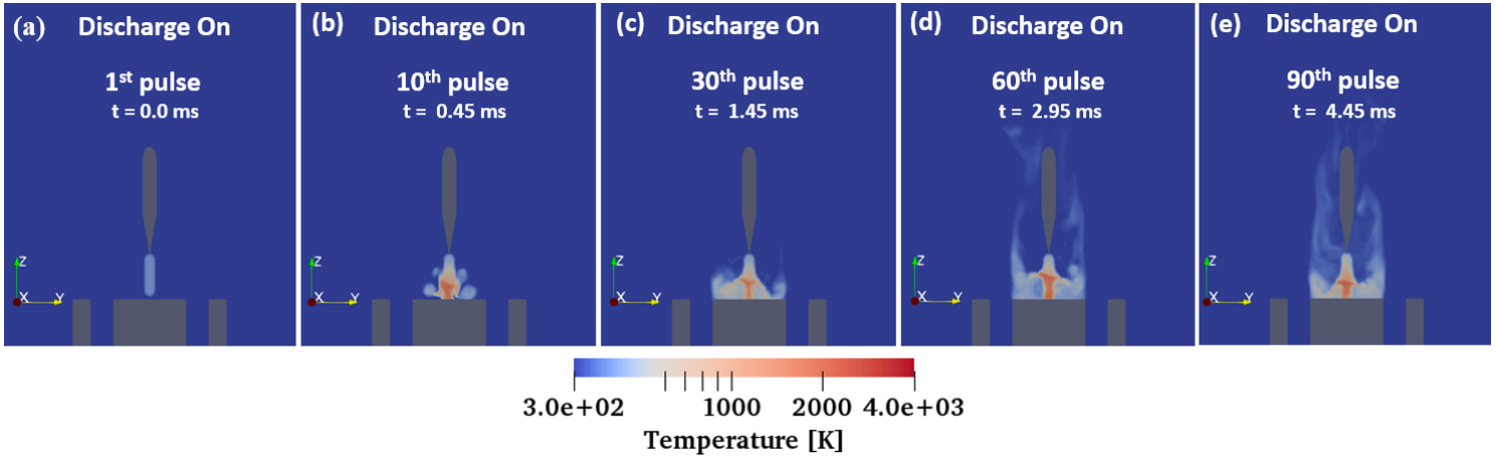

Figure 6.4: *Simulation of the ignition attempt of the MiniPAC configuration by a series of NRP discharges, case LES-T, Only the thermal effects are taken in account ($\eta = 0$). Instantaneous 2-D temperature fields are shown at the:* 1^{st} *(a),* 10^{th} *(b),* 30^{th} *(c),* 60^{th} *(d),* 90^{th} *(e) plasma pulses. Ignition never occur even after* 90 *pulses.*

Figure 6.5: *Simulation of the ignition attempt of the MiniPAC configuration by a series of NRP discharges, case LES-TC, both the thermal and the chemical effects are taken in account ($\eta = 0.35$). Instantaneous 2-D temperature fields are shown at the: 1^{st} (a), 5^{th} (b), 10^{th} (c) plasma pulse and at $t = 5.8$ ms (d) and $t = 7.5$ ms when the pulses generator is off. The flame ignites at the 5^{th} pulse (b) and transits to form a V flame in (d) and (e).*

These observations are confirmed by the temporal evolution of computational domain maximum temperature, plotted in Fig. 6.6. When only thermal effects are considered, the temperature never reaches the burnt gases temperature level, despite the unceasing plasma pulsations. Indeed, despite two peaks at 2000 K observed at $t = 0.75$ ms and $t = 2.75$ ms, the maximal temperature fluctuates around 1200 K. At the opposite, when both chemical and thermal plasma effects are considered, ignition is clearly identified after the 5^{th} pulse. A peak above 4000 K is then reached at the center of the discharge. The combustion is even sustained when the NRP discharges are turned off after the 10^{th} pulse. Figure. 6.7 shows the temporal evolution of the maximal O concentration computed in the LES. The LES-TC case exhibits a significant production of atomic oxygen O by the discharge whose concentrations reach 1.2 $mol.m^{-3}$ just before ignition. When the discharge is turned off, atomic oxygen O concentration decreases to equilibrium conditions. Situation is very different in LES-T case, where the oxygen concentration remains equal to zero and no ignition is observed.

These results are qualitatively consistent with experimental campaigns conducted at EM2C laboratory, where flame ignition is always successful after a series of NRP discharges. Unfortunately, the exact number of discharges required to ignite the flame is not known, preventing quantitative validation of the simulations against experimental measurements.

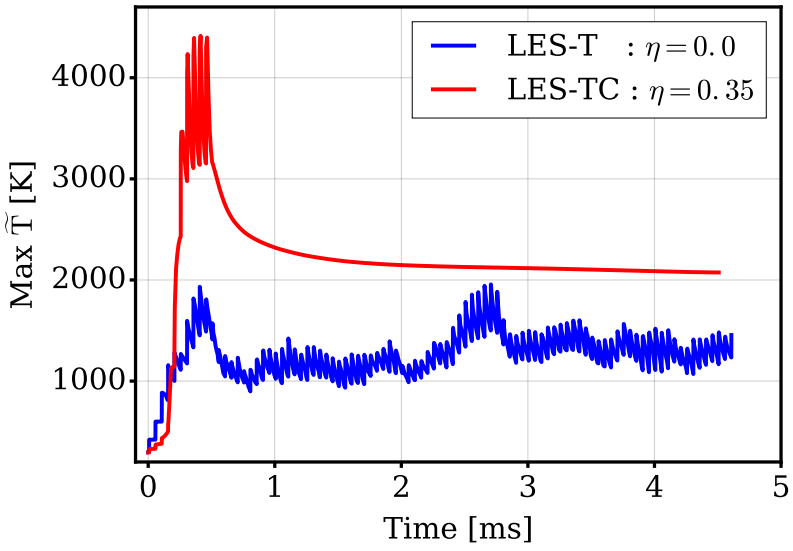

Figure 6.6: *Temporal evolution of the maximum value of gas temperature in the MiniPAC simulations. The mixture ignites after 5 pulses for case LES-TC (red), whereas ignition never occurs for case LES-T (blue).*

To explain the difference between the two cases, an analysis of pulses-flow in-

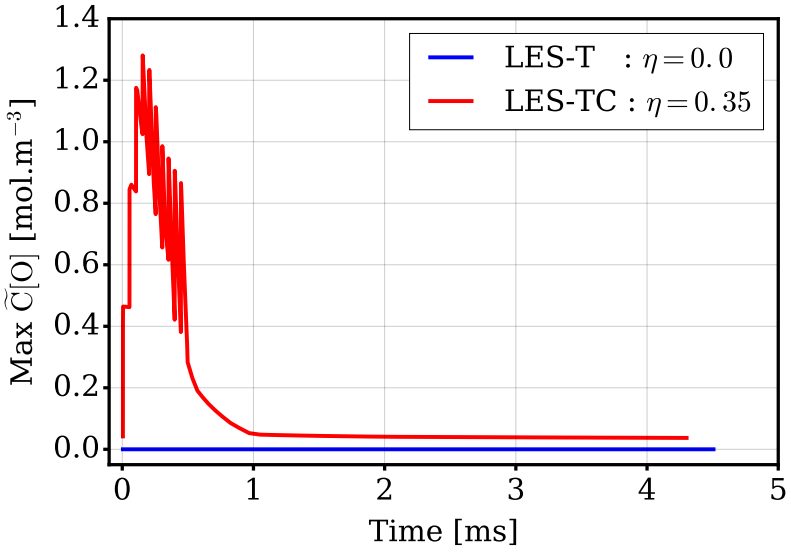

Figure 6.7: *Temporal evolution of the maximum atomic oxygen O concentration in the MiniPAC simulations, LES-TC (red), LES-T (blue)*

.

teraction in the discharge zone is performed in the LES-T case to identify the reasons that prevent ignition of the mixture. The mechanism by which atomic O counteracts these effects and leads to the ignition of the flame in the LES-TC case is then investigated.

Figure. 6.8 shows the instantaneous 2-D temperature field on the centerline plane of the Mini-PAC burner before, during and after the 25^{th} pulse when the maximum temperature has reached a steady state as shown in Fig. 6.6. Before the pulse, Fig. 6.8(a) shows that the heat deposited by the previous pulses has been strongly diffused all over the recirculation zone, maintaining a low temperature in the discharge zone whose maximum does not exceed 1000 K. The deposition of the 25^{th} pulse, Fig. 6.8(b), generates a hot kernel of quasi-cylindrical shape, part of which overlaps with the heat of the previous pulses, increasing the maximum temperature to 1200 K. Figure. 6.8(c) and (d) show then the evolution of the kernel from its initial quasi-cylindrical shape to a toroidal shape induced by the hydrodynamic discharges effects described in Section. 4.4, which convects the heat outside the discharge zone, bringing the maximum temperature down to 1000 K. This behavior is repeated at each pulse as shown in Fig. 6.6. The total heat energy of the mixture is increased with each energy deposition without however an increase in the maximum temperature which continues to vary between 1000 K and 1300 K. The analysis of the chemical reactions shows that in a temperature range of [1000 K, 1300 K], the reaction of CH_4 oxidation by O_2, $O_2 + CH_4 = HO_2 + CH_3$, that initiates the combustion, evolves very slowly as its reaction rate, which follows the Arrhe-

nius formula $K = A\exp(-\frac{T_a}{T_g})$, has a high activation temperature $T_a \approx 6000$ K compared to the gas temperature $T_g \approx 1200$ K and small Arrhenius constant A = 9.10^{13} m.mol^{-1}.s^{-1}.

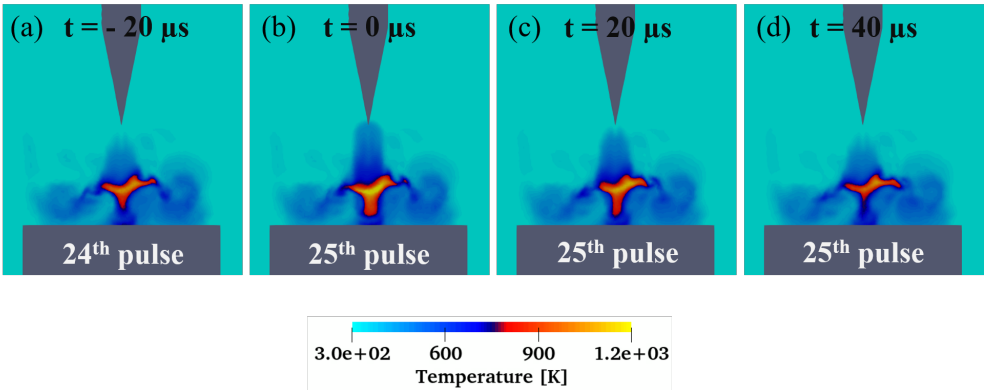

Figure 6.8: *Instantaneous 2-D temperature field on the centerline plane of the Mini-PAC burner before, during (t = 0) and after the 25th pulse in the LES-T case. The kernel evolves from its initial cylindrical shape to a toroidal shape after the pulse, images (c) and (d) convecting the heat away from the discharge zone.*

When atomic O is produced by the discharge, the combustion is initiated by an other reaction, the CH_4 oxidation by atomic O chemical reaction: $CH4 + O = OH + CH3$. The constant rate of this reaction has a smaller activation temperature $T_a \approx 1500$ K and a higher Arrhenius constant A = 4.10^{14} m.mol^{-1}.s^{-1} which under the conditions created by the NRP discharge, high atomic O concentration, starts and evolves very quickly even at low temperature.

6.5 Conclusion

In this chapter, the phenomenological NRP discharges model (Castela et al. (2016)) implemented in YALES2 CFD code has been used to simulate the ignition sequence of the Mini-PAC configuration, a bluff-body turbulent premix burner representative of industrial combustion systems.

To understand the role of the heat and species dissociation induced by the discharges in the turbulent flame ignition mechanism, two numerical computations have been performed. First, only the thermal effects of the discharge (ultra-fast heating and slow heating due to vibrational energy relaxation) were taken into account. Then both the thermal and chemical effects (mainly O2 dissociation into O) were considered.

The results show that in the first simulation the ignition never occur, whereas in

the second simulation flame ignition occurs after only 5 pulses. LES data post-processing shows that the fresh gases entrainment in the discharge zone induced by the discharge hydrodynamic effects plays a crucial role in the ignition process as it maintains a low temperature in the inter-electrode region preventing the ignition of the flame when only the thermal effects are considered. When the chemical effects are taking into account, the significant amount of atomic O produced by the consecutive pulses enhances the fuel oxidation reactions, allowing the initiation of the combustion even at low temperature.

Chapter 7

Scenario of plasma-assisted ignition

In this chapter, a low-order plasma-assisted ignition model is derived. The numerical simulations of flames ignition by NRP discharges have shown that ignition success or failure results from a competition between the residence time of the reacting gases in the discharge channel and the combustion chemistry time scale. This phenomena is here modeled by a perfectly stirred reactor (PSR) whose volume matches the discharge channel diameter. A flow of reactive gases passing through the PSR is used to reproduce the gases circulation in the discharge zone. NRP discharges are applied inside the reactor to initiate the combustion of the injected mixture. This model is used to build-up plasma-assisted ignition diagrams which indicate the number of pulses, the ignition delay and the total deposited energy required to ignite the mixture inside the PSR reactor as a function of gases residence time and the discharge parameters. The results of the parametric studies are analyzed to define the optimal strategy to adopt in order to ensure an efficient flames ignition by NRP discharge.

Contents

7.1 Introduction

Analysis of the Mini-PAC simulations results conducted in Chapter. 6 suggests that ignition success or failure results from a competition between the time scales of flow mixing and combustion chemistry. The atomic oxygen O produced by NRP discharges accelerates the fuel consumption particularly when a large amount is formed in the discharge zone. One way to achieve that is to accumulate the effects of the pulses by imposing a high pulse repetition frequency (PRF) as indicated by experimental and numerical studies of the flow-tunnel configuration in Chapter. 5. Another solution will be to increase the energy of the pulses since the amount of O_2 dissociated into atomic O is proportional to the deposited energy. To identify the most efficient solution in terms of ignition delay and energy consumption, a low-order model based on a perfectly stirred reactor (PSR) is developed to perform parametric studies of flames ignition by NRP discharges at low CPU cost.

The chapter is organized as follows. The flames ignition by NRP discharges low-order PSR model is first presented in Section. 7.2. The model is then used in Section. 7.3 to study the effect of atomic oxygen by considering, as done in the Mini-PAC simulations, two cases. In the first one, only thermal effects of the discharges are taken into account and in the other one, both thermal and chemical effects are considered. The number of pulses, the ignition delay and the total deposited energy required to ignite the reactor are computed in the two cases for a varying gases residence time and a constant pulse energy and pulse repetition frequency (PRF). The results are compared to the Mini-PAC ignition LES to validate the low-order approach. In section. 7.4, the effects of the pulse energy are investigated. Computation are performed considering both thermal and chemical effects of the discharges for varying gases residence time and pulse energy and a constant pulse repetition frequency (PRF). Next, the effects of pulse repetition frequency (PRF) are examined in Sections. 7.5. Similar computations are preformed, fixing in this case the pulse energy and varying the pulse repetition frequency. The results of the varying pulse energy and the varying pulse frequency studies are compared to identify which solution is the most efficient. The conclusions of the different investigations are summarized in Section. 7.6.

7.2 Perfectly Stirred Reactor (PSR) model

The low-order flames ignition by NRP discharges model is based on a Perfectly stirred reactor (PSR) schematized in Fig. 7.1, whose volume matches the discharge channel of diameter d, filled with fuel-oxidizer mixture in which NRP discharges are applied using Castela et al. (2016) phenomenological model. The gases convection by the flow and by the hydrodynamic effects of the NRP discharges (Section. 4.4) is reproduced by an imposed gases flow passing through

the PSR at velocity V. The residence time of the mixture in the PSR is therefore given by $\tau = d/V$.

The PSR balance equations reads:

$$\frac{dh}{dt} = \frac{1}{\tau}\left(\sum_{k=1}^{K} Y_{k0}h_{k0} - \sum_{k=1}^{K} Y_k h_k\right) - \frac{Q_h}{\rho V} + \dot{E}^p_{chem} + \dot{E}^p_{heat} + \dot{R}^p_{VT} \tag{7.1}$$

$$\frac{dY_k}{dt} = \frac{1}{\tau}\left(Y_{k0} - Y_k\right) + \frac{W_k\dot{\omega}^c_k}{\rho} + \frac{W_k\dot{\omega}^p_k}{\rho} \tag{7.2}$$

$$\frac{de_{vib}}{dt} = \frac{1}{\tau}\left(e_{vib0} - e_{vib}\right) + \dot{E}^p_{vib} - \dot{R}^p_{VT} \tag{7.3}$$

where 0 subscript denotes fresh gases properties flowing in the PSR. The rate of deposited thermal and chemical energies $\dot{E}^p_{chem}$, $\dot{E}^p_{heat}$ and $\dot{E}^p_{vib}$ are closed according to Eq. (2.46), Eq. (2.48) and Eq. (2.49). The relaxation rate of vibrational energy $\dot{R}^p_{VT}$ is modeled by Eq. (2.31) and the plasma chemistry sources terms $\dot{\omega}^p_k$ is closed by Eq. (2.43), Eq. (2.44) and Eq. (2.45).

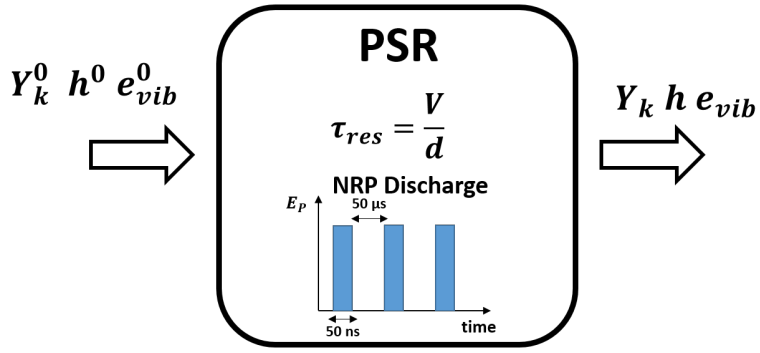

Figure 7.1: *Perfectly Stirred Reactor (PSR) model for plasma-assisted ignition.*

For all the studied cases, the PSR is filled initially and fed all along the simulation with a methane-air mixture at an equivalence ratio ϕ =0.95, initial temperature T_i = 300 K and at atmospheric pressure which corresponds to the operating conditions encountered in the Mini-PAC configuration.

7.3 Effect of O production

To study the effect of atomic oxygen two cases are considered, PSR-T case which refers to simulations conducted by considering only thermal effects (η = 0.0)

and PSR-TC case which refers to the computations that account for chemical plasma effects ($\eta = 0.35$). The other parameters of the discharge are the same for both cases with a pulse energy equal to 3.5 mJ and a pulse repetition frequency equal to 20 kHz.

Temperature temporal evolution in PSR-T and PSR-TC cases for gases residence time $\tau = 3.10^{-4}$ s is shown as an example in Fig.7.2. PSR-T simulation requires 12 pulses to ignite the mixture whereas only 6 pulses are needed by PSR-TC. For the same amount of deposited energy, the chemical effect of O radical is more important than the temperature on the ignition process. As discuss previously, due to its high reactivity, the atomic oxygen O enhances the hydrocarbon oxidation reactions even at low gas temperatures, which reduces the combustion chemistry time scale and therefore the ignition delays.

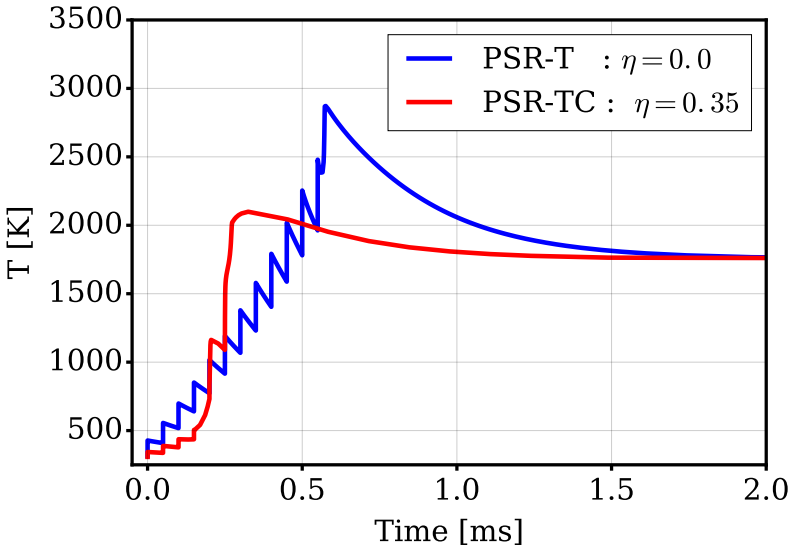

Figure 7.2: *temperature temporal evolution for both PSR-T (blue) and PSR-TC (red) simulations for $\tau = 0.3$ ms. For PSR-TC case, ignition occurs after 6 pulses, whereas for PSR-T case, ignition occurs after 12 pulses.*

PSR results are used to established a plasma-assisted ignition diagram. For each PSR simulation, the pulse generator is maintained until 80% of the fuel mass fraction is consumed. Following this criteria, the minimal number of pulses, the ignition delay and the total amount of energy required to ignite the mixture inside the reactor are plotted in term of the recirculation zone residence time in Fig. 7.3, Fig. 7.4 and Fig. 7.5 respectively. Blue and red symbols correspond to PSR-T and PSR-TC solutions, respectively. For a given residence time, the production of atomic oxygen considerably reduces the number of pulses needed for ignition decreasing therefore the ignition delay and the minimum ignition energy. The difference between PSR-T and PSR-TC is even more pronounced

when the residence times decreases. The critical residence time ($\tau_{critical}$) below which ignition never occurs equals 0.15 ms for pure thermal discharges, whereas it decreases to 0.08 ms when the production of atomic O is accounted for.

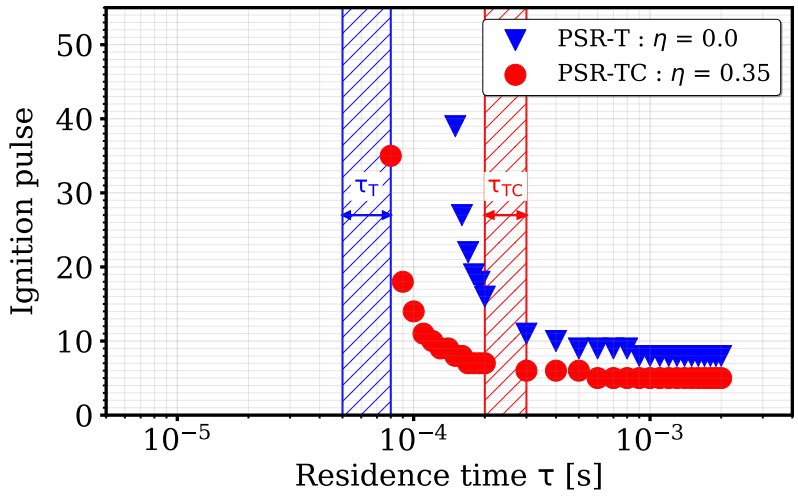

Figure 7.3: *plasma-assisted ignition diagram. The number of pulses required to ignite the methane-air mixture in terms of the residence time. Blue symbols correspond to the PSR-T case. Red symbols correspond to the PSR-TC case. Residence times τ_T for the LES-T case and τ_{TC} for the LES-TC case are indicated by the red and the blue hatched area, respectively.*

To validate the PRS modeling, a comparison with the Mini-PAC ignition simulations have been performed. Practical residence times have been estimated from the maximal velocity reached within the recirculation vortices induced by the discharge in the 3-D simulations. By this way, two residence times 0.05 ms $< \tau_T <$ 0.08 ms and 0.2 ms $< \tau_{TC} <$ 0.3 ms are estimated from LES-T and LES-TC solutions, respectively. Note that a higher amount of heat is deposited in LES-T, the gas expansion is more important and the velocity is larger than in LES-TC. It explains why $\tau_T < \tau_{TC}$. Residence times τ_T and τ_{TC} encountered in the LES are indicated in Fig. 7.3 by red and blue area. According to the PSR-TC diagram, the flame should ignite after 6-7 pulses. This is consistent with LES-TC simulations where ignition occurs between 5 and 10 pulses. The blue area is however located outside the ignition conditions whatever the number of discharges, which is consistent with the ignition failure observation in LES-T.

7.4 Effect of pulse energy

The effect of pulses energy on the ignition process is investigated in this section. The PSR is filled with the same methane-air mixture as previously ($\phi = 0.95$,

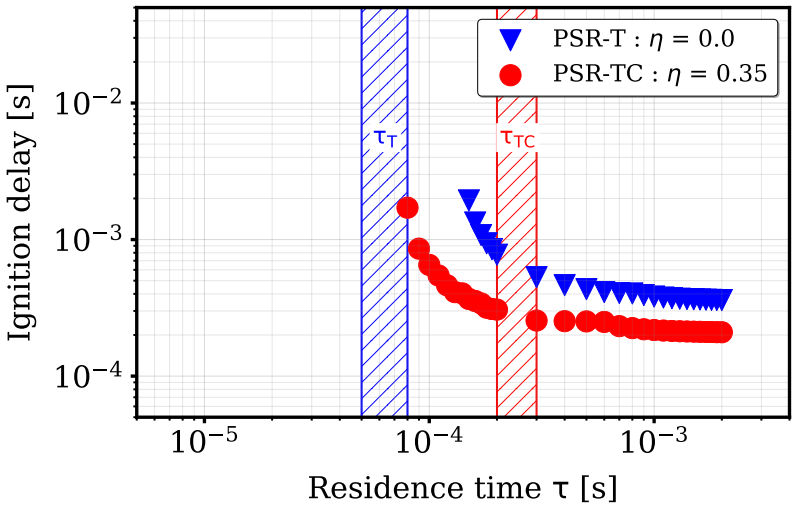

Figure 7.4: *plasma-assisted ignition diagram. The ignition delay, time required to ignite the methane-air mixture, in terms of the residence time. Blue symbols correspond to the PSR-T case. Red symbols correspond to the PSR-TC case. Residence times τ_T for the LES-T case and τ_{TC} for the LES-TC case are indicated by the red and the blue hatched area, respectively.*

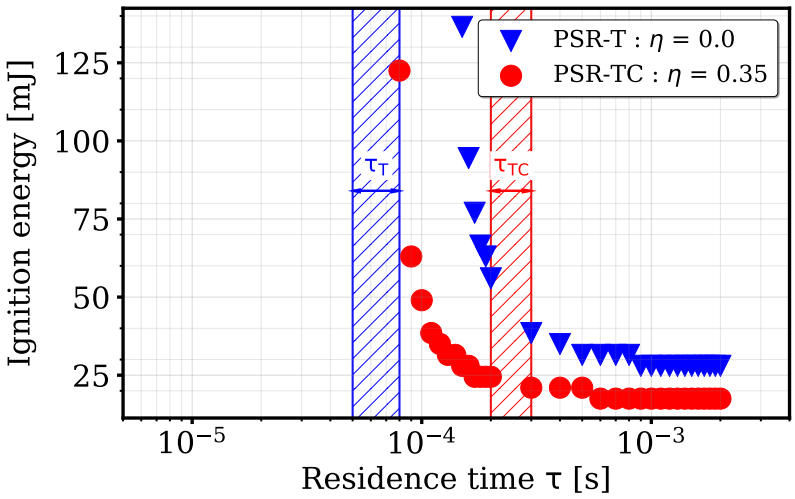

Figure 7.5: *plasma-assisted ignition diagram. The minimum energy required to ignite the methane-air mixture in terms of the residence time. Blue symbols correspond to the PSR-T case. Red symbols correspond to the PSR-TC case. Residence times τ_T for the LES-T case and τ_{TC} for the LES-TC case are indicated by the red and the blue hatched area, respectively.*

T_0 = 300 K, P = 1 atm). Only the PSR-TC case that takes into account the dissociation of O_2 into O is considered (η = 0.35). The pulse repetition frequency (PRF) is constant equal to 20 kHz. The pulses energy values considered

for the study are the following :

1. E_{pulse} = 0.5 mJ.
2. E_{pulse} = 1.0 mJ.
3. E_{pulse} = 2.0 mJ.
4. E_{pulse} = 3.0 mJ.
5. E_{pulse} = 3.5 mJ (Mini-PAC case).
6. E_{pulse} = 4.0 mJ.
7. E_{pulse} = 5.0 mJ.

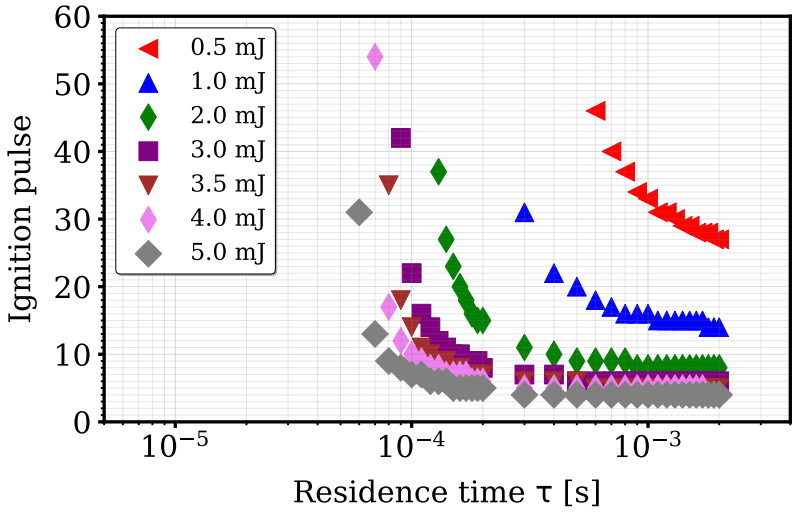

Figure 7.6: *plasma-assisted ignition diagram. The number of pulses required to ignite the methane-air mixture in terms of the residence time for various pulse energy E_{pulse}. The methane-air mixture equivalence ratio and pulse repetition frequency are constant equal to $\phi = 0.95$ and PRF = 20 kHz, respectively.*

Figure. 7.6, Fig. 7.7 and Fig. 7.8 plot the number of pulses, the ignition delay and the total deposited energy required to ignite the reactor as function of the gases residence time for the different pulse energy values. For a fixed residence time, the results show that increasing the pulse energy reduces the number of pulses required to ignite, resulting in a reduction of the ignition delay. In terms of energy, this operation leads to a higher consumption for high residence times $\tau > 5 \cdot 10^{-4}$ while for low residence times $\tau < 5 \cdot 10^{-4}$, the increase of the pulse energy allows on the contrary to reduce the total energy cost in addition to reducing the ignition delay.

Increasing the pulses energy also decreases the ignition delay. Figure. 7.9 plots the critical residence time ($\tau_{critical}$) below which ignition never occurs. The results shows that the critical residence time significantly decrease when the energy per pulse increases. For instance multiplying the energy by 10, from

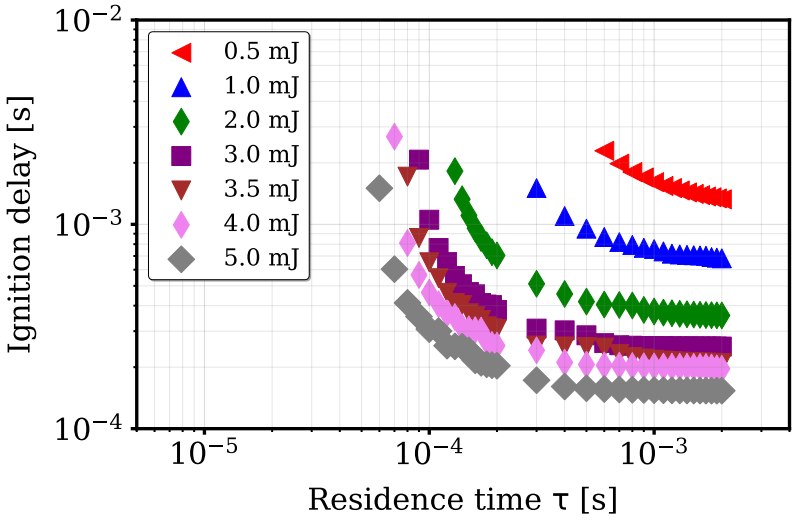

Figure 7.7: *plasma-assisted ignition diagram. The ignition delay, time required to ignite the methane-air mixture, in terms of the residence time for various pulse energy E_{pulse}. The methane-air mixture equivalence ratio and pulse repetition frequency are constant equal to $\phi = 0.95$ and PRF = 20 kHz, respectively.*

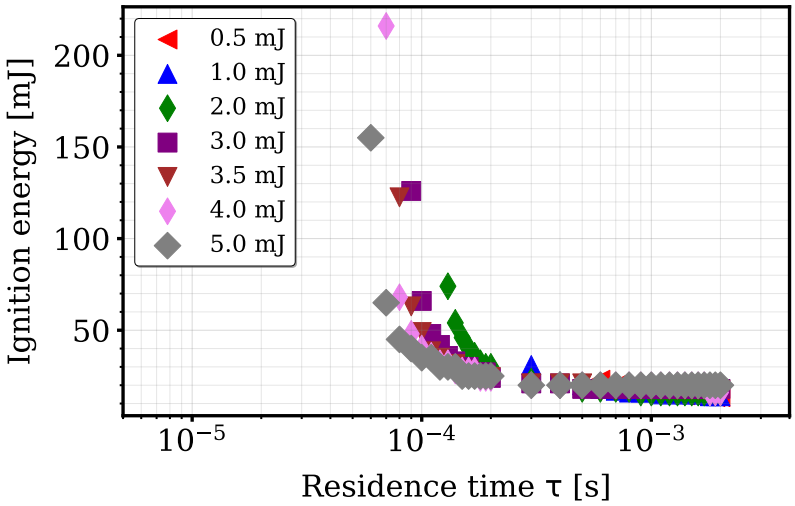

Figure 7.8: *plasma-assisted ignition diagram. The minimum energy required to ignite the methane-air mixture in terms of the residence time for various pulse energy E_{pulse}. The methane-air mixture equivalence ratio and pulse repetition frequency are constant equal to $\phi = 0.95$ and PRF = 20 kHz, respectively.*

E_{pulse} 0.5 to 5 mJ, divides the critical residence time by 10, from $\tau_{critical} = 6.0 \cdot 10^{-4}$ to $6.0 \cdot 10^{-5}$ s. However, this is accompanied by a significant increase of energy consumption.

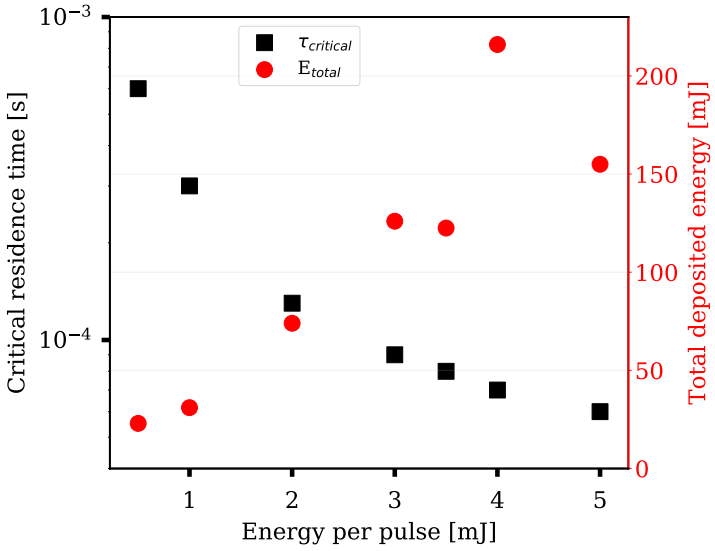

Figure 7.9: *Critical residence time $\tau_{critical}$ (black square) and total deposited energy at this residence time E_{total} (red circle) for different values of pulse energy E_{pulse} with a constant pulse repetition frequency PRF = 20 kHz.*

7.5 Effect of pulse repetition frequency

Another solution to improve the efficiency of flames ignition by NRP discharges is to increase the pulse repetition frequency (PRF). As shown in the flow tunnel ignition study, at high pulse repetition frequency a fully coupled pulses interaction regime is obtained. With the accumulation of pulses effect in the discharge zone a a voluminous hot reactive kernel is formed which leads in most cases to a successful flame ignition. To investigate the impact on the ignition delay, the domain of ignition and the energy efficiency of this solution a parametric study using the PSR low-order model is conducted here.

As done in the previous PSR computations, the reactor is filled with a methane-air mixture ($\phi = 0.95$, $T_0 = 300$ K, P = 1 atm). Only the PSR-TC case that takes into account the dissociation of O_2 into O is considered ($\eta = 0.35$). The pulse energy in this case is constant $E_{pulse} = 3.5$ mJ and the pulse repetition frequency (PRF) is changed. PRF values are the following :

1. PRF = 2 kHz.
2. PRF = 5 kHz.
3. PRF = 10 kHz.
4. PRF = 20 kHz, (Mini-PAC case).
5. PRF = 50 kHz.
6. PRF = 100 kHz.

7. PRF = 200 kHz.

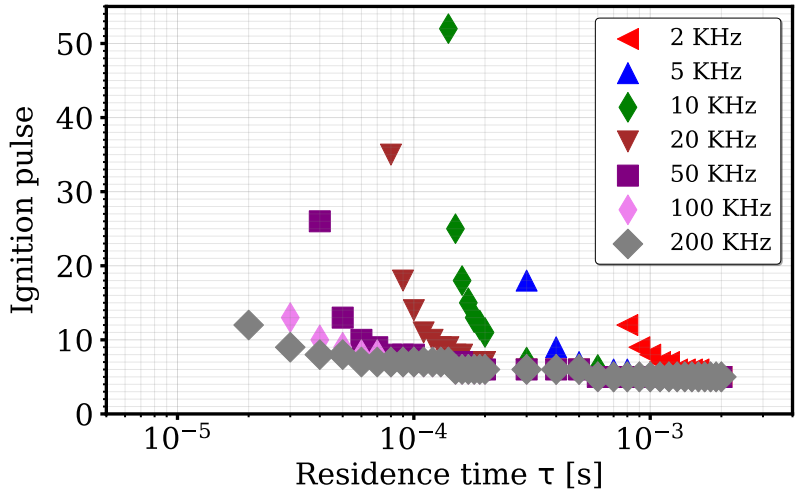

Figure 7.10: *plasma-assisted ignition diagram. The number of pulses required to ignite the methane-air mixture in terms of the residence time for various pulse repetition frequency PRF. The methane-air mixture equivalence ratio and pulse energy are constant equal to $\phi = 0.95$ and $E_{pulse} = 3.5$ mJ, respectively.*

The number of pulses, the ignition delay and the total deposited energy required to ignite the methane-air mixture inside the reactor as function of the gases residence time for the different pulse repetition frequencies are plotted in Fig. 7.10, Fig .7.11 and Fig .7.12 respectively. As expected, for a given residence time increasing the pulse frequency decreases the number of pulses, the ignition delay and the ignition energy. As shown in Fig. 7.13 that plots the critical residence time ($\tau_{critical}$) for the investigated values of pulse repetition frequency (PRF) along with the total required energy at this residence time, the critical residence time $\tau_{critical}$ is significantly reduced when PRF is increased. This method seems to be especially interesting when high frequencies are used because in addition to extending the ignition domain it allows to reduce the energy cost. For instance multiplying the frequency by 2 from PRF = 5 kHz to 10 kHz divided the critical residence time by 2 from $\tau_{critical} = 3.0 \cdot 10^{-4}$ to $\tau_{critical} = 1.4 \cdot 10^{-4}$ s but increases the cost by three times, from $E_{total} = 63$ mJ to $E_{total} = 182$ mJ. While, multiplying the PRF = 5 kHz by 40 to reach a high frequency of 200 kHz not only reduces the critical residence time, from $3.0 \cdot 10^{-4}$ to $2.0 \cdot 10^{-5}$ but also reduces the energy cost, from 63 mJ to 42 mJ.

Results show that increasing the pulse repetition frequency is much more energy-efficient way to reduce the ignition delays and extend the ignition domain compared to the pulse energy increase method. For instance, a series of pulses at $E_{pulse} = 3.5$ mJ and PRF = 50 kHz is able to reduce the critical residence time

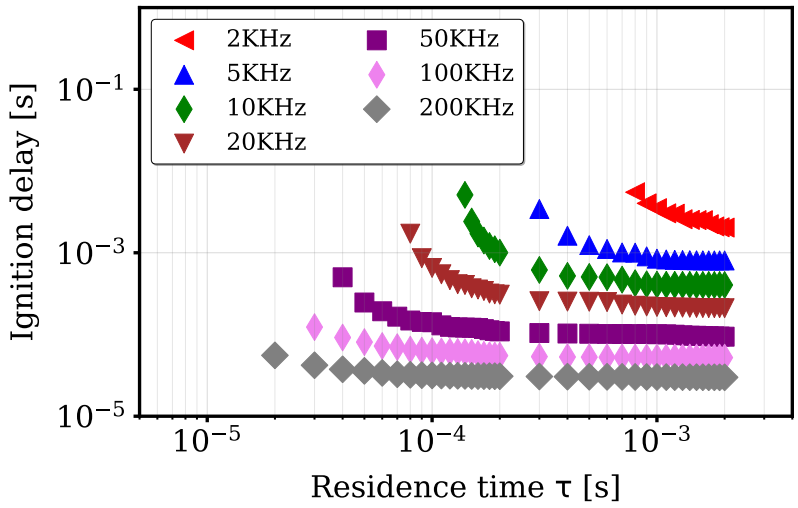

Figure 7.11: *plasma-assisted ignition diagram. The ignition delay, time required to ignite the methane-air mixture, in terms of the residence time for various pulse repetition frequency PRF. The methane-air mixture equivalence ratio and pulse energy are constant equal to $\phi = 0.95$ and $E_{pulse} = 3.5$ mJ, respectively.*

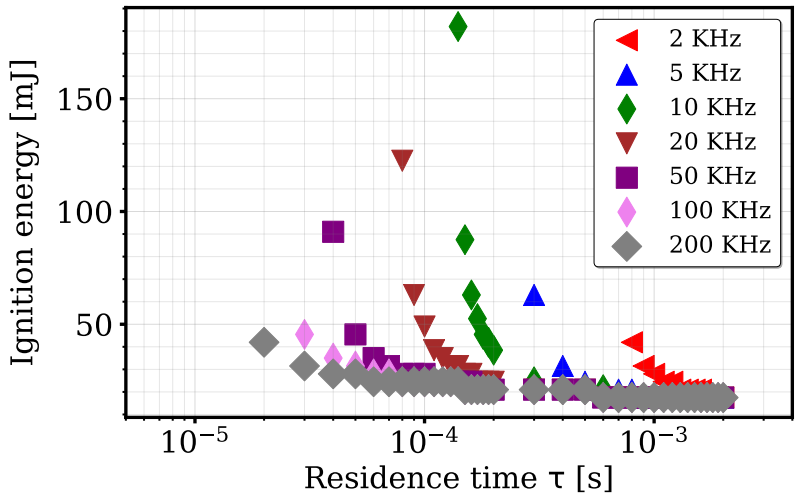

Figure 7.12: *plasma-assisted ignition diagram. The minimum energy required to foignite the methane-air mixture in terms of the residence time for various pulse repetition frequency PRF. The methane-air mixture equivalence ratio and pulse energy are constant equal to $\phi = 0.95$ and $E_{pulse} = 3.5$ mJ, respectively.*

($\tau_{critical}$) to $4.0 \cdot 10^{-5}$ s with a total deposited energy of 91.0 mJ while a series of pulses at $E_{pulse} = 5$ mJ and PRF = 20 kHz only reduces it to $6.0 \cdot 10^{-5}$ s with a higher energy cost of 155 mJ. Higher frequencies do even better, for example at $E_{pulse} = 3.5$ mJ and PRF = 200 kHz the critical residence time is $4.0 \cdot 10^{-5}$ with an ignition obtained for a total deposited energy of 42 mJ.

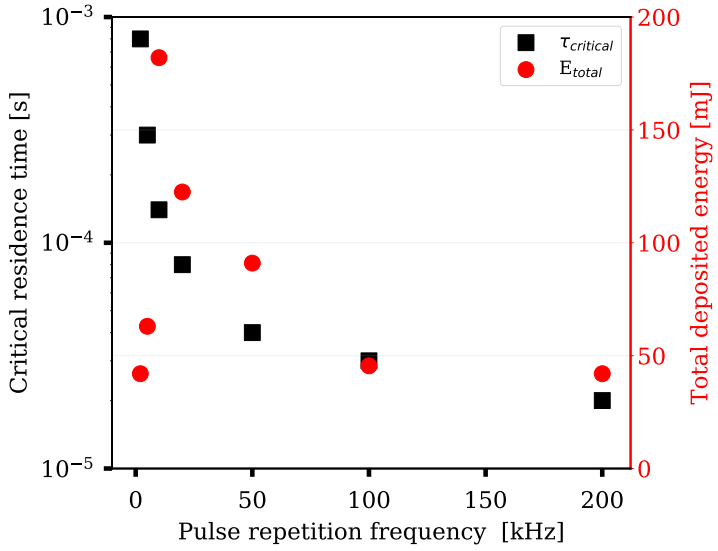

Figure 7.13: *Critical residence time $\tau_{critical}$ (black square) and total deposited energy at this residence time E_{total} (red circle) for different values of pulse repetition frequency (PRF) with a constant pulse energy E_{pulse} = 3.5 mJ.*

7.6 Conclusion

The numerical simulations of the Mini-PAC and the flow-tunnel ignition by NRP discharges have shown that ignition success or failure results from a competition between the residence time of the reacting gases in the discharge channel and the combustion chemistry time scale. Based on this hypothesis, a low-order model of flame ignition by NRP discharge has been derived in this chapter. In this model, NRP discharges are applied in perfectly stirred reactor (PSR) whose volume matches the discharge channel of diameter d, to ignite the methane-air mixture continuously injected inside the reactor. The flow of gas passing through the PSR reproduces the gases circulation in the discharge zone.

The PSR model has been used to build-up plasma-assisted ignition diagrams which indicate the number of pulses, the ignition delay and the total deposited energy required to ignite the mixture inside the reactor as a function of gases residence time. A parametric study has been first carried out to confirm the results obtained in the LES of the Mini-PAC burner ignition by considering for a varying gases residence time two cases. A case where only the thermal effects of the discharges are taken into account and a case where both the thermal and chemical (O_2 dissociation into atomic O) effects are considered. The results have confirmed that the production of radical O that plays a major role in the enhancement of combustion chain-branching reactions that trigger the flame ignition, especially when a significant amount is accumulated in the discharge

zone.

Parametric studies have been then performed to identify the most efficient way to ensure an significant accumulation of atomic O in the discharge zone for successful ignitions. The first investigated solution consisted on increasing the pulse energy to increase the amount of O produced at each pulse. The second solution consisted on increasing the pulse repetition frequency to promote O accumulation. The results have shown that both solutions lead to a reducing the ignition delay and extending the ignition domain. However, in terms of energy efficiency, increasing the pulse repetition frequency has proven to be a much better solution as it consumes much less energy.

Part III

Numerical simulations of flames stabilization by NRP discharges

Chapter 8

Review of flames stabilization by NRP discharges

This chapter is a short review of recent Plasma-Assisted Combustion experiments performed with Nanosecond Repetitively Pulsed (NRP) discharges. NRP discharges have been successfully used to stabilize ultra-lean premixed flames on several laboratory-scale hydrocarbon-air flames but also in test rigs representative of a gas turbine environment at atmospheric and high pressure. This technique is very efficient because the energy consumption of the plasma is typically less than 1% of the power released by the flame.

Contents

8.1 Lean flames stabilization by NRP discharges

Operating at lean combustion regimes to reduce pollutants emission has shown to cause, in addition to the ignition problems, difficulties to stabilize and maintain the flames once ignited. Due to the low flame temperatures encountered in these regimes, the chemical reactions are greatly slowed down resulting often in incomplete combustion, which can even lead in some cases to the complete extinction of the combustion chamber, causing safety issues. Despite the proven efficiency of plasma discharges in improving the combustion process, their use in combustion systems to increase flame stability has for a long time been prohibited by their energy cost. However, the recent development of NRP discharges which consume less energy compared to conventional plasma discharges while significantly improving combustion has made this solution practical and more affordable. In the last few years, several experimental research teams have therefore studied the impact of NRP discharges on flames stabilization in lean regimes and near the extinction limits.

The extension of the Lean Blow Out (LBO) of an aeronautical high-power, combustor using NRP plasma discharges was demonstrated by Barbosa et al. (2015). The burner consists of a two-stage swirled injector connected to a rectangular combustion chamber with optical access ports. Both stages are supplied with air, while only the primary stage is fed with fully premixed air and propane C_3H_8. The outlet of the combustion chamber is open to the atmosphere. 10 ns NRP discharges are applied at 30 kHz using a pulse generator for an electrical power of 350 W (0.7% of the flame thermal power). The initial conditions are set to $Q_{air} = 105$ N.m^3.h^{-1} and $Q_{C_3H_8} = 2.1$ N.m^3.h^{-1} corresponding to the maximal burner power P = 52 kW and a global equivalence ratio $\phi = 0.47$. Then, the fuel flow rate is gradually decreased until the Lean Blow Out (LBO) limit. Figure. 8.1 shows CH* images of the flame as the equivalence ratio ϕ is decreased with and without plasma. The NRP discharges extend the LBO limit from $\phi_g = 0.40$ to $\phi_g = 0.11$ (global equivalence ratio), which corresponds to an extension of 70%

The ability of NRP plasma discharges to enhance the lean stability and blow out limits of flames at high pressure was also shown by Di Sabatino and Lacoste (2020); Di Sabatino et al. (2021). In a rectangular combustion chamber with a square section of 85 × 85 mm^2 and a length of 150 mm, fed by a swirler injector with a methane-air mixture, the effects of two discharge regimes, NRP glows and NRP sparks, were analyzed for different levels of pressure. The results indicated in Fig. 8.2, show that the NRP discharges effectively extended stability and blow-off limits for all the pressures considered, from atmospheric pressure up to a pressure of 5 bar. The study also shows that the most efficient plasma actuation of the flame is obtained for a ratio between the plasma power deposited by NRP discharges and the thermal power released by the flame of

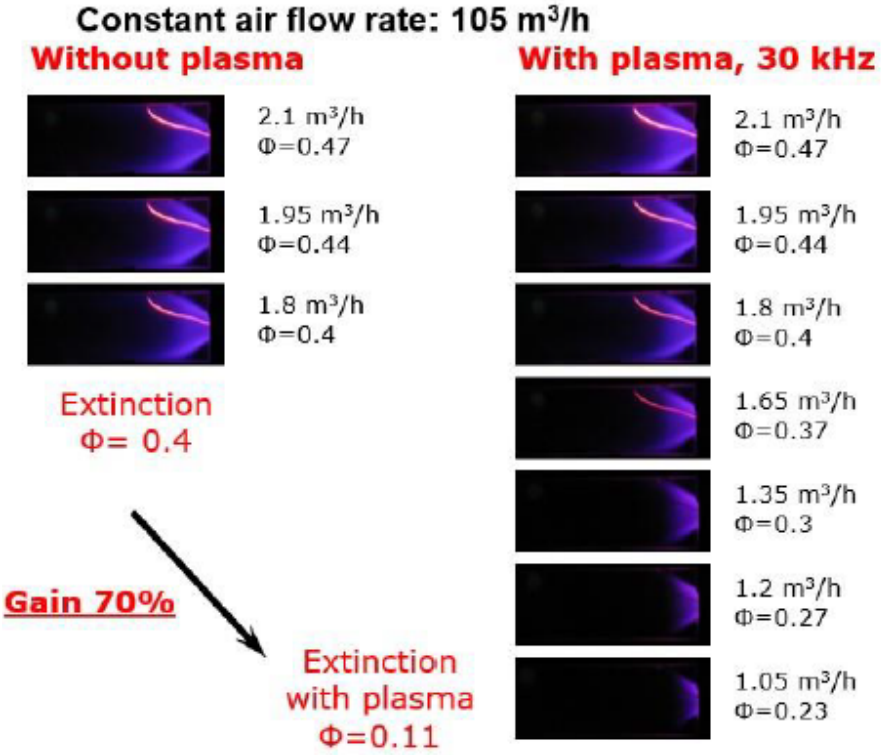

Figure 8.1: *Illustration of the LBO reduction by CH* imaging (Barbosa et al. (2015)). The bright filament visible in the photos is the anode heated by burnt gases.*

about 1%. Above 1%, adding more plasma power has only a marginal effect on flame stabilization.

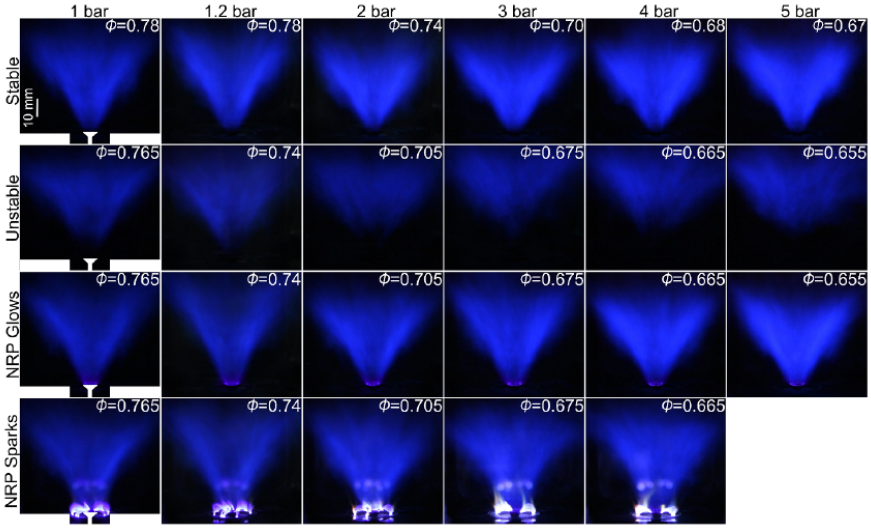

Figure 8.2: *Flames at pressures from 1 to 5 bar, for stable conditions (first row), unstable conditions (second row), with NRP glows (third row), and with NRP sparks (fourth row), Extracted from (Di Sabatino and Lacoste (2020)).*

Another recent work of Vignat et al. (2021) report an improvement of lean blow-out performances for liquid fuels. The experiment was performed on SICCA-Spray burner, a laboratory-scale atmospheric test rig equipped with a swirl spray injector representing a single sector of a gas turbine. Three fuels and injection conditions are considered: perfectly premixed methane–air, liquid heptane C_7H_{16}, and liquid dodecane $C_{12}H_{26}$ injected as hollow cone sprays. The fuel flow rate is kept constant and the air flow rate is slowly increased until LBO occurs. The NRP discharges are applied at 20 kHz and the ratio of electrical and thermal power is equal to 2%. A low frequency combustion oscillation arises near the LBO limit $\phi = 0.57$. Spray flames blow-out at this point. When NRP discharges are applied, the flames continues to burn beyond this limit. As shown in Fig. 8.3, the LBO limit is extended in average by $\Delta\phi = 0.05$ for both liquid fuels, and $\Delta\phi = 0.019$ for methane. The beginning of the low frequency oscillation is also delayed by $\Delta\phi \approx 0.02$ for all three fuels.

On laboratory-scale, combustion enhancement by NRP discharges was demonstrated by Pilla et al. (2006) on the Mini-PAC burner, a bluff-body premixed propane-air configuration of a maximal theoretical power of 25 kW (Note that the experiments described in Section. 6.2 and Section. 9.2 were performed on a new version of this Mini-PAC burner). The spontaneous emission of OH radicals has been recorded for a propane-air flame of an equivalence ratio ϕ

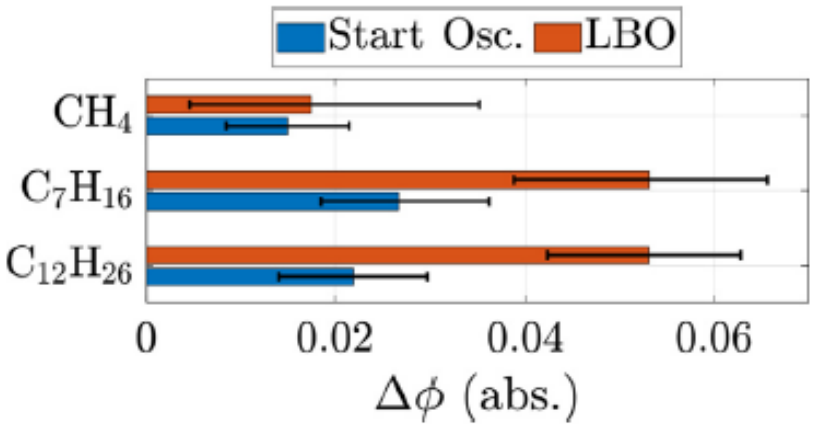

Figure 8.3: *Reduction of the equivalence ratio, $\Delta\phi$, at the start of the oscillations (in blue), and at the LBO (in brown) by NRP discharges for gas fuel (CH_4) and liquid fuels (C_7H_{16}, $C_{12}H_{26}$). Extracted from (Vignat et al. (2021)).*

= 0.8 at high flow rate without and with the assistance of NRP discharges. Without plasma, the burner presents a low combustion efficiency as shown in Fig. 8.4 (left). When a repetitively pulsed plasma is applied to the flame, significant increase of the combustion efficiency is observed, Fig. 8.4 (right). The region of OH emission is widely extended. Overall, it was found that with NRP discharges a stable flame regime could be obtained at equivalence ratios 10% leaner than without the NRP discharges with a plasma power that doesn't exceed 0.3% of the flame power.

The Mini-PAC burner have been retained in the PASTEC project as the target configuration chosen to study the mechanisms of flames stabilization by NRP discharges. The experimental characterization and the numerical study of the configuration are presented in the following chapter.

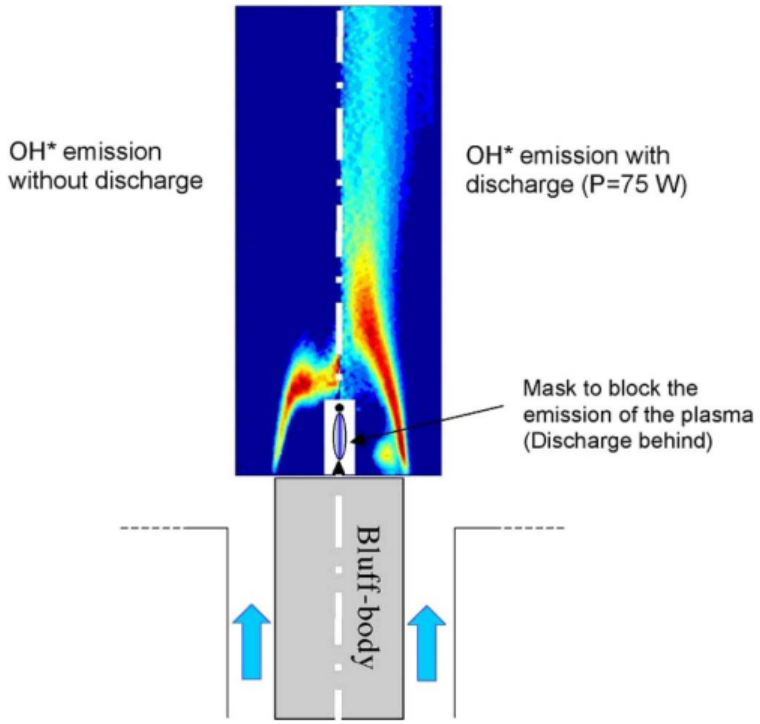

Figure 8.4: *Comparison of OH emission with and without discharge after Abel transform; air: 14.7 m^3h^{-1}, propane: 0.5 mm^3h^{-1} (ϕ = 0.83). Flame power: 12.5 kW, discharge power: 75 W. Emission of the plasma was blocked to prevent saturation of the ICCD. Extracted from (Pilla et al. (2006)).*

Chapter 9

Numerical simulations of turbulent flame stabilization by NRP discharges

In the present chapter, High-performance computations of a lean bluff-body turbulent premixed methane-air flame stabilized by NRP discharges are performed. The experimental characterization of the target configuration, the Mini-PAC burner, and the NRP discharges, conducted at EM2C and CORIA laboratories are discussed. Large Eddy Simulations of a non-assisted flame and a plasma-assisted flame are then performed by combining the semi-empirical plasma model developed by Castela with an analytical combustion mechanism. Results are eventually compared to experimental data.

Contents

9.1 Introduction

Flames stabilization by nanosecond repetitively pulsed (NRP) discharges is investigated experimentally and numerically in the framework of the PASTEC project in order to identify and understand the mechanisms of combustion enhancement by non-equilibrium plasma. The objective of this work is to perform Large Eddy Simulations of flame stabilization by NRP discharges using the recently developed phenomenological plasma model (Castela et al. (2016)).

The chapter is structured as follows. The experimental characterization of the target configuration, the Mini-PAC burner, and the NRP discharges used to stabilize the flame are presented in Section. 9.2. Then, Section. 9.3 introduces the numerical and semi empirical plasma models used for the LES of the Mini-PAC flame stabilization by NRP discharges along with the operating and initial conditions of the simulations. The results of 3-D computations of a non-assisted flame and a plasma-assisted flame are presented and compared in Section. **??**. Comparisons between numerical simulations and experimental measurements are performed in Section. 9.5. Finally, the conclusions and discussion are presented in Section. 9.6 .

9.2 Mini-PAC Configuration

9.2.1 Flame characterization

The target configuration retained for the study is the Mini-PAC burner, which stands for mini Plasma Assisted-Combustion. The burner is similar to the configuration of (Pilla et al. (2006)), with a some modifications. The experiments are conducted with methane instead of propane. The shape and the size of the electrodes are changed compared to the Mini-PAC ignition experiment presented in Section. 6.2. The schematic of the burner is presented in Fig. 9.1. The internal diameter of the injection tube of the burner is 16 mm, and the bluff-body diameter is 10 mm. The Reynolds number, based on the diameter of the burner outlet, the bulk velocity, and the gas kinematic viscosity is about 14,000. The gas flow is therefore in the turbulent regime. A recirculation zone above the bluff-body stabilizes the generated turbulent flame. The NRP discharges are initiated in the recirculation zone, which is mainly composed of burnt gas. High-voltage nanosecond pulses are applied across a gap of 5 mm, between a horizontal tungsten electrode and a vertical tungsten electrode. The vertical electrode is mounted on the grounded bluff-body. The diameter of the electrodes is 1 mm.

A map of the burner operating conditions measured at EM2C and CORIA laboratories in lean regimes is shown in Fig. 9.2. A Stable Flame region in which a developed, stable, V-shape flame forms, see Fig. 9.2, is observed for low air

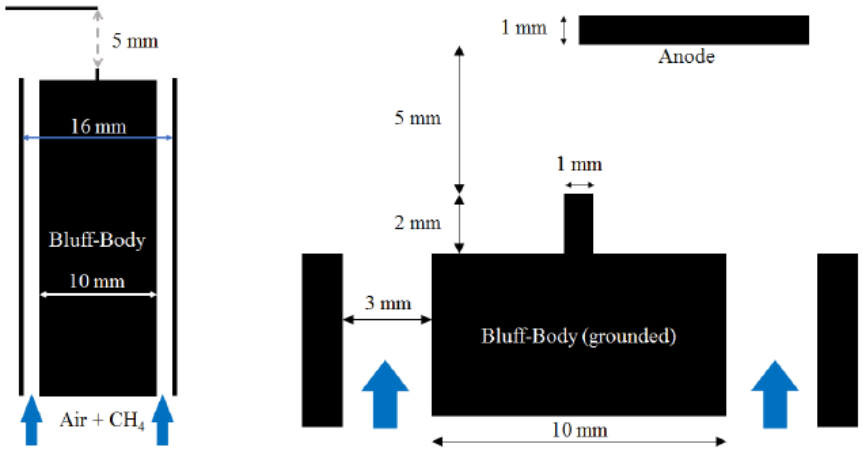

Figure 9.1: *Schematic of the Mini-PAC burner and electrode configuration*

flow-rate. For high air flow-rate, a significant part of methane is not burnt, and the flame is confined in the recirculation zone downstream of the bluff-body. This part is defined in Fig. 9.2 as the Weak Flame region. Finally, an Intermittent Flame region appears between the two previous regions. In this case, the flame oscillates between the Stable and Weak flames. The limits of the different zones are shown in colored lines in Fig. 9.2. the limit of extinction lies between $\phi = 0.7 - 0.8$ in the considered range. The operating point investigated in this work is represented by a black triangle (Weak Flame region, $\phi = 0.8$, $Q_{air} = 16\ m^3.h^{-1}$).

Photographies of non-assisted and plasma-assisted flames at this operating point (equivalence ratio $\phi = 0.8$, bulk velocity of $U_b = 43.3\ m.s^{-1}$ and a Reynolds number of $Re = 1.6\ 10^4$) are shown in Fig. 9.3. Without discharge (left), a weak and incomplete combustion is restricted to the bluff-body wake. However, the application of NRP discharges enhances the flame which develops into a stable, V-shape form(right).

In this chapter, numerical simulations of the Mini-PAC flame stabilization by NRP discharge in the described operating conditions are performed using the phenomenological model of (Castela et al. (2016)). The objective is first to validate the ability of the numerical modeling to reproduce the effects of the NRP discharges on combustion then in a second time to give new insights into the plasma flame interaction mechanisms.

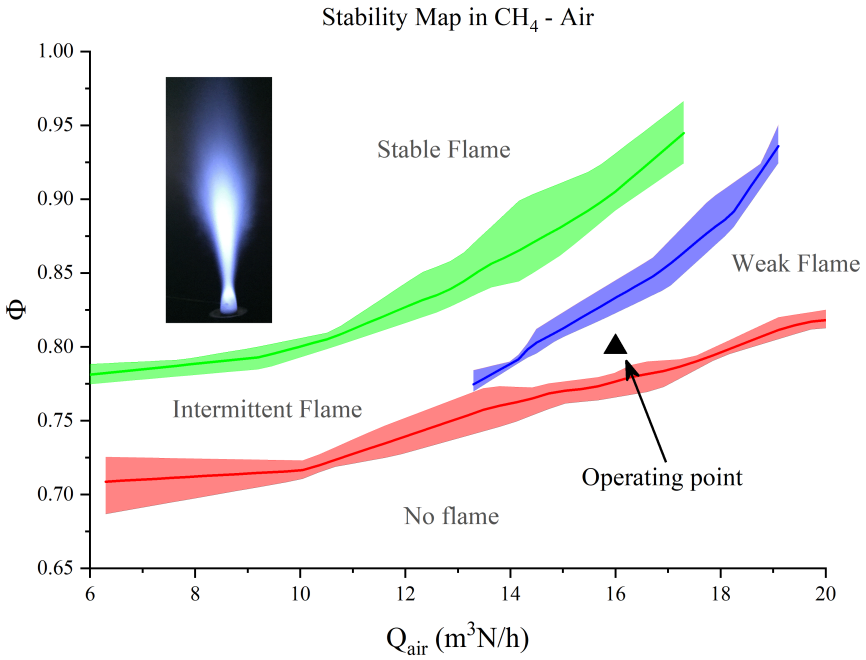

Figure 9.2: *Operating conditions of the mini-PAC burner (no NRP discharge applied). The PASTEC flame is represented by a black triangle and lies in the Weak Flame zone if no NRP discharges are applied. Pictures of the flame are inserted in the top left (stable) and bottom right (weak) corners. The filled areas represent the measurement uncertainty. Extracted from Minesi (2020)*

Figure 9.3: *Photographs of the lean flame ($\phi = 0.8$) without (left) and with (right) NRP discharges applied at 20 kHz. Extracted from (Blanchard et al. (2021))*

9.2.2 Discharge characterization

The NRP discharges model proposed by (Castela et al. (2016)) is based on the observations that the deposition of energy in air or a hydrocarbon-air mixture during a NRP discharge pulse, is mainly reponsible of an electronical and vibrational excitation of N_2 molecules (Rusterholtz et al. (2013)). The nanosecond-scale relaxation of the generated electronic excited states $N_2(B)$ and $N_2(C)$, by quenching with the surrounding molecules, induces an ultra-fast increase of the temperature and the ultra-fast dissociation of O_2 into atomic O (**?**; Popov (2013b); Rusterholtz et al. (2013)). Whereas, the microsecond-scale relaxation of the vibrational excited states $N_2(v)$ induces a slow gas heating. To make sure that the same behavior is observed when NRP discharges are applied in a mixtures of lean flame burnt gases as it is the case for the Mini-PAC flame stabilization experiment and that the NRP discharges model is still valid, a detailed experimental characterization of the discharges has been performed by (Minesi et al. (2022)) and (Blanchard et al. (2021); Blanchard et al. (2021)) for these operating conditions.

The number densities of electrons and excited electronic states were measured by quantitative Optical Emission Spectroscopy (OES) in (Minesi et al. (2022)). Figure. 9.4 shows the number densities of $N_2(B)$, $N_2(C)$, OH(A), NH(A), $N_2^+(B)$, CN(B) and electrons plotted for locations near the electrodes and in the middle of the gap. The number densities of the electronic excited states $N_2(B)$, $N_2(C)$ increase during the energy deposition (0 - 10 ns) then decrease once the reduced electric field is turned off. Other species such as CN(B) or OH(A) are also produced during and after the pulse. Contrary to the N_2 excited states, CN(B) and OH(A) reach their peak of number density after the pulse which indicates that they are not produced by electron impact as it's the case for $N_2(B)$ and $N_2(C)$ but that they are formed by other processes of energy transfer. The electrons number density is between 10^{15} and 10^{15} cm^{-3} which is expected for NRP discharge operating at spark regime. As for NRP discharges in pure air, the main species produced during the pulse are the excited states of N_2. The relaxation of these states leads later to the formation of other chemical species. It is interesting to note that the number density of $N_2(B)$ is about 10-40 times higher than the density of $N_2(C)$. This ratio, obtained in the burnt gases, is similar to what was obtained for NRP discharges in pure air (Rusterholtz et al. (2013)). The measurement the gas temperature from the distribution of N2(C) rotational states in (Minesi et al. (2022)) and (Blanchard et al. (2021)) shows that during the pulse, approximately 20% of the electrical energy deposition is converted into heat.

In view of these results, the phenomenological model of the NRP discharge is still valid. The relaxation process of the N_2 excited states in this case is not yet identified. However, given that a significant amount of O_2 is still present

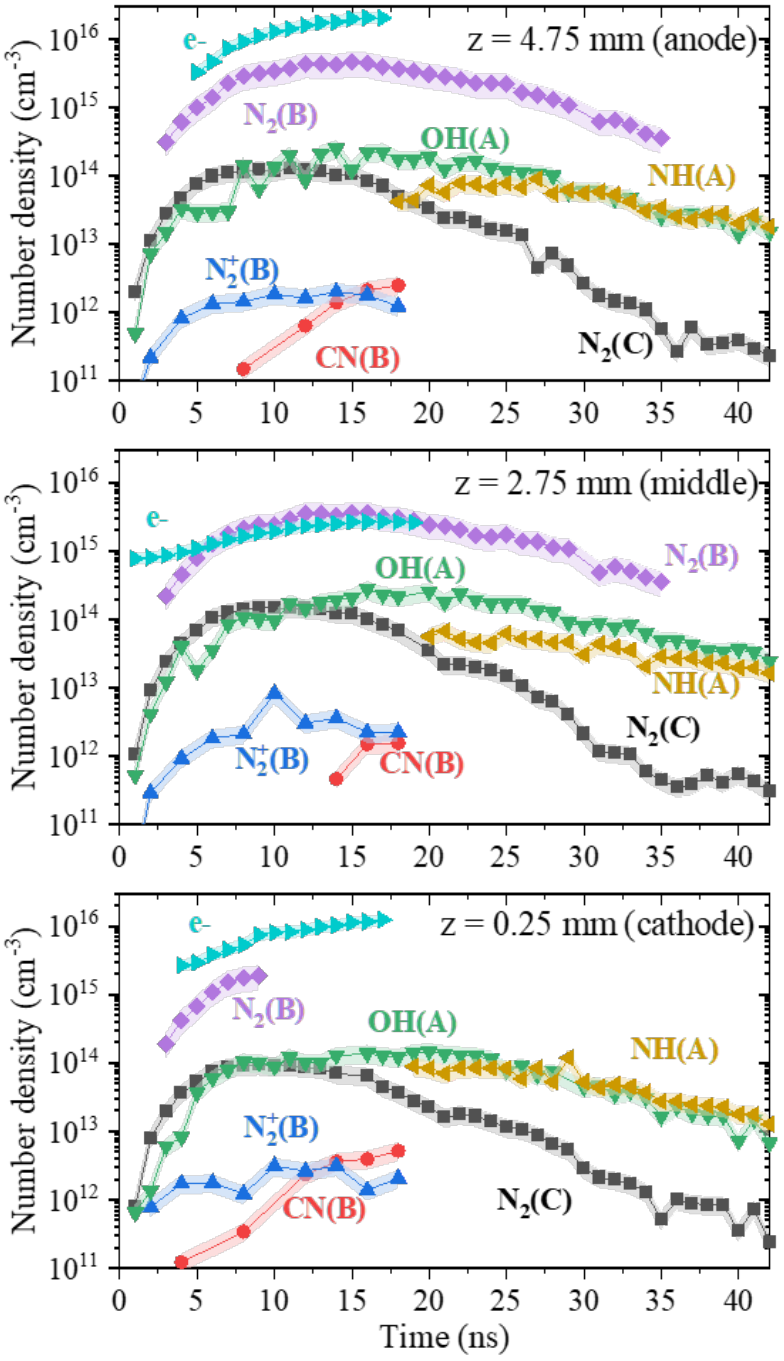

Figure 9.4: *Evolution of the $N_2(B)$, $N_2(C)$, OH(A), NH(A), $N_2^+(B)$, CN(B) and electrons number densities under the PASTEC conditions (ϕ = 0.8, f = 20 kHz, E_p= 2.0 mJ). The results are displayed at three locations: near the anode at z = 4.75 mm (top), in the center of the inter-electrode gap at z = 2.75 mm (middle), and near the cathode at z = 0.25 mm (bottom). Extracted from (Minesi et al. (2022))*

in the lean flame burnt gases, the postulate taken is that it is similar to the fresh gases case described by the reaction of O_2 dissociation in atomic O (**??**). This hypothesis will be verified by comparing the results of the numerical simulations with the experimental measurements.

The averaged current and voltage traces of the pulse, measured experimentally by (Blanchard et al. (2021)) using electrical probes, are represented in Fig. 9.5 along with the calculated energy when discharges are applied continuously at 20 kHz. Due to the impedance mismatch between the cable, the plasma, and the pulse generator, several reflections occur at the electrode and also at the pulser output. About 80% (1.6 mJ) of the total energy is deposited by the incident pulse and the remaining energy is deposited within 300 ns by multiple low-energy reflections leading to a total of 2 mJ deposited energy. The ratio of electric discharge power over flame thermal power is about 0.3%.

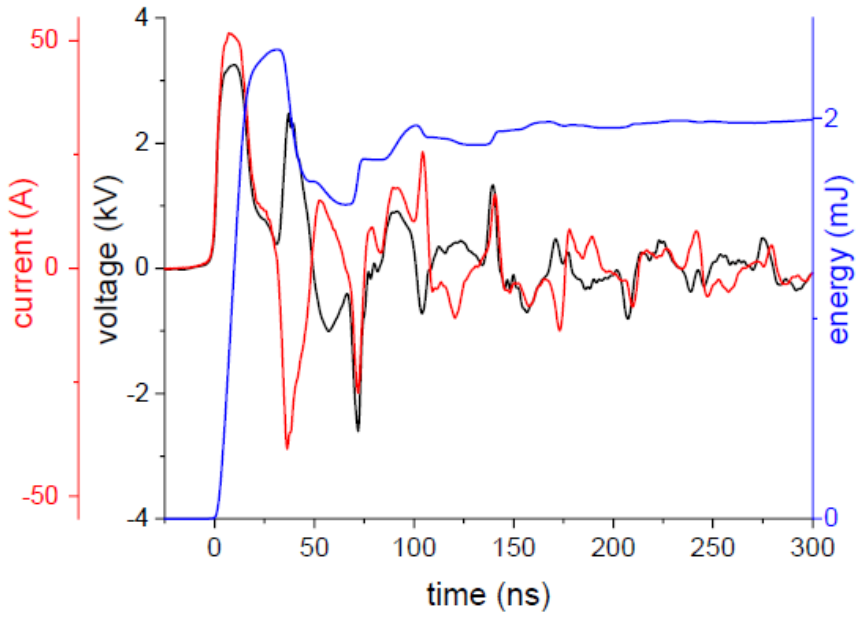

Figure 9.5: *Voltage (black line), current (red line) and energy (blue line) measurements. Extracted from (Blanchard et al. (2021))*

The diameter of the discharge was measured experimentally by (Blanchard et al. (2021)) using the methodology introduced in (Rusterholtz et al. (2013)). It is defined as the full width at half-maximum of the total emission of the $N_2(C)$ radial profile extracted from the Abel inversion of the $N_2(C)$ emission spectra images. The discharge can be approximated by a cylinder of 1.0 mm diameter by 5 mm height.

9.3 Numerical set-up

Large Eddy Simulations (LES) of the MiniPAC flame stabilization by NRP discharges are performed using the YALES2 unstructured finite-volume low-Mach number solver (Moureau et al. (2011)). The time integration is performed using a fourth-order temporal scheme coupled with a centered fourth order scheme for spatial discretization. The sub-grid Reynolds stresses tensor is closed using the Dynamic Smagorinsky model (Germano et al. (1991)). The analytical LU19 kinetic scheme involving 19 species and 184 reactions is used for the methane-air mixture chemistry (Lu and Law (2008)). Species equations are coupled with turbulence using the Thickened Flame model for LES (TFLES) (Colin et al. (2000)) and the Charlette sub-grid scale flame wrinkling model (Charlette et al. (2002)). The mesh, shown in Fig. 9.6 (right), along with the 3D Mini-PAC model(left), consists of 140 millions tetrahedral elements refined in the plasma discharge zone, cells size equals 0.1 mm, to ensure that the small turbulence scales and laminar flame thickness are well resolved and no sub-grid scale model or TFLES coupling is necessary. In the flame zone, the cells size varies from 0.1 mm to 0.2 mm. In this region, TFLES model is used to capture the turbulence-flame interaction, triggered by a dynamic sensor.

The discharge properties have been set to be consistent with experimental measurements. The pulse energy and the pulse repetition frequency are equal to E_p = 2.0 mJ and PRF = 20 kHz. The discharge, shown in Fig. 9.6 (left), has a cylindrical shape filtered with the spatial function $F(r) = erfc[(r/a)^b]$ where r is the radial distance from the discharge axis, a and b are geometric parameters, fitted to well reproduce the discharge radius, 1.0 mm, and length, 5.0 mm, and have a sufficient number of point at discharge interface to avoid high gradients that can cause numerical issues.

A reactive LES is first conducted without NRP discharges until reaching a steady-state solution. The 2-D mean axial velocity (a) and the heat release rate (b) on the centerline plane of the Mini-PAC configuration are shown in Fig. 9.7. An inner recirculation zone is clearly identified behind the bluff-body. The velocity magnitude in this zone is very low ($\|\overrightarrow{u_z}\| < 6.5\ m.s^{-1}$) compared to the rest of the flow where it varies between 20 m.s^{-1} and 50 m.s^{-1}. The heat release rate indicative of the flame front, the zone where the mixture burns, shows that the flame is confined to the recirculation zone. Figure. 9.8(a) shows the 2-D mean temperature field (left) of the same simulation on the centerline plane of the Mini-PAC configuration. In agreement with the experimental observations, the burnt gases are confined in the recirculation zone. Their temperature is around 2000 K, which corresponds well to the theoretical value of

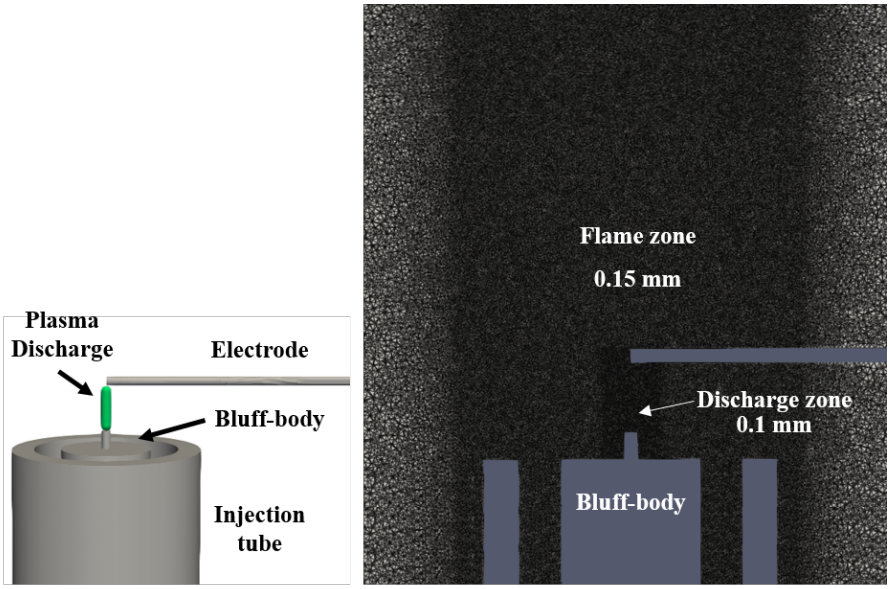

Figure 9.6: *(left) Mini-PAC burner 3-D model. (Right) Mini-PAC mesh,* 140 *millions tetrahedral elements. Cells size equals* 0.1 *mm in the discharge zone while in the flame zone it ranges from* 0.1 *mm to* 0.2 *mm.*

1993 K expected for a methane-air premixed flame at an equivalence ratio $\phi =$ 0.8. The mean CH_4 mass fraction, represented in Fig. 9.8(b), shows that the methane is only consumed in the recirculation zone and that large amount is not burnt. The non-assisted combustion is incomplete.

From the steady state, a solution has been taken and defined as the initial condition, t = 0 s, for two LES: one still without activating plasma (case NP) and a second one with applying an uninterrupted series of NRP discharges at a frequency of 20kHz (case P).

9.4 LES results

9.4.1 Global impact of NRP discharges

The global impact of NRP discharges on the total heat release is evidenced in Fig. 9.9, which plots the temporal evolution of the thermal flame power:

$$P = \int_V (\Xi/F)\overline{\dot{\omega}}_H dV \tag{9.1}$$

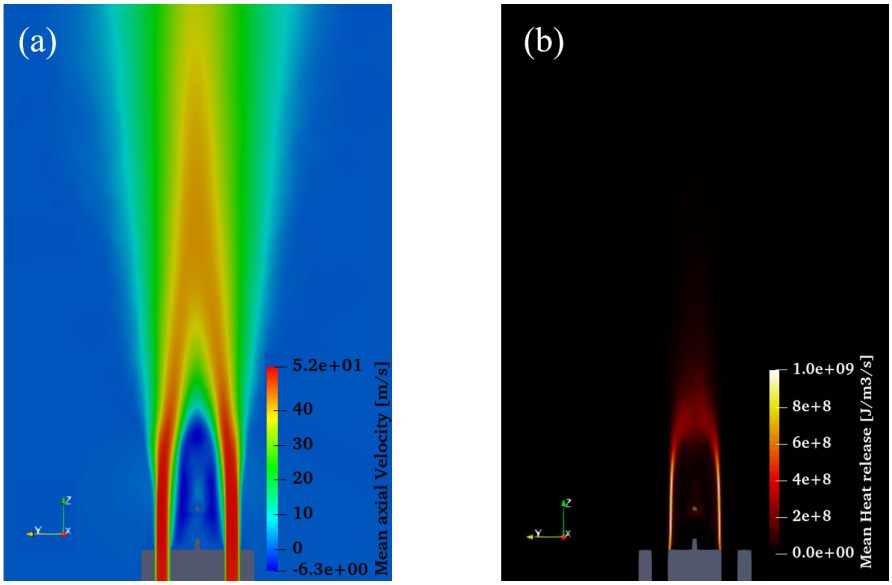

Figure 9.7: *Numerical solution of the 2-D mean axial velocity (a) and heat release rate (b) on the centerline plane of the Mini-PAC configuration for the non-assisted flame.*

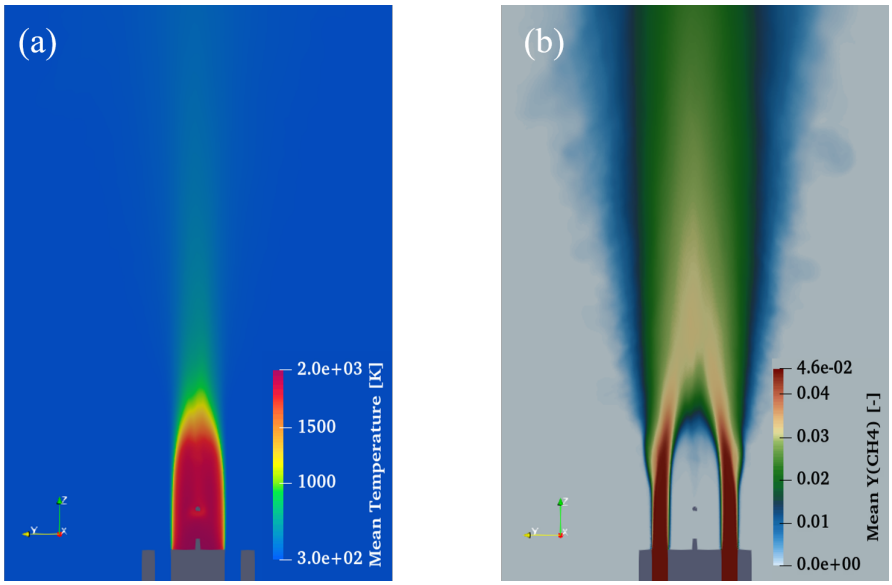

Figure 9.8: *Numerical solution of the 2D mean temperature (a) and methane (CH_4) mass fraction (b) on the centerline plane of the Mini-PAC configuration for the non-assisted flame.*

where $\overline{\dot{\omega}}_H$ is the filtered heat release rate and $\int_V$ denotes the volumetric integral over the whole computational domain V. Without NRP discharges, the flame power oscillates around 700 W. However, when the electrical discharges are turned on, the total heat released by the combustion increases gradually during a transient period of approximately 10 ms (200 pulses) and then oscillates around a value of 1600 W.

To identify the reasons of the flame power increase, the LES-resolved $\mathcal{R}$ and total $\mathcal{A}$ flame surfaces are computed as (Veynante and Vervisch (2002)):

$$\mathcal{R} = \int_V \overline{|\nabla c|} dV \quad \text{and} \quad \mathcal{A} = \int_V \Xi \overline{|\nabla c|} dV \tag{9.2}$$

where c is a progress variable defined from the temperature to reach 0 and 1 in the fresh and burnt gases, respectively. Two observations are made from the analysis of the temporal evolution of $\mathcal{R}$ and $\mathcal{A}$ plotted in Fig. 9.10. First, $\mathcal{R}$ is very close to $\mathcal{A}$ and in practice 95% of the flame wrinkling is resolved at the LES scale. The grid resolution is here sufficiently fine to limit turbulent combustion modeling errors. Second, the flame surface evolution follows the same trend than the flame power plotted in Fig. 9.9.

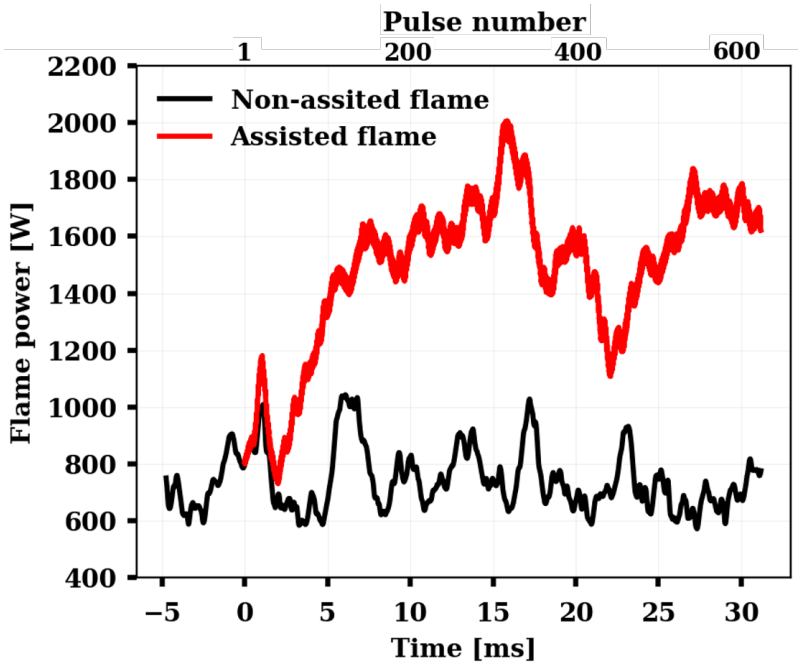

Figure 9.9: *Temporal evolution of the total thermal flame power for cases NP (black) and P (red).*

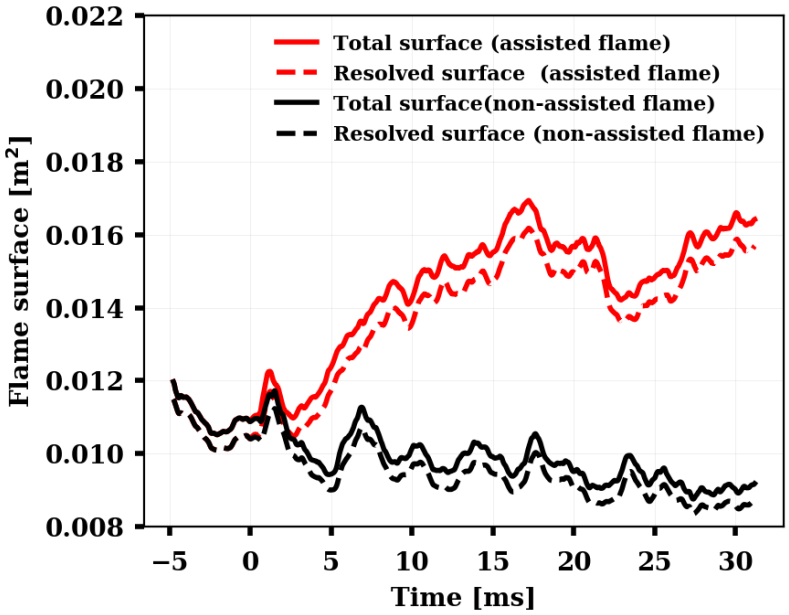

Figure 9.10: *Temporal evolution of the flame surface for cases NP (black) and P (red). Dashed lines represent the flame surface resolved at the LES filter scale, while solid lines include also the subgrid flame wrinkling contribution.*

The mean gains in power (η_P) and total flame surface ($\eta_{\mathcal{A}}$) induced by the NRP discharges are defined as:

$$\eta_P = \langle P_P \rangle \,/\, \langle P_{NP} \rangle \quad \text{and} \quad \eta_{\mathcal{A}} = \langle \mathcal{A}_P \rangle \,/\, \langle \mathcal{A}_{NP} \rangle \tag{9.3}$$

where $\langle \varphi \rangle$ denotes temporal averaging of variable φ. P and NP subscripts refer to simulations with and without plasma, respectively. To remove the transient state following by the discharges activation, the mean gains are computed for the period [7ms,20ms]. It comes that $\eta_P = 2.13$ and $\eta_{\mathcal{A}} = 1.54$. The ratio $\eta_{\mathcal{A}}/\eta_P = 0.72$, which means that approximately 70 % of the gain in flame power is explained by an increase of the total flame surface. As it will be shown further, the rest of the gain (30%) is explained by a local increase of the heat release (and the flame consumption speed) in the periphery of the bluff-body recirculation zone.

9.4.2 Impact of NRP discharges on the heat release field

Figure. 9.11 shows two instantaneous snapshots from cases NP (left) and P (right), taken at the same time instant t= 20 ms, of the flame surface (defined as the iso-surface of $c^* = 0.5$) colored by the heat release. Without NRP discharges, only a weak reaction zone limited to the recirculation zone

behind the bluff body is visible. Indeed, because of the low burning velocity under lean conditions, the flame front cannot propagate outside the recirculation zone. Figure. 9.11 (right) plots the flame surface after 400 pulses. In comparison with case NP, the heat released by the flame increased significantly and the reaction zone extended downstream. As expected from the previous global analysis, the flame surface is developed. The pulsation of the electrical discharges enables the recirculation zone to act as a flame holder.

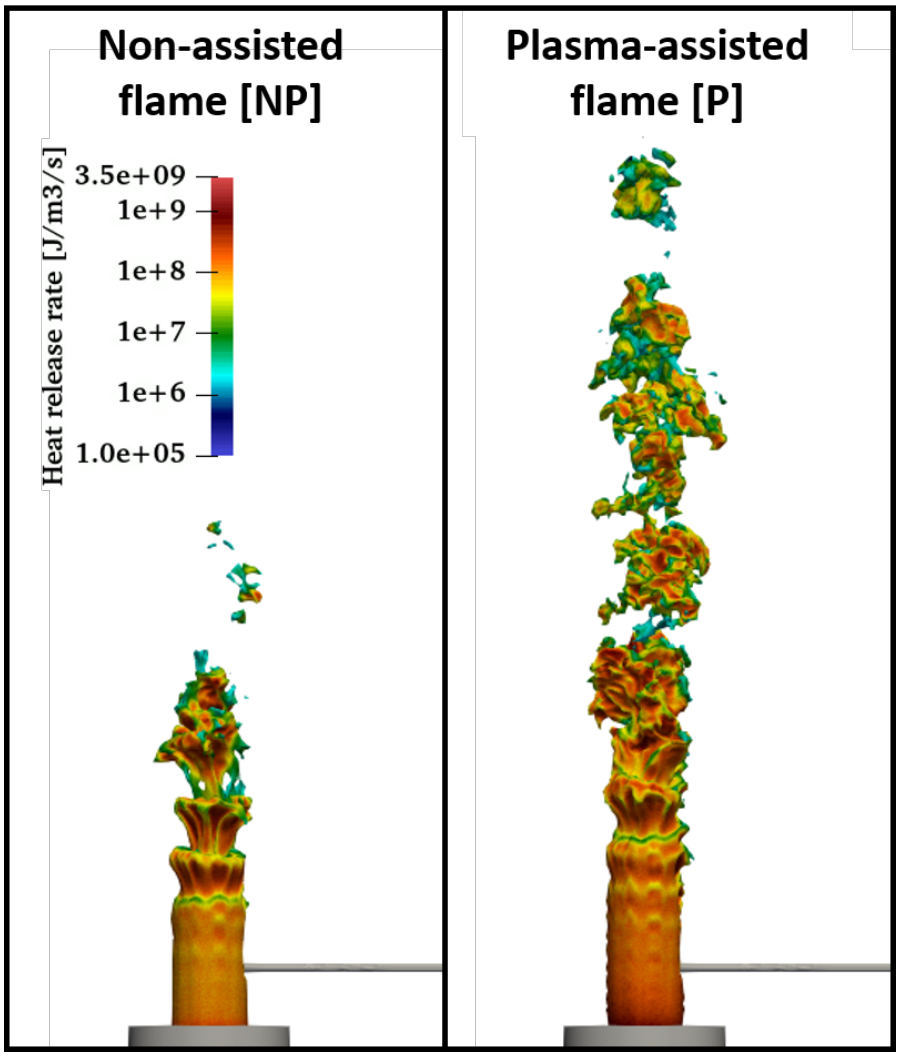

Figure 9.11: *Instantaneous snapshots taken at the same time instant* t= 20 *ms of* $c^* = 0.5$ *iso-surface colored by the heat release for cases NP (left) and P (right).*

9.5 Comparison with the experiment

Quantitative comparisons between experiments and simulations are performed to assess the ability of the model to capture the dynamics of the plasma interaction with the flame.

9.5.1 Gas Temperature at the center of the discharge

The gas temperature evolution at the center of the discharge obtained in the simulation of the MiniPAC burner plasma assisted flame (case P), is shown in Fig. 9.12. The temperature predicted at the beginning of pulse 1 corresponds to the flame temperature without plasma. For a premixed methane-air flame at an equivalence ratio $\phi = 0.8$ and an initial temperature of 300 K at atmospheric pressure, the adiabatic flame temperature is 1993 K which is consistent with the simulation temperature of 1986 K. The cumulative effects of the train of pulses at 20 kHz is responsible of a temperature increase of 1250 K over the first 10 pulses approximately 0.5 ms. After that, a steady state is reached. The temperature increases at each pulse by approximately 800 K, from 3200 K to 4000 k then decreases before the following one by approximately the same amount, from 4000 K to 3200 K.

The value of the temperature at the same location, center of the discharge, has been measured by (Blanchard et al. (2021)) using spectroscopy emission method. Figure. 9.13 shows the comparison between the measured values (black square) and numerical results (red circles) corresponding to the discrete values of the temperature at the measurement times, the beginning of the 10 first pulses then the 25, 50, 100 and 250 pulse. The experiment and the numerical simulation are in good agreement. The temperature increase over the first 10 discharges is indeed well observed experimentally and the steady state value is also close to the measured one.

9.5.2 OH number densities

The second comparison concerns the evolution of OH profile along the line that passes through the center of the discharge, 4.5 mm above the bluff body, indicated in Fig. 9.14. The numerical results are compared to the OH-LIF measurements obtained by (Minesi (2020)). The LIF intensity obtained in the measurements is proportional to the density of the rotational state excited by laser radiation, in this case, OH (X, v = 0, J = 3). A correction is applied to the signal to determine the total OH density using Eq. (9.4) :

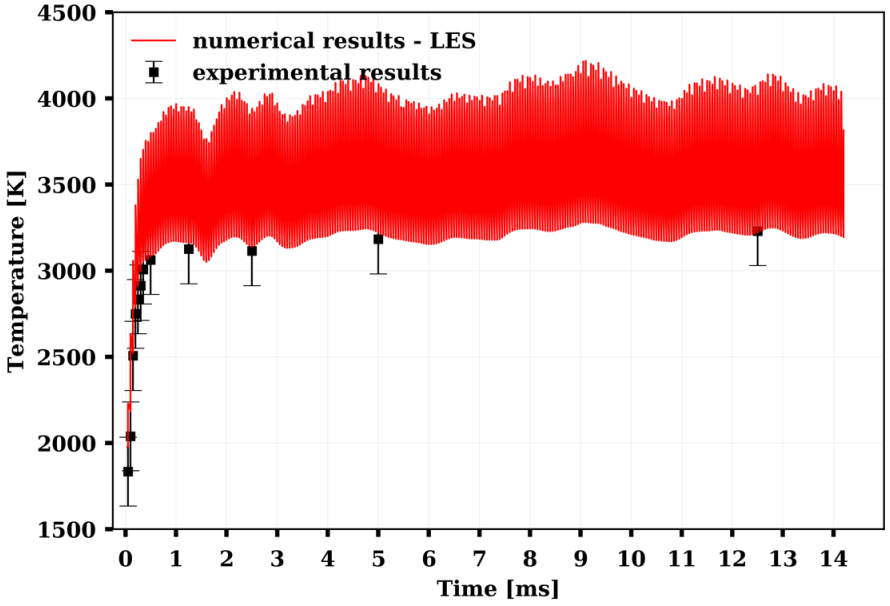

Figure 9.12: *Comparison between the temperature measured by spectroscopy emission (black square) and the temperature obtained in the LES simulation (red line) at the center of the discharge zone when NRP discharge is applied.*

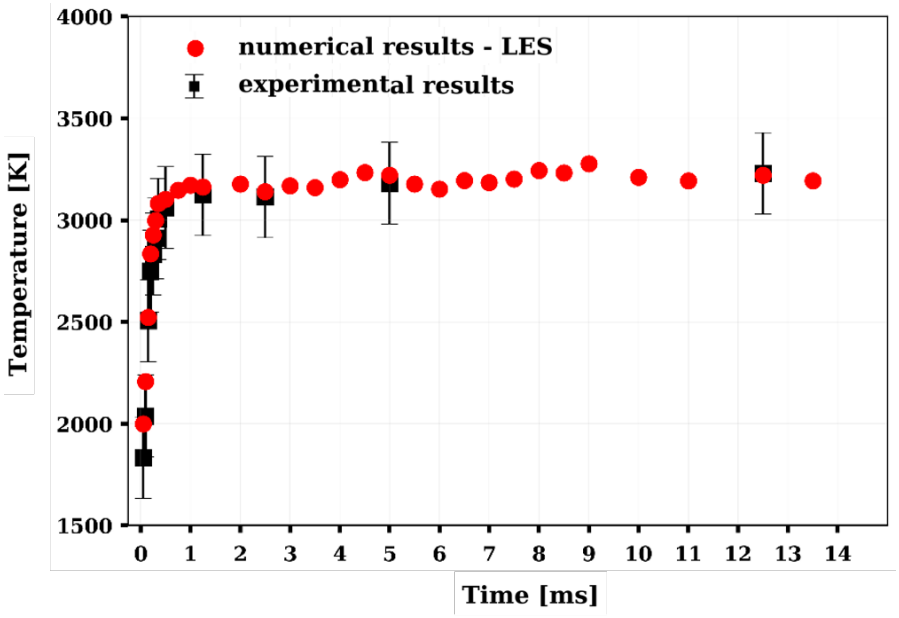

Figure 9.13: *Comparison between the temperature measured by spectroscopy emission (black square) and the temperature obtained in the LES simulation (red circles) at the beginning of the 10 first pulses then the 25^{th},50^{th},100^{th} and 250^{th} pulse.*

$$\frac{OH_{J=3,v=0}}{OH_{tot}} = \frac{(2J+1)\exp\left(-\frac{J(J+1)\Theta_{\text{rot},OH}}{T}\right)}{T/\Theta_{\text{rot},OH}} \frac{1}{\left[1-\exp\left(-\frac{\Theta_{\text{vib},OH}}{T}\right)\right]^{-1}} \quad (9.4)$$

where $\Theta_{\text{rot},OH} = 27K$ and $\Theta_{\text{vib},OH} = 5378K$, (Huber and Herzberg (1979)).

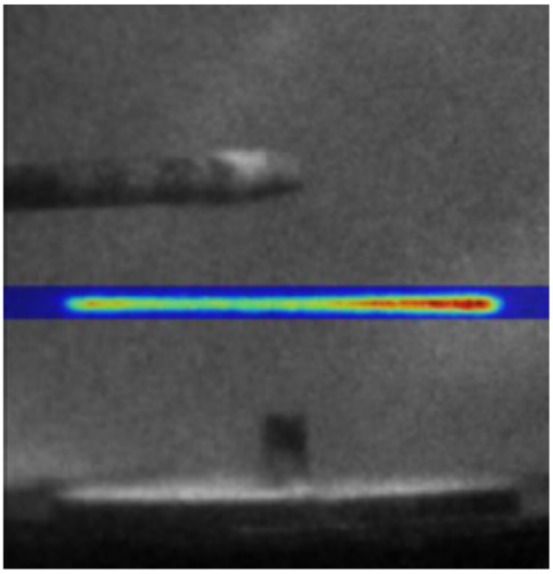

Figure 9.14: *Picture of the Mini-PAC burner taken with the ICCD camera (black and white) with a non-saturated LIF signal superimposed (false colors). Extracted from (Minesi (2020)).*

The simulated OH number density (lines) is compared to the corrected LIF signal (squares) in Fig. 9.15. The LIF signal and the OH number density are normalized to match at the flame front (r = 5 mm) in the steady state of the non-assisted flame used as the initial condition t = 0 ms, before the NRP discharge deposition. The experimental and numerical values in this case, represented by grey squares and grey lines respectively, are in a very good agreement. The OH density is null in the fresh gases (x> 5 mm). it increases and reaches a maximum in the flame front (4 mm< x< 5 mm) then decrease slowly toward the equilibrium in the burnt gases (x < 4 mm). When the NRP discharge pulses are applied, the OH density increases. First in the discharge zone where the energy is deposited, pulse 1 to pulse 10. Then, convected by the flow, in all the region between discharge zone (center of the bluff-body) and the flame front (edges of the bluff-body), pulse 10 to pulse 100. The comparison of the

numerical results and the experiment measurements shows once more a good agreement with a 4 times increase of the OH number density in the discharge zone and 1.5 times increase in the flame front.

Figure. 9.15 shows also that the flame width, distance between the two flame front, increases between pulse 20 and pulse 100 by approximately 0.4 mm. This effect observed experimentally is also well capture by the numerical simulation.

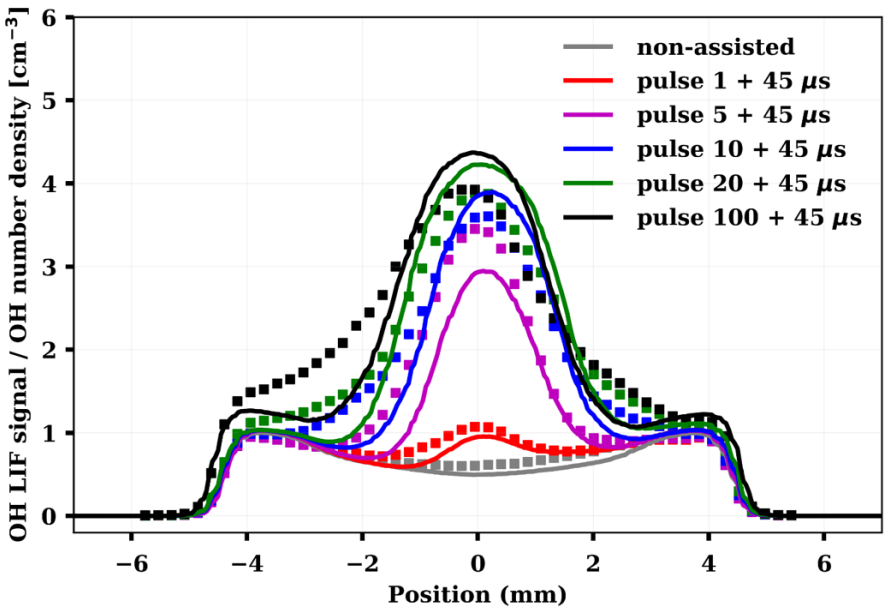

Figure 9.15: *Comparison of normalized LES simulation OH number density (solid lines) with the normalized corrected OH-LIF signal (colored squares) after the 1^{st}, 5^{th}, 10^{th}, 20^{th}, 100^{th} pulses.*

The good agreement between the experimental measurements and the numerical results shows that the phenomenological model captures well the effects of NRP discharges applied in flame burnt gases.

9.6 Conclusion

This chapter presents the first Large Eddy Simulations of turbulent premixed flame stabilization by NRP discharges. The numerical investigations have been conducted with phenomenological plasma model implemented in the CFD low-Mach number code YALES2. The target configuration is the Mini-PAC burner, a premixed bluff-body turbulent methane-air flame. The experimental study of this configuration showed that at lean regime without the assistance of plasma discharges the combustion is incomplete and only a small weak flame is observed behind the bluff-body. For the same operating conditions, when NPR

discharges are applied to the flame, the combustion is enhanced and the flame surface and power are significantly increased.

The numerical simulations performed in this chapter have shown that without NRP discharges, the reaction zone is limited to the low-velocity recirculation zone that forms behind the bluff body. Because of the low burning velocity under lean conditions, the flame front cannot propagate to high-velocity regions outside the recirculation zone. Due to an incomplete combustion, a significant amount of methane is not burnt. When NRP discharges are applied, the reactivity is significantly increased in the recirculation zone which acts as a flame holder allowing the flame to propagate downstream increasing the flame surface and power.

To understand the interaction mechanisms between the plasma and that lead to combustion enhancement a detailed numerical analysis is presented in the next chapter.

Chapter 10

Mechanism of stabilization by NRP discharges

In this chapter, Large Eddy Simulations of the Mini-PAC burner are analyzed in order to understand the mechanisms of flame stabilization by NRP discharges. Comparisons between the non-assisted flame case (NP) and plasma-assisted flame case (P) are first performed to identify the local and the global effects induced by the NRP discharges. A detailed chemical investigation is then conducted to explain these effects and the way they interact and enhance combustion.

Contents

10.1 Introduction

The objectives of this study are to give new insights into the plasma flame interaction mechanisms through the numerical analysis of the LES of plasma-assisted turbulent combustion performed on the Mini-PAC configuration in Chapter. 9

The chapter is divided in three sections. Investigation of the Mini-PAC plasma assisted combustion simulations is conducted in Section. 10.2 to identify the local and global effects induced by the NRP discharges. In Section. 10.3, detailed chemical analyses conducted in the discharge zone and at the flame front are preformed to understand and describe the plasma-flame interaction mechanisms that lead to combustion enhancement. Finally the study conclusions are summarized in Section. 10.4.

10.2 Global and local effects of NRP discharges.

To understand how the NRP discharges, located at the center of the bluff-body of the Mini-PAC configuration, allows the enhancement of the combustion and the development of the flame, it is first necessary to identify all the global and local effects induced by NRP discharges.

Figure. 10.1 shows temperature 2-D instantaneous fields from the non-assisted flame case NP (left) and the plasma-assisted flame case P (right), taken at the same time instant t= 15 ms, after 300 pulses. Without NRP discharges, the high temperature region, flame burnt gases with a temperature around 1950 K, is limited to the recirculation zone above the bluff body. Occasionally, small hot packets are released downstream without however allowing the flame to propagate and develop. When NRP discharges are applied, an important increase of the temperature is observed in the discharge zone, from 1950 K to 4000 K, and in all the zone below the electrode, temperature around 3500 K. The high temperature region has extended outside the recircuation zone. A similar comparison of the OH concentration 2-D fields at t= 15 ms is shown in Fig. 10.2. In the NP case, the OH confined to the recirculation zone with a small packets released from time to time has a concentration between 0.02 and 0.04 mol.m^{-3}. When NRP discharges are applied, a significant production of OH takes place in the discharge zone where the concentration reaches 0.15 mol.m^{-3}. The increase of OH concentration extends to the whole area under the electrodes and also downstream convected by the flow. As for the temperature, the OH region has extended outside the recirculation zone. Finally the heat release rate, indicative of the flame front, is shown for the two cases at the same time instant in Fig. 10.3. As seen previously, in comparison with case NP, the heat released by the assisted-flame increased significantly specially in the recirculation zone where the effects of discharges, heat and chemical species

production, are important and the reaction zone extended downstream.

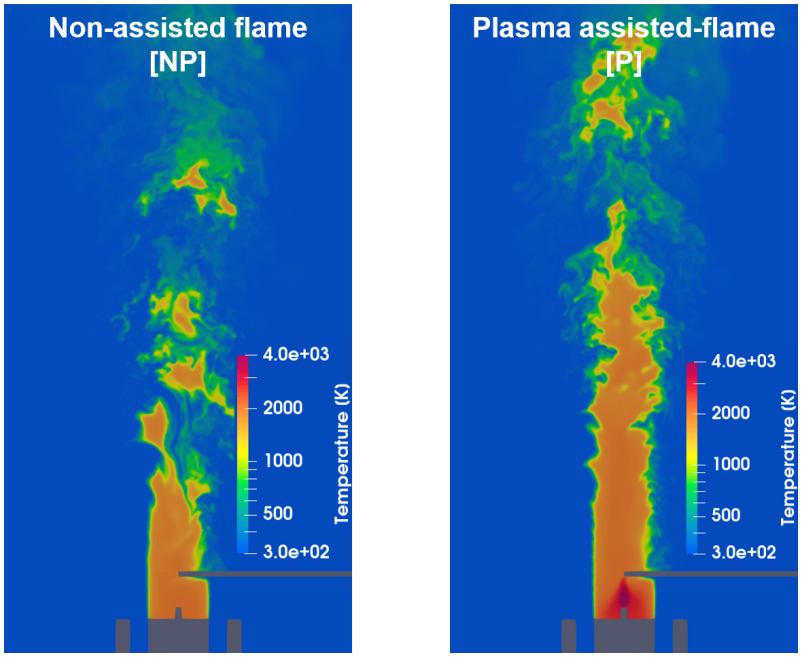

Figure 10.1: *Instantaneous snapshots taken at the same time instant t= 15 ms of the temperature for non-assisted flame case NP (left) and plasma-assisted flame case P (right).*

10.3 Chemical influence of NRP discharges

Average thermo-chemical quantities are computed over the period [10ms,20ms], for both cases NP and P. Radial profiles then are extracted at the position indicated in Fig. 10.3(left), located 4.5 mm above the bluff body, which crosses both the center of the discharges and the bluff-body recirculation zone. Mean radial heat release and methane consumption rates are plotted in Figs. 10.4 (top) and (bottom), respectively. The peak of heat release observed in both NP and P cases corresponds to the flame reactive layer, whose position was also evidenced in Fig. 9.11. The application of NRP discharges at the center of the bluff-body (x=0) causes a significant increase of heat release rate in the reactive layer located at 4 mm $<$ r $<$ 5 mm, which is accompanied by an increase of the methane consumption. The methane source term and the heat release rate are affected by the same factor ($\approx$2.2), which means that the increase of the heat release rate is directly related to the increase of the methane consumption when NRP discharges are applied.

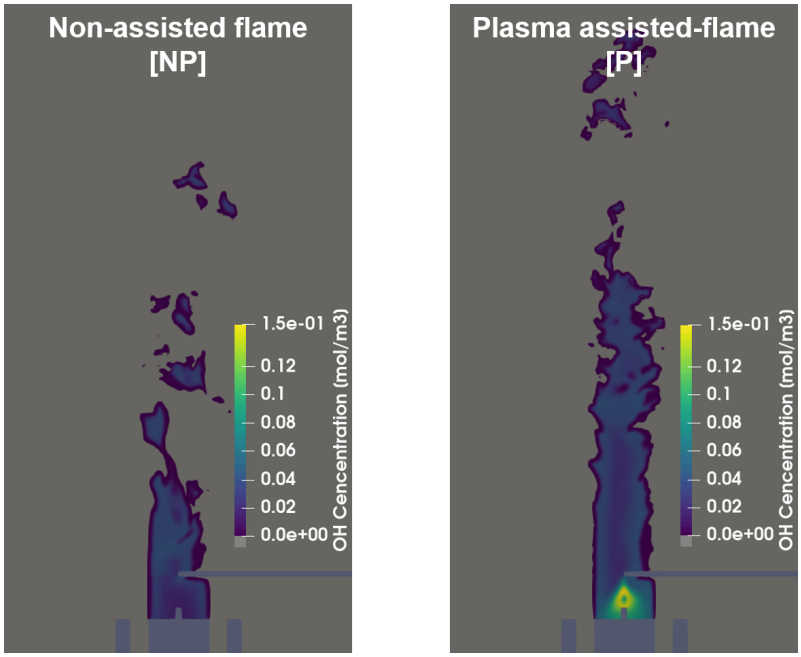

Figure 10.2: *Instantaneous snapshots taken at the same time instant t= 15 ms of the OH concentration for non-assisted flame case NP (left) and plasma-assisted flame case P (right).*

Figure. 10.5 shows the mean radial profile of temperature across the recirculation zone. For case NP, the temperature of the burnt gases contained within the recirculation zone is around 1950K which corresponds to the adiabatic flame temperature of a methane-air mixture at an equivalence ratio of 0.8. However, for the plasma-assisted flame, the mean temperature increases up to 3500K in the plasma zone, where the thermal energy is deposited. This energy is convected by the flow from the center to the periphery of the recirculation zone and induces a temperature increase in the flame front, i.e. at 4 mm $<$ r $<$ 5 mm.

Figures. 10.6 and 10.7 plot the mass fraction of species H_2O-CO_2-O_2-CO and OH-O-H_2-H, repectively. Without plasma, the chemical composition within the recirculation zone corresponds to thermo-chemical equilibrium condition of the methane-air mixture with equivalence ratio of 0.8. When plasma is activated, both H_2O et CO_2 are highly consumed in the discharge zone. At the opposite, the mass fractions of the other species, in particular O and OH, increases significantly.

Figure. 10.8 (left) and (right) shows the chemical pathway diagram in the plasma region during and after a pulse, respectively. The thickness of the arrow is proportional to the reaction rates integrated within the discharge zone. As discussed in Rusterholtz et al. (2013); Castela et al. (2016), O_2 is mainly disso-

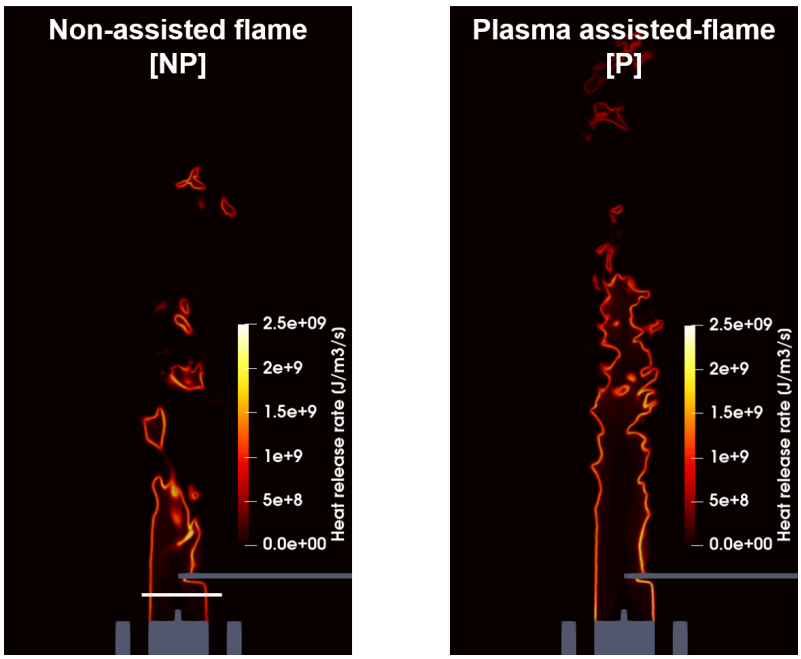

Figure 10.3: *Instantaneous snapshots taken at the same time instant t= 15 ms of the heat release rate for non-assisted flame case NP (left) and plasma-assisted flame case P (right). The white line shows the position of radial profiles represented in the following plots, 4.5 mm above the bluff body.*

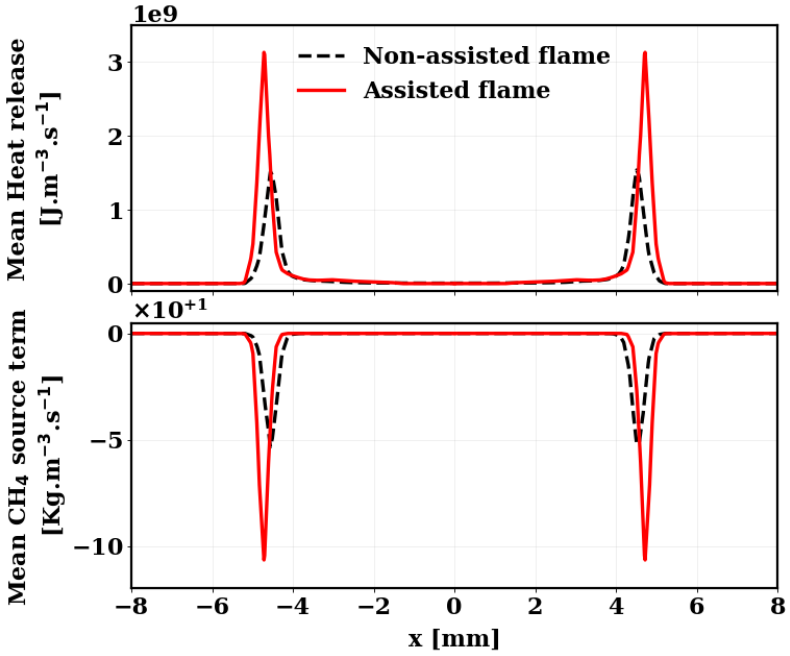

Figure 10.4: *Comparison of mean flame heat release rate (top) and mean CH_4 source term (bottom) radial profiles 4.5 mm above the bluff body for cases NP (dashed black line) and P (red line).*

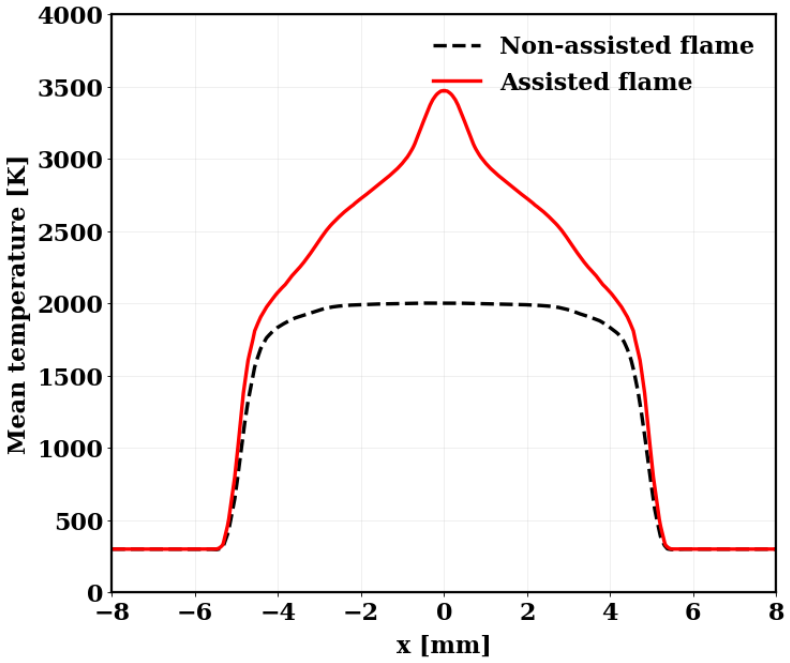

Figure 10.5: *Comparison of mean temperature at 4.5 mm above the bluff body for cases NP (dashed black line) and P (red line).*

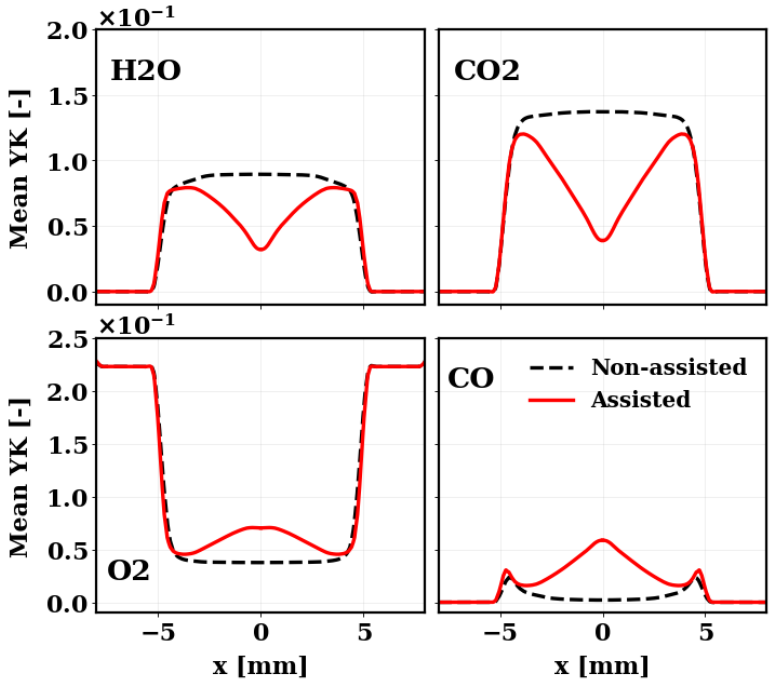

Figure 10.6: *Comparison of mean species mass fractions (H_2O, CO_2, O_2, CO) at 4.5 mm above the bluff body for cases NP (dashed black line) and P (red line).*

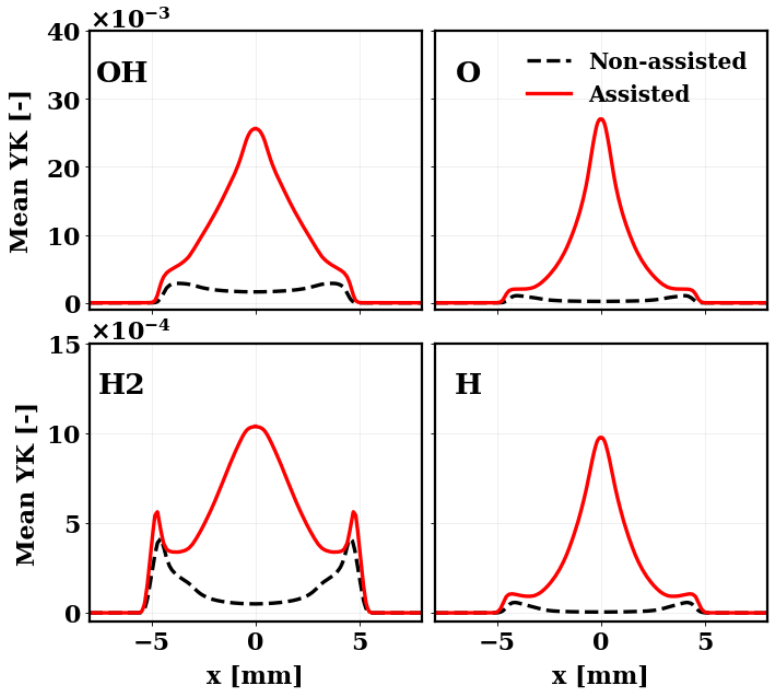

Figure 10.7: *Comparison of mean species mass fractions (OH, O, H_2, H) at 4.5 mm above the bluff body for cases NP (dashed black line) and P (red line).*

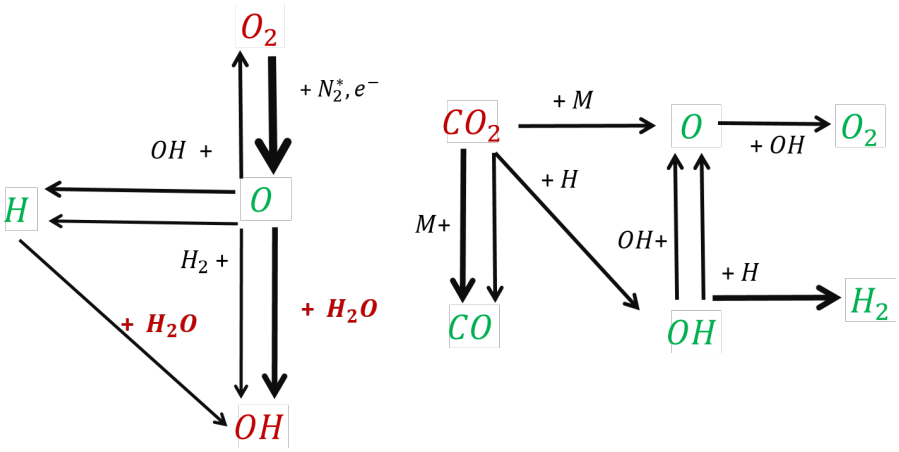

Figure 10.8: *chemical pathways in the discharge zone during (left) and after (right) a pulse.*

ciated into O atoms during an electric pulse (Fig. 10.8 (left)), by the relaxation of nitrogen electronic state. The, the atomic oxygen produced by the discharge reacts with H_2O contained in the burnt gases to produce OH and H. As shown in Figure. 10.8 (right), chemical pathways are completely different after the pulse. CO_2, the main reactant, is consumed by heat and radicals produced during the pulse, leading to a production of CO, H_2, O_2, O and OH. Fig. 10.6 and 10.7 show that, among the species produced in the discharge zone, those with a long lifespan such as OH, O_2 and H_2 are convected up to the flame front in large quantities. At the opposite, species with a shorter lifespan such as O, H does not survive outside the discharge zone.

A second chemical analysis, shown in Fig. 10.9, is performed in the flame reactive layer (4 mm < r < 5 mm) front to identify the CH_4 consumption pathways without and with NRP discharges. Without plasma, CH_4 is mainly consumed by OH, H and O trough the following three elementary reactions:

$$CH_4 + OH \rightarrow CH_3 + H_2O \qquad (R_1)$$

$$CH_4 + H \rightarrow CH_3 + H_2 \qquad (R_2)$$

$$CH_4 + O \rightarrow CH_3 + OH \qquad (R_3)$$

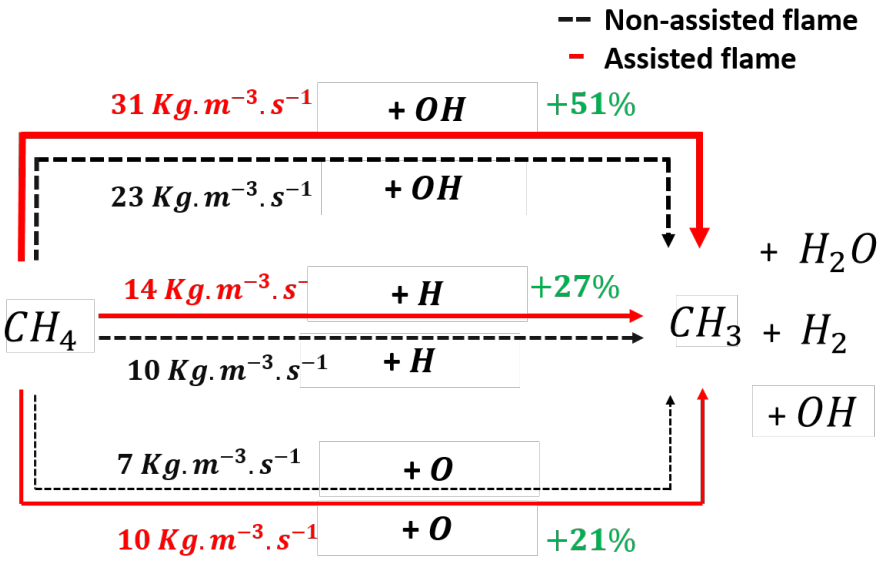

Figure 10.9: *CH4 consumption pathways in the flame front without NRP discharges (dashed black line) and with NRP discharges (red line).*

The impact of the plasma on the rate of progress of reactions R_1, R_2 and R_3 is indicated in Fig. 10.9. As discussed previously, NRP discharges supply the reaction zone with OH, H_2 and O_2. The increase of OH concentration will enhance directly the reaction R_1 by 51%. H_2 and O_2 are dissociated into H and O radicals in the flame reaction zone, increasing therefore also the rate of reactions R_2 and R_3 by 27% and 21%, respectively.

In conclusion, the discharges produces heat and species (OH,H_2,O_2), which are convected within the recirculation zone. Because of its longer lifespan, OH is the main plasma-induced species that reaches the flame front and enhance significantly the chemical reactivity at the flame basis surrounding the recirculation zone. Such local increase of the reactivity enhances the heat release in the periphery of the recirculation zone but also acts as a flame-holder which enables the turbulent flame surface development, increasing the total combustion efficiency.

10.4 Conclusion

The Large Eddy Simulations of the Mini-PAC burner flame stabilization by NRP discharges have been analyzed in this chapter in order the identify and understand the mechanisms of combustion enhancement by non-equilibrium plasma. Comparisons between non-assisted flame and plasma-assisted flame

showed that the NRP discharges pulses induce a significant increase of temperature and an important production of radicals which will enhance the combustion allowing the flame to propagate and develop in high-velocity regions downstream the recirculation zone. A detailed chemical analysis of the simulations results concludes the following mechanisms of interaction between the NRP discharge and the turbulent premixed flame:

1. The electrical pulses generate a plasma in the discharge zone, which produces O atom and heat.
2. During the pulse, O reacts with H_2O to form mainly OH, through the reaction $O + H_2O \rightarrow 2OH$. After the pulse, CO_2 reacts in the inter-electrode region to form H_2 and O_2.
3. Because of their long lifespan, OH, H_2 and O_2 are the main plasma-induced species convected to the flame front thanks to the bluff-body recirculation zone.
4. OH, H_2 and O_2 are consumed with CH_4 in the flame reactive layer surrounding the recirculation zone and locally increase the flame heat release rate. This local increase of the heat release in the vicinity of the recirculation zone is responsible of 30% of the gain in flame power induced by the plasma.
5. The local increase of heat release rate anchored the turbulent flame front which can develop downstream.
6. The total flame surface is increased, increasing the combustion efficiency by 70%.

These results are based on the assumption that O_2 dissociation is the key chemical effect of plasma on combustion chemistry. Future works will aim to challenge this hypothesis by extending the plasma combustion model to account for the dissociation of other species present in the recirculating burnt gases, such as CO_2 and H_2O dissociation induced by the discharge plasma chemistry.

Conclusion and perspectives

Plasma-assisted combustion model:

Experimental studies of plasma-assisted combustion have shown that Nanosecond Repetitively Pulsed (NRP) discharges are a very efficient way to improve flame ignition and stability in lean regimes. These discharges generate a non-equilibrium plasma that induces a local heating and an important production of active species sufficient to enhance the combustion. The aims of this thesis have been to perform numerical simulations of turbulent flames ignition and stabilization by NRP discharges in order to investigate and understand the mechanisms of interaction plasma-flame that lead to combustion enhancement. The simulations have been carried out using the phenomenological plasma model developed by Castela et al. (2016) to capture the effects of the NRP discharge on combustion without solving the electric field and the detailed plasma chemistry reducing therefore CPU cost of the computations. Based on detailed experimental and numerical investigations of NRP discharges, the model considers that the discharge power is split into three contributions: a chemical energy that leads to ultra-fast dissociation of species O_2 into O, a thermal energy that leads to ultra-fast gas heating and a vibrational energy that will relax into gas heating but with a higher time scale compared to the previous two phenomena. The influence of these thermal and chemical effects on the flame are captured through a dedicated source terms in energy and species balance equations and by adding a balance equation for the vibrational energy. This model has been implemented in the low-Mach CFD code YALES2. Results of different test cases performed with YALES2 solver have been compared to previous experimental and numerical results and have allowed the validation of the model.

Mechanisms of flame ignition by NRP discharges:

The dynamic of flame ignition by a single NRP discharge pulse has been previously investigated by Castela et al. (2017) using the phenomenological plasma model. The simulations have shown that the fast energy deposition during the pulse induces an entrainment of fresh gases towards the center of the discharge channel. This phenomenon changes the topology of the hot ignition kernel generated by the pulse from an initial cylindrical shape to a toroidal one, which

significantly reduces the temperature and the concentration of reactive species inside the kernel and leads to its extinction. To cope with this dissipative hydrodynamic effect, Castela suggested to apply a series of pulses to supply, pulse after pulse, the hot kernel with heat and radicals until the flame ignites. Following this study, the dynamic of flame ignition by a series of NRP discharge pulses have been investigated in the present work. 3-D Large Eddy Simulations (LES) of a flowing methane-air mixture ignition, the flow tunnel configuration, have been performed. The results have shown that depending on the flow and discharge parameters, three pulses interaction regimes can be obtained. A fully coupled regime in which the pulses are deposited on top of each other, creating a large ignition kernel that develops into a self-propagating flame. A partially coupled regime in which the hot reactive kernel created by each pulse partially merge, resulting on elongated shape kernel which only under very favorable conditions develops into a self-sustaining flame but most of the cases fails to ignite the reactive mixtures. A decoupled regime in which the generated kernel are spaced apart and independent of each other. The kernels quench under the discharge hydrodynamic effects and the flow turbulence and don't lead to a successful ignition. Results analysis has shown that the pulses interaction regimes are controlled by two characteristic times. The residence time of the gases in the discharge zone, which mainly depend on the flow velocity and the inter-pulse time, the period between two consecutive pulses, given by the inverse of the pulse repetition frequency (PRF). This study indicates that to operate at a fully coupled pulses interaction regime and ensure an efficient ignition of reactive mixtures the NRP discharges must be applied in low-velocity region at high pulse repetition frequency.

The previous methodology that consists in coupling the phenomenological NRP discharge model with the LES combustion formalism in the YALES2 code to perform numerical simulations of plasma assisted combustion has been used to simulate the ignition sequence of the Mini-PAC configuration, a bluff-body turbulent premix burner representative of industrial combustors. The NRP discharges have been applied in low-velocity recirculation zone that forms behind the bluff-body at a pulse repetition frequency of 20 kHz to ensure a fully coupled pulses interaction regime. Two cases have been considered. In the first one, only the thermal effects, ultra-fast heating and slow heating due to the vibrational energy relaxation, are taken in account. In the second one both the thermal effects and the chemical effects due to O2 dissociation into O, are taken in account. Results have shown that in the first case the ignition does not occur even after 100 pulses. The cumulative effect of the NRP discharges is affected by the fresh gases recirculation induced by the discharge which prevent the temperature from reaching a sufficiently high value to allow ignition. In the second case the ignition occurs after 5 pulses. Even though the temperature does not reach a high value, the presence of the radical O, a very active species, produced by the discharges allows the oxidation of the methane and

consequently the ignition of the flame.

The numerical simulations of the Mini-PAC and the flow-tunnel ignition by NRP discharges have shown that ignition success or failure results from a competition between the residence time of the reacting gases in the discharge channel and the combustion chemistry time scale. Based on this hypothesis, a low-order model of flame ignition by NRP discharge has been derived. In this model, NRP discharges are applied in perfectly stirred reactor (PSR) whose volume matches the discharge channel of diameter, to ignite the methane-air mixture continuously injected inside the reactor. The flow of gas passing through the PSR reproduces the gases circulation in the discharge zone. The model has been used to build-up plasma-assisted ignition diagrams which indicate the number of pulses, the ignition delay and the total deposited energy required to ignite the hydrocarbon-air mixture inside the reactor as a function of gases residence time. Parametric studies have been performed to investigate the impact of O production and the discharge parameters: pulse energy, pulse repetition frequency, on the efficiency of the ignition process. The results have confirmed that the atomic O produced during the discharge enhances the methane oxidation reactions, reducing the combustion chemistry time scale and leading to a successful ignition. The results have also shown that the most energy-efficient way to ensure an significant production of atomic O consist on applying the pulses at high repetition frequencies.

Mechanisms of flame stabilization by NRP discharges:

The last part of this work have been dedicated to the study of the mechanisms of flames stabilization by NRP discharges. To understand the physical and chemical mechanisms involved in plasma-assisted combustion, 3-D Large Eddy Simulations (LES) of a lean bluff-body turbulent premixed methane-air flame stabilization by NRP discharges, the Mini-PAC configuration, have been conducted. The numerical simulations performed using the phenomenological plasma model implemented in the YALES2 code, have shown that without NRP discharges, the flame is confined in the low-velocity recirculation zone that forms behind the bluff body. Due to the low burning velocity under lean conditions, the flame front cannot propagate to high-velocity regions outside the recirculation zone. The combustion in this case is incomplete and a significant amount of methane is not burnt. When NRP discharges are applied, the reactivity is significantly increased in the recirculation zone which acts as a flame holder allowing the flame to propagate downstream increasing the flame surface and power.

The chemical analysis performed at the flame basis have shown that the heat and the radical O produced by NRP discharges induce the dissociation of main burnt gases species H_2O and CO_2 into radicals OH, H, CO, O and species

H_2, O_2. The species with long lifespan OH, H_2 and O_2 are convected from the center of the bluff-body recirculation zone to the flame front where they are consumed increasing the chemical reactivity. This causes a local increase of heat release rate that attaches the turbulent flame front which can develop downstream.

Perspectives:

The numerical investigation of flames ignition and stabilization by NRP discharges have shown that the major interest of these discharges is the significant production of radical species which directly interact with the combustion chemistry mechanism. Two mechanisms of interaction plasma flame have been identified. When NRP discharges are applied in fresh gas, a mixture of air and hydrocarbon, the enhancement of the combustion is done through the reaction of O radical produced by the discharge and the fuel. When the discharges are applied in burnt gases, containing combustion products H_2O, CO_2, the interaction and the enhancement of the combustion is done through the OH species which has a longer life span than the O species and can therefore propagate over a longer distance to the place containing fuel. A comparison between these two interaction mechanisms could be carried out in the future in order to identify which one is the more efficient in terms of combustion enhancement but also in term of energy consumption. This will allow to know if the NRP discharges should be applied in the fresh gases or in the burnt gases which will condition the positioning of the electrodes in future combustion systems.

The extension of the Lean Blow-Out (LBO) limit observed by Barbosa et al. (2015) in the BIMER configuration, a rectangular cross section combustion chamber equipped with a two-stage aeronautical multipoint swirl injector, could be investigated numerically using the phenomenological plasma model in order to identify and understand the mechanisms involved in this process.

Future works should also focus on the improvement of the phenomenological plasma model. The simulations have here been performed by assuming that the production of O species is the only chemical effect induced by the NRP discharge. This assumption is not restrictive with respect to the modeling strategy, which can be extended to account for other radicals production and possible fuel dissociation induced by the plasma discharge.

Another aspect to improve concerns the prediction of pollutant emissions in plasma assisted combustion simulations. The combustion kinetic schemes used in the simulations should include species such as NOx and/or soot in order to examine the impact of the NRP discharges on their formation mechanisms and be able to estimate their total production and thus see if plasma assisted lean combustion can effectively reduce pollutant emissions.

Finally, while this study has allowed to understand the mechanisms of ignition and stabilization by NRP discharges of fossil-fuel flames which also apply to the future e-fuel flames due to their similarities in term of chemical properties and reaction pathways, the mechanisms that intervene in the case of hydrogen and ammonia flame and their efficiency remain not well known nor understood. Numerical research projects such as the PLasma-Assisted combustion of Turbulent HydrOgeN flames (PLATHON) project proposed by Benoît Fiorina could be conducted using the phenomenological plasma model to answer these questions.

Synthèse en Français

Introduction

La réduction des émissions polluantes dans les moteurs d'avion et les turbines à gaz est devenue un enjeu majeur pour les industriels en raison des réglementations environnementales de plus en plus accrues. Une solution efficace pour réduire la formation de polluants tel que les oxydes d'azote (NO_x) consiste maintenir une température de flamme relativement faible à l'intérieur des chambres de combustion, ce qui peut être réalisé en utilisant des systèmes de combustion pré-mélangés opérant dans des régimes pauvres. Cependant, Opérer à de faibles températures de combustion à pour conséquence le ralentissement des réactions chimiques ce qui entraîne souvent une combustion incomplète, des difficultés à initier la combustion ainsi que l'apparition d'instabilités de combustion qui peuvent conduire dans certains cas à l'extinction de flammes, ce qui pose problème en terme de sécurité.

Une solution prometteuse pour initier la combustion et améliorer la stabilité de flammes en régimes pauvres, consiste à appliquer des décharges électriques à la base de la flamme (Starikovskiy and Aleksandrov (2013); Ju and Sun (2015)). Les décharges électriques génèrent localement un plasma hors équilibre qui interagit avec le mélange réactif et améliore considérablement le processus d'allumage et la stabilité des flammes dans une large gamme d'applications de combustion (Starikovskiy and Aleksandrov (2013); Ju and Sun (2015)).

Parmi les différents types de décharges, les décharges NRP (Nanosecond Repetitively Pulsed discharges Kruger et al. (2002)) se sont révélées particulièrement efficace pour initier et contrôler les processus de combustion (Bak et al. (2012); Xu et al. (2015); Lefkowitz and Ombrello (2017); Kim et al. (2020); Choe et al. (2021)). Dans la plupart des cas rapportés dans la littérature, les plasmas de non-équilibre pour l'allumage et la stabilisation de la flamme sont obtenus typiquement avec une puissance d'au plus 1% de la puissance libérée par la flamme (Pilla et al. (2006); Barbosa et al. (2015); Blanchard et al. (2021); Di Sabatino and Lacoste (2020)). La bonne efficacité d'un tel procédé est due au fait que l'énergie de la décharge électrique est dépensée pour l'ionisation, l'excitation et

la dissociation des molécules plutôt que de simplement augmenter la température du gaz (Stancu et al. (2010); Montello et al. (2013)). La relaxation des molécules excitées par des réactions d'extinction par collision avec des molécules entraîne une augmentation ultra-rapide (quelques nanosecondes) des radicaux et de la température du gaz à l'intérieur du canal de décharge (Lo et al. (2012); Rusterholtz et al. (2013); Adamovich et al. (2015)) . Dans des conditions typiques, jusqu'à 35% de l'oxygène moléculaire peut être dissocié dans la région inter-électrode (Rusterholtz et al. (2013); Popov (2013a)). Une telle concentration élevée de radicaux a un effet positif à la fois sur les phénomènes d'allumage et sur la stabilisation de la flamme.

Malgré cette efficacité prouvée, les mécanismes fondamentaux de la combustion assistée par plasma ne sont pas bien compris. De même, les outils numériques dont les ingénieurs ont besoin pour évaluer les performances des décharges NRP dans des configurations industrielles n'existent pas. Pour répondre à ces questionnements et besoins, le projet ANR PASTEC (Plasma-ASsiTEd Combustion) a été mis en place avec pour objectif le développement et la validatio contre des expériences d'une stratégies de modélisation adaptée pour la réalisation de simulations de combustion assistée par plasma dans des systèmes de combustion turbulents réalistes. Les simulations permettront de mieux comprendre les mécanismes d'interaction plasma-flamme.

Objectifs et plan de la thèse

Cette travaux de thèse s'inscrivent dans le cadre du projet PASTEC et ont pour objectif le développement, la mise en place et la validation d'une stratégie de modélisation numérique adaptée à la simulation de la combustion assistée par plasma dans des configurations académiques et industrielles. La stratégie ainsi développée est utilisée pour réaliser des simulations d'allumage et de stabilisation de flammes par des décharges NRP dont les résultats sont ensuite analysés pour comprendre les mécanismes d'interaction entre les décharges plasma et la combustion.

Le manuscrit est divisé en trois parties:

Partie I: est consacré à l'élaboration, l'implémentation et la validation d'une stratégie de modélisation pour la simulation de la combustion assistée par plasma. Le chapitre. 2, présente les différents types de décharges plasma et leurs caractéristiques, en mettant l'accent sur la décharge NRP (Nanosecond Repetitively Pulsed) et leurs effets sur la combustion. Les modèles numériques conventionnels de combustion assistée par plasma et leurs limites sont ensuite passés en revue. Enfin, un nouveau modèle phénoménologique de plasma est introduit et décrit. Ce modèle est retenu dans ces travaux pour réaliser des simulations 3-D de la combustion assistée par plasma. Dans le chapitre. 3,

le code YALES2 utilisé pour les simulations est présenté. Les principes fondamentaux de la modélisation de la combustion turbulente sont brièvement décris. L'approche LES et le modèle de combustion turbulente TFLES sont ensuite détaillés. Enfin, le couplage entre l'ensemble des équations LES et le modèle phénoménologique de décharge du NRP est présenté et validé à travers une série de cas test.

La partie II: est consacrée à l'étude numérique d'allumage de flammes par décharges NRP. Le chapitre. 4 discute des limites des dispositifs d'allumage conventionnels et des avantages des décharges NRP pour l'allumage des chambres de combustion pauvres. Une étude numérique tridimensionnelle de l'allumage d'une flamme par une seule impulsion de décharge NRP et de l'impact des effets hydrodynamiques de la décharge, réalisée à l'aide du modèle phénoménologique de plasma, est ensuite présentée. Le chapitre. 5 est consacré à la simulation de l'allumage de la configuration "flow-tunnel" par une série d'impulsions de décharge NRP et à l'étude de l'impact des paramètres d'écoulement et de la décharge sur l'efficacité de l'allumage. Dans le chapitre. 6, le modèle phénoménologique de décharge NRP est utilisé pour simuler l'allumage d'un brûleur pré-mélangé turbulent, la configuration Mini-PAC, représentative des brûleurs industriels. Les résultats de la simulation sont analysés pour identifier les mécanismes d'interaction entre les effets thermiques et chimiques induits par les décharges et la cinétique de combustion. Dans le chapitre. 7, un modèle d'ordre bas d'allumage assisté par plasma basé sur un réacteur parfaitement agité (PSR) est dérivé. Le modèle est utilisé pour réaliser des études paramétriques d'allumage de flammes par décharges NRP afin d'identifier les paramètres optimaux à utiliser pour initier la combustion.

La partie III: est consacrée à l'étude numérique de la stabilisation de flammes par décharges NRP. Une revue des expériences récentes de combustion assistée par plasma réalisées avec des décharges NRP est présentée dans le chapitre. 8. Dans le chapitre. 9, des simulations numériques de la stabilisation de flamme turbulente par décharge NRP sont effectuées sur la configuration Mini-PAC en utilisant le modèle phénoménologique de plasma. Les résultats sont comparés aux mesures expérimentales obtenues dans le cadre du projet PASTEC. Dans le chapitre. 10, une analyse chimique détaillée des simulations Mini-PAC est menée afin de comprendre les mécanismes de stabilisation de la flamme par les décharges NRP.

Conclusions gènèrales

Partie I: Modèle de combustion assistée par plasma

Les études expérimentales de la combustion assistée par plasma ont montré que les décharges NRP sont un moyen très efficace pour améliorer l'allumage et la

stabilité de flammes dans les régimes de combustion pauvres. Ces décharges génèrent un plasma hors-équilibre qui induit un échauffement local et une production importante d'espèces réactives suffisantes pour améliorer la combustion. Afin d'étudier et comprendre les mécanismes d'interaction plasma-flamme qui conduisent à l'amélioration de la combustion, des simulations numériques d'allumage et de stabilisation de flammes par décharges NRP ont été effectuées en utilisant le modèle phénoménologique de plasma développé par Castela et al. (2016) pour capturer les effets de la décharge NRP sur la combustion sans résoudre le champ électrique et la chimie détaillée du plasma réduisant ainsi le coût CPU des calculs. Basé sur des études expérimentales et numériques détaillées des décharges NRP, le modèle considère que l'énergie déposée par la décharge peut être divisée en trois contributions : une énergie chimique qui conduit à une dissociation ultra-rapide de l'espèce O_2 en O, une énergie thermique qui conduit à un chauffage ultra-rapide du gaz et une énergie vibrationnelle qui se relaxe en chaleur mais avec des échelles de temps plus élevées par rapport aux deux phénomènes précédents. L'influence de ces effets thermiques et chimiques sur la combustion est capturée par des termes sources dédiés dans les équations de transport d'énergie et d'espèces et par l'ajout d'une équation de bilan pour l'énergie vibrationnelle. Ce modèle a été implémenté dans le code CFD YALES2. Les résultats de différents cas d'essai réalisés avec le solveur YALES2 ont été comparés aux résultats expérimentaux et numériques et ont permis la validation du modèle.

Partie II: Mécanismes d'allumage de flammes par décharges NRP

La dynamique d'allumage de flamme par une seule impulsion de décharge NRP a été étudiée précédemment par Castela et al. (2017) en utilisant le modèle phénoménologique de plasma. Les simulations ont montré que le dépôt rapide d'énergie pendant l'impulsion induit une recirculation des gaz avec un entraînement de gaz frais vers le centre de la décharge. Ce phénomène change la topologie du noyau d'allumage crée par l'impulsion qui évolue, sous l'effet de l'entraînement des gaz, de sa forme initiale cylindrique à une forme toroïdale. Ceci à pour conséquence la décroissance rapide de la température et de la concentration des espèces réactives à l'intérieur du noyau qui finit par s'éteindre. Pour faire face à ces effets hydrodynamiques dissipatifs, Castela a proposé d'appliquer une série d'impulsions pour alimenter, impulsion après impulsion, le noyau en chaleur et en radicaux jusqu'à l'allumage de la flamme. La dynamique de l'allumage de flammes par une série d'impulsions de décharge NRP a été étudiée dans le présent travail. Des simulations LES (Large Eddy Simulations) 3-D d'allumage d'un écoulement de méthane-air, injecté dans la chambre de combustion "flow-tunnel", ont été réalisées. Les résultats ont montré qu'en fonction des paramètres de l'écoulement et de la décharge, trois régimes d'interaction des impulsions peuvent être obtenus. Un régime entièrement couplé dans lequel les impulsions sont déposées les unes sur les autres, créant

un noyau d'allumage volumineux qui se développe en une flamme. Un régime partiellement couplé dans lequel les noyaux réactifs chauds créés par chaque impulsion fusionnent partiellement, créant un noyau de forme allongée qui peut évoluer dans des conditions très favorables en une flamme. Un régime découplé dans lequel les noyaux générés sont espacés et indépendants les uns des autres. Les noyaux s'éteignent sous l'effet des effets hydrodynamiques de la décharge et de la turbulence de l'écoulement et ne conduisent pas à un allumage réussi. L'analyse des résultats a montré que les régimes d'interaction des impulsions sont contrôlés par deux temps caractéristiques. Le temps de séjour des gaz dans la zone de décharge, qui dépend principalement de la vitesse de l'écoulement, et le temps inter-impulsion, la période entre deux impulsions consécutives, donnée par l'inverse de la fréquence de répétition des impulsions. Cette étude indique que pour fonctionner dans un régime d'interaction d'impulsions entièrement couplées et garantir ainsi un allumage efficace des mélanges réactifs, les décharges NRP doivent être appliquées dans une région à faible vitesse à une fréquence de répétition des impulsions élevée.

La méthodologie précédente qui consiste à coupler le modèle phénoménologique de décharge NRP avec le formalisme de combustion LES dans le code YALES2, a ensuite été utilisée pour simuler la séquence d'allumage de la configuration Mini-PAC, un brûleur pré-mélangé turbulent avec accroche flamme représentatif des brûleurs industriels. Les décharges NRP ont été appliquées dans la zone de recirculation à faible vitesse qui se forme derrière l'accroche flamme à une fréquence de répétition des impulsions de 20 kHz pour assurer un régime d'interaction des impulsions entièrement couplées. Deux cas ont été considérés. Dans le premier, seuls les effets thermiques, le chauffage ultra-rapide et le chauffage lent dû à la relaxation de l'énergie vibratoire, sont pris en compte. Dans le second, les effets thermiques et les effets chimiques avec la dissociation de O_2 en O sont pris en compte. Les résultats ont montré que dans le premier cas, l'allumage n'est pas réussi même après 100 impulsions. L'effet cumulatif des décharges du NRP est affecté par la recirculation des gaz frais induite par la décharge qui empêche la température d'atteindre une valeur suffisamment élevée pour permettre l'allumage. Dans le second cas, l'allumage se produit après 5 impulsions. Même si la température n'atteint pas une valeur élevée, la présence du radical O, une espèce très réactive, produite par la décharge permet l'oxydation du méthane et par conséquent l'allumage de la flamme.

Les simulations numériques de l'allumage du Mini-PAC et du flow-tunnel par décharges NRP ont montré que le succès ou l'échec de l'allumage résulte d'une compétition entre le temps de résidence des gaz chauds réactifs dans la zone de décharge et l'échelle de temps de la chimie de la combustion. Sur la base de cette hypothèse, un modèle d'ordre bas d'allumage de flamme par décharge NRP a été dérivé. Dans ce modèle, les décharges NRP sont appliquées dans un réacteur parfaitement agité (PSR) dont le volume correspond au diamètre du la zone de

décharge, pour allumer le mélange méthane-air injecté en continu à l'intérieur du réacteur. Le flux de gaz traversant le PSR reproduit la circulation des gaz dans la zone de décharge. Le modèle a été utilisé pour établir des diagrammes d'allumage assisté par plasma qui indiquent le nombre d'impulsions, le délai d'allumage et l'énergie totale déposée nécessaire pour enflammer le mélange hydrocarbure-air à l'intérieur du réacteur en fonction du temps de séjour des gaz. Des études paramétriques ont été réalisées pour étudier l'impact de la production d'O et des paramètres de décharge : énergie des impulsions, fréquence de répétition des impulsions, sur l'efficacité du processus d'allumage. Les résultats ont confirmé que l'O atomique produit pendant la décharge renforce les réactions d'oxydation du méthane, réduisant ainsi l'échelle de temps de la chimie de la combustion et conduisant à un allumage réussi. Les résultats ont également montré que la manière la plus efficace en terme d'énergie pour assurer une production significative d'O atomique, consiste à appliquer les impulsions à des fréquences de répétition élevées.

Partie III: Mécanismes de stabilisation de flammes par décharges NRP

La dernière partie de ce travail a été consacrée à l'étude des mécanismes de stabilisation des flammes par les décharges NRP. Afin de comprendre les mécanismes physiques et chimiques impliqués dans la combustion assistée par plasma, des simulations 3-D à grandes échelles (LES) d'une flamme pré-mélangée méthane-air turbulente et pauvre, la configuration Mini-PAC, ont été réalisées. Les simulations numériques réalisées en utilisant le modèle phénoménologique de plasma implémenté dans le code YALES2, ont montré que sans les décharges NRP, la flamme est confinée dans la zone de recirculation à faible vitesse qui se forme derrière l'accroche flamme. En raison de la faible vitesse de combustion dans des conditions pauvres, le front de flamme ne peut pas se propager vers des régions à haute vitesse en dehors de la zone de recirculation. Dans ce cas, la combustion est incomplète et une quantité importante de méthane n'est pas brûlée. Lorsque des décharges NRP sont appliquées, la réactivité du mélange est significativement augmentée dans la zone de recirculation ce qui augmente la vitesse de la flamme permettant à cette dernière de se propager en aval, augmentant à la fois la surface et la puissance de la flamme.

L'analyse chimique réalisée à la base de la flamme a montré que la chaleur et le radical O produit par les décharges NRP induisent la dissociation des espèces présentent dans les gaz brûlés H_2O et CO_2 en radicaux OH, H, CO, O et espèces H_2, O_2. Les espèces à longue durée de vie tel que le OH, H_2 et O_2 sont transportées du centre de la zone de décharge vers le front de flamme où elles réagissent avec le CH_4, ce qui augmente la réactivité chimique. Cela provoque une augmentation locale du taux de dégagement de chaleur et de la vitesse de flamme lui permettant de de propager en aval dans les zone de haute vitesse.

Conclusion

L'étude numérique de l'allumage et de la stabilisation des flammes par décharges NRP a montré que l'intérêt majeur de ces décharges est la production importante d'espèces radicalaires qui interagissent directement avec la chimie de la combustion. Deux mécanismes d'interaction plasma-flamme ont été identifiés. Lorsque les décharges NRP sont appliquées dans un gaz frais, mélange d'air et d'hydrocarbure, l'amélioration de la combustion se fait par la réaction du radical O produit par la décharge avec le combustible. Lorsque les décharges sont appliquées dans des gaz brûlés, contenant des produits de combustion H_2O, CO_2, l'interaction et l'amélioration de la combustion se font par l'intermédiaire de l'espèce OH qui a une durée de vie plus longue que les espèces O et qui peut donc se propager sur de longue distance vers l'endroit contenant du combustible.

References

Adamovich, I. V., T. Li, and W. R. Lempert (2015). Kinetic mechanism of molecular energy transfer and chemical reactions in low-temperature air-fuel plasmas. *Philosophical transactions. Series A, Mathematical, physical, and engineering sciences 373*. *(p. 17, 71, 176)*

Akal, D., O. Öztuna, and M. K. Büyükakın (2020). A review of hydrogen usage in internal combustion engines (gasoline-lpg-diesel) from combustion performance aspect. *International Journal of Hydrogen Energy 45*(60), 35257–35268. *(p. 2)*

Aleksandrov, N. L., S. V. Kindysheva, E. N. Kukaev, S. M. Starikovskaya, and A. Y. Starikovskii (2009). Simulation of the ignition of a methane-air mixture by a high-voltage nanosecond discharge. *Plasma Physics Reports 35*(10), 867–882. *(p. 71)*

Aleksandrov, N. L., S. V. Kindysheva, E. N. Kukaev, S. M. Starikovskaya, and A. Y. Starikovskii (2010). Mechanism of ultra-fast heating in a non-equilibrium weakly ionized air discharge plasma in high electric fields. *Journal of Physics D: Applied Physics 43*, 255201. *(p. 35)*

Bagheri, B., J. Teunissen, U. Ebert, M. M. Becker, S. Chen, O. Ducasse, O. Eichwald, D. Loffhagen, A. Luque, D. Mihailova, J. M. Plewa, J. van Dijk, and M. Yousfi (2018). Comparison of six simulation codes for positive streamers in air. *Plasma Sources Science and Technology 27*(9), 095002. *(p. 24)*

Bak, M. S., H. Do, M. G. Mungal, and M. A. Cappelli (2012). Plasma-assisted stabilization of laminar premixed methane/air flames around the lean flammability limit. *Combustion and Flame 159*, 3128–3137. *(p. 18, 25, 26, 28, 175)*

Bak, M. S., H. Do, M. G. Mungal, and M. A. Cappelli (2013). Studies on the stability limit extension of premixed and jet diffusion flames of methane, ethane, and propane using nanosecond repetitive pulsed discharge plasmas. *Combustion and Flame 160*(11), 2396–2403. *(p. 18)*

Barbosa, S., G. Pilla, D. A. Lacoste, P. Scouflaire, S. Ducruix, C. O. Laux, and D. Veynante (2015). Influence of nanosecond repetitively pulsed discharges on the stability of a swirled propane/air burner representative of an aeronautical combustor. *Philosophical Transactions of the Royal Society 373*, 20140335. *(p. xvii, 3, 4, 18, 134, 135, 172, 175)*

Barleon, N. (2022). *Detailed modeling and simulations of Nanosecond Repetitively Pulsed Discharges for Plasma-Assisted Combustion.* Ph. D. thesis, Institut National Polytechnique de Toulouse, France. *(p. 28)*

Barleon, N., L. Cheng, B. Cuenota, O. Vermorel, and A. Bourdon (2022). Investigation of the impact of nrp discharge frequency on the ignition of a lean methane-air mixture using fully coupled plasma-combustion numerical simulations. *Proceedings of the Combustion Institute*. *(p. x, 27, 28)*

Blanchard, V., N. Q. Minesi, Y. Bechane, B. Fiorina, and C. O. Laux (2021). Experimental and numerical characterization of a lean turbulent premixed flame stabilized by nanosecond discharges. *AIAA Scitech 2022-2255*. *(p. xviii, 143, 144, 153)*

Blanchard, V., N. Q. Minesi, S. Stepanyan, G. D. Stancu, and C. O. Laux (2021). Dynamics of a lean flame stabilized by nanosecond discharges. *AIAA Scitech 2021-1700*. *(p. xviii, 4, 18, 144, 146, 175)*

Bothien, M. R., A. Ciani, J. P. Wood, and G. Fruechtel (2019). Toward decarbonized power genera- tion with gas turbines by using sequential combustion for burning hydrogen. *J. Eng. Gas Turbines Power 141*(12), 121013. *(p. 2)*

Bradley, D., C. Sheppard, I. Suardjaja, and R. Woolley (2004). Fundamentals of high-energy spark ignition with lasers. *Combustion and Flame 138*, 55–77. *(p. 74)*

Bray, K. N. C. (1996). The challenge of turbulent combustion. *In Symposium (International) on Combustion 26*, 1–26. *(p. 47)*

Breden, D., L. L. Raja, C. A. Idicheria, P. M. Najt, and S. Mahadevan (2013). A numerical study of high-pressure non-equilibrium streamers for combustion ignition application. *Journal of Applied Physics 114*(8), 083302. *(p. 71)*

Brynolf, S., M. Taljegard, M. Grahn, and J. Hansson (2018). Electrofuels for the transport sector: A review of production costs. *Renewable and Sustainable Energy Reviews 81*, 1887–1905. *(p. 1)*

Cardoso, J. S., V. Silva, R. C. Rocha, M. J. Hall, M. Costa, and D. Eusébio (2021). Ammonia as an energy vector: current and future prospects for low-carbon fuel applications in internal combustion engines. *Journal of Cleaner Production 296*, 126562. *(p. 2)*

Casey, T. A., J. Han, M. Belhi, P. G. Arias, F. Bisetti, H. G. Im, and J.-Y. Chen (2017). Simulations of planar non-thermal plasma assisted ignition at atmospheric pressure. *Proceedings of the Combustion Institute 36*(3), 4155–4163. *(p. 28, 71)*

Castela, M. (2016). *Direct numerical simulations of plasma-assisted ignition in quiescent and turbulent flow conditions.(p.78-79)*. Ph. D. thesis, Ecole CentraleSupelec. *(p. 81)*

Castela, M., B. Fiorina, A. Coussement, O. Gicquel, N. Darabiha, and C. O. Laux (2016). Modelling the impact of non-equilibrium discharges on re-

active mixtures for simulations of plasma-assisted ignition in turbulent flows. *Combustion and Flame 166*, 133–147. *(p. x, xi, xii, 11, 13, 28, 31, 32, 35, 37, 41, 52, 54, 55, 56, 57, 58, 59, 60, 61, 62, 71, 79, 103, 106, 115, 118, 140, 141, 144, 162, 169, 178)*

Castela, M., S. Stepanyan, B. Fiorina, A. Coussement, O. Gicquel, N. Darabiha, and C. O. Laux (2017). A 3-d dns and experimental study of the effect of the recirculating flow pattern inside a reactive kernel produced by nanosecond plasma discharges in a methane-air mixture. *Proceedings of the Combustion Institute 36*, 4095–4103. *(p. xii, xiii, 66, 71, 72, 73, 74, 103, 169, 178)*

Caudal, J. (2013). *Simulation numerique du reformage auto-thermique du methane*. Ph. D. thesis, Ph.D Thesis, Ecole Centrale Paris. (p. 68,69, 71). *(p. 55, 61)*

Celestin, S. (2008). *Study of the dynamics of streamers in air at atmospheric pressure*. Ph. D. thesis, Ecole centrale de Paris, France. *(p. 22, 23)*

Chanrion, O. and T. Neubert (2008). A pic-mcc code for simulation of streamer propagation in air. *Journal of Computational Physics 227*(15), 7222–7245. *(p. 22)*

Charlette, F., D. Veynante, and C. Meneveau (2002). A power-law wrinkling model for les of premixed turbulent combustion: Part i non dynamic formulation and initial tests. *Combustion and Flame 131*, 159–180. *(p. 50, 89, 107, 147)*

Cheng, L., N. Barleon, B. Cuenota, O. Vermorel, and A. Bourdon (2022). Plasma assisted combustion of methane-air mixtures: Validation and reduction. *Combustion and Flame 240*. *(p. 26)*

Chintala, V. and K. A. Subramanian (2017). A comprehensive review on utilization of hydrogen in a compression ignition engine under dual fuel mode. *Renewable and Sustainable Energy Reviews 70*, 472–491. *(p. 2)*

Choe, J. and W. Sun (2022). Experimental investigation of non-equilibrium plasma-assisted ammonia flames using nh2* chemiluminescence and oh planar laser-induced fluorescence. *Proceedings of the Combustion Institute 000*, 1–8. *(p. ix, 4)*

Choe, J., W. Sun, T. Ombrello, and C. Carter (2021). Plasma assisted ammonia combustion: Simultaneous no x reduction and flame enhancement. *Combustion and Flame 228*, 430–432. *(p. 4, 175)*

Clements, R., P. Smy, and J. Dale (1981). An experimental study of the ejection mechanism for typical plasma jet igniters. *Combustion and Flame 42*, 287–295. *(p. 66)*

COFFEE, T. P. (1984). Kinetic mechanisms for premixed, laminar, steady state methane/air flames. *Combustion and Flame 55*, 161–170. *(p. 60, 107)*

Colin, O., F. Ducros, D. Veynante, and T. Poinsot (2000). A thickened flame model for large eddy simulations of turbulent premixed combustion. *Physics of Fluids 12*(7), 1843–1863. *(p. 48, 50, 89, 107, 147)*

Coussement, A. (2012). *Direct numerical simulation and reduced chemical schemes for combustion of perfect and real gases*. Ph. D. thesis, Ph.D Thesis, Ecole Centrale des Arts et Manufactures. (p. 68). *(p. 55, 61, 72)*

De Joannon, M., G. Langella, F. Beretta, A. Cavaliere, and C. Noviello (2000). Mild combustion: Process features and technological constrains. *Combustion Science and Technology 153*(1), 33–50. *(p. 3)*

Di Sabatino, F., T. F. Guiberti, J. P. Moeck, W. L. Roberts, and D. A. Lacoste (2021). Actuation efficiency of nanosecond repetitively pulsed discharges for plasma-assisted swirl flames at pressures up to 3 bar. *Journal of Physics D: Applied Physics 54*, 075208. *(p. 134)*

Di Sabatino, F. and D. A. Lacoste (2020). Enhancement of the lean stability and blow-off limits of methane-air swirl flames at elevated pressures by nanosecond repetitively pulsed discharges. *Journal of Physics D: Applied Physics 53*, 355201. *(p. xvii, 4, 18, 134, 136, 175)*

Dumitrache, C., A. Gallant, N. Minesi, S. Stepanyan, G. D. Stancu, and C. O. Laux (2019). Hydrodynamic regimes induced by nanosecond pulsed discharges in air: mechanism of vorticity generation. *Journal of Physics D: Applied Physics 52*, 364001. *(p. xiii, 74, 75, 76, 77)*

Elbaz, A. M., S. Wang, T. F. Guiberti, and W. L. Roberts (2022). Review on the recent advances on ammonia combustion from the fundamentals to the applications. *Fuel Communications 10*, 100053. *(p. 2)*

Esakov, I., L. Grachev, K. Khodataev, and D. Van Wie (2004). Experiments on propane ignition in high-speed airflow using a deeply under critical microwave discharge. *42nd AIAA aerospace sciences meeting including the new horizons forum and aerospace exposition, Reno, Nevada*. *(p. 3)*

Fiorina, B., D. Veynante, and S. Candel (2015). Modeling combustion chemistry in large eddy simulation of turbulent flames. *Flow, Turbulence and Combustion 94*(1), 3–42. *(p. 47)*

Fiorina, B., R. Vicquelin, P. Auzillon, N. Darabiha, O. Gicquel, and D. Veynante (2010). A filtered tabulated chemistry model for les of premixed combustion. *Combustion and Flame 157*(3), 465–475. *(p. 48)*

Flitti, A. and S. Pancheshnyi (2009). Gas heating in fast pulsed discharges in n2-o2 mixtures. *The European Physical Journal 45*, 21001. *(p. 35)*

Frenklach, M. and H. Wang (1994). *Detailed Mechanism and Modeling of Soot Particle Formation. In: Bockhorn, H. (eds) Soot Formation in Combustion.* Springer Series in Chemical Physics. *(p. 2)*

Galletti, C., A. Parente, M. Derudi, R. Rota, and L. Tognotti (2009). Numerical and experimental analysis of no emissions from a lab-scale burner fed with hydrogen-enriched fuels and operating in mild combustion. *International Journal of Hydrogen Energy 34*, 8339–8351. *(p. 3)*

Germano, M., U. Piomelli, P. Moin, and W. H. Cabot (1991). A dynamic subgrid-scale eddy viscosity model. *Physics of Fluids A: Fluid Dynamics 3*(7), 1760–1765. *(p. 46, 89, 107, 147)*

Hagelaar, G. J. M. and L. C. Pitchford (2005). Solving the boltzmann equa-

tion to obtain electron transport coefficients and rate coefficients for fluid models. *Plasma Sources Science and Technology 14*(4), 722–733. *(p. 25)*

Haworth, D. C. (2010). Progress in probability density function methods for turbulent reacting flows. *Progress in energy and combustion science 36*(2), 168–259. *(p. 47)*

Heywood, J. (1988). Internal combustion engines fundamentals. *McGraw-Hill, Inc.*. *(p. 2)*

Huber, K. P. and G. Herzberg (1979). Molecular spectra and molecular structure, molecular spectra and molecular structure. *Springer US*. *(p. 155)*

Hänggi, S., P. Elbert, T. Bütler, U. Cabalzar, S. Teske, C. Bach, and C. Onder (2019). A review of synthetic fuels for passenger vehicles. *Energy Reports 5*, 555–569. *(p. 2)*

Ilbas, M., I. Yılmaz, T. N. Veziroglu, and Y. Kaplan (2005). Hydrogen as burner fuel: modelling of hydrogen-hydrocarbon composite fuel combustion and nox formation in a small burner. *Fuel Communications 29*(11), 973–990. *(p. 2)*

International-Energy-Agency (2022). World energy outlook 2021. https://www.iea.org/reports/world-energy-outlook-2021. *(p. 1)*

Ju, Y. and W. Sun (2015). Plasma assisted combustion: Dynamics and chemistry. *Progress in Energy and Combustion Science 48*, 21–83. *(p. ix, 4, 13, 16, 71, 175)*

Kerstein, A. R., W. T. Ashurst, and F. A. Williams (1988). Field equation for interface propagation in an unsteady homogeneous flow field. *Physical Review A 37*(7), 2728. *(p. 48)*

Kim, G. T., C. S. Yoo, S. H. Chung, and J. Park (2020). Effects of non-thermal plasma on the lean blowout limits and co/nox emissions in swirl-stabilized turbulent lean-premixed flames of methane/air. *Combustion and Flame 212*, 403–414. *(p. 4, 18, 175)*

Kim, W., H. Do, M. M. G., and M. A. Cappelli (2007). Investigation of no production and flame structure in plasma enhanced premixed combustion. *Proceedings of the Thirty-One Symposium on Combustion 31*(2), 3319–3326. *(p. 4, 18)*

Klimov, A., V. Bityurin, A. Kuznetsov, B. Tolkunov, N. Vystavkin, and M. Vasiliev (2004). External and internal plasma-assisted combustion. *42nd AIAA aerospace sciences meeting including the new horizons forum and aerospace exposition, Reno, Nevada*. *(p. 4)*

Kobayashi, H., A. Hayakawa, K. K. A. Somarathne, and E. C. Okafor (2018). Science and technology of ammonia combustion. *Proceedings of the Combustion Institute 37*, 109–133. *(p. 2)*

Kobayashi, K., S. Tomioka, and T. Mitani (2004). Supersonic flow ignition by plasma torch and h2/o2 torch. *Journal of Propulson and Power 20*, 294–301. *(p. 3)*

Kolmogorov, A. N. (1941). The local structure of turbulence in incompressible viscous fluid for very large reynolds numbers. *Doklady Akademiia*

Nauk SSSR 30, 301–305. *(p. 43)*

Kono, M., K. Niu, T. Tsukamoto, and Y. Ujiie (1989). Mechanism of flame kernel formation produced by short duration sparks. *Symposium (International) on Combustion Institute 22*, 1643–1649. *(p. xiii, 66, 74, 75)*

Kozak, T. and A. Bogaerts (2014). Splitting of co2 by vibrational excitation in non-equilibrium plasmas: a reaction kinetics model. *Plasma Sources Science and Technology 23*(4), 045004. *(p. 25)*

Kraushaar, M. (2011). *Application of the compressible and low-mach number approaches to large eddy simulation of turbulent flows in aero-engines*. Ph. D. thesis, INPT. *(p. 42)*

Kruger, C. H., C. O. Laux, L. Yu, D. M. Packan, and L. Pierrot (2002). Nonequilibrium discharges in air and nitrogen plasmas at atmospheric pressure. *Pure and Applied Chemistry 74*(3), 337–347. *(p. 4, 15, 17, 175)*

Kulikovsky, A. A. (1997). Positive streamer between parallel plate electrodes in atmospheric pressure air. *Journal of Physics D: Applied Physics 30*(3), 441–450. *(p. 22, 24)*

Kuo, K. K. and R. Acharya (2012). *Fundamentals of Turbulent and Multiphase Combustion*. John Wiley Sons. *(p. 48)*

Kushner, M. J. (2003). Modeling of microdischarge devices: Pyramidal structures. *Journal of Applied Physics 95*(3), 846–859. *(p. 23)*

Landau, L. and E. Teller (1936). Zur theorie der sohdldispersion. *Physik. Z. Sowjetmion, 10, 34.*. *(p. 33)*

Law, C. (2006). *Combustion physics*. Cambridge University Press: Cambridge. *(p. ix, 3)*

Lefebvre, A. H. and D. R. Ballal (2010). *GAS Turbine Combustion Alternative Fuels and Emissions*. (3rd ed.). Taylor Francis. *(p. 2, 66)*

Lefkowitz, J. K., S. D. Hammack, C. Carter, and T. Ombrello (2020). Elevated oh production from nphfd and its effect on ignition. *Proceedings of the Combustion Institute 000*, 1–8. *(p. xv, 95, 99, 100, 102)*

Lefkowitz, J. K. and T. Ombrello (2017). An exploration of inter-pulse coupling in nanosecond pulsed high frequency discharge ignition. *Combustion and Flame 180*, 136–147. *(p. vii, xiii, xiv, 4, 18, 79, 81, 82, 83, 84, 85, 86, 95, 102, 175)*

Li, C., U. Ebert, and W. Hundsdorfer (2010). Spatially hybrid computations for streamer discharges with generic features of pulled fronts: I. planar fronts. *Journal of Computational Physics 229*(1), 200–220. *(p. 22)*

Lim, M., R. Anderson, and V. S. Arpaci (1987). Prediction of spark kernel development in constant volume combustion. *Combustion and Flame 69*(3), 303–316. *(p. 66)*

Lindstedt, P. (1998). Modeling of the chemical complexities of flames. *Proceedings of the Combustion Institute 1*(27), 269–285. *(p. 72)*

Lo, A., G. Cleon, P. Vervisch, and A. Cessou (2012). Spontaneous raman scattering: a useful tool for investigating the afterglow of nanosecond

scale discharges in air. *Applied Physics B 107*, 229–242. *(p. 17, 176)*

Loeb, L. and J. Meek (1940a). The mechanism of spark discharge in air at atmospheric pressure. i. *Journal of Applied Physics 11*(6), 438–447. *(p. 22)*

Loeb, L. and J. Meek (1940b). The mechanism of spark discharge in air at atmospheric pressure. ii. *Journal of Applied Physics 11*(7), 459–474. *(p. 22)*

Lu, T. and C. K. Law (2008). A criterion based on computational singular perturbation for the identification of quasi steady state species: a reduced mechanism for methane oxidation with no chemistry. *Combustion and Flame 154*(4), 761–774. *(p. 147)*

Magnussen, B. F. and B. H. Hjertager (1977). On mathematical modeling of turbulent combustion with special emphasis on soot formation and combustion. *Symposium (International) on Combustion 16*(1), 719–729. *(p. 47)*

Majda, A. and J. Sethian (1985). The derivation and numerical solution of the equations for zero mach number combustion. *Combustion science and technology 42*(3-4), 185–205. *(p. 42)*

Maly, R. and M. Vogel (1979). Initiation and propagation of flame fronts in lean ch4-air mixtures by the three modes of the ignition spark. *Symposium (International) on Combustion 17*(10), 821–831. *(p. xii, 15, 66, 67, 68)*

Mao, X. and Q. Chen (2018). Effects of vibrational excitation on nanosecond discharge enhanced methane-air ignition. *AIAA Journal 56*(11), 4312–4320. *(p. 71)*

Marek, C., T. Smith, and K. Kundu (2005). Low emission hydrogen combustors for gas turbines using lean direct injection. *41st AIAA/ASME/SAE/ASEE joint propulsion conference exhibit, Tucson, Arizona*, 695. *(p. 3)*

Masiol, M. and R. M. Harrison (2014). Aircraft engine exhaust emissions and other airport-related contributions to ambient air pollution: A review. *Atmospheric Environment 95*, 409–455. *(p. 2)*

Menon, S. and W. H. Calhoon-Jr (1996). Subgrid mixing and molecular transport modeling in a reacting shear layer. *Symposium (International) on Combustion 26*, 59–66. *(p. 47)*

Mercier, R. (2015). *Turbulent combustion modeling for Large Eddy Simulation of non-adiabatic stratified flames.* Ph. D. thesis, Ecole Centrale Paris. *(p. x, 45)*

Merotto, L., M. Balmelli, W. Vera-Tudela, and P. Soltic (2022). Comparison of ignition and early flame propagation in methane/air mixtures using nanosecond repetitively pulsed discharge and inductive ignition in a pre-chamber setup under engine relevant conditions. *Combustion and Flame 237*, 111851. *(p. 18, 71)*

Midilli, A. and I. Dincer (2008). Hydrogen as a renewable and sustainable solution in reducing global fossil fuel consumption. *International Journal*

of Hydrogen Energy 33(16), 4209–4222. *(p. 1)*

Millikan, R. C. and D. R. White (1963). Systematics of vibrational relaxation. *Journal Chemical Physics 39*(12), 3209–3213. *(p. 31, 33)*

Minesi, N. (2020). *Thermal spark formation and plasma-assisted combustion by nanosecond repetitive discharges*. Ph. D. thesis, Université Paris-Saclay, France. *(p. xviii, xix, 142, 153, 155)*

Minesi, N. Q., V. P. Blanchard, E. Pannier, G. D. Stancu, and C. O. Laux (2022). Plasma-assisted combustion with nanosecond discharges. i: Discharge effects characterization in the burnt gases of a lean flame plasma. *Plasma Sources Science and Technology 31*, 045029. *(p. xviii, 144, 145)*

Moin, P., K. Squires, W. Cabot, and S. Lee (1991). A dynamic subgrid-scale model for compressible turbulence and scalar transport. *Physics of Fluids A: Fluid Dynamics 3*(11), 2746–2757. *(p. 46)*

Montello, A., Z. Yin, D. Burnette, I. V. Adamovich, and W. R. Lempert (2013). Picosecond cars measurements of nitrogen vibrational loading and rotational/translational temperature in non-equilibrium discharges. *Journal of Physics D: Applied Physics 46*(46), 464002. *(p. 17, 176)*

Moureau, V., P. Domingo, and L. Vervisch (2011). Design of a massively parallel cfd code for complex geometries. *Comptes Rendus Mécanique C. R. Mecanique 339*, 141–148. *(p. 41, 50, 54, 89, 107, 147)*

Nakaya, S., S. Iseki, X. Gu, Y. Kobayashi, and M. Tsue (2017). Flame kernel formation behaviors in close dual-point laser breakdown spark ignition for lean methane/air mixtures. *Proceedings of the Combustion Institute 36*(3), 3441–3449. *(p. 66)*

Nicoud, F. and F. Ducros (1999). Subgrid-scale stress modelling based on the square of the velocity gradient tensor. *Flow, Turbulence and Combustion 62*(3), 183–200. *(p. 46)*

Nicoud, F., H. B. Toda, O. Cabrit, S. Bose, and J. Lee (2011). Using singular values to build a subgrid-scale model for large eddy simulations. *Physics of Fluids 23*(8). *(p. 46)*

Pai, D., D. A. Lacoste, and C. O. Laux (2008). Images of nanosecond repetitively pulsed plasmas in preheated air at atmospheric pressure. *IEEE Transactions on Plasma Science 36*(4), 974–975. *(p. ix, 15)*

Pancheshnyi, S. (2005). Role of electronegative gas admixtures in streamer start, propagation and branching phenomena. *Plasma Sources Science and Technology 17*(4), 645–653. *(p. 22)*

Pancheshnyi, S. V., D. A. Lacoste, A. Bourdon, and C. O. Laux (2006). Ignition of propane-air mixtures by a repetitively pulsed nanosecond discharge. *IEEE Transactions on Plasma Science 34*(6), 2478–2487. *(p. 4, 18)*

Park, C. (1993). Review of chemical-kinetic problems of future nasa missions, i: Earth entries. *Journal of Thermophysics and Heat Transfer 7*(3), 385–39. *(p. 31)*

Pilla, G., D. Galley, D. A. Lacoste, F. Lacas, D. Veynante, and C. O. Laux.

(2006). Stabilization of a turbulent premixed flame using a nanosecond repetitively pulsed plasma. *IEEE Transactions on Plasma Science 34*(6), 2471–2477. *(p. xvii, 4, 18, 136, 138, 140, 175)*

Poinsot, T. and D. Veynante (2012). *Theoretical and numerical combustion*. Third Edition by T. Poinsot. *(p. x, 18, 44, 46, 47, 49)*

Pope, S. B. (1985). Pdf methods for turbulent reactive flows. *Progress in energy and combustion science 11*(2), 119–192. *(p. 47)*

Pope, S. B. (2000). *Turbulent Flows*. 1st edition. Cambridge University Press. *(p. 44)*

Popov, N. (2001). Investigation of the mechanism for rapid heating of nitrogen and air in gas discharges. *Plasma Physics Reports 27*(10), 886–896. *(p. 25, 29, 35)*

Popov, N. A. (2007). The effect of nonequilibrium excitation on the ignition of hydrogen-oxygen mixtures. *High Temperature 45*, 261–279. *(p. 71)*

Popov, N. A. (2011). Fast gas heating in a nitrogen oxygen discharge plasma: I. kinetic mechanism. *Journal of Physics D: Applied Physics 44*(28). *(p. 25, 29, 31)*

Popov, N. A. (2013a). Fast gas heating initiated by pulsed nanosecond discharge in atmospheric pressure air. *AIAA Aerospace Sciences Meeting, Grapevine, TX*, 105251. *(p. 35, 176)*

Popov, N. A. (2013b). Fast gas heating initiated by pulsed nanosecond discharge in atmospheric pressure air. *AIAA Aerospace Sciences Meeting, Grapevine, TX, 2013-105251.*. *(p. 108, 144)*

Quader, A. (1976). What limits lean operation in spark ignition engines-flame initiation or propagation? *SAE Technical Paper 760760*. *(p. 3)*

Refael, S. and E. Sher (1985). A theoretical study of the ignition of a reactive medium by means of an electrical discharge. *Combustion and Flame 59*(1), 17–30. *(p. 15, 66)*

Rivarolo, M., G. Riveros-Godoy, L. Magistri, and A. F. Massardo (2019). Clean hydrogen and ammonia synthesis in paraguay from the itaipu 14 gw hydroelectric plant. *ChemEngineering 3*(4), 87. *(p. 1)*

Rusterholtz, D. (2012). *Nanosecond Repetitively Pulsed Discharges in Atmospheric Pressure Air*. Ph. D. thesis, Ecole Centrale Paris. *(p. x, 52)*

Rusterholtz, D. L., D. A. Lacoste, G. D. Stancu, D. Z. Pai, and C. O. Laux (2013). Ultrafast heating and oxygen dissociation in atmospheric pressure air by nanosecond repetitively pulsed discharges. *Journal of Physics D: Applied Physics 46 464010*, 464010. *(p. x, xi, 15, 17, 29, 35, 37, 52, 53, 54, 55, 56, 58, 59, 108, 144, 146, 162, 176)*

Sharma, A., V. Subramaniam, E. Solmaz, and L. L. Raja. (2019). Coupled computational studies of non-thermal plasma based combustion ignition. *In AIAA Scitech 2019 Forum. American Institute of Aeronautics and Astronautics*. *(p. 71)*

Sher, E., J. Ben-Ya'ish, and T. Kravchik (1992). On the birth of spark channels. *Combustion and Flame 89*(2), 186–194. *(p. 15, 66)*

Shibkov, V. M., A. V. Chernikov, A. P. Ershov, R. S. Konstantinovski, L. V. Shibkova, and V. V. Zlobin (2004). propane-butane-air mixture ignition and combustion in the aerodynamic channel with the stagnant zone. *42nd AIAA aerospace sciences meeting including the new horizons forum and aerospace exposition, Reno, Nevada*. *(p. 4)*

Stancu, G. D., F. Kaddouri, D. A. Lacoste, and C. O. Laux (2010). Atmospheric pressure plasma diagnostics by oes, crds and talif. *Journal of Physics D: Applied Physics 43*(12), 124002. *(p. 17, 29, 176)*

Starikovskaia, S. M. (2006). Plasma assisted ignition and combustion. *Journal of Physics D: Applied Physics 39*(16). *(p. 15)*

Starikovskiy, A. and N. Aleksandrov (2013). Plasma-assisted ignition and combustion. *Progress in Energy and Combustion Science 39*, 61–110. *(p. x, 4, 13, 17, 29, 30, 71, 175)*

Tacina, R., C.-P. Mao, and C. Wey (2003). Experimental investigation of a multiplex fuel injector module for low emission combustors. *41st Aerospace Sciences Meeting and Exhibit, 6-9 January 2003, Reno, Nevada. AIAA 2003-827.*. *(p. 3)*

Takana, H. and H. Nishiyama (2014). Numerical simulation of nanosecond pulsed dbd in lean methane–air mixture for typical conditions in internal engines. *Plasma Sources Science and Technology 23*, 034001. *(p. 28)*

Takita, K., T. Uemoto, T. Sato, Y. Ju, G. Masuya, and K. Ohwaki (2000). Ignition characteristics of plasma torch for hydrogen jet in an airstream. *Journal of Propulson and Power 16*, 227–233. *(p. 3)*

Teets, R. and J. Sell (1988). Calorimetry of ignition sparks. *SAE transactions 97*, 371–383. *(p. 68)*

Teunissen, J. and U. Ebert (2017). Simulating streamer discharges in 3d with the parallel adaptive afivo framework. *Journal of Physics D: Applied Physics 50*(47), 474001. *(p. 22)*

Tholin, F. (2012). *Numerical simulation of nanosecond repetitively pulsed discharges in air at atmospheric pressure : Application to plasma-assisted combustion.* Ph. D. thesis, Ecole centrale de Paris, France. *(p. 22, 23)*

Tholin, F. and A. Bourdon (2013). Simulation of the hydrodynamic expansion following a nanosecond pulsed spark discharge in air at atmospheric pressure. *Journal of Physics D: Applied Physics 46*, 365205. *(p. ix, 26, 27)*

Tholin, F., D. Lacoste, and A. Bourdon (2014). Influence of fast-heating processes and o atom production by a nanosecond spark discharge on the ignition of a lean h2/air premixed flame. *Combustion and Flame 161*(5), 1235–1246. *(p. 24, 28, 71)*

Townsend, J. S. (1910). *The Theory of Ionisation of Gases by Collision.* London, Constable. *(p. 22)*

Valera-Medina, A., R. Marsh, J. Runyon, P. Pugh, D. Beasley, T. Hughes, and P. Bowen (2017). Ammonia–methane combustion in tangential swirl burners for gas turbine power generation. *Applied Energy 185*, 1362–1371.

(p. 2)

Vantieghem, S. (2011). *Numerical simulations of quasi-static magnetohydrodynamics using an unstructured finite volume solver: development and applications*. Ph. D. thesis, Universite Libre de Bruxelles. *(p. 42)*

Verhoeven, D. (1997). Spark heat transfer measurements in flowing gases. *Revue de l'Institut Français du Pétrole 52*(4), 453–464. *(p. 68)*

Veynante, D. and L. Vervisch (2002). Turbulent combustion modeling. *Progress in Energy and Combustion Science 28*(3), 193–266. *(p. 150)*

Vignat, G., N. Minesi, P. Rajendram Soundararajan, D. Durox, A. Renaud, V. Blanchard, C. O. Laux, and S. Candel (2021). Improvement of lean blow out performance of spray and premixed swirled flames using nanosecond repetitively pulsed discharges. *Proceedings of the Combustion Institute 38*(4), 6559–6566. *(p. xvii, 136, 137)*

Wang, W., R. Snoeckx, X. Zhang, M. S. Cha, and A. Bogaerts (2018). Modeling plasma-based co2 and ch4 conversion in mixtures with n2, o2, and h2o: The bigger plasma chemistry picture. *The Journal of Physical Chemistry C 122*(16), 8704–8723. *(p. 25)*

Williams, S., S. Popovic, L. Vuskovic, C. Carter, L. Jacobson, S. Kuo, D. Bivolaru, S. Corera, M. Kahandawala, and S. Sidhu (2004). Model and igniter development for plasma assisted combustion. *42nd AIAA Aerospace Sciences Meeting and Exhibit, Reno, NV, AIAA*. *(p. 3)*

Xu, D. A., D. A. Lacoste, and C. O. Laux (2015). Ignition of quiescent lean propane-air mixtures at high pressure by nanosecond repetitively pulsed discharges. *Plasma Chemistry and Plasma Processing 272-4324*, 1–19. *(p. xii, 4, 18, 69, 70, 71, 175)*

Züttel, A., A. Remhof, A. Borgschulte, and O. Friedrichs (2010). Hydrogen: the future energy carrier. *Phil Trans Ser A Math Phys Eng Sci 368(1923):3329-42*. *(p. 1)*